The consequences of gas slug ascent in a stratified magma on Strombolian eruption dynamics

A thesis by Antonio Capponi
MSc (Sapienza, University of Rome)

Submitted in fulfilment of the requirements for the degree of

Doctor of Philosophy at Lancaster University,

January 2016.

To my Father

…now playing 3D chess with Mr Spock…

Declaration

I confirm that this work is my own, except where otherwise stated, and has not been submitted for a higher degree elsewhere. Excerpts of this thesis have been published in journals, as indicated within.

Antonio Capponi

January 2016

You know the greatest danger facing us is ourselves, an irrational fear of the unknown. But there's no such thing as the unknown, only things temporarily hidden, temporarily not understood

James T. Kirk

Abstract

Strombolian volcanic activity, one of the most common on Earth, results from the bursting of large gas pockets (*slugs*) following ascent through relatively low-viscosity magma within the volcanic conduit. However, this paradigm was forged when the complex rheology of the magma at Stromboli, the model-type volcano for this activity, was still poorly constrained. Textural and petrological evidence has recently suggested the presence of viscous, degassed magma layers in the upper portion of the conduit at Stromboli. This layer acts as a plug, through which slugs burst, controlling the eruptive dynamics. To date, little has been done to integrate this scenario into current models of volcanic eruptions and interpretation of geophysical signals. This study investigates slug ascent through a rheologically stratified magma column using analogue laboratory experiments, numerical modelling and 3D computational fluid dynamic simulations. The results illustrate (1) the range of slug flow configurations that develop in a rheologically stratified column, (2) the relevance of such configurations to Strombolian-type volcanoes, and (3) the key parameters controlling the transition in flow configurations. Each identified configuration encompasses processes affecting slug expansion and burst: for example, dynamic narrowing and widening of the conduit, instabilities along the falling liquid film and slug break-up. These complexities lead to variations in eruption magnitude, style and consequent geophysical signals. The similarity between laboratory infrasonic waveforms, whose amplitudes are strongly dependant on the flow configuration in which the slugs burst, and measured infrasonic signals from Stromboli suggests that the slug burst through a plug represents a viable first-order mechanism for the generation of volcano-infrasonic signals. Furthermore, the presence of a plug seems to be a pre-requisite for the generation of eruptive pulses observed in single explosions at Stromboli, and the interaction between an ascending slug and the liquids promotes magma mingling, therefore affecting the properties of the ejecta.

Auxiliary Content

Included with this thesis is one DVD, providing the Supplementary Material for the manuscripts of Del Bello et al. (2015), Capponi et al. (2016a) and Capponi et al. (2016b). The DVD is arranged in the following folders, each of which contains several video (*.mp4) files and the PDF version of the published papers:

- Chapter 5 Del Bello et al. 2015 (published paper):
  Video V01, V02, V03, V04 and V05
  Del Bello et al. 2015, PDF file
- Chapter 6 Capponi et al. 2016a (published paper):
  Video V01, V02, V03, V04, V05, V06 and V07
  Capponi et al. 2016b, PDF file
- Chapter 8 Capponi et al. 2016b (published paper):
  Video 1, 2, 3, 4, 5, 6 and 7

A full description of the videos can be found at the end of each relevant chapter (Chapter 5, §5.8; Chapter 6, §6.7; Chapter 8, §8.8).

The Supplementary Material for Chapter 5, Chapter 6 and Chapter 8 is also available online at the following addresses:
http://dx.doi.org/10.1016/j.epsl.2015.04.034 (Del Bello et al. 2015)
http://dx.doi.org/10.1016/j.epsl.2015.12.028 (Capponi et al. 2016a)
http://dx.doi.org/10.1007/s00445-016-1001-z (Capponi et al. 2016b)

Acknowledgements

A huge thanks goes to Steve Lane and Mike James, for their constant encouragement, patience, support and the very thoughtful discussions. They provided an incredible amount of advice and inspiration. Thanks for caring so much about my work and sharing your knowledge with me. Also, thanks for the many (many) unscheduled meetings and prompt replies every time I showed up at your door unannounced!

I want to thank Jacopo Taddeucci, Elisabetta Del Bello, Damien Gaudin, Piergiorgio Scarlato, Daniele Andronico, with whom I spent amazing days on Stromboli during my secondments, discussing (also) about science while working on Pizzo (or eating fantastic pizza).

I want to express my great thankfulness to my family, for their unconditional encouragement. Their support in this and all my other adventures allowed me to reach this stage in my life. Likewise, thanks to all my distant friends, for your friendship and support. In particular, thanks to Alessia for the many serious and (mostly) non-serious discussions we had. Not less importantly, I would like to thank Kara Thrace, always full of surprises.

I would also like to thank many friends from LEC: Victor, Lisi, Kirsty, Giovanni, Lucas, Anson, Bea, Nando, Joe, Tom, Peter, Jenny, Laura, and many more, for welcome distractions, coffee/tea and cake… lots of cake!

Once again, I thank my dear friend Silvia, always present, supportive and with an unlimited supply of good advices. My thanks to Seba, Luciano and Mara as well: you always make me feel like I am home.

Last but not least, I must thank the big family NEMOH. Thanks Paolo Papale, Raffaela Pignolo and Alessandro Fornaciai for the creation and support of an amazing group of crazy people and for believing in us. And thanks to all the NEMOHs: Cristian, Julie, Karen, Damien, Johannes (aka Giovanni), Léna, Laura, Eduardo, Claudio, Alex, Samantha, Pablo, Hannah, Werner, Francisco, Deepak, Beatriz. I had the most amazing time with you guys: I doubt I could have had better years during my PhD. Looking forward to see you again, doing science while having great time!

Table of contents

List of figures

Chapter 2

Chapter 3

Chapter 4

Chapter 5

Chapter 6

Chapter 7

Chapter 8

List of tables

List of symbols and abbreviations

Latin alphabet

A'	*Film cross section*	*dimensionless*
A	*Tube cross sectional area*	m^2
Ar	*Archimedes number*	*dimensionless*
c	*Sound speed*	*343 m/s*
D or d	*Conduit/tube diameter*	*m*
Eo	*Eötvös number*	*dimensionless*
Fr	*Froude number*	*dimensionless*
g	*Gravitational acceleration*	$9.81\ m/s^2$
h_0	*Initial height of the liquid above the slug*	*m*
h	*Height of the liquid above the slug*	*m*
h_1'	*Initial height of low-viscosity liquid above the slug*	*m*
h_3' or h_p	*Initial height of the plug*	*m*
h_1	*Height of low-viscosity liquid above the bubble*	*m*
h_2	*Height of low-viscosity intrusion*	*m*
h_3	*Depth from the plug top to the intrusion*	*m*
h_{lim}	*Depth at which the slug become unstable*	*m*
h'_{lim}	*Dimensionless form of* h_{lim}	*dimensionless*
L_0	*Initial slug length*	*m*
L_a	*Length of the slug at atmospheric pressure*	*m*
L'_a	*Dimensionless form of* $L_{a\ lim}$	*dimensionless*
$L_{a\ lim}$	*Critical length that a slug can reach without becoming unstable*	*m*
L or L_s	*Slug length*	*m*
M	*Gas mass*	*kg*
Mo	*Morton number*	*dimensionless*
N_f	*Inverse viscosity*	*dimensionless*
P_0	*Initial gas slug pressure*	*Pa*
P or P_s	*Slug pressure*	*Pa*
P'	*Slug pressure during expansion*	*Pa*
P_a	*Pressure above the liquid surface*	*Pa*
P_h	*Static liquid pressure at the slug nose*	*Pa*
P^*_h	*Static liquid pressure at the slug nose during gas expansion*	*Pa*
P_L	*Pressure variations at the base of the apparatus*	*Pa*
Ps	*Poiseuille number*	*dimensionless*
P_{slim}	*Limiting pressure below which a slug becomes unstable*	*Pa*
P^*_{slim}	*Dimensionless form of* P_{slim} *(James et al. 2009)*	*dimensionless*
$P'_{s\ lim}$	*Dimensionless form of* P_{slim} *(Del Bello et al. 2012)*	*dimensionless*
q	*Mass flux*	$kg\ s^{-1}\ m^{-2}$
r_c	*Conduit/tube radius*	*m*
r_s	*Slug radius*	*m*
r_p	*Viscous annulus radius*	*m*

r_ϕ	*Intrusion radius*	*m*
Re	*Reynolds number*	*dimensionless*
Re_b	*Slug Reynolds number*	*dimensionless*
S, V_st and v_st	*Distance between the slug base and its initial position*	*m*
T	*Temperature*	*°C*
T	*Time*	*s*
U_f	*Mean flow velocity in a pipe*	*m/s*
V_0	*Initial volume of gas*	*ml*
V_a	*Volume that the slug would have at ambient pressure*	m^3
V'_a	*Non-dimensional slug volume*	*dimensionless*
V_s,	*Slug ascent velocity*	*m/s*
V^0_s	*Bubble terminal ascent velocity*	*m/s*

Greek alphabet

ΔL	*Slug length increase during expansion*	*m*
ΔP_A	*Gas pressure changes above the liquid surface, with respect to the vacuum chamber pressure*	*Pa*
$\Delta P_A\hat{}$	*Peak excess pressure*	*Pa*
ΔP_b	*Theoretical estimate of the peak dynamic overpressure in the slug at burst*	*Pa*
γ	*Heat capacity ratio*	*dimensionless*
γ_s	*Slug Stability Index*	*dimensionless*
λ	*Falling liquid film thickness*	*m*
λ'	*Dimensionless falling liquid film thickness*	*dimensionless*
μ	*Viscosity*	*Pa s*
μ_1	*Viscosity of the underlying magma*	*Pa s*
μ_2	*Viscosity of the plug*	*Pa s*
μ^*	*Viscosity contrast*	*dimensionless*
σ	*Surface tension*	*N/m*
π	*Pi*	*3.14*
ρ	*Density*	kg/m^3
ρ_1	*Low-viscosity liquid density*	kg/m^3
ρ_2	*Plug density*	kg/m^3

Abbreviations

ASG	*Active Strain Gauge*
a.s.l.	*above sea level*
C1	*Configuration 1*
C2	*Configuration 2*
C3	*Configuration 3*
CC	*Central Crater*

CF	*Collapsing Foam*
CFD	*Computational Fluid Dynamic*
DAQ	*Data Acquisition*
fps	*frames per second*
HK	*High potassium*
HP	*High Porphiricity*
IMAQ	*Image Acquisition*
LP	*Long Period or Low-Porphyricity*
MAX	*Measurements & Automatic Explorer*
NEC	*North-East Crater*
NEMOH	*Numerical, Experimental and stochastic Modelling of vOlcanic processes and Hazard*
PoCL	*Power over Camera Link*
RSD	*Rise Speed Dependent*
SWC	*South-West Crater*
TDMS	*Technical Data Management Streaming*
VI	*Virtual Instruments*
VLP	*Very Long Period*

Chapter 1 - Introduction

Strombolian volcanoes are abundant and characterized by relatively mild, impulsive events resulting from the burst of large gas pockets – *slugs* – decoupling from low-viscosity magma (e.g., Blackburn et al. 1976; Parfitt 2004). These volcanoes, although generally steady in time, can show a variety of eruptive styles ranging from passive degassing (e.g., Harris and Ripepe 2007a, b), through mild Strombolian explosions (e.g., Patrick et al. 2007), up to vigorous paroxysmal eruptions (e.g., Houghton and Gonnermann 2008). However, the mechanism(s) responsible for these transitions, mirrored in variations in explosion magnitude, and associated with geophysical signals and textural properties of the ejecta, is/are still unknown and frequently subject to debate. This study aims to provide new insights into this issue, with a focus on the variability of Strombolian explosions.

Despite a large body of literature concerning the general mechanism behind Strombolian explosions and the parameters determining the changes in eruptive dynamics (e.g., Vergniolle and Brandeis, 1996; Houghton and Gonnermann 2008; James et al. 2009; Del Bello et al. 2012; Lane et al. 2013), these studies have almost always investigated the ascent, expansion and burst of slugs in rheologically uniform media. Recent petrological studies (e.g., Lautze and Houghton 2006; Gurioli et al. 2014) suggest the presence of a highly crystalline magma in the upper portion of the conduit, which could act as a plug and favour mingling of magmas with different physical properties in the uppermost part of the conduit. This idea was originally proposed qualitatively by Barberi et al. (1993), suggesting that "*the upper part of the Stromboli conduit is filled with a dense, degassed, viscous magma … … It would represent an obstacle to the rising gas bubbles, which would accumulate under the degassed, viscous layer up to the time overpressure required for the Strombolian blast is reached"* (Barberi et al., 1993; Gurioli et al. 2014). However, knowledge of the origin, properties and petrological constraint for a possible viscous layer is still limited. Indeed, the few detailed studies on a plug, all based on textural and petrological analyses of field samples, cover only a limited range of possible styles of activity at Strombolian volcanoes (e.g., Lautze and Houghton 2005, 2006; Gurioli et al. 2014). Furthermore, despite providing important rheological constraints (i.e., density and viscosity of the plug), there are no information about properties such as layer thickness and timescales of formation, although it has been proposed that any variation in the properties of this layer (i.e., thickness and viscosity) may affect not only explosion style and magnitude (e.g., Lautze and Houghton 2006; Leduc et al. 2015), but also the properties of the ejecta and the associated geophysical signals (e.g., Lyons et al. 2012; Gurioli et al. 2014). Furthermore, possible additional complexities due to the presence of a plug may have been revealed by high-speed videography, where the ejection pulses within a single Strombolian eruption likely result from changes in the flow pattern, with collapses of the liquid film surrounding long slugs generating pressure fluctuations (Taddeucci et al. 2012a; Gaudin et al. 2014). Given this recent textural and field evidence, the scenario of a gas slug ascending and bursting in a rheologically uniform melt seems now too simplistic to explain all the variability observed at Strombolian-type volcanoes in explosive activity, geophysical signals and the textural properties of ejecta.

This study challenges the assumption of a rheological uniform magma column, providing insights into the role played by an upper viscous layer at the top of the conduit (a "*plug"*) on the eruption dynamics. The scenario of a gas slug ascending through a rheologically stratified magma column is investigated using first-order analogue laboratory experiments, numerical modelling and 3D computational fluid dynamic simulations. The results presented here illustrate how the presence of a plug leads to complex flow configurations, variations in gas slug overpressure and, consequently, in the range of burst processes observed at the surface. The implications of each flow configuration on eruption dynamics are being discussed, with a particular focus on Stromboli volcano (Italy). Stromboli is indeed one of the few open-vent volcanoes in the world where it is possible to constantly witness the explosive activity and acquire data from the crater terrace in a relatively safe environment. For this reason, Stromboli, the model volcano for Strombolian-style eruptions, has always represented an ideal natural laboratory; nonetheless, the modelling developed in this study and the volcanic implications can be applied to other Strombolian-type volcanoes worldwide characterized by similar activity.

Chapter 2 will first introduce the necessary background on Strombolian eruptions, their dynamics and the source mechanisms for the associated geophysical signals. Chapter 3 will introduce the background on the dimensionless scaling methods, followed by an overview of the main experimental investigations concerning the processes involved with the ascent, expansion and burst of slugs in a single-viscosity system. Laboratory experiments are the core of this study, thus a detailed description of the experimental apparatus, procedures, data-logging system and how data were processed is presented in Chapter 4.

Data presentation and discussions will be covered in Chapters 5 to 8 in form of manuscripts. The first experimental investigation on a gas slug ascending in a rheologically stratified conduit (Chapter 5; Del Bello et al. 2015, *Earth and Planetary Science Letters*, 423: 210–218) will introduce the key changes in the flow pattern due to the presence of a plug, and their possible effects on the generation of eruptive pulses, mingled pyroclasts and variations in explosion magnitude. A second manuscript, built on the work of Del Bello et al. (2015), will present (1) the main flow configurations that develop for a gas slug ascending in a rheologically stratified conduit, identified during a comprehensively scaled experimental campaign and (2) the development of a 1D numerical model aimed to illustrate the relevance of the identified configurations to Strombolian-type volcanoes. The implications of each flow configuration on eruption magnitude, style and ejecta properties are explored as well (Chapter 6; Capponi et al. 2016a, *Earth and Planetary Science Letters,* 435: 159–170). The effects of the flow configuration on geophysical signals will be detailed in Chapter 6, together with a comparison between laboratory waveforms and natural infrasonic data from Stromboli volcano (Chapter 7; Capponi et al. *in preparation*).

Finally, the practical part of the study uses field data collected at Stromboli to investigate the styles of Strombolian behaviour, illustrating for the first time the exact control of the vent conditions (open vent vs. debris-covered vent) on eruptive dynamics. This has been done by detailing how a more superficial cover can affect (1) the vent processes for each style observed and (2) the intensity of the explosions, plume dynamics, nature of the ejecta and contribute to the generation of a plug increasing the viscosity of the shallower magma (Chapter 8; Capponi et al. 2016b, *accepted for publication* in *Bulletin of Volcanology*). All obtained results will be then summarized and discussed in Chapter 9, highlighting the achieved knowledge. Ultimately, this study is motivated by the necessity of improving our understanding of volcanic events by strengthening the link between fluid dynamic processes occurring in the conduit, field observations and detectable geophysical signals.

Chapter 2 - Strombolian activity: A review

Volcanic eruptions have always fascinated humankind since prehistory, although at that time any manifestation of their power could only be attributed to acts of Gods. Considered as the "safety valves" for the Earth by the Greek philosopher Strabo (64 BC-AD 24), for centuries volcanoes have been major protagonists on Earth, where are praised for their fertile soil or feared for their destructive power.

However, now as before, whether incandescent effusive events, picturesque mild explosions or dramatic plumes up to the stratosphere, what is seen at the surface is only a fraction of the processes acting from the depth of the Earth up to the shallow volcanic conduit. These unseen and unpredictable processes can lead to secondary violent events even in volcanoes usually not life-threatening.

It is therefore of fundamental importance to understand the whole eruption dynamics, including the general mechanisms beyond volcanic eruptions as well as their detailed conduit dynamics and the role of physical parameters controlling such events.

2.1 The birth and life of a bubble

What drives a volcanic eruption? A simple – yet accurate – answer would be: volatiles. Indeed, regardless the styles of activity, volatiles play a fundamental role in determining the physical evolution of magmas. Volatiles, either dissolved or exsolved, affect magma viscosity, compressibility, buoyancy, fragmentation and, ultimately, have complete control on eruptive style: from effusive volcanism, relatively mild explosive eruptions up to violent Plinian and phreatic-magmatic events.

Magmas are three-phase systems comprising a crystalline phase of plagioclase, clinopyroxene and olivine (solid phase) in equilibrium with a shoshonitic melt (liquid phase), in which several volatile species – particularly water and carbon dioxide – are dissolved (gas phase) (general composition for a basaltic magma; e.g., Métrich et al. 2001). After water (H_2O) and carbon dioxide (CO_2), the most abundant volatiles are hydrogen sulphide (H_2S), sulphur dioxide (SO_2), Chlorine (Cl) and Fluorine (F) (e.g., Wallace 2005).

2.1.1 Bubble nucleation

At depth the gasses are dissolved within the melt. The higher the pressure the greater is the amount of volatile that can be dissolved. The degree of solubility depends also on the properties of the hosting magma: in silicic magmas solubility is greater compared to basaltic magmas. When the density of the magma is less than the surrounding rocks, it will start to rise and during the magma ascent toward the surface pressure decreases (Wilson and Head 1981). As this happens, magmatic differentiation starts: crystals form removing from the original magma elements such as Aluminium (Al), Magnesium (Mg), Iron (Fe) and Calcium (Ca). As crystals form, liquid composition changes and the melt becomes enriched with elements that do not crystallize and volatiles. As pressure decreases during ascent, gas concentration increases: if the concentration reaches a critical point, the melt may be vapour saturated, and it then starts to exsolve, the gas phase vesiculating (i.e., the gas phase exsolves from the magma nucleating bubbles). Because of their high concentration (Wallace and Anderson 2000), H_2O and CO_2 are the gas contributing most to magma vesiculation. Bubble nucleation can be homogenous, when bubbles start to nucleate spontaneously as soon as the pressure drops to saturation point. It can also be heterogeneous, when any crystal in the magma acts as a nucleation site and bubbles nucleate even for a slight oversaturation (e.g., Mangan et al. 2004).

2.1.2 Bubble growth

Viscous magmas do not allow the bubble to grow, due to lower diffusivity of H_2O in acid melts, leading to the continuous formation of microscopic bubbles (10-200 μm radius, Sparks 1978; Proussevitch et al. 1993) and causing an increase in magma overpressure; thus, at the surface the gas is released violently in the atmosphere. In contrast, magmas characterized by relatively low-viscosity, typical of basaltic volcanism, allow an easy segregation of the gas phase and for the bubbles to grow more freely (e.g., Sparks 1978), and for viscosity less than $\approx 10^9$ Pa s magmas can expand freely without developing a strong overpressure (Barclay et al. 1995). Numerical models suggest that for magma ascent rates between 1 m/s to 100 m/s, degassing rates in basaltic systems are sufficient to keep the dissolved volatile concentration at equilibrium with the decreasing ambient pressure, and degassing do not start until the magma rises to at least 1500-200 m of depth, depending on initial depth of rise (Proussevitch and Sahagian 1996).

Once a bubble is formed in a low-viscosity magma, it starts to grow and ascend through the conduit. The growth behaviour will be controlled by both viscosity and diffusivity: initially, growth is rapid and mainly controlled by an efficient diffusion process of the gas from the magma to the bubble; the only parameter limiting the rate of increase of the bubble is the viscosity of the magma. Then, as the bubble grows, its internal pressure increases until an equilibrium pressure between the gas and the magma cannot be maintained by the diffusive flux, and the parameter limiting the growth is the expansion of the bubble (Toramaru 1995). Furthermore, the presence of bubbles itself may affect magma rheology, leading to either an increase or decrease of magma viscosity depending on the bubble shape (Llewellin et al. 2002).

As the growth proceeds, the bubble ascends buoyantly through the magma column leading to an efficient outgassing that results in effusive volcanism. Or the bubbles can grow during ascent, and start to interact between each other. If this is the case, bubble behaviour is controlled by magma viscosity, ascent velocity and discontinuities within the conduit. As soon as the liquid bridges between the bubbles rupture, coalescence takes place: this process can lead to the formation of larger gas pockets (*gas slugs*) that burst at surface generating a Strombolian eruption (e.g., Sparks 2003; Parfitt 2004).

2.2 Origin of the volcanic slugs

Two models exist and try to explain the formation of gas slugs: the *Rise Speed Dependent* (*RSD*) and the *Collapsing foam* (*CF*). Both models assume that slugs are formed by coalescence of smaller bubbles at depth, but they differ in explaining the mechanism of bubble coalescence.

According to the RSD model (Wilson and Head 1981; Parfitt and Wilson 1995; Parfitt 2004), large gas bubbles are generated by coalescence of smaller ones rising in the conduit due to their different speeds relative to the magma. If the ascent velocity of the magma is relatively low, the bubbles within it have enough time to coalesce. The rise speed of the bubbles depends on their size: larger bubbles are faster, able to catch up smaller ones, coalesce with them and increase their volume while ascending through the conduit. This leads to the formation of large bubbles that occupy almost the entire section of the conduit and burst at the magma free surface, resulting in a Strombolian eruption (*Fig. 2.1*). In more rapidly ascending magma, the bubbles do not have time to rise sufficiently far through the column to coalesce into a slug before the magma is erupted. Here, bubbles start to grow by diffusion and decompression while more bubbles are formed during the ascent. The gas volume fraction increases until it is large enough (60-95%) to trigger fragmentation of the magma, after which the gas-magma mixture accelerates resulting in the eruption of a jet of gas and magma fragments, i.e. Hawaiian eruption (Parfitt 2004). The transition between Hawaiian and Strombolian activity occurs with a theoretical magma rise speed of ~0.01-0.1 m s^{-1} (Parfitt and Wilson 1995). The model also suggests that major Strombolian explosions arise when the magma rise speed is too high to produce purely Strombolian activity but too low to yield purely Hawaiian activity (Parfitt 2004).

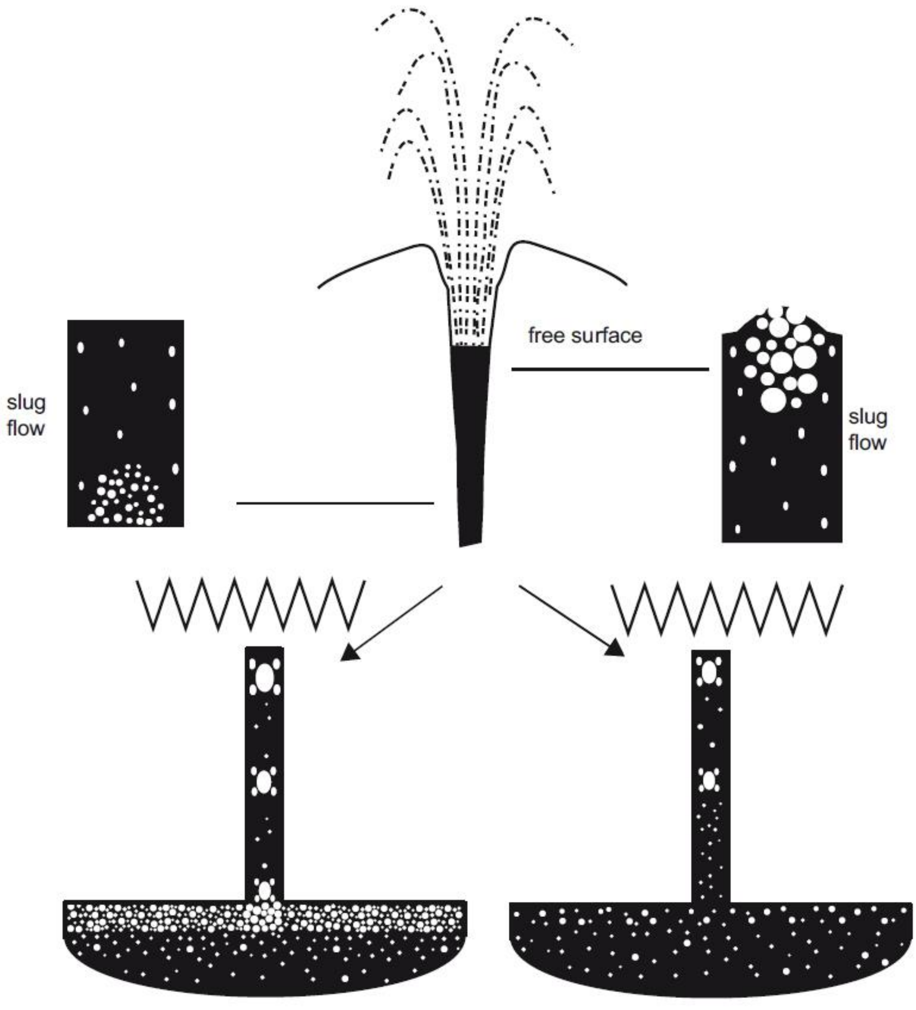

Figure 2.1 Conceptual models for the origin of the slugs: (**left**) Collapsing foam and (**right**) Rise Speed Dependent model (Houghton and Gonnermann 2008).

According to the CF model (Vergniolle and Jaupart 1986; Jaupart and Vergniolle 1988, 1989), bubble nucleation and growth occur inside a magma chamber. The bubbles rise and accumulate at the roof of the chamber creating a foam layer. Once this layer reaches a critical thickness, if magma viscosity is relatively low, the foam collapses entirely forming a large gas slug that erupts into the conduit, producing an annular flow regime and, ultimately, Hawaiian activity. With higher viscosity, the foam collapses partially and periodically, producing a series of large bubbles that enters the conduit and ascends through it, leading to Strombolian activity (*Fig. 2.1*).

Both the *Rise Speed Dependent* and *Collapsing Foam* models agree that gas segregates from the magma and generates gas pockets that burst at the magma free surface. When applied to the 1983-1986 Pu'u 'O'o eruption of Kilauea Volcano, Hawaii, the estimated magma rise speed – obtained using gas volume fluxes during fountaining activity and lava outpouring – ranged between ~0.3 m/s and ~0.01 m/s. These values matched the speed predicted by the RSD model, 0.3 m/s for Hawaiian activity, 0.001 m/s for Strombolian activity. In contrast, the CF model explained the eruptions in terms of CO_2 exsolving within the magma chamber and forming the foam layer at its roof. But field data showed that CO_2 only contributed for the ~3% of the total volume of erupted gas: there were no indications of an increase of CO_2 capable to justify gas accumulation at depth, disproving the model. However, there are volcanic systems, such as Stromboli, in which seismic (Chouet et al. 1999) and spectroscopic (Burton et al. 2007a) data suggest gas accumulation several hundred meters beneath the surface. In this case CF could provide a valid explanation (Parfitt 2004).

In all likelihood these two main mechanisms represent the end members of a much wider range of processes and the mechanism beyond these explosions is probably a mix of the two models. The presence of an "ideal" roof at the top of a reservoir as described by the CF model is unlikely, but bubbles might be collected in the conduit beneath structural obstacles, regions of geometrical or inclination changes or at the boundaries with a strong rheological discontinuity. Here they could accumulate, coalesce and – at some point – ascend, continuing to grow and coalesce on their way up to the surface.

Two alternative models, developed to explain variations in seismic and acoustic measurements, try to explain gas coalescence; though, these are similar to both RSD and CF models. Bubbles can nucleate and grow in the magma due to decompression during its ascent (*free coalescence* model, *Fig. 2.2a*) or can accumulate at a barrier at depth, encouraging gas coalescence and the formation of larger bubbles (*forced coalescence* model, *Fig. 2.2b*; Ripepe and Gordeev 1999). Either way, when the bubbles reach the magma free surface, their bursts generate a series of infrasonic pulses whose amplitude relates to bubble volume and overpressure (~0.5 m radius can produce small infrasonic pulses of 0.4-1.3 Pa; Ripepe and Gordeev 1999). For a bubble of 0.5 m radius generated according to the *forced coalescence* model, the pressure drop in the magma can reach values up to 2.2×10^4 Pa, greater than the *free coalescence* model (80-800 Pa depending on the initial volume). This value is consistent with tremor ground displacement of $\sim10^{-5}$ m measured at Stromboli, strengthening the theory that a structural barrier like, e.g., a dyke, may be a control factor for gas coalescence and degassing style (Ripepe and Gordeev 1999).

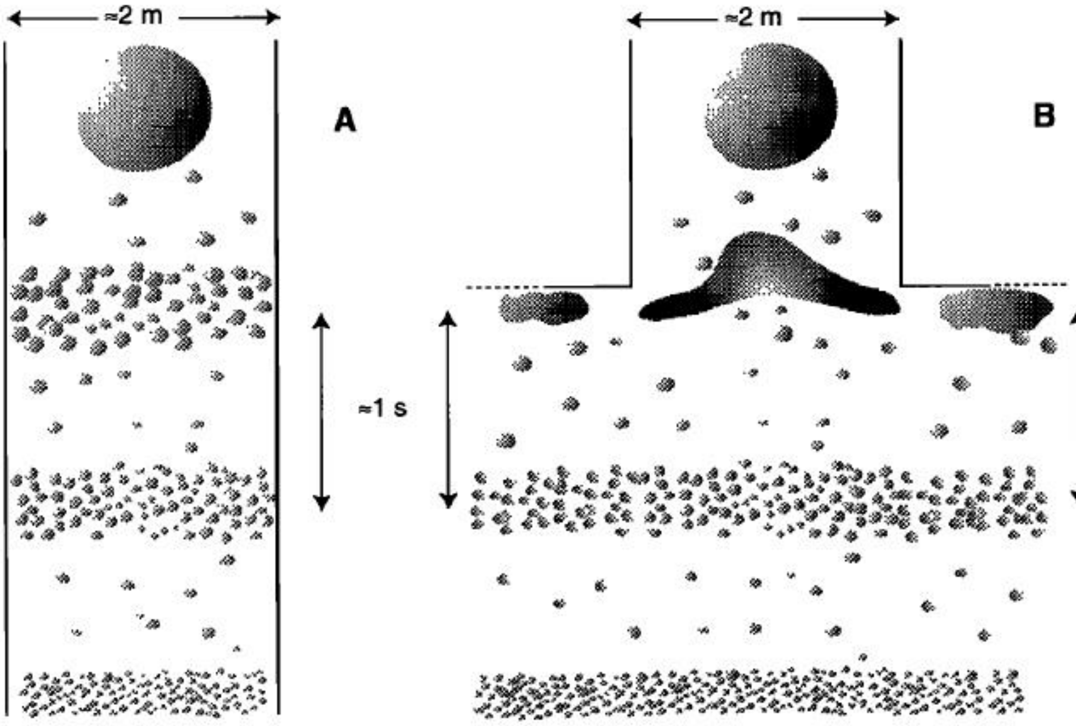

Figure 2.2 Conceptual models for gas coalescence: (**a**) Free coalescence model and (**b**) Forced coalescence model (Ripepe and Gordev 1999).

Once gas bubbles rise through the conduit, the flow can be organized in four main regimes, depending on the gas supply. Bubbly flow describes the ascent of numerous small bubbles that do not interact. Increasing gas supply results in an increase in bubble concentration, favouring bubble coalescence and the creation of a population of bubbles of different size. In slug flow, slugs occupy almost the entire section of the conduit, surrounded by a falling liquid film and each slug is separated by liquid bridges. The distance between each slug decreases with increasing gas flux, the slug can get closer and the liquid starts to be locally dragged by the slugs, creating an unstable flow (churn flow). The transition to annular flow occurs after the complete destruction of the liquid bridges between the slugs, following a further increase of the gas influx, and the liquid is now dragged upward by the gas (*Fig. 2.3*) (e.g., Vergniolle and Brandeis 1986; Seyfried and Freundt 2000; Pioli et al. 2012).

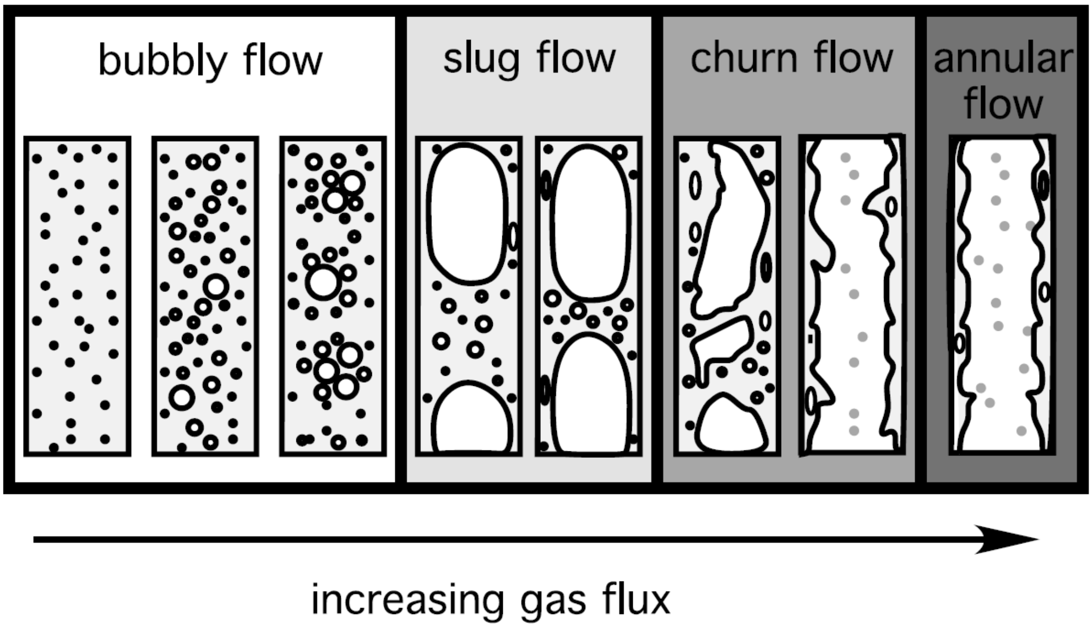

Figure 2.3 Conceptual sketches for idealized vertical two-phase flow patterns in a vertical volcanic conduit filled with a low-viscosity magma (grey shades). For a low gas flux, small and numerous bubbles (white shades) do not interact between each other (bubbly flow). Increasing the gas flow, bubble concentration increases. When smaller bubbles coalesce, slugs form, separated by liquid bridges (slug flow). Increasing the gas flow, the slugs get closer until the gas starts to drag locally the liquid at the walls of the bubbles (churn flow). For greater gas flow, the liquid bridges between the slugs are completely destroyed and the liquid is dragged by the gas (annular flow; Pioli et al. 2012).

The slug flow is then the flow regime associated with Strombolian eruptions, indeed explained in terms of ascent and burst of individual large pockets of gas at the magma free-surface. This study will focus on the processes associated with the expansion and burst of slugs ascending within the shallower part of the volcanic conduit, resulting in a Strombolian eruption. A large body of literature exists concerning the processes beyond this activity and so far the burst of large slugs at surface has been supported by both direct (e.g., thermal, high-speed, UV imaging) and indirect (e.g., seismic and acoustic measurements) observations. Strombolian activity characterizes several mafic volcanoes worldwide, like, e.g., Stromboli and Etna (Italy), Yasur (Vanuatu), Erebus (Antarctica), Nyiragongo (Democratic Republic of the Congo) and Kīlauea (USA). However, the majority of the studies have been conducted at Stromboli volcano (Aeolian Islands, Italy). Indeed Stromboli represents the perfect site for studying Strombolian activity: its crater terrace is relatively easy to access and it erupts constantly, typically every 10-15 minutes, from a variable number of vents in plain view (*Fig. 2.4*).

The following sections will introduce the necessary background on the current understanding of processes involved in Strombolian eruptions and measurement techniques relevant to this study.

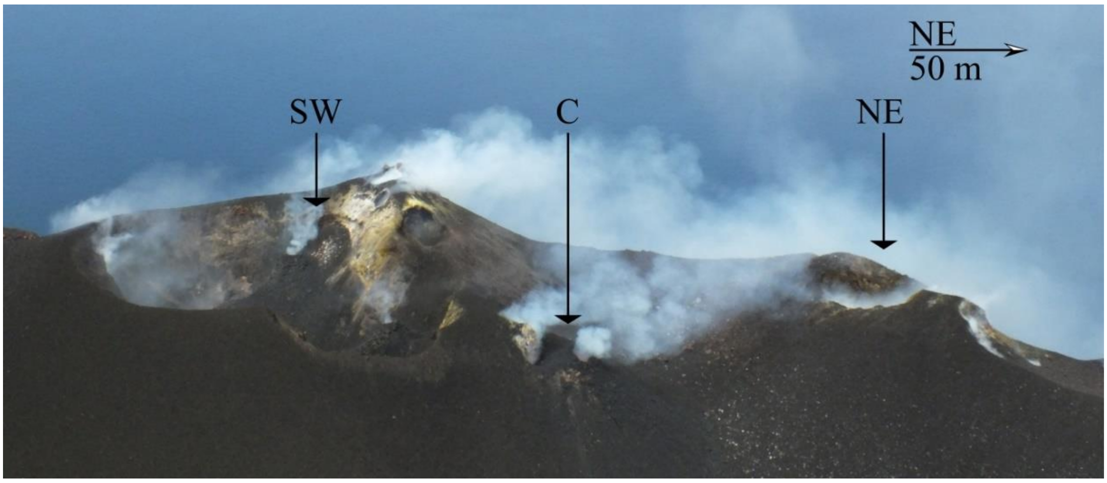

Figure 2.4 View of the crater terrace at Stromboli (~800 m a.s.l.), comprising the North-East (NE), Central (C) and South-West (SW) vent areas, from Pizzo Sopra la Fossa on 18 May 2014 (photo by A. Capponi).

2.3 Strombolian eruptions

Strombolian activity is named after one of the most active volcanoes on Earth, Stromboli (Aeolian Islands, Italy), whose activity has been reported since the days of Ancient Rome, where it was already known as the "Lighthouse of the Mediterranean".

Jules Verne, in 1864, described Stromboli as "*a volcano from which escaped, from one quarter of an hour to the other, with a very loud explosion, a lofty jet of flame mingled with pumice stone, cinders, and lava. I could feel the convulsions of nature in the mountain, which breathed like a huge whale, throwing up from time to time fire and air through its enormous vents*" (Voyage au centre de la Terre, Chapter XLIII). More than a century later, this description still applies to the current activity observed not only at Stromboli but also at many other Strombolian-type volcanoes worldwide. In a less poetic way, it is now generally accepted that the relatively mild and impulsive events – known as "normal" Strombolian eruptions – result from the burst of large individual gas pockets (*slugs*) that decouple from a low viscosity magma deep in the plumbing system and ascend through it. As result, a gas-pyroclasts mixture is ejected at several tens to hundreds of metres of height and a number of measurable geophysical signals are produced: e.g., ground deformation, seismic and infrasonic signals (e.g., Cashman and Sparks 2013).

These volcanoes are usually not life-threatening and, being relatively steady in time, have always attracted researchers, tourists and favoured the establishment of villages and cities nearby. However, they can show a wide range of styles, from passive degassing (e.g., Ripepe et al. 2002; Harris and Ripepe 2007b), mild explosions of variable magnitude (e.g., Patrick et al. 2007; *Fig. 2.5*), up to more violent events characterized by a greater explosivity compared to the normal Strombolian explosions (e.g., Parfitt and Wilson 1995). The latter, known as "major explosions" and "paroxysms", can cause severe damage to the settled areas around the volcanoes and human losses, with the paroxysms capable of triggering landslides and tsunamis (e.g., the 2002 paroxysm at Stromboli; Bonaccorso et al. 2003).

Figure 2.5 The normal Strombolian activity can show a wide range of styles with, e.g., ash-free (**left**) and ash-rich (**right**) explosions occurring at the same vent at Stromboli (photos by A. Capponi, May 2014).

Variations in style of basaltic explosive eruptions can be defined qualitatively also as functions of mass flux and degree of fragmentation. Low mass flux characterizes the normal Strombolian activity, with discrete bursts and ejection of coarse juvenile bombs, often mixed with cool, recycled blocks and lapilli. An increase in mass flux leads to both violent Strombolian eruptions and Hawaiian eruptions, depending on the degree of fragmentation, with the development of more frequent major Strombolian eruptions for a higher degree of fragmentation (*Fig.2.6*, Valentine and Gregg 2008).

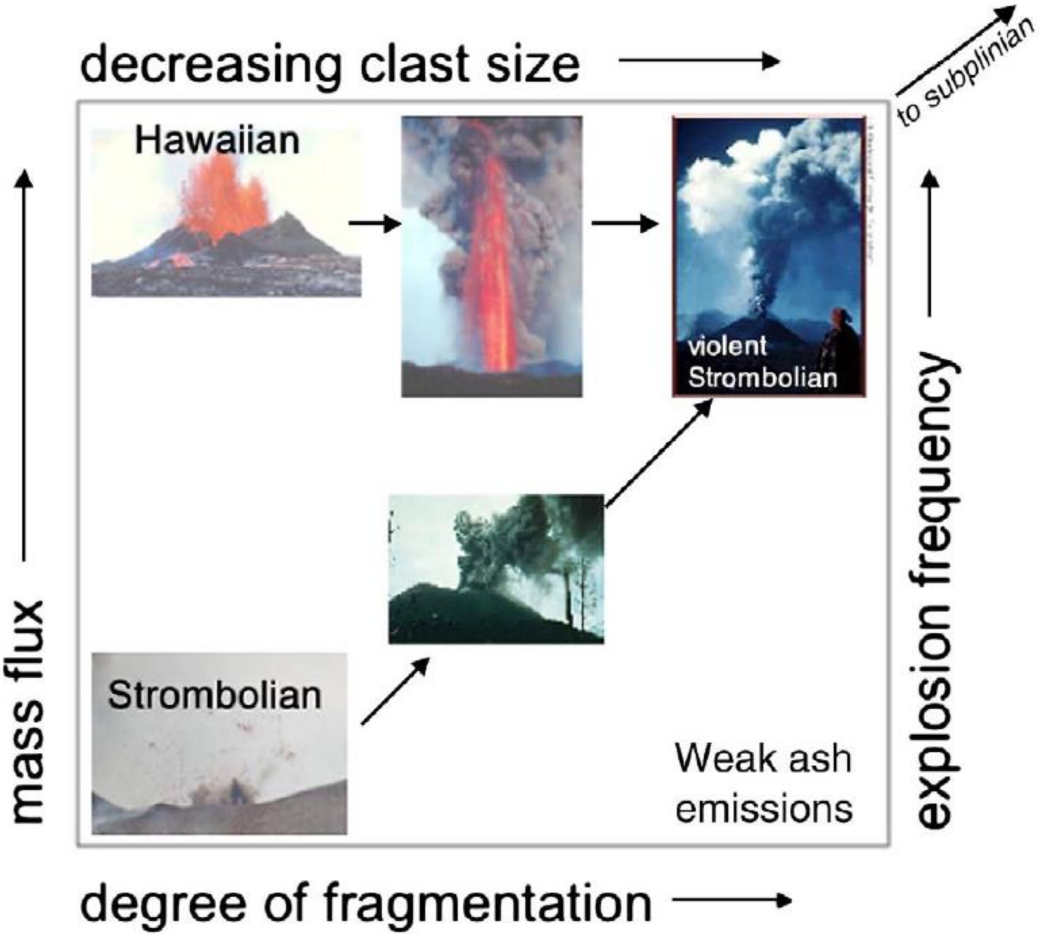

Figure 2.6 Qualitative diagram showing the transition between basaltic explosive eruptions as functions of mass flux (and explosion frequency) and degree of fragmentation (Valentine and Gregg 2008).

In the last decades, our understanding of the dynamics of Strombolian eruptions have advanced via interpretation of seismic (e.g., Chouet et al. 2003, 2008; Marchetti and Ripepe 2005), infrasonic (e.g., Ripepe and Marchetti 2002; Gerst et al. 2008; Johnson and Ripepe 2011; Lane et al. 2013; Spina et al. 2015), geochemical (e.g., Allard et al. 1994; Francalanci et al. 2005), thermal and high-speed video data (e.g., Patrick et al. 2007; Harris and Ripepe 2007b, Harris et al. 2012; Taddeucci et al. 2012a, 2012b; Gaudin et al. 2014) and laboratory studies (Seyfried and Freundt 2000; Lane et al. 2001; James et al. 2004, 2008, 2009; Llewellin et at. 2012; Del Bello et al. 2012). Yet, despite a wealth of information, several important questions are still open, the answers to which will play an important role in improving our understanding of the mechanisms behind a Strombolian eruption.

In particular, the variations in style within the normal Strombolian activity can be quite impulsive and have been explained in terms of either how gas exsolves and separates from the magma (e.g., Parfitt 2004; Houghton and Gonnermann 2008) or variations in the rheological properties of the magma in the shallow conduit (e.g., Taddeucci et al. 2004; Valentine et al. 2005; Andronico et al. 2008; Leduc et al. 2015). However, the dynamics and the cause of variations in style and intensity are still debated. Recent textural and field observations point to the coexistence of magmas with different rheological properties in the shallower conduit. The cooling and degassing of the uppermost part of the magma column may lead to the formation of a more crystallized, evolved and viscous magma layer, acting as a plug, through which the slugs burst. The thickness and properties of this layer not only may affect explosion style and vigour (e.g., Lautze and Houghton 2006), but also the properties of the ejecta and the associated geophysical signals (e.g., Lyons et al. 2012; Gurioli et al 2014). Indeed, gas ascent, expansion and burst are assumed to be the main source mechanisms for both seismic and acoustic signals, although the exact mechanism producing both of them is still debated. The presence of a possible plug would add further complexities that need to be taken into consideration, further complicating interpretations.

This particular issue will be addressed in this study, moving from the main simplification in current modelling of the fluid dynamics involved in a Strombolian eruption (i.e., the assumption of a rheologically uniform magma) to consider the effect of a viscous layer at the top of the conduit on eruptive dynamics and its effect on the generation of geophysical signals.

2.4 Eruptive dynamics

The "normal" Strombolian activity is characterized by both degassing and explosive activity. The non-passive degassing activity, known as "puffing", comprises rapid and repeated emissions of discrete pockets of high-temperature gas from the vents (Harris and Ripepe 2007a). At Stromboli, puffing activity is mainly centred on only one vent at any given time, although switching from one vent to another is often observed (Ripepe and Marchetti 2002; Ripepe et al. 2007). The explosive activity is triggered by the arrival and burst of large gas bubbles at the surface or cluster of bubbles, representing also the source mechanism for any fluctuations in the gas exit velocity (Chouet et al. 1974; Blackburn et al. 1976). These relatively mild and impulsive events usually last a few to tens of seconds, ejecting a mixture of gas-pyroclasts at several tens to hundreds of meters of height (e.g., Taddeucci et al. 2015). However, any variation in the frequency and volumes of the slugs may result in variability in both eruptive style and explosions magnitude. Three main types of explosions are indeed explained in terms of 1) the explosion of a single bubble, 2) the explosion of a large bubble followed by smaller ones and 3) arrival at surface of a train of bubbles, similar in size and bursting at regular intervals with increasing depth (Ripepe et al. 1993). An increase in magma and gas flux at depth could also lead to more frequent and stronger explosions triggered by the ascent and burst of larger slugs compared to period of less intense activity, and producing jets of gas-pyroclasts ejected at greater heights; this suggests a direct link between explosion frequency and eruption intensity (Taddeucci et al. 2013a).

The explosive activity can be further categorized in ballistic-dominated eruptions, with little or totally absence of plume (*Type 1*) or in ash-rich both ballistic-rich and -poor explosions (*Type 2*), as revealed by thermal imagery (Patrick et al. 2007; Harris et al. 2012). *Type 2* eruptions can be further divided in *Type 2a* and *2b*. The *Type 2a* displays the emission of an ash plume containing significant ballistic particles; the *Type 2b* shows only a convective ash plume with the ejection of a minor amount of ballistic particles (*Fig. 2.7*, Patrick et al. 2007). Individual vents at Stromboli can maintain *Type 1* or *Type* 2 phases for days or weeks. Due to their nature, *Type 1* explosions seem to result from the burst of a gas slug at the magma free surface with emission of hot scoria that represent fragments of the magma surrounding the slug. This cannot be the case of the *Type 2* eruptions, dominated instead by fine fragmentation and clouds of fine ash. Such scenario could be explained by a change in the magma rheology or backfilling of the vent. In the first case, an increase in magma viscosity could lead to an increase in magma fragmentation up to a finer scale: e.g., for Mount Etna the increase of viscosity was linked to the increase of magma crystallinity, leading to brittle fragmentation (Taddeucci et al. 2002, 2004). In the latter case, the vent can be obstructed by material that fell back in the vent after an eruption or for inner collapses of the crater walls. This material could be re-worked by subsequent eruptions, with the milling between particles producing fine particles (e.g., Patrick et al. 2007).

Until recently, these explosion types have always been associated with a relatively low ejection velocity of the pyroclasts, ranging between 65-100 m/s (Chouet et al. 1974; Blackburn et al. 1974; Weill et al. 1992; Ripepe et al. 2001; Patrick 2007; Patrick et al. 2007). However, the gas-pyroclasts mixture ejected during the explosions can comprise of two main phases: an initial high-velocity spray of small particles (2-64 mm in diameter) that can reach velocity up to 213 m/s. For such small particles, the high velocity could be explained by coupling with the gas phase; these particles are carried out by the initial high-velocity gas phase producing jets. After a certain height these jets lose momentum and their ascent became dependent by buoyancy with a resulting deceleration. This phase can then be followed by sprays of both large and small particles at lower velocities, between 9 and 129 m/s, and in this case the particles were not coupled with the gas phase (Harris et al. 2012).

The bursting of meter-sized bubbles at the surface (*Fig. 2.8*), however, represents only a fraction of the complexities comprising "simple" Strombolian explosions. Maximum and average ejection velocities of the pyroclasts derived from high-speed videos are much higher than those estimated until now, twice higher than the ones derived from thermal data, up to 405 m/s. Furthermore, explosions at open-vent volcanoes like, e.g., Stromboli and Yasur (Taddeucci et al. 2012; Gaudin et al. 2014) are characterized by successive pressure release pulses related to pressure fluctuations likely caused by oscillations in the falling liquid film surrounding long slugs or the continuous bursting of multiple bubbles at surface. These processes result in up to hundreds (minimum of 3 up to 300) of ejection velocity peaks (*Fig. 2.9*, Gaudin et al. 2014). The largely variable results in velocity measurements over the years mainly is due to both the difficulties of direct measurements – still a challenging task – and the lack of precise field measurement techniques (e.g., Chouet et al. 1974; Ripepe et al. 1993), now available (e.g., Harris et al. 2012; Gaudin et al. 2014). The importance of trying to get increasingly precise measurements on the ejection velocity of pyroclasts derives by the role played by this parameter in the understanding of the Strombolian dynamics. Indeed, understanding its history is one of the key to calculating important eruptive parameters, such as energies, gas pressures and gas volumes, and to interpret secondary effects such as shock and pressure waves. These parameters, in turn, are necessary boundary conditions for conduit modelling, providing a reference frame for a variety of studies.

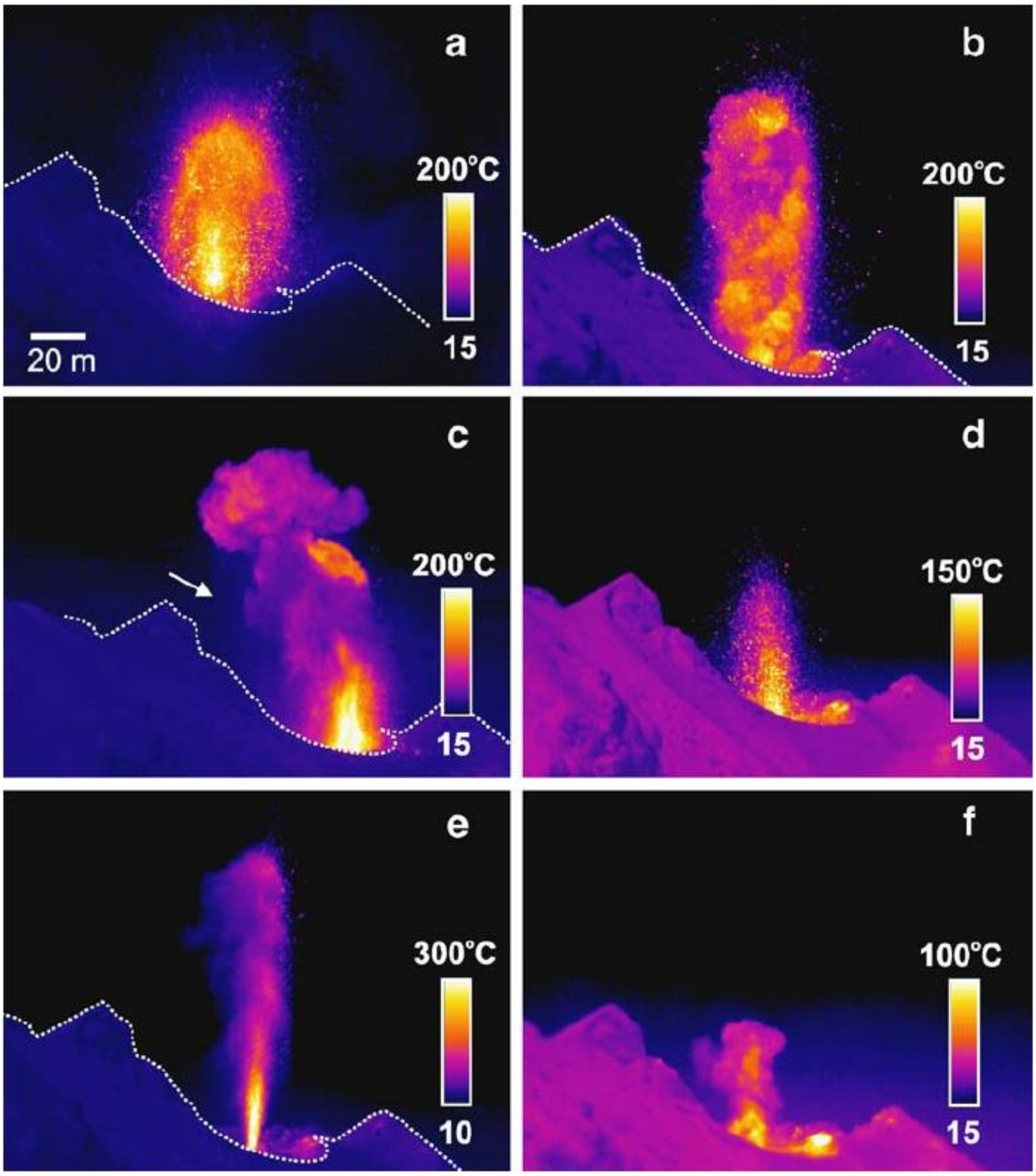

Figure 2.7 The varying styles in the "normal" activity at Stromboli: (**a**) *Type 1* eruption, poorly collimated; (**b**) *Type 2a* eruption with high-velocity ash plume; (**c**) *Type 2b* eruption with low-velocity plume; (**d**) *Type 1* eruption, ballistic-rich and ash-free; (**e**) *Type 1* eruption, well collimated; (**f**) *Type 2b* eruption, ballistic-free (Patrick et al. 2007).

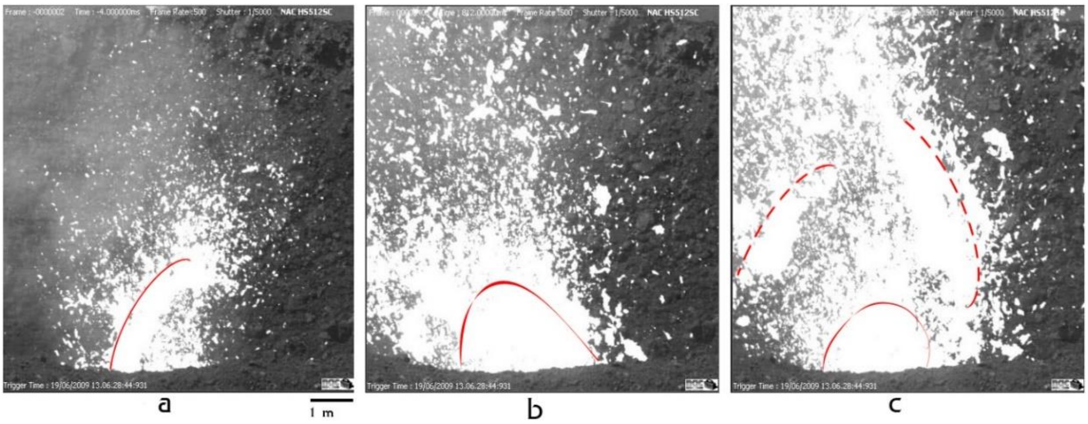

Figure 2.8 Representative frames of an explosion at Stromboli, showing (**a**) fragments of a bubble's wall exiting the vent followed by the arrival (**b**) and burst (**c**) of two more bubbles at the surface; solid line indicates the head of a bubble, polylines the fragmenting bubble's wall (Capponi 2010).

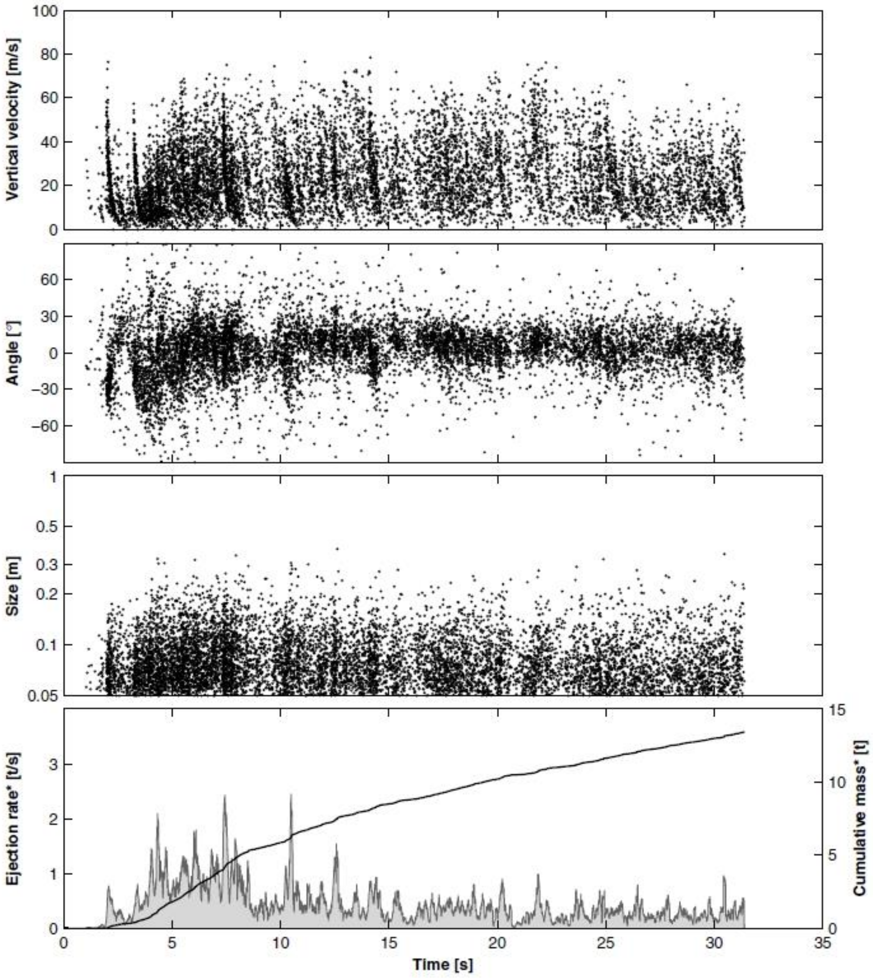

Figure 2.9 Ejection velocity for pyroclasts ejected during a single Strombolian explosion at the SW vent at Stromboli. Together with the velocity, for each pulse the exit angle, size and cumulative mass over time of the pyroclasts can be measured (Gaudin et al. 2014).

Gas emissions during explosive activity are usually richer in CO_2 and SO_2, and CO_2/SO_2, ratios are three to five times higher than those during the quiescent emissions. Thus, the gas phase driving the Strombolian explosions seems to derive from a deeper source rich in CO_2 and with a magma source under confining pressure of ~70 to 80 MPa, corresponding to a depth between ~2.7 and 0.8 km below the vents, deeper than the source location suggested by interpretation of seismic signals (Chouet et al. 2003; Marchetti and Ripepe 2005). These emissions are relatively steady over time, suggesting a reproducible source process. Smaller and higher frequency eruptions seem to have a greater H_2O/CO_2 ratio: smaller explosions may have a more shallow origin, driven by H_2O rich gas slugs (Burton et al. 2007a) at depths matching the ones derived from inversion of seismic signals, where discontinuities in the conduit may disrupt the flow promoting differential bubble rise speed and coalescence (Chouet et al. 2008).

However, the source mechanism of seismic signals at shallow depth does not imply necessarily the formation of a gas slug, but could be associated with a structural discontinuity or rheological changes deeper in the conduit where ascending slugs undergo an abrupt flow pattern change before bursting at the magma free-surface.

2.4.1 Textural studies

In a broader sense, eruptive styles can be linked to the ejecta through grain size of the products, with the *Type 1* explosions ejecting coarse-grained pyroclasts and bombs, and the *Type 2* explosions fine-grained particles (e.g., Lautze and Houghton 2006; Patrick et al. 2007).

However, through a more detailed analysis, fresh ejecta associated with eruptions of different style and intensity at Stromboli show at least three different textures, likely produced by mingling process driven by the ascent of gas slug through a region of more evolved magma at the top of the column: low density (LD), high-density (HD) and transitional (TT) textures (*Fig. 2.10*). The LD and HD textures are visually different, with the LD one consisting of a clear pale brown glass, the highest number density of small- and medium-sized spherical bubbles together with larger and irregularly shaped bubbles. The HD texture, in contrast, consists of a dark brown glass, with few small spherical bubbles and few large, irregular bubbles. The TT texture is characterized by a honey-coloured glass, with an intermediate number of sub-spherical bubbles, and a continued presence of large, irregular bubbles (Lautze and Houghton 2006). The textural variations mirror different processes occurring in different zones of the shallow conduit: the "fresh" magma (LD textures) rises from depth as liquid film surrounding the gas slug, and mingles with the more evolved, viscous and crystalized magma (HD textures) seating at the top of the conduit during the slug ascent. Then, the less viscous magma not erupted following the bubble burst drains back on the column, evolving toward transitional (TT textures) and – eventually – high-viscosity magma (*Fig. 2.10*, Lautze and Houghton 2006). Viscosity measurements yield an approximate viscosity range of 2000-2600 Pa s and a density of ~1300 kg/m^3 for the LD magma, and 3000-5000 Pa s and a density of ~2650 kg/m^3 for the HD magma. Any variation in the properties of the high-viscosity layer (e.g., thickness, viscosity) could lead to different eruptive styles (and, thus, distinct textural variations in samples); indeed, both thickness and viscosity of a viscous layer could affect the behaviour of an ascending slug and its overpressure; however, they do not provide any information about properties such as layer thickness and timescales of formation (Lautze and Houghton 2006). A greater variability in textural variations can be found in ash samples from Stromboli. These textural variations are likely to be controlled, during magma fragmentation and quenching, by rheological properties such as temperature and viscosity and linked to the occurrence of small-scale fluctuations in the magma properties. These fluctuations seem to be caused by mingling between a more evolved and degassed magma and new ascending magma in the very shallow part of the conduit, during the normal Strombolian activity (D'Oriano et al. 2011).

Textural, chemical and rheological variations are not confined in coarse or fine pyroclasts, but can be also found in bombs associated with *Type 1* explosions, further endorsing the possibility that a more viscous magma layer exists at the top of the conduit affecting both ejecta properties and eruptive style (Gurioli et al. 2014). Based on textural observations, four main textural facies were defined: 1) highly porphyrytic, vesciculated regions, with a microlite-poor glass (HP facies); 2) highly porphyritic and vesciculated regions, with microlite-rich glass (HPM facies); 3) highly porphyritic and vescicle-poor regions with microlite-rich glass (HPD facies); 4) highly porphyritic, transitional facies between vescicle-poor and vescicle-rich regions (HPDs facies). All these facies are mingled and randomly distributed in the bombs, with the HP facies characterizing the fresh and less viscous magma, and the mircolite-rich magma (HPM, HPD and HPDs facies) characterizing a more viscous and degassed magma layer. Viscosity measurements yield a viscosity range of 50-500

Pa s and density of 900 kg/m^3 for the fresh (HP) magma, of 1.2-53.1 × 10^6 Pa s and density of 1300 kg/m^3 for the viscous layer (HPD + HPDs, and HPM) and a medium viscosity of 6640 Pa s for a possible mixed region of high-/low-viscosity magma (Gurioli et al. 2014). Also in this case, there is no information available regarding layer thickness and timescale of formation. Thus, a scenario can be defined in which the interaction between the magmas lead to the generation of a mixed region of high-viscosity and low-viscosity magmas at the top of the conduit, or to a well-defined viscous layer capping the fresh magma and acting as a plug, through which gas slugs, ascending through a fresh magma column, burst. The latter could also explain the rather fast propagation velocity of the fragmentation wave and the slug ascent velocity, derived by the geophysical signals and difficult to explain with the ascent and burst of unimpeded slugs (Gurioli et al. 2014).

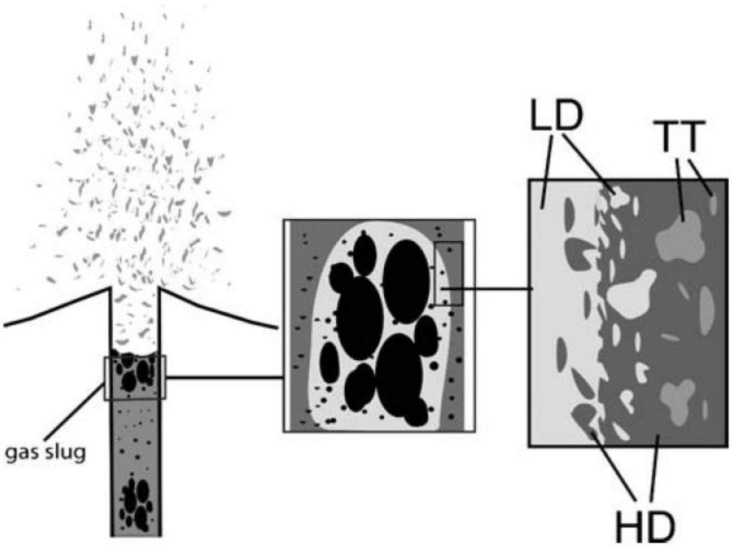

Figure 2.10 Schematic illustration of fresh and low-density magma (LD) rising in the conduit with gas slugs, and mingling with more evolved, high-density magma (HD) occuring both at slug border and at the magma free surface (Lautze and Houghton 2006).

2.4.2 A refined classification

All the recent textural and geochemical evidence motivated a refinement in the classification of the normal Strombolian activity, resulting in the addition of a new eruption type, the *Type 0*. These explosions feature the emission of relatively few and high-velocity (150-250 m/s) small pyroclasts, together with material that fell back in the vent from previous explosions and re-worked from the following events (Leduc et al. 2015). The revised classification suggests that, while the *Type 1* and *2* eruptions involve a slug burst through a region of a degassed magma layer or recycled material at the top of the column respectively, the *Type 0* ones result from the arrival and burst of slugs at the surface of a fresh magma column, free of any degassed magma volume or layer of recycled material (*Fig. 2.11*). Thus, these explosions represent the most direct expression of the canonical Strombolian paradigm.

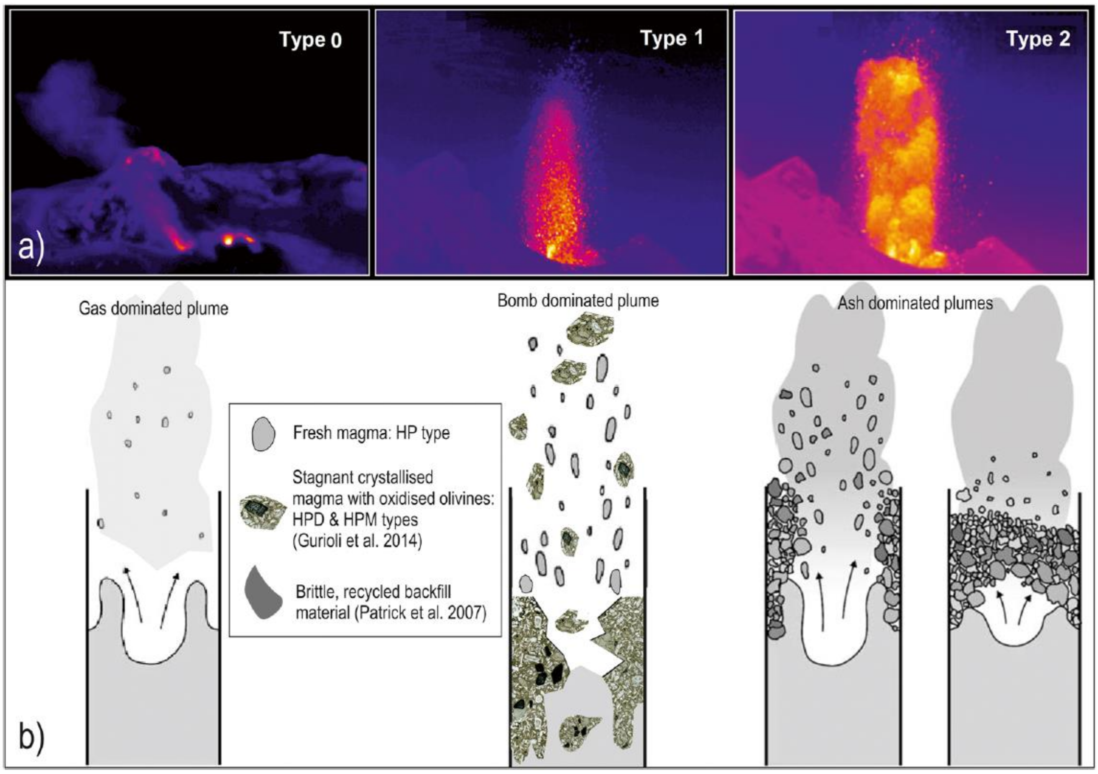

Figure 2.11 (**a**) *Type 0*, *1* and *2* explosions as seen by thermal videography. (**b**) Conceptual sketches illustrating the origin for each explosion type. *Type 0* explosions occur for a slug bursting in a fresh magma column; *Type 1* and *2* explosions are produced by slugs bursting through a more evolved magma layer capping the conduit or through debris covers respectively (Leduc et al. 2015).

The refined classification includes the presence of a region of degassed, more crystallized and viscous magma at the top of the conduit, often observed in field samples (e.g. Lautze and Houghton 2005; Colò et al. 2010; D'Oriano et al. 2011; Gurioli et al. 2014) and now generally accepted, but still not included in models of eruptive dynamics, along with its potential role in affecting eruption dynamics and the properties of ejected pyroclasts. Despite the majority of the studies corroborating the presence of a more viscous magma layer capping the conduit having been conducted at Stromboli (due to the ease of data collection), the presence of a more evolved magma layer is likely possible in other Strombolian-type volcanoes worldwide, where open vent conditions and interval times between explosions may allow the cooling and degassing of the uppermost part of the magma column.

This new classification, supported by the textural and geochemical analysis of field samples, shows a shift in the way eruptions are interpreted, i.e., contemplating the presence of magmas with different rheologies in the conduit.

Variability in eruptive dynamics, field data and geophysical signals, to date, has always been explained in terms of fluid dynamic processes within a rheologically uniform medium. In light of this new evidence, and the possible implications on the eruptive dynamics, interpretation of the observed phenomena and complexities in field data (e.g., velocity fluctuations identified by high-speed video, occurrence of mingled pyroclasts) seems to benefit from the possible presence of rheological impedances at the top of the conduit. The same physical situation could also change how geophysical signals are interpreted. In particular, interpretation of seismic measurements, so far signals characterized by the higher level of uncertainty about source mechanisms, may also improve. Indeed, the presence of a possible rheology contrast within the conduit could lead to generation of regions where flow patterns can be disrupted, leading to pressure fluctuations coupled to the conduit, representing a viable source for seismic signals.

The following section explores how the interpretation of infrasonic and seismic data has evolved over the years, to the point that some relationships between different geophysical signatures and eruptive styles are now difficult to explain with simplified models of slug burst in a rheologically uniform magma.

2.5 Seismo-acoustic studies

Indirect observations of volcanic activity comprise acquisition and interpretation of geophysical signals, such as seismic and acoustic signals, associated with processes occurring within the conduit and at the vent pre- and syn-eruption. Infrasonic and seismic networks are two of the main monitoring tools used both for risk mitigation and to constrain fluid-dynamic processes in the conduit and slugs metrics. Until recently most of the field campaigns were focused on the acquisition and study of a single or few data types only, but in the last few years multi-parametric campaigns have become a standard in order to acquire the most complete dataset possible, capable to constrain the higher number of parameters possible. Indeed, the integration of both direct and indirect observations is essential for the creation of better models (e.g., Harris and Ripepe 2007a; Calvari et al. 2012; Gurioli et al. 2014; Spina et al. 2015).

Acoustic waves and seismic signals are generated by changes in the pressure within the conduit and in the atmosphere, associated with the coalescence, ascent and burst of gas bubbles. Intensity of these changes is a function of conduit geometry, magma rheology and the properties of the bubbles (e.g., James et al. 2006, 2009; Lane et al. 2013).

Basaltic volcanoes can be characterized by a wide range of viscosity, from low-viscosity (e.g., Vergniolle and Brandeis 1994; Vergniolle and Brandeis 1996) up to intermediate and higher viscosity magmas (e.g., Johnson et al. 2003, 2004); however, acoustic signals from Strombolian-type volcanoes worldwide, regardless of the viscosity, seem to share a similarity between explosions and acoustic signals, strengthening the theory that this style is driven by a common mechanism, the bursting of large overpressured gas bubbles (*Fig. 2.12*, Vergniolle et al. 2004). A typical waveform is characterized by a first compressional high-amplitude, low-frequency pulse followed by higher frequency signals.

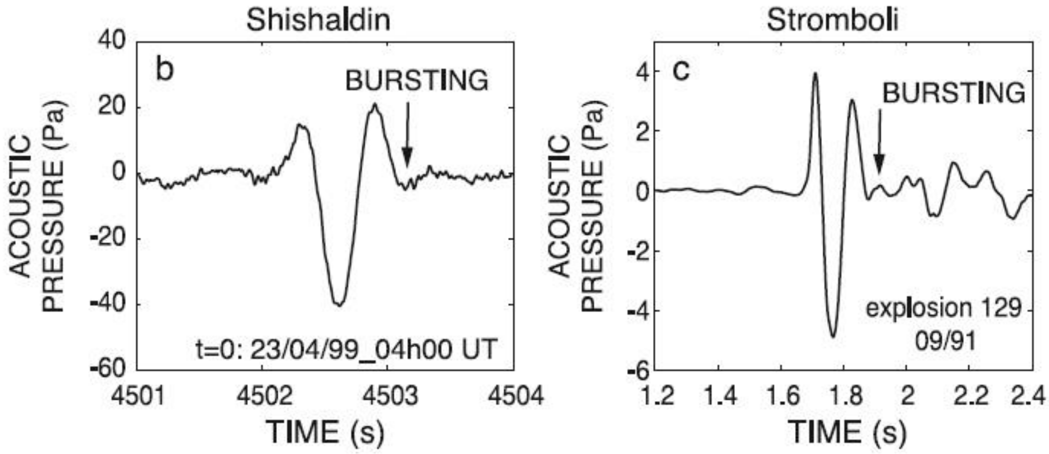

Figure 2.12 Similarities between acoustic waveforms recorded at Shishaldin volcano (Alaska, USA) and Stromboli volcano (Italy) (Vergniolle et al. 2004).

As the origin of volcanic sound, it was initially proposed that the acoustic source geometry resembles that of a dipole, due to fluid interaction with solid boundaries (Woulff and McGetchin 1976, based on measurements acquired at Volcan Acatenango, Guatemala). However, early field measurements were limited to a frequency range from 50 Hz to 5 kHz and the much wider range (e.g., from 4 Hz to 20 kHz, Vergniolle and Brandeis 1994) allowed a more in-depth interpretation of acoustic measurements.

It seems that the source of the sound is not in the conduit and part of the acoustic energy is released prior to the bubble bursting itself (Vergniolle and Brandeis 1994).

Explosion characterized by a low seismic activity can have a more energetic acoustic signal, the opposite of what is expected. In case of a deep source below the surface, the energy should go preferentially to the ground; if the reverse happens then the source is very shallow. The signal associated with the explosions is characterized first by very low frequencies, followed by both higher frequencies and again lower frequencies (*Fig. 2.13a*). These features could be related to the vibration of a large gas pocket prior to its bursting at the magma free surface (low frequencies), its bursting (high frequencies) and the drainage of magma down in the conduit (low frequencies coda; *Fig. 2.13b*, Vergniolle and Brandeis 1994).

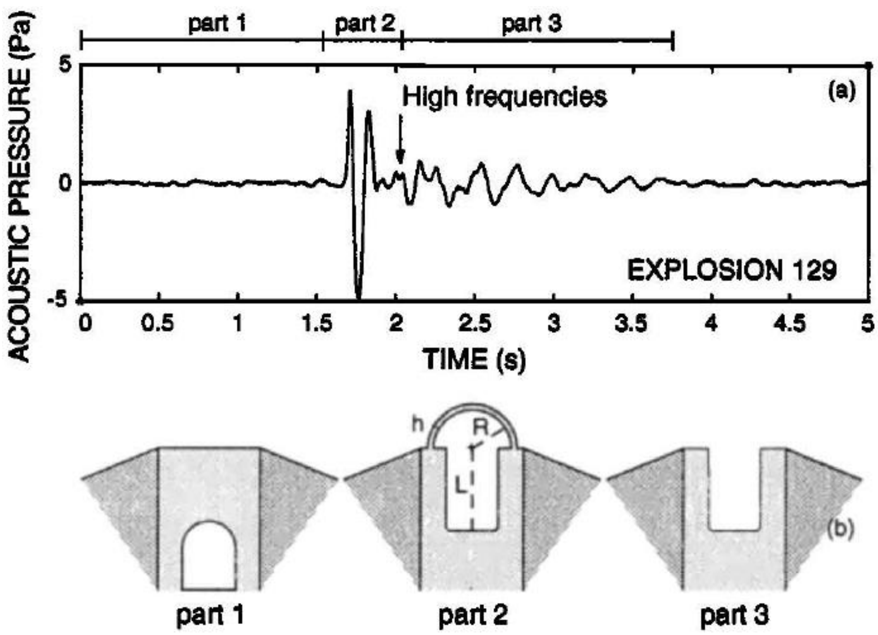

Figure 2.13 (**a**) Acoustic signal associated with an explosion from the Easter vent at Stromboli and (**b**) proposed model for the origin of the sound. **Part 1**: a bubble rises through the conduit; **Part 2**: oscillations of the bubble's cap at the magma free-surface; **Part 3**: drainage of the magma back in the conduit after the bubble burst (Vergniolle and Brandeis 1994).

In more detail, pressurised gas bubbles, instead of immediately bursting upon reaching the surface of the magma column, rest at the magma free surface for several seconds and vibrate around their equilibrium pressure before they finally burst. The bubbles burst close to the minimum of their suggested oscillation cycle, i.e. when they have reached their smallest dimension of the contraction phase, following their initial expansion (Vergniolle and Brandeis 1996). Bubbles can grow from a diameter of two metres to a diameter of more than five metres with a wall thickness of 1 cm, before the bubbles deflate and contract again to a size of 2 m, at which point they burst. This was proposed following the development of a model in which synthetic waveforms were fitted to real acoustic data from Stromboli and Shishaldin volcano, Alaska (*Fig. 2.14*). The fit between observed and synthetic waveforms was good for constraining both frequency and amplitude but failed to reproduce the acoustic pressure from the real bursting process after the first oscillation cycle (Vergniolle and Brandeis 1994, 1996; Vergniolle et al. 1996, 2004).

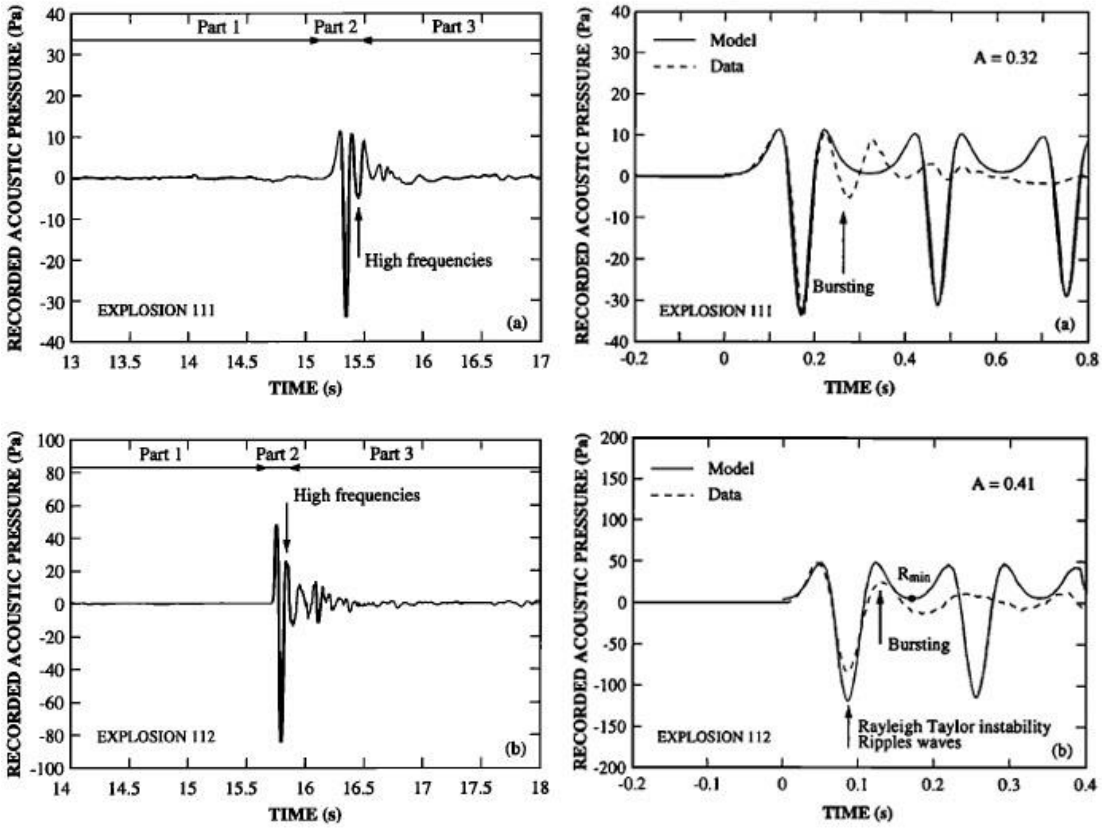

Figure 2.14 (**left**) Acoustic signals recorded at 250 m from the Easter vent at Stromboli in April 1992 (explosion 111 and 112). The marks indicate the onset of higher frequencies. (**right**) Comparison between measured and synthetic waveforms for explosions 111 and 112. The fit for the signals onset is good, but the model fails to reproduce the pressure variation induced by the bursting process (Vergniolle and Brandeis 1996).

However, it should be noted that observations of these processes have never been published and there is no real qualitative or quantitative confirmation about their occurrence. Also, for a slug of a given dimension ascending and bursting within a conduit the burst process depends on the delicate equilibrium between the pressure within the slug and the magmastatic pressure above the slug. So it seems unlikely that a bubble can increase its diameter, stand over the magma free surface and undergo a cycle of oscillations for several seconds without bursting or breaking up (e.g., James et al. 2009; Del Bello et al. 2012).

The same variability observed in the eruptive style seems to be reflected in the acoustic signature as well. *Type 1* explosions, short-lived, highly energetic and scoria-rich, produce short (1-3 s) high pressure infrasonic waves (20-80 Pa). *Type 2* explosions, long lasting and ash-rich, produce long signals (5-15 s) with low pressure (10-30 Pa). It could be then possible to identify different explosion types by using acoustic pressure signatures (Ripepe and Marchetti 2002). At Stromboli, where several vents are constantly active, the variability in the waveforms generated by the same vent may reflect variations in gas overpressures and volumes. Longer acoustic signals, instead of oscillations of the bubble at the magma free surface, could be explained in terms of harmonic signals generated from conduit resonance (Ripepe and Marchetti 2002; Harris and Ripepe 2007a).

Acoustic signals produced at Erebus Volcano resemble those from Stromboli (Vergniolle et al. 1996), both in terms of waveform shapes and travel time differences between the acoustic and seismic signal. The constant lag between the onsets of both signals points to a repetitive and common source mechanism and, as further evidence, there is a consistent relationship between maximum excess acoustic pressure and maximum seismic displacement (Johnson et al. 2003). It is possible then that volcanic sound sources are often volume sources (Johnson et al. 2004), i.e., sound is produced by introducing additional volume into the atmosphere, which during Strombolian explosions is mostly volcanic gas.

An increase in the gas content can lead both to a more vigorous volcanic activity, mirrored by changes in infrasonic activity (e.g., Colò et al. 2010; Taddeucci et al. 2013a) but also to a more-developed magma vesiculation, reflected in changes in the textural features of the ejecta (Colò et al. 2010). If vesiculation processes and variations in infrasonic pressure are indeed found dependent to variations in the gas content in the magma, such process would leave a trace on the infrasonic signals. So, by comparing bubble size distribution in ejected scoria and the amplitude distribution of infrasonic signals, it should be possible to associate different volcanic activity, to textural variations in the products and to different kind of signals. Thus, monitoring infrasound may be an alternative way to investigate vesiculation process and eruptive dynamics in open conduit systems (Colò et al. 2010). When applied to Stromboli, infrasonic amplitudes < 5 Pa and > 5 Pa were indeed linked to “puffing” and explosive activity respectively, by comparing bubble size distributions of scoria to rate and amplitude of infrasonic activity for each style (Colò et al. 2010).

This link bears an important role, because it implies that infrasonic surveillance, together with analysis of field samples, could represent a means to correlate textural variations with degassing rates in the shallower conduit. This provides the first insights in the link between a possible interaction among different magmas, textural changes within a single pyroclast and geophysical signal, moving away from the general assumption of a single viscosity magma filling the conduit, implicitly used so far in the interpretation of infrasonic signals.

Another key component in the monitoring of active volcanoes is volcanic seismology: almost every eruption is preceded by seismic activity and explosions and flow changes within the conduit are associated with volcanic tremors. Continuous seismic surveillance not only increases the chance of successful forecasts, but provides also the opportunity of recording several years of seismicity, establishing a baseline for evaluating possible precursors. So far, more than 200 volcanoes are seismically monitored (Chouet et al. 2013). Until recently the seismometers were only limited to high-frequency signals, between 0.7 and 30 Hz; modern broadband seismometers cover a much wider band, between 0.02 and 50 Hz. Four basic types of seismic events can be detected depending on the characteristic frequencies: high-frequency events, low-frequency event, explosions and volcanic tremors. Of these, high-frequency events (Volcano Tectonic, VT, events, 5-15 Hz) are generated by shear fracture and can be used to determine stress orientation, while low-frequency (LF) events (long period, LP, events, 1-5 Hz, generally 2-3Hz) are thought to be caused by fluid dynamic processes within the conduit, but there are still a lot of uncertainties about their meaning (Chouet et al. 2013; McNutt and Roman 2015). With the introduction of the broadband seismometers, capable of detecting frequencies too low for short-period seismometers, a new simple long period waveform associated with explosive events was detected (*Fig. 2.15*), the “very long period”, VLP, with periods ranging from 3 to 100 s or longer and frequency down to 0.01 Hz. The onset of these waveforms is explained in terms of pre-eruptive depressurization, probably caused by the movement of fluid through a narrow section of the plumbing system (Neuberg et al. 1994; Chouet et al. 2003). This conduit reduction triggers the expansion of the gas, ultimately leading to the eruptions (Neuberg et al. 1994). VLP signals can be generated by quite small source regions at shallow depths of 1.5 km or less, and seem to be related to volumetric displacement caused by bubble coalescence or by the passage of a slug at a geometrical discontinuity in the conduit (Chouet et al. 2008, 2013). Thus, it seems that there is a strong link between VLP signals (in the range 2-100 s) and perturbations in the flow pattern due to the passage of slugs through discontinuities.

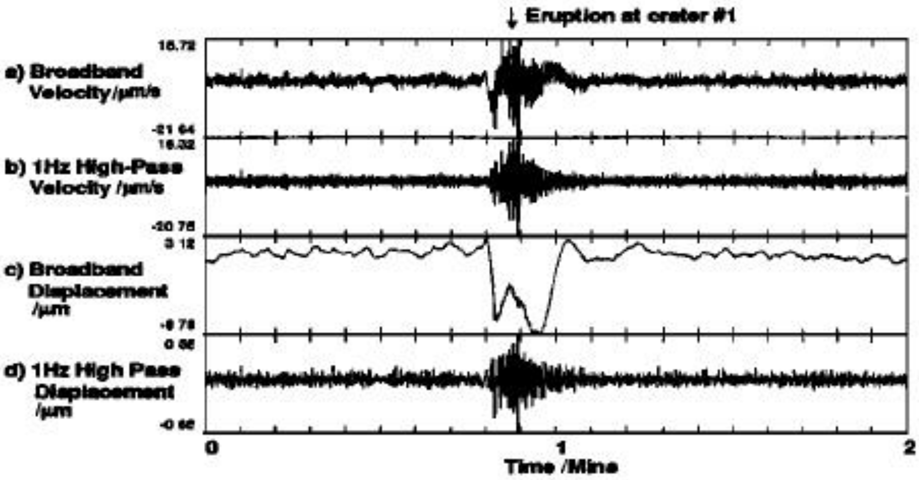

Figure 2.15 Comparison between broadband (**a**) and simulated short-period signal (**b**) and displacement (**c**) for an eruption at the SW crater at Stromboli. Broadband displacement shows a long period waveform not detected by the short-period trace (**d**; Neuberg et al. 1994).

This seems to be valid for a gas slug ascending and bursting either within a conduit (e.g., Stromboli) or at the surface of a lava lake (e.g., Mount Erebus; Aster et al. 2003; Chouet et al. 2013). Seismic data from both scenarios show how each explosion is preceded by a variable VLP onset, which repeatability indicates a non-destructive or self-reconstructing source mechanism in the near-surface conduit system. Their variability in timing and polarity suggests a well-connected plumbing system with multiple sites where ruggedness of the conduit, even the smallest ones, can act as a bubbles trap for slug coalescence, with slugs ascending from different depths and paths (e.g., Vergniolle and Brandeis 1996; Vergniolle et al. 1996) as well as any change in conduit geometry or inclination (Chouet et al. 2003, 2008, 2013). When multiple vents are in place and active, the eruptive differences between each vent and the explosion frequency also suggest that the slugs are affected by the shallow conduit geometry (Chouet et al. 2008).

Strong volumetric stress changes leading to conduit pressurization are induced by bubbles entrapment and coalescence at depth, detected in the VLP as an initial inflation of the conduit (*Figs. 2.16, 2.17*). This phase is followed by depressurization of the conduit in response to the decrease of the magmastatic head due to the expansion and burst of the slug, resulting in a deflation and then again an inflation

(*Fig. 2.16*). For a slug not constrained by the conduit geometry, i.e., in a lava lake, first gas expansion and expansive displacement generate VLP oscillations; then, when the bubble arrives at the surface, it bursts disrupting the lava lake surface and generating a reaction force that may contribute to the excitation of the VLP signal (*Fig 2.17*). After the burst, the drainage of the liquid film surrounding the slug back into the conduit leads to an increase of the magmastatic head and a subsequent repressurization of the conduit, detected in the seismic signal as a final inflation (*Fig. 2.16,* Chouet et al. 2003, 2008); or a similar inflation is triggered by the rapid removal of upper conduit material first, and the refill of the lava lake then, contributing to the coda in the VLP (*Fig. 2.17,* Aster et al. 2003).

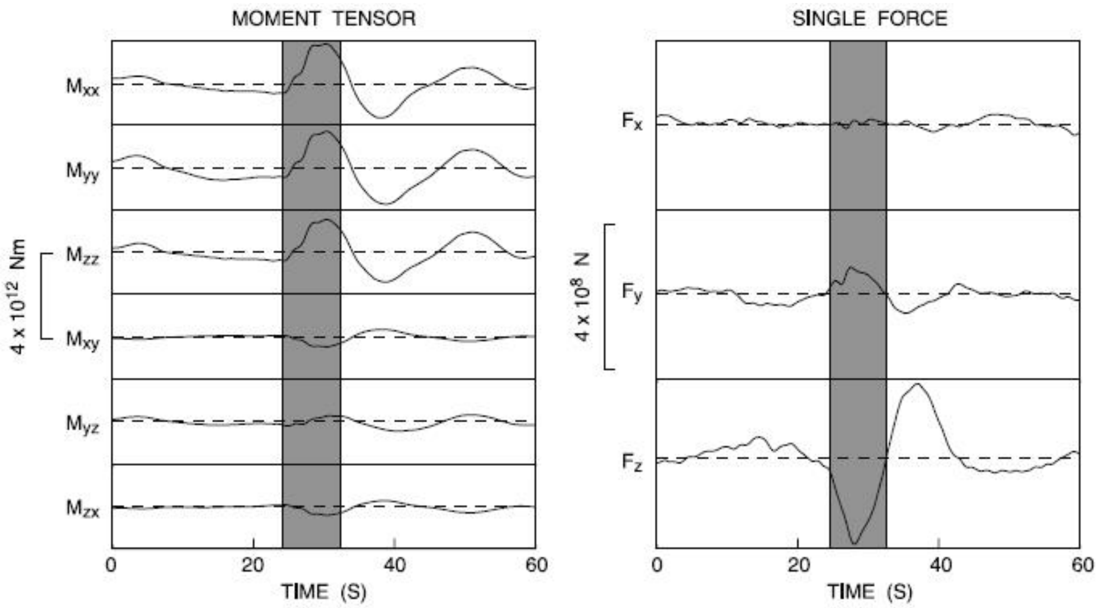

Figure 2.16 Six moment tensors and three additional single force components for a *Type 2* event at Stromboli. The shading zones represent the interval in which the inflation-deflation-inflation cycle occurs (Chouet et al. 2003).

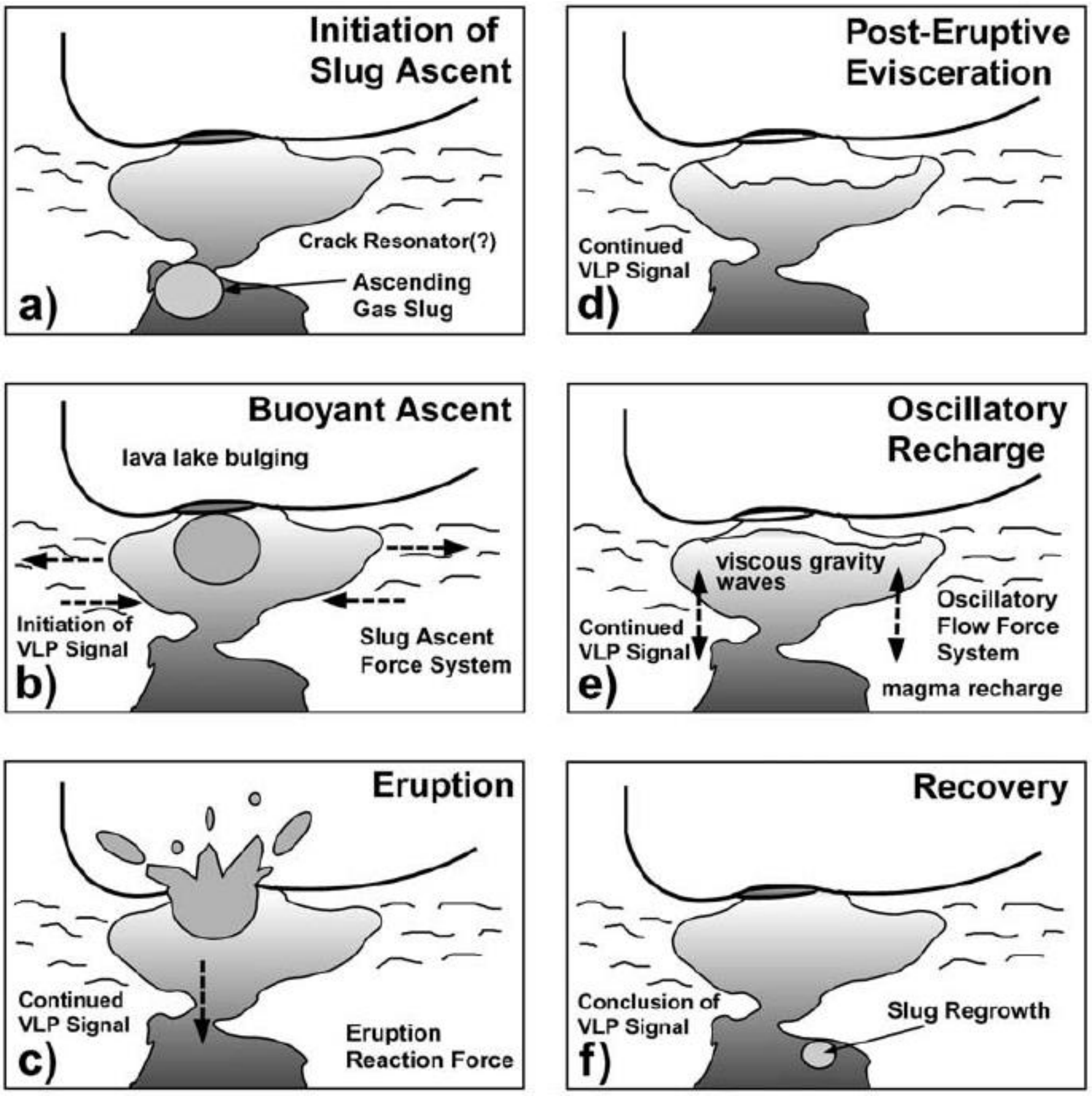

Figure 2.17 Conceptual model of a Strombolian eruption at Erebus Volcano. (**a**) A trapped gas slug starts to ascend; (**b**) during its rising, the slug excites the initial VLP signal; (**c**) the slug bursts at the surface disrupting the lava lake surface and applying a reaction force to the system; (**d**, **e**) the coda in the VLP is linked to the rapid removal of upper conduit material, and persists through the refill of the lava lake; (**f**) the VLP signal ceases after the reconstruction of the lava lake surface and in the meantime a new slug is growing at depth (Aster et al. 2003).

In particular, at Stromboli, differences in explosive activity are reflected in seismic signals, with *Type 1* and *2* explosions generating in the band 2-30 s two distinct VLP groups, with stable waveforms (*Fig. 2.18a*), at the NE and SW craters. NE crater features a high-frequency content (> 0.1 Hz) and short duration (20 s), while the signals from the SW crater show a lower frequency (< 0.1 Hz) and longer duration (~30 s). The differences mirror different crater activity with the NE crater usually characterized by short-lived (<10 s) scoria-rich explosions, and the SW characterized by long-lasting (>20 s), sustained ash rich emissions (Marchetti and

Ripepe 2005). Any variation in inclination and orientation represents a discontinuity in the conduit that could favour flow disruption, differential bubble rise speed, bubble coalescence and separation from the magma. Two main distinct dike structures, each one characterized by different variations in inclination and diameter, as part of a more complex system of fissures underlying the vents, seem to be the origin for the disruptions in the flow pattern at Stromboli, favouring the coalescence of bubbles. The location of the source mechanisms is at elevations of 520 m a.s.l. (*Type 1*) and 480 m a.s.l. (*Type 2*), approximately 160 m northwest the crater terrace (*Fig. 2.18b;* Chouet et al. 2003, 2008, 2013; Marchetti and Ripepe 2005).

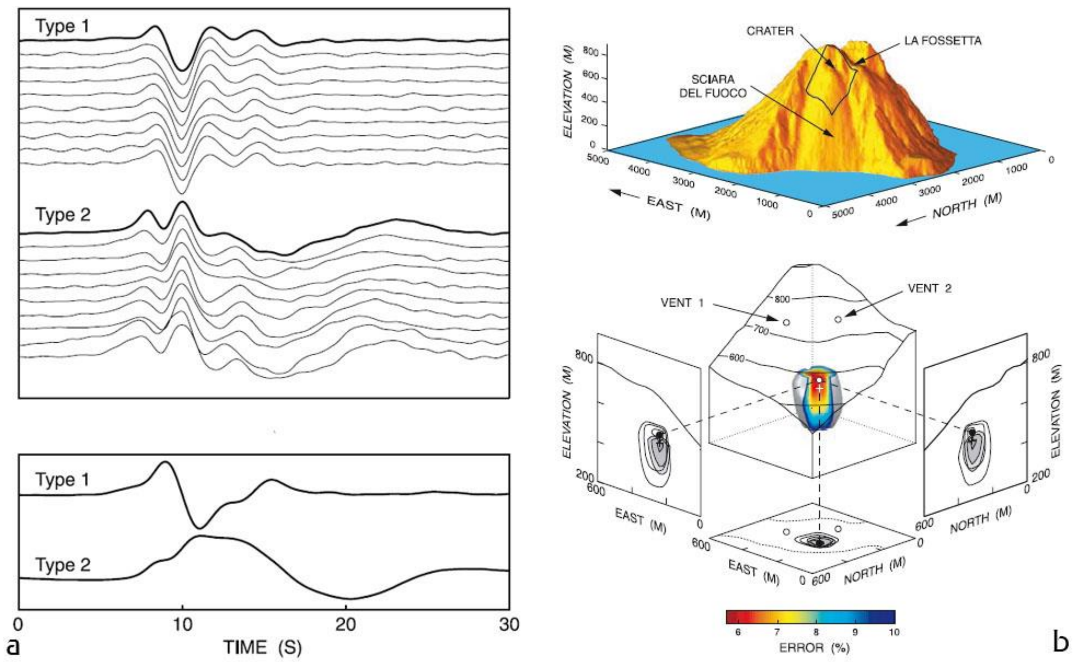

Figure 2.18 (**a**) Normalized component of velocity (upper diagram) and displacement seismograms (lower diagram) for 10 *Type 1* and 10 *Type 2* events at Stromboli shows similarities of waveforms between the two types of events. (**b**) Source locations of the Type 1 and Type 2 events inferred through waveform inversion of the seismic signals, at a depth of 220 m and 260 m beneath the active vents (modified from Chouet et al. 2003).

Considering a magma density of 2600 kg/m^3, the magma free surface at a depth of 20 m below the vent and a magma column 220 m and 260 m height, a magma static pressure of 5.1 MPa and of 6.05 MPa seem to characterize the *Type 1* and *Type 2* events respectively. These values lead to a gas pressure of 7.5 MPa for the upper source and 15.0 MPa for the lower source. The peak of the initial inflation phase observed in the moment tensors components correlates with the maximum amplitude of the downward force for both the *Type 1* events, 0.8 × 10^8 N, and for the *Type 2* event, of 2.4 × 10^8 N (Chouet et al. 2003). Such values are supported by laboratory experiments, demonstrating how pressure variations induced by a slug passing through geometrical changes in the conduit diameter led to magnitude forces and pressures comparable to the ones estimated by Chouet et al. (2003) to explain the VLP signals from Stromboli (James et al. 2006). More evidence linking variations in eruptive styles with changes in seismo-acoustic signals can be revealed by continuous geophysical monitoring at Stromboli, highlighting any variation at the several and constantly active vents characterized by different styles (McGreger and Lees 2004). Well collimated, gas- and ballistic-rich eruptions, ash-free, 10 to 20 s in duration, coexist with ash-poor with minor bombs explosions that reach heights up to 300 m, while a third vent area is characterized by a continuous degassing activity producing loud jet-like acoustic noise, with few associated ejecta. Each style shows a unique seismic (Chouet et al. 2003; McGreger and Lees 2004) and acoustic (McGreger and Lees 2004) signature (*Fig. 2.19*); the repetitive waveforms classes observed in both signals across stations suggest source similarities and, for the VLP, a non-destructive source. The low-frequency (5-10 s period) seismic signal constantly generated by the same vents also indicates that the source geometry is stable. With each geophysical signature always associated with a specific vent, it may be possible that the vents are linked to distinct conduit structures at a deeper level within the plumbing system, likely ~ 200 m below the surface (e.g., Chouet et al. 2003). However, there are some common features between the three crater zones: e.g., the events from the Hornito (Central crater) share similar shape and period with explosions form both the NEC and SWC zone. So, although it is possible to recognize the Hornito from its distinctive geophysical signature, there could still be a connection between the craters. Anyway, the clear differences in the signals suggest an intricate conduit geometry (McGreger and Lees 2004), probably more complex than the two crack model imaged by the VLP signals (e.g., Chouet et al. 2003, 2008, 2013).

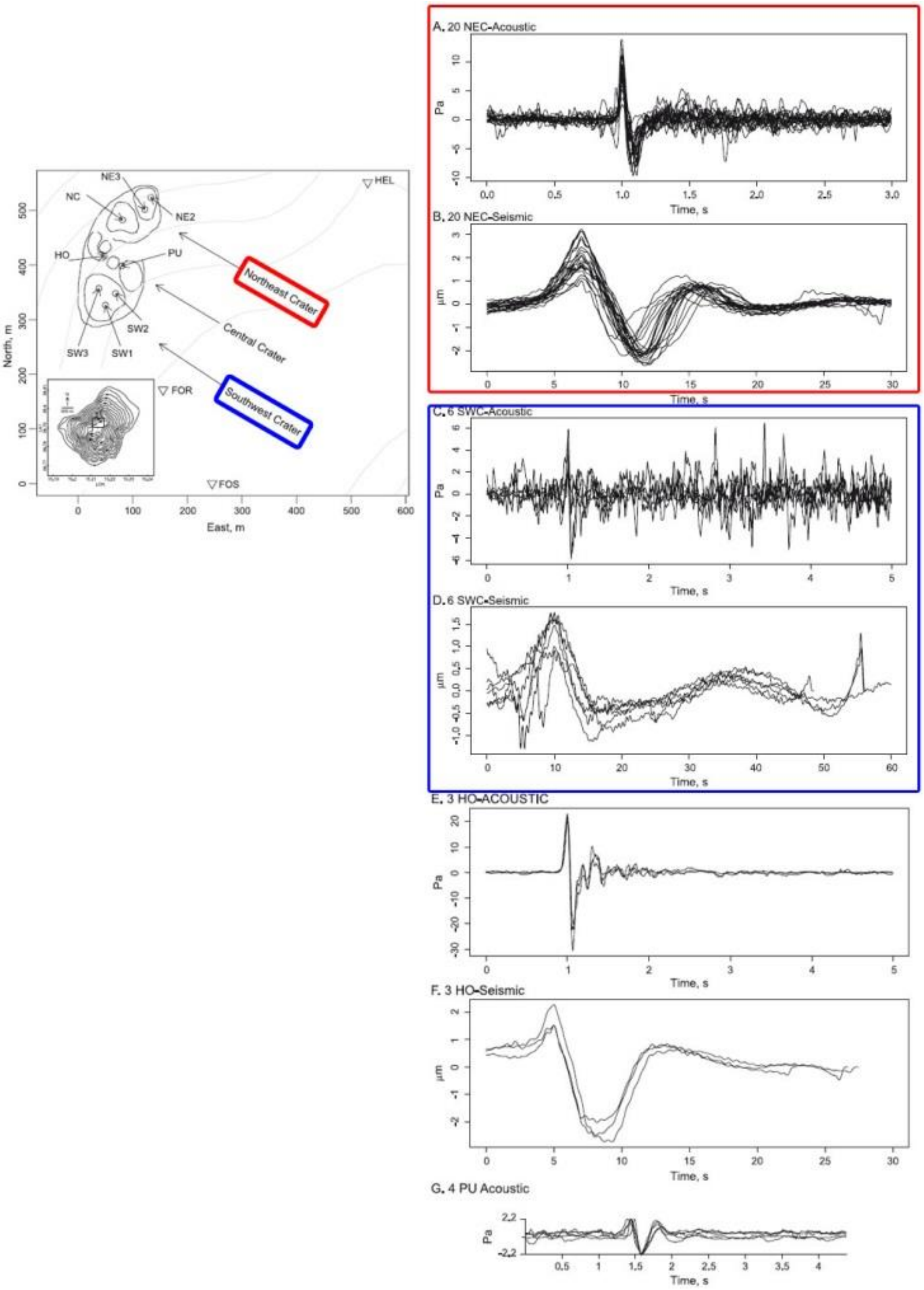

Figure 2.19 Map of Stromboli crater terrace, showing different groups of vents and the associated acoustic and seismic signals, demonstrating the repetitive nature of the waveforms in all the three main crater zones (modified after McGreger and Lees 2004).

Thus, bubbles coalesce, expand during ascent and burst generating seismic and infrasonic signals. These processes occur at variable depths and signals propagate through the Earth (seismic) or the atmosphere (infrasonic). So, it is reasonable to expect both a delay in the arrival time of each signal at the sensors and a difference in frequency and amplitude (Ripepe et al. 2001). When the gas moves upward in the conduit, it induces a force directed downward in the liquid, detected as a low-frequency seismic signal, whose onset occurs a few seconds before the infrasonic onset (with a time delay depending on the distance from the active vents). As the bubble bursts at the liquid surface, a ground-coupled infrasonic wave arrives at the sensor, detected as the high-frequency onset of the infrasonic signal that coincides with the high-frequency component of the seismic signal. A second delay occurs between the infrasonic signals and the actual visual observation of any kind of activity (*Fig. 2.20*, Ripepe et al. 2001). The level of the magma however, is not stable on time, and so any measured time delay would not be stable in time as well, and could be used to calculate a mean magma level (~120 m below the crater terrace for Stromboli). Any delay between the seismic and infrasonic could be also the result of variations in the magma gas sound speed and different magma column height above the coalescence level, covered by the expanding gas (Ripepe et al. 2001).

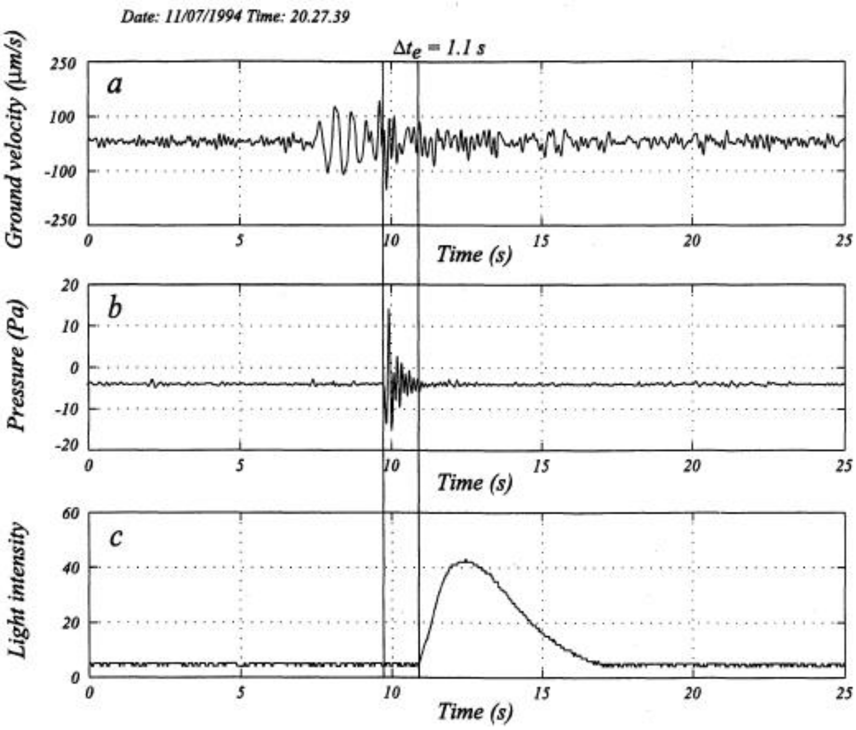

Figure 2.20 Time delays between (**a**) seismic, (**b**) acoustic and (**c**) thermal signals from an eruption at Stromboli (Ripepe et al. 2001).

Explosive degassing is not the only activity showing a clear and repetitive seismic signal, although direct observations of the activity help in linking the actual measurements to the style of activity. In the absence of visible explosive activity at surface, the continuous bursting of small gas bubbles at the magma free surface somewhere deep in the conduit can still be recognised as a sequence of weak (~1-2 Pa) pressure pulses (Ripepe et al. 1996). These signals, for their cyclic nature and short time delays (0.8-1.2 s), are interpreted as volcanic tremor. The cyclic bursting is also supported by a continuous infrasonic activity, whose fluctuations show a strong correlation with tremor amplitude, suggesting a possible common source mechanism (Ripepe et al. 1996). Furthermore, during effusive activity, and in the absence of explosive Strombolian activity, stable VLP signals can be detected, identical to the ones produced by *Type 1* and *2* activities. The same source mechanism may be responsible for the pre-eruptive VLP and the effusive phase do not induce significant changes to the source processes. The continuous presence of stable VLP signals could indicate that the coalescence and expansion of the gas continue uninterrupted and that Strombolian activity actually does not cease but occurs deeper in the conduit without superficial expression, even during an effusive phase. However, during these phases the seismic source seems to migrate, first deepening, and then moving toward the surface, in correspondence of the renewal of the normal Strombolian activity. Since the stability of the signals does not suggest a change in the geometry of the conduit, this migration could suggest a control of the source by a physical or rheological discontinuity (such as a density or a viscosity contrast) within the shallow magma column (Marchetti and Ripepe 2005).

Thus, the source of the VLP signals seems to remains stable only during the persistent explosive activity at Stromboli, while during anomalous activity (e.g., effusive and paroxysmal events) it migrates. The changes in the VLP source location, amplitude and occurrence rate could indicate changes in the conditions of the shallow conduit and hence in the mechanism generating the VLP events (e.g., Giudicepietro et al. 2009). Also, a larger VLP amplitude seems to correlate with more energetic explosions and a general increase in the VLP amplitude and longer oscillations characterize anomalous activity. All suggest a difference between both the source mechanism and energy of the signals of normal and anomalous activity (e.g., Andronico et al., 2008, Pistolesi et al. 2011, Calvari et al. 2012). This evidence may imply a link between different flow conditions, abrupt flow pattern change due to structural discontinuities or rheological variations, changes in the geometry of the shallow conduit and the degree of slug overpressurization, but so far the nature of these changes and diversity is still debated.

It is also possible to extract from the seismic signals information about ground displacement and tilt, by filtering the seismometers below their natural response period. The ascent and expansion of bubbles in basaltic magma can produce ground displacement, although relatively minor, detected as inflation and deflation of the volcanic edifice (Nishimura 2009). However, very little is known about ground displacement at Strombolian-type volcanoes because, due to the nature of the events, deformations are probably too small and require the installation of dedicated and high sensitivity instruments near the vent, an often difficult – if not impossible – task (e.g., Genco and Ripepe 2010). The possibility of using data from the seismic surveillance network, together with the installation - when possible - of dedicated tiltmeters, recently improved our understanding of ground deformation induced by Strombolian activity. This allowed to identify at Stromboli a sequence of in-vent inflation-deflation cycles: each explosion was preceded by a slow inflation, lasting in the order of hundreds of seconds (~200 s), immediately followed by a sharp deflection. The inflation was related to conduit pressurization prior the explosion and explosive degassing, followed by a deflation resulting from the gas-and-fragments release in the atmosphere. Furthermore, the rates of change of the inflation increased ~10 times in the 10-20 s before the eruption, suggesting a sudden acceleration of the gas in the shallower part of the conduit, in agreement with the dynamics of near-surface gas slug expansion (Genco and Ripepe 2010).

Furthermore, the presence of a cap at the top of the magma column in open-vent volcanoes characterized by Strombolian and Vulcanian eruptions seems to have a strong influence on conduit pressurization. First gas bubbles accumulate beneath the cap, causing inflations of the vent area. Then, as the gas makes its way through the cap, the inflation phase is followed by deflation of the vent (Nishi et al. 2007; Nishimura et al. 2013; Lyons et al. 2012; Kawaguchi and Nishimura 2015). However, detailed data on ground displacement for plugged conduits in Strombolian-type volcanoes are still lacking.

Both seismic and infrasonic data proved capable to provide an important window on source processes related to magma transport and fluid dynamics processes. Still, seismology and infrasound alone cannot fully unveil the conduit dynamics and the link between the flow processes and the generation of these signals. In order to better understand and model the mechanisms responsible for the wide variations in such signals, laboratory experiments and numerical models are necessary to link the unseen processes to the recorded data. Indeed, the dynamics proposed by Chouet et al. (2003, 2008, 2013) are mainly supported by experimental results (James et al. 2004, 2006), demonstrating how strongly these two methodologies depend on each other, linking pressure and ground forces changes obtained in much more simplified and controlled environment to the ones produced by the undeniable more complex and often unpredictable volcanic systems. Furthermore, seismic and infrasonic data can be explained in terms of perturbations in a two-phase flow and gas releases, but without been directly associated with processes occurring in the conduit. Indeed, the only directly observable result of such processes is the activity at surface; thus, field observations play an important role in designing both laboratory experiments, development of models of eruptive dynamics and interpretation of geophysical signals.

Ultimately the key to better understand the eruptive dynamics lies not in the successful acquisition of the best multi parametric dataset but in the integration of data processing/interpretation and correlation of model and laboratory results with field evidence.

Chapter 3 - Modelling and experimental background

Much of what is known about gas bubbles ascending in a liquid-filled pipe has been published in the chemical engineering and fluid dynamic literature. Indeed, the long bullet-shaped bubbles - *Taylor bubbles*, known as *gas slugs* in volcanology - can be found in many industrial applications: hydrocarbon production in oil wells and their transportation in pipelines, cooling systems of nuclear reactors, power station steam boilers, transport and handling of cryogenic fluids, gas absorption units, heat exchangers and air-lift reactors. Therefore, a large body of industrial literature exists on the two-phase flow regime (e.g., Davies and Taylor 1950; Goldsmith and Mason 1962; White and Bearmore 1962; Brown 1965; Zukosky 1966; Wallis 1969; Campos and Guedes de Carvalho 1988a, b; Viana et al. 2003; Nougueira et al. 2006a, b).

The volcanological importance arises because Strombolian eruptions are interpreted as the arrival and burst of slugs at the magma free surface. Furthermore, their ascent, expansion and burst are assumed to be the main source mechanisms for seismic and acoustic signals (e.g., Vergniolle and Brandeis 1996; Chouet et al. 2008, James et al. 2006; Lane et al. 2013). Hence, understanding the dynamics of slug expansion/pressurization in the conduit is crucial to constrain the parameters controlling changes in the flow pattern, pressure variations and, potentially, the transition between eruptive styles.

The following sections will provide the necessary background on the dimensionless parameters needed to scale laboratory conditions with low-viscosity magmatic systems and on the theoretical, numerical and experimental investigations that led to the current understanding of fluid dynamics involved with the slug ascent in a single-viscosity system. From now on, Taylor bubbles will be referred as *slugs* or, simply, *bubbles*.

3.1 Dimensionless parameters

The characteristics and behaviour of slugs are dependent on several physical parameters, including properties of the liquid (viscosity μ, density ρ, surface tension σ) and internal diameter of the pipe D. In order to scale the laboratory experiments to a real volcanic conduit filled with low-viscosity magma, all these quantities can be re-cast as the following dimensionless numbers (e.g., White and Beardmore 1962; Wallis 1969; Seyfried and Freundt 2000).

The Morton number, *Mo*, represents the ratio between the viscous and surface tension forces:

$$Mo = \frac{g\mu^4}{\rho\sigma^3} \quad (1),$$

where g is the gravitational acceleration.

The Eötvös number, *Eo*, represents the ratio between buoyancy and surface tension forces:

$$Eo = \frac{\rho g D^2}{\sigma} \quad (2).$$

For *Mo* > 10^{-6} (Seyfried and Freundt 2000) and *Eo* > 40 (Viana et al. 2003), the surface tension can be neglected and the Morton and Eötvös numbers can be combined to eliminate σ and derive a new dimensionless quantity, the inverse viscosity, N_f:

$$N_f = \left[\frac{Eo^3}{Mo}\right]^{\frac{1}{4}} = \frac{\rho}{\mu}\sqrt{gD^3} \quad (3),$$

where r_c is the pipe radius. Inverse viscosity is a key parameter: if N_f for a laboratory system is similar to that for the rise of a gas slug in a magma-filled volcanic conduit, then the experiment is likely to be a good analogue of the natural process. The inverse viscosity can be further related to the slug Reynolds number (Llewellin et al. 2012), often found in literature (e.g. Nogueira et al. 2006a, b), representing the ratio between inertial and viscous forces:

$$Re_b = \frac{\rho V_s D}{\mu} = Fr N_f \quad (4),$$

where V_s is the slug ascent velocity and Fr is the Froude number, which represents a dimensionless measure of slug ascent velocity as the ratio between inertial and gravitational forces:

$$Fr = \frac{V_s}{\sqrt{gD}} \quad (5).$$

3.2 Slug features

Slug morphology can be divided into four regions (*Fig. 3.1*): 1) a hemispherical nose, 2-3) a body, surrounded by a falling liquid film, 4) a tail with variable shape (flat, hemispherical, concave, turbulent) and 5) a wake region. The body region can be further divided into an upper (2), where the developing falling liquid film is accelerating and thinning, and a lower part (3), where the forces acting on the film are in equilibrium and the film has a constant thickness, λ.

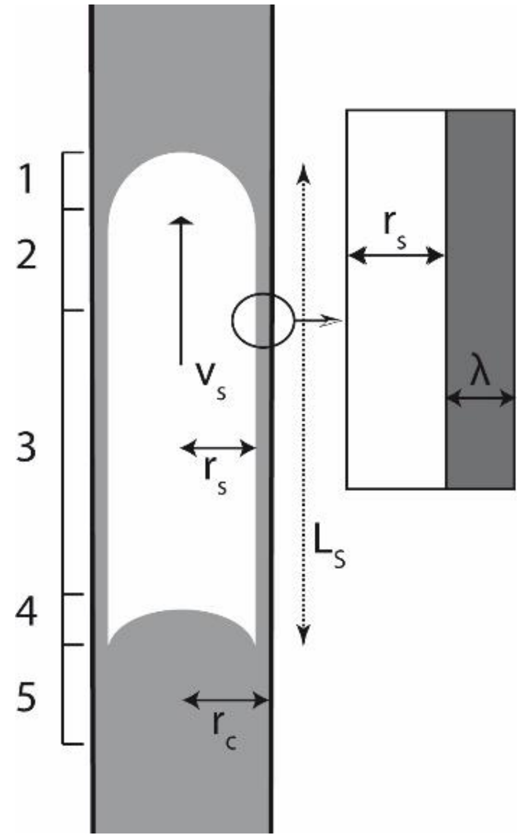

Figure 3.1 Conceptual representation of a slug of length L_s and radius r_s rising with an ascent velocity V_s in a pipe of radius r_c. The bubble can be divided into 5 regions: **1**) nose, **2**) upper and **3**) lower body, **4**) tail and **5**) wake. The falling liquid film achieves its equilibrium thickness λ only in the lower part of the body.

Gas slugs ascending in a stagnant liquid can be relatively long and fill almost the entire cross section of the pipe, surrounded by a falling liquid film (e.g., Viana et al. 2003), with the bubble nose always hemispherical shaped. The shape of the tail and nature of the wake are strongly dependent on the balance of viscosity and inertia (*Fig 3.2;* Davies and Taylor 1950; Viana et al. 2003). Variations in both density ratio (liquid density/gas density) and viscosity ratio (liquid viscosity/gas viscosity) induce small effects in the bubble dynamics. In contrast, variations in Eo and N_f induce significant changes in both bubble shapes and wake structure. For low values of N_f the bubble encounters the highest resistance from the surrounding liquid and higher viscous shear forces, facilitating the elongation of the bubble. The bubble is hemispherical both at the nose and the tail, and the falling liquid film is thicker. Increasing N_f , the liquid becomes less viscous, the film thickness decreases, the long and slim shape of the bubbles changes into shorter and fatter shapes, confining the liquid film into a thinner region. At higher N_f the bottom of the bubble becomes more dimpled and elongated and the wake length increases (*Fig. 3.3, upper panel*; Kang et al. 2010). Greater values of *Eo* lead to an elongated and indented slug tail, and generation of two distinct wakes. The higher *Eo*, the more the tail tips from the top to the bottom, mirroring a reduction in surface tension forces. Variations in *Eo* do not lead to changes in the nose shape or in the falling film region (*Fig. 3.3, lower panel*).

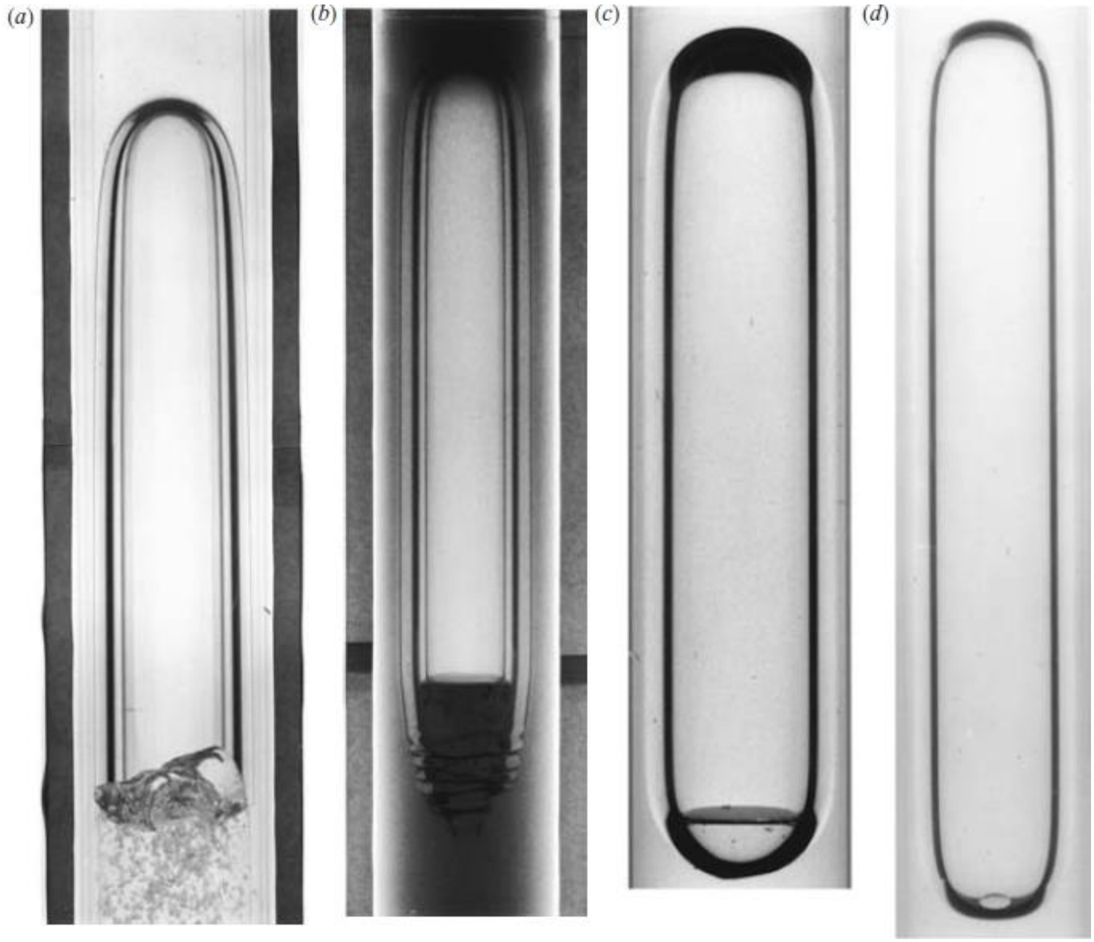

Figure 3.2 Bubbles rising in a pipe filled with (**a**) water (1 mPa s), (**b**) Purolub 150 oil (480 mPa s), (**c**) silicone oil (1300 mPa s), (**d**) silicone oil (3900 mPa s) (Viana et al. 2003).

The wake, for N_f < 500, is closed and axisymmetric. For 500 < N_f < 1500 the wake is still closed but unaxisymmetric until, for N_f > 1500, the flow in the wake becomes turbulent, with a clear recirculatory motion (*Fig. 3.4*; Campos and Guedes de Carvalho *1988*). The same evolution of the wake region is observed in computational fluid dynamic (CFD) simulations, for the same experimental conditions (*Fig. 3.5;* Taha and Cui 2006). Furthermore, for low and moderate range of N_f, the length of the wake is linearly dependent on N_f and the bubble shape is viscosity and surface tension dependent and not affected by the bubble length (Taha and Cui 2006).

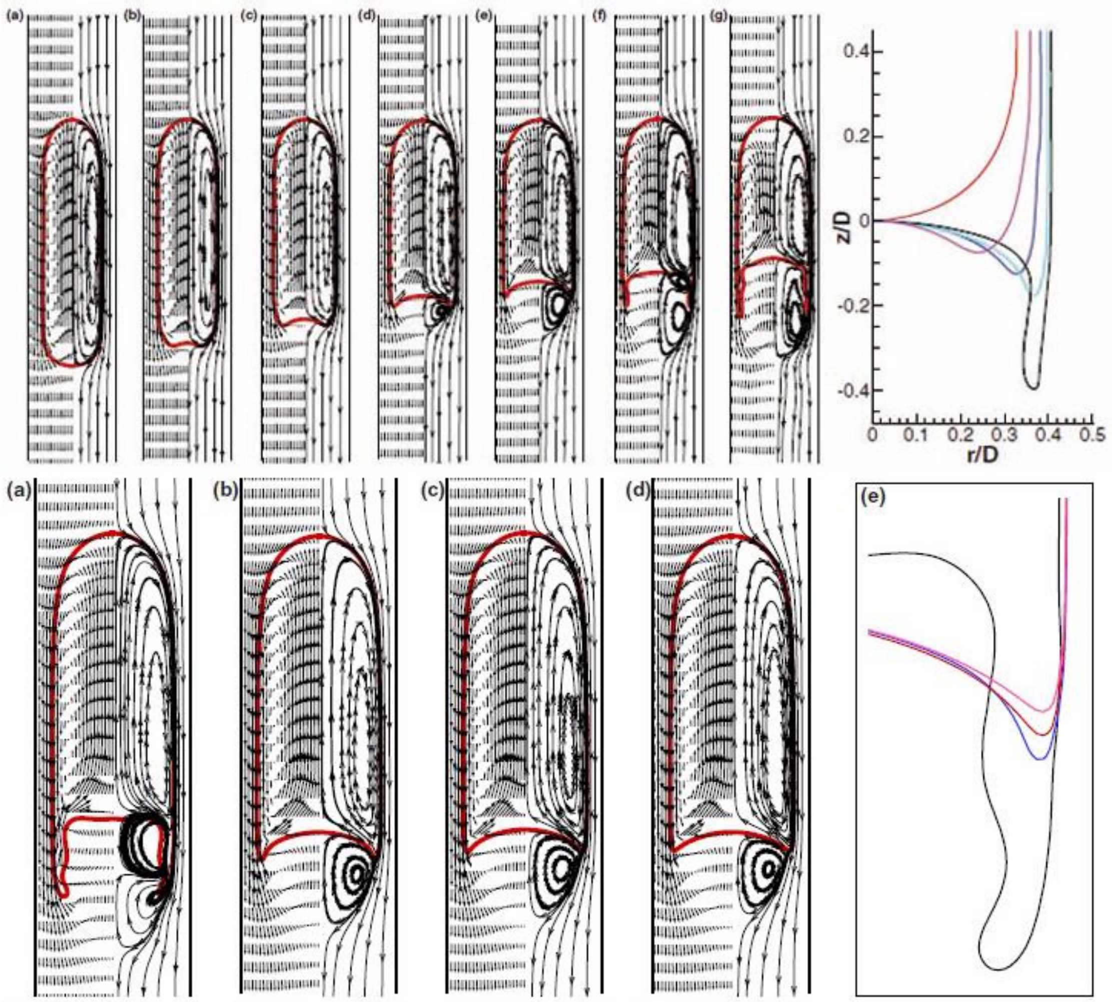

Figure 3.3 (**Upper Panel**) Effect of the inverse viscosity on the shape and the wake flow patterns of a slug: (**a**) N_f = 10, (**b**) N_f = 25, (**c**) N_f =45, (**d**) N_f = 100, (**e**) N_f = 200, (**f**) N_f = 300, (**g**) N_f = 450. (**h**) Changes in the tail region with different N_f; tail tips from the top to the bottom represent a progressive increase in N_f. (**Lower panel**) Effect of the Eötvös number on the shape and the wake flow patterns of a slug: (**a**) *Eo* = 304, (**b**) *Eo*= 203, (**c**) *Eo*=152, (**d**) *Eo* = 122; (**e**) changes in the tail region with varying *Eo* numbers; tail tips from the top to the bottom represent a progressive reduction in surface tension forces (modified from Kang et al. 2010).

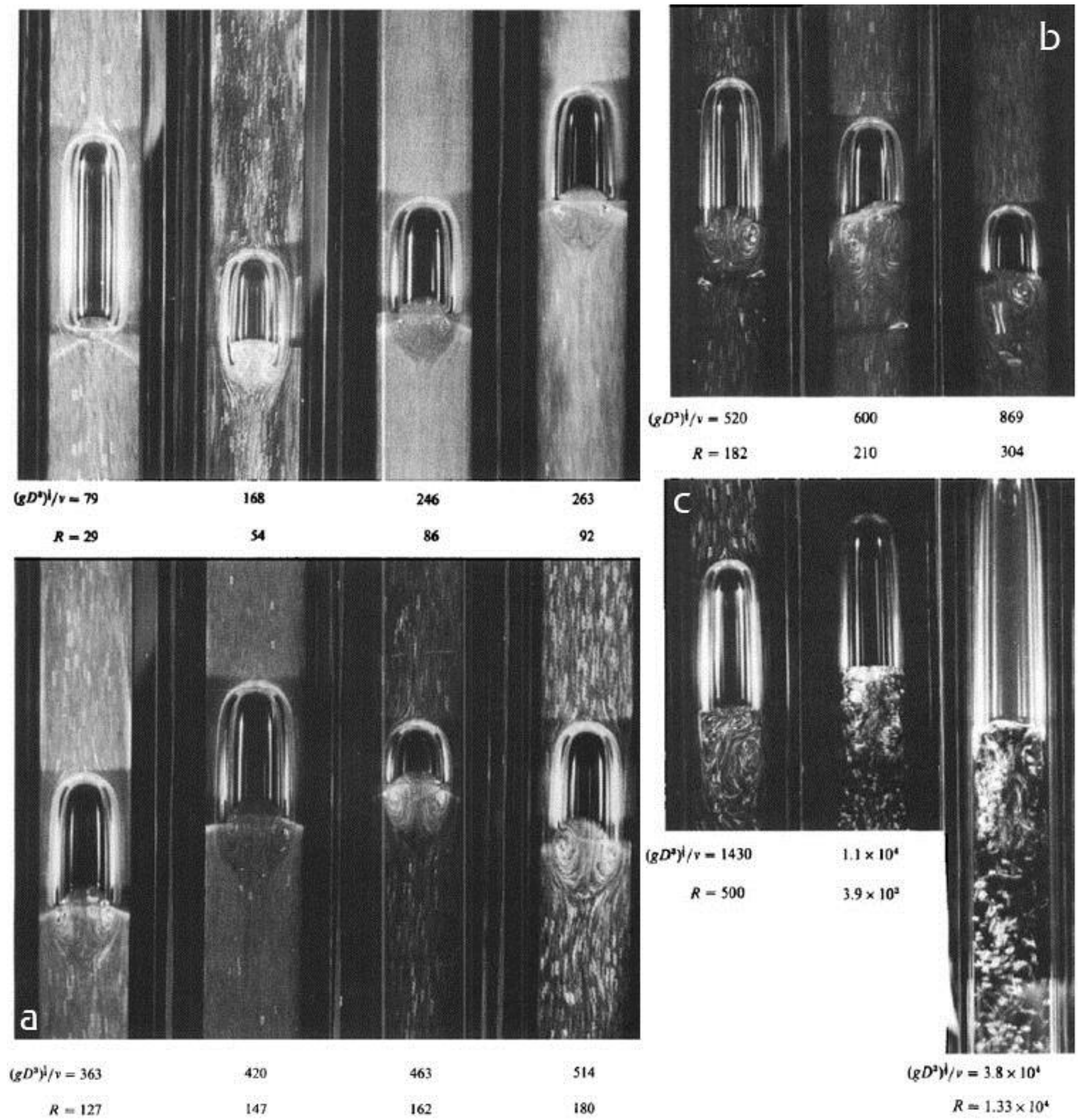

Figure 3.4 Different flow patterns in the wake of slugs rising in liquid-filled tubes depending on the inverse viscosity. (**a**) For $N_f < 500$ a closed axisymmetric wake is formed. (**b**) For $500 < N_f < 1500$ the bubble is characterized by a closed unaxisymmetric wake. (**c**) For $N_f > 1500$, the flow in the wakes becomes turbulent, with recirculatory motion (modified from Campos and Guedes de Carvalho 1988).

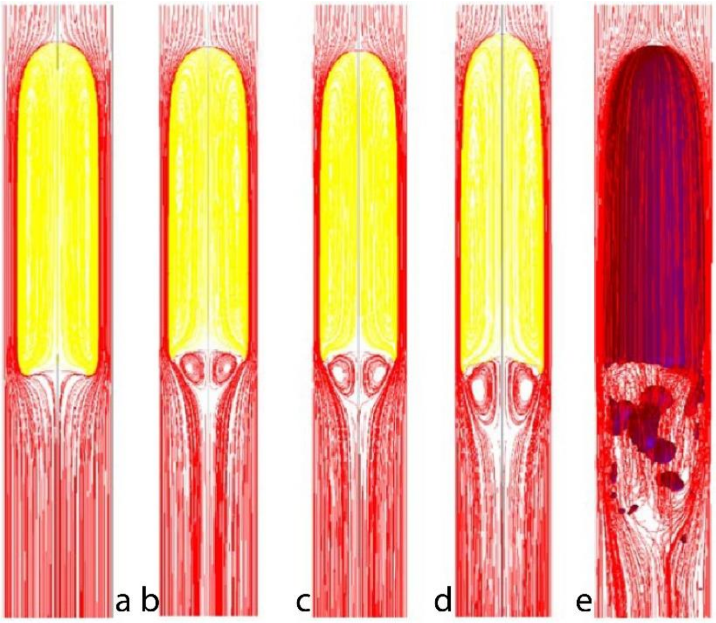

Figure 3.5 Different flow patterns in the wake of a slug in a tube filled with glycerol solutions at different values of N_f; for 500 < N_f < 155 the wake is still closed but losing its symmetry around the tube axis (**a**: N_f = 84, **b**: N_f = 176, **c**: N_f = 205, **d**: N_f = 325); for N_f > 1500 the wake is finally open and turbulent (**e,** N_f = 1528) (Taha and Cui 2006).

In the region just above the slug, the nose of the bubble displaces outwards the liquid ahead of it and the velocity decreases with the distance from the nose. The flow around the ascending slug nose is laminar. Then, the direction of the velocity vectors changes, moving downward away from the slug axis and toward the tube wall (*Fig. 3.6a*, Nogueria et al. 2006a, b). Indeed, the liquid head above the bubble flows into the falling liquid film allowing bubble rise and leading to the development of a strong radial velocity component (*Fig. 3.7*, Bugg and Saad 2002). As the liquid film thickness decreases, moving from the bubble nose to the bubble body, its velocity increases in order to maintain a constant flow rate, with maximum values at the gas-liquid interface and minimum at the tube wall (*Fig. 3.6a;* Nogueria et al. 2006a, b). The radial velocity component is still strong moving down below the top of the bubble, especially near the gas-liquid interface, while it decreases significantly in the body region. The maximum velocity in the developing film is half way between the gas-liquid interface and the tube wall; the film accelerates and thins until it is fully developed and the shear stress at the wall supports its weight; at this point the radial velocity is zero (*Fig. 3.7,* Bugg and Saad 2002). As the liquid drains from the falling film to the region below the bubble's tail, it starts to decelerate in order to occupy the entire cross sectional area of the tube. Here, a complex liquid recirculation region forms, characterized by a mean velocity equal to the bubble velocity (*Fig. 3.6b*).

Streamlines for this recirculation zone clearly show two toroidal vortexes and the symmetry of the flow (*Fig. 3.6c*, Nogueria et al. 2006a, b). The fluid just beneath the bubble moves at the same velocity of the bubble (*Fig. 3.7*, Bugg and Saad 2002).

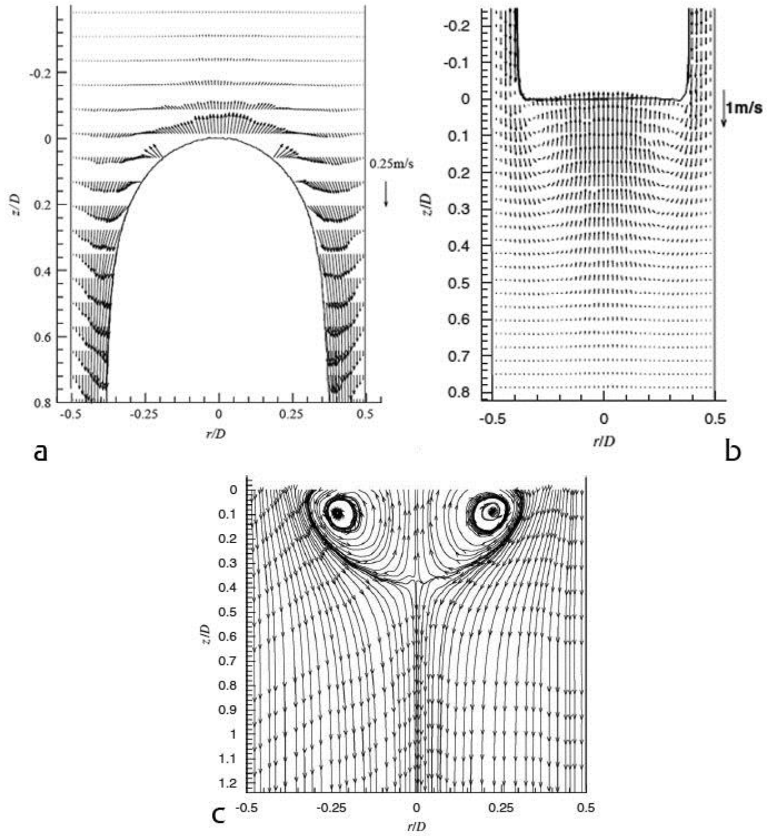

Figure 3.6 Velocity profile around (**a**) the nose and (**b**) the tail of a slug rising in a stagnant aqueous solution for N_f = 200. (**c**) Streamlines in the wake region resulting by averaging the flow fields in the wake of ten different slugs rising in a stagnant aqueous solution for N_f = 200 (modified from Nogueira et al. 2006a, b).

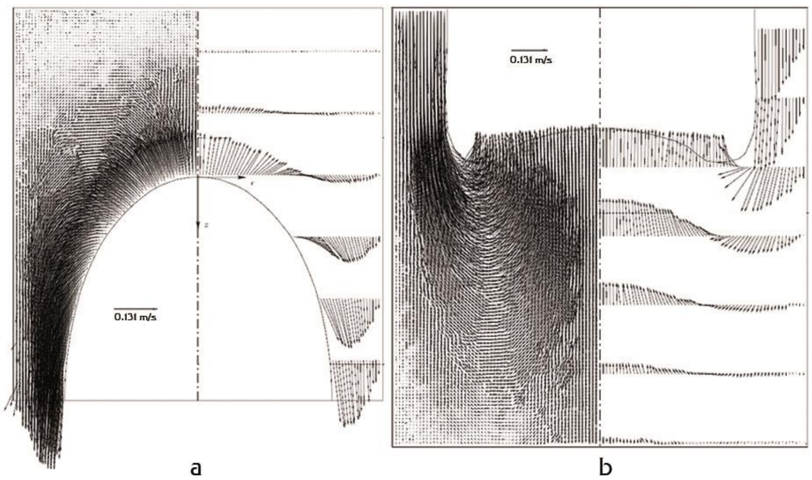

Figure 3.7 PIV (particle image velocimetry) measurements for the velocity field around (**a**) the nose and (**b**) the wake regions of a slug rising with a bubble terminal velocity of 0.131 m/s in a pipe filled with olive oil (ρ = 911 kg/m^3, μ = 0.08 Pa s), showing axial and radial velocity component (modified from Bugg and Saad 2002).

3.3 Slug ascent velocity

The Froude number for a slug ascending in a stagnant liquid, considering both viscous and surface tension forces negligible, and assuming potential flow conditions and a laminar flow within the liquid film, has a constant value of 0.351 (Dumitrescu 1943). This solution relates the slug velocity (V_s) to the gravitational acceleration and the pipe diameter through $V_s = 0.351\sqrt{gD}$. A similar result was achieved by Davies and Taylor (1950) who estimated a Fr value of 0.328. Both solutions describe the velocity of a bubble in low-viscosity liquids quite well, but the assumption of an inviscid liquid is restrictive, especially in volcanological application.

Indeed, depending on the liquid rheology, the velocity of a bubble would be affected by viscous, inertial and interfacial forces. For Eo < 3.4, capillary forces hinder the ascent of a bubble within a pipe diameter of 0.50 cm, a viscosity of ~0.001 Pa s, corroborating previous investigations (Eo < 4, Gibson 1913; Eo < 3.36, Hattori 1935; Eo < 3.37, Bretherton 1961). For Eo > 70 the inertial forces dominate, and the influence of surface tension and viscous forces becomes negligible for $Mo < 10^{-8}$. Viscous effects are negligible for $N_f > 3\times10^5$. The maximum value achieved for the Froude number (accounting for variations due to gas expansion) is 0.345 (in agreement with Dumitrescu, 1943); this velocity is only a function of Eo and N_f (hence of conduit diameter and liquid properties respectively). For a bubble ascending in a pipe, when a critical value of bubble size is reached (depending on the liquid properties) its velocity is as a function of the curvature of the cap and not of the size (White and Bearmore 1962). These relationships are summarized in the correlation in *Fig. 3.8*, valid for Eo < 1000 and $Mo < 10^6$ (White and Bearmore 1962).

However, the velocity of the slug is determined from the nose of the bubble, correcting for the expansion of the gas. Thus, the graphical correlation is strictly valid in a system where expansion does not take place, and it is not valid in a dynamic system in which the gas expands as it approaches the surface.

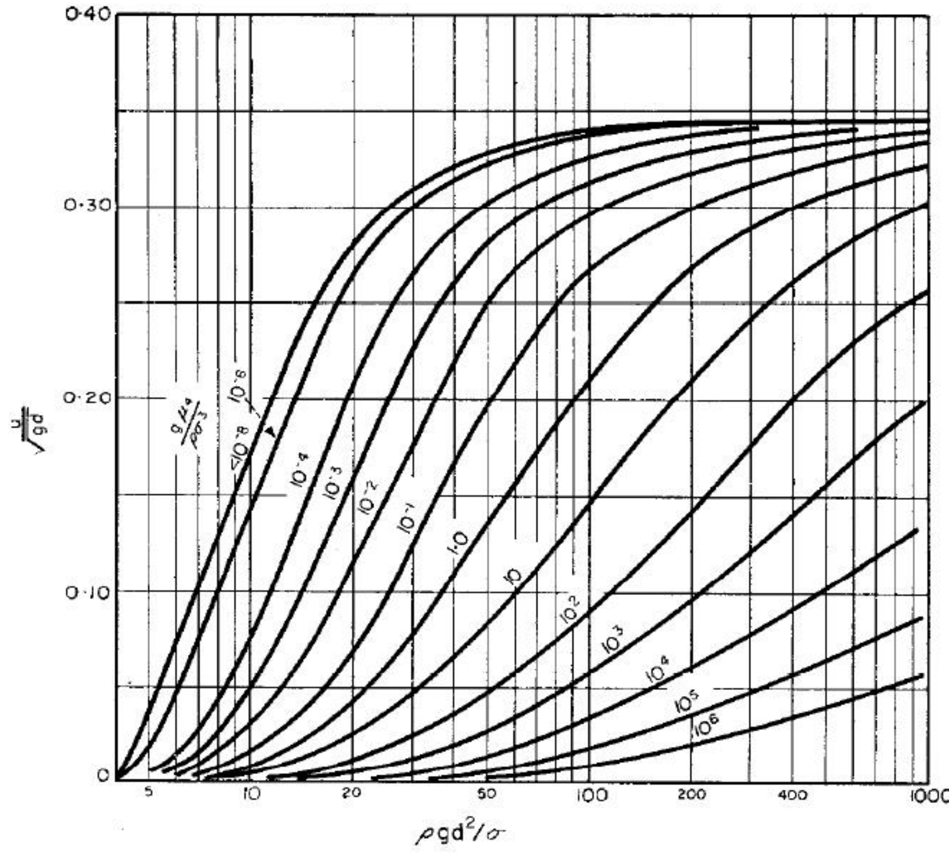

Figure 3.8 Graphical correlation for the dimensionless ascent velocity (Froude number, $u/\sqrt{gd}$) as a function of the conduit diameter (Eötvös number, $\rho gd^2/\sigma$) and for $4 < Eo < 1000$. $Eo = 4$ (Gibson 1913) is considered here as a standard value, valid for an hemispherical shaped bubble and a contact angle of the liquid on the surface equal to zero. Different liquid rheology are represented by the Morton number ($g\mu^4/\rho\sigma^3$) in the range $10^{-8} < Mo < 10^6$. The Poiseuille number - the balance between viscous and gravitational forces, $Ps = (v_s\mu)/(\rho gD^2)$ - represents the velocity when inertial forces can be neglected (White and Beardmore 1962).

For a bubble in a laminar flow, with the radius of the pipe much smaller than the bubble length, ascending in both the inertial and viscous regimes, the bubble velocity can be related to the thickness of the falling film via:

$$V_s = \frac{2\rho g\lambda^3}{3\mu r_c} \quad (6),$$

assuming that the film thickness is much thinner than the pipe radius ($\lambda << r_c$). The film thickness is independent of the Reynolds number (Re, $Re = (\rho V_s r_c/\mu)$) for $10^{-5} < Re < 1$. Taking into account the interfacial tension, velocity remains almost constant for fixed values of σ and r_c over a wide range of increasing viscosity. Regardless of the viscosity, bubble deformation does not change for constant Eo (Goldsmith and Mason 1962), and the geometries of the bubbles are similar (Brown 1965).

Considering the radius of the bubble (r_s) instead that of the pipe (r_c), the ascent velocity becomes $V_s = 0.496\sqrt{gr_s}$ (where the bubble radius $r_s = r_c - \lambda$) and can be related to the terminal ascent velocity of the bubble, including the retarding effect of the liquid viscosity, through the general correlation (Brown 1965):

$$V_s^0 = 0.496\sqrt{gR}\sqrt{1 - \frac{-1+\sqrt{1+2NR}}{N}} \quad (7),$$

where $N = \sqrt[3]{14.5\frac{\rho^2 g}{\mu^2}}$ (8).

The limits of this solution are:

- Viscosity: $N_f > 120$
- Surface tension: $\frac{\rho g R^2}{\sigma}\left(1 - \frac{-1+\sqrt{1+2NR}}{NR}\right)^2 > 5$

Based on all the previous numerical and experimental results and new experimental data (Zukosky 1966), when *Re* > 200, the velocity can be considered independent from viscous effects, and controlled solely by the surface tension, $\sum = [\sigma/\rho g r^2]$. For Σ < 0.1, the ascent velocity equals to $V_s = 0.351\sqrt{gD}$ (in agreement with Dumitrescu, 1943). Experimentally, for fixed Reynolds number (*Re* ~700 and ~200) and increasing Σ, a velocity decrease is evident, demonstrating the strong control of the surface tension. For fixed Σ and decreasing *Re* (i.e., increasing viscosity), the velocity first increases as result of the decreasing Σ; then, at *Re* ~50 a velocity drop occurs, regardless of Σ (Zukosky 1966). The effects of viscosity and surface tension can be related by

$$V_s\{Re, \Sigma\} \approx v_b\{\infty, \Sigma\} f\{Re\} \quad (9),$$

then expressed in numerical form by Viana et al. (2003), fitting the original experimental data points:

$$Fr_z(\infty, \Sigma) = 0.4664 + 0.3473\Sigma - 5.3928\Sigma^2 + 10.532\Sigma^3 - 6.7095\Sigma^4 \ (\Sigma < 0.6) \quad (10),$$

$$f(Re) = \frac{1}{(1+44.72/Re^{1.8})^{0.279}} \quad (11).$$

For inclined pipes and varying diameters, the velocity of a bubble increases as the inclination angle decreases, from vertical to horizontal position. Regardless of the conditions, the bubble’s shape is always stable (Zukosky 1966).

All the published data on slug ascent velocity from the last 7 decades were collected, reprocessed and integrated with new experimental data by Viana et al. (2003) to provide a new “universal correlation” for calculating the Froude number. The original and cumbersome correlation was simplified by Llewellin et al. (2012), for *Eo* > 40 and $10^{-1} < N_f < 10^5$:

$$Fr = 0.34\left[1 + \left(\frac{31.08}{N_f}\right)^{1.45}\right]^{-0.71} \quad (12).$$

Thus, knowing the liquid properties and pipe radius, it is possible to calculate the ascent velocity. Note that Froude number is a function of the inverse viscosity only as well. Therefore, from (12), the Reynolds number ($Re = FrN_f$) is also a function of the inverse viscosity only (Llewellin et al. 2012). So far, when σ is negligible, (12) is the recommended equation for calculating the ascent velocity of a non-expanding gas slug or the base of an expanding gas slug.

3.4 The falling liquid film

For slug ascent in a low-viscosity liquid, the slug fills almost the entire cross-section of a pipe and it is surrounded by a thin falling liquid film. When ascending in a higher viscosity liquid, the area of the tube occupied by the slug decreases, the slug length increases and the falling film around it thickens. Being able to measure the Froude number is also a requirement for predicting the thickness of this film, $\lambda = r_c - r_s$, where r_c is the conduit radius and r_s the bubble radius.

For a gas slug ascending in a volcanic conduit filled with low-viscosity magma, the slug velocity can be related to λ through the parameter $N = \sqrt{14.5\,(\rho^2 g/\mu^2)}$ and then λ is derived as (Brown 1965; Seyfried and Freundt 2000):

$$\lambda = \frac{\sqrt{1+ND-1}}{N} \quad (13).$$

The above solution is re-cast in dimensionless form (dimensionless film thickness, $\lambda' = \lambda/r_c$):

$$\lambda' = 2\frac{\sqrt{1N}-1}{N} \quad (14),$$

predicting λ as a function of magma viscosity (Llewellin et al. 2012; Seyfried and Freundt 2000). The solution derived by Batchelor (1967), based on a balance between viscous and gravitational forces acting on the film and assuming $\lambda << r_c$, was implemented in models of slugs ascending in a conduit filled with low-viscosity magma by Vergniolle (1998) and James et al. (2008):

$$\lambda = \left(\frac{3\mu r_c V_s}{2\rho g}\right)^{\frac{1}{3}} \quad (15).$$

This solution is similar to the one derived by Brown (1965). However, Brown (1965) considers the Froude number based on the bubble radius instead of the pipe radius, while Batchelor (1967) assumes a falling film thinner than the pipe radius. The same solution can be simplified assuming the Froude number constant, Fr = 0.34 (Llewellin et al. 2012):

$$\lambda' = 0.9\left(\frac{\mu^2}{\rho^2 r_c^3 g}\right)^{\frac{1}{6}} = \left(\frac{2.04}{N_f}\right)^{\frac{1}{3}} \quad (16).$$

For 10 < N_f < 450 and maintaining the Eötvös number fixed at 203, Fr increases for N_f < 200, above which Fr remains constant; the film thickness decreases for increasing N_f. Also the shape of the bubble changes for increasing N_f, from long and slim shapes into shorter and fatter shapes, confining the liquid film into a shorter region (Kang et al. 2010, §3.2). Then, the film thickness can be related to N_f via:

$$\frac{\lambda}{D} = 0.32Ar^{-0.1} \quad (17),$$

where Ar is the Archimedes number, Ar = N_f^2, and expressed as $\lambda' = 0.64N_f^{-0.2}$ (Llewellin et al. 2012)

Thus, the main solutions for the thickness of the falling film can be re-cast in terms of dimensionless film thickness, λ', as a function of the inverse viscosity only, N_f, demonstrating, when surface tension is negligible, the strong control of N_f on λ' (Llewellin et al. 2012). Indeed λ' is independent of N_f for $N_f \leq 10$; in the range $10 \leq N_f \leq 10^4$, λ' decreases as N_f increases; for $N_f \geq 10^4$ λ' is again independent (*Fig. 3.9*). Furthermore, all the published data were compared and integrated with new experimental results (Llewellin et al. 2012). The shape of the nose and body of the bubbles and the ascent velocity (measured for each value of N_f) are independent of bubble length, increasing due to the gas expansion. The shape of the tail and the nature of the wake are dependent of the inverse viscosity. Following these results an empirical model for λ' can be derived:

$$\lambda' = 0.204 + 0.123\tanh(2.66 - 1.15\log_{10} N_f) \quad (18),$$

valid for $0.1 < N_f < 10^5$ (Llewellin et al. 2012).

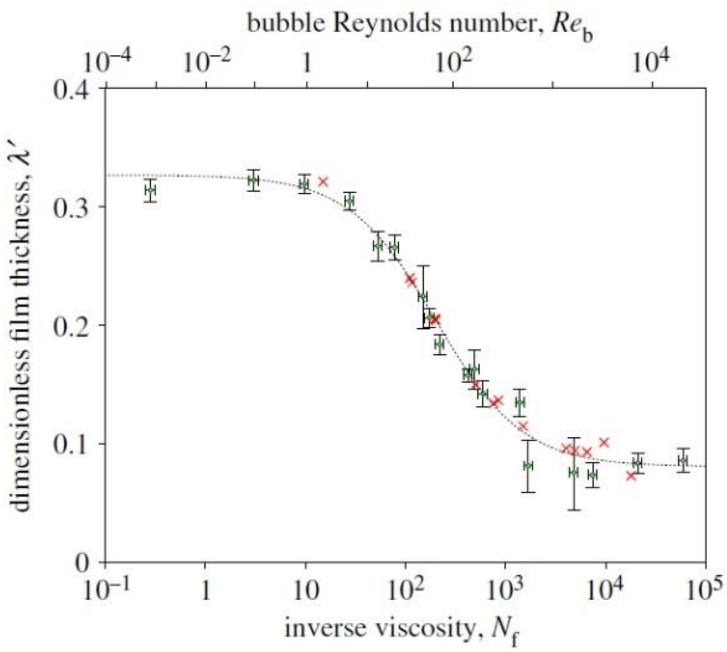

Figure 3.9 Relationship between the dimensionless film thickness, inverse viscosity and the bubble Reynolds number. New experimental data on slugs ascending in a pipe of different diameters and filled with different Newtonian liquids (circle) and literature data (crosses; Nogueira el al. 2006) show the strong control of the inverse viscosity on the film thickness, independent from $N_f < 10$ and $> 10^4$ (Llewellin et al. 2012).

3.5 Eruptive parameters

During the ascent within the conduit, the behaviour of gas slugs is controlled by parameters including conduit geometry, gas mass and magma rheology. These parameters affect the evolution of gas expansion and hence control explosion energy and the associated geophysical signals. Some of these physical parameters are used as boundary conditions for models of conduit dynamics and to scale experiments to low-viscosity magmatic systems using dimensionless parameters (in particular equations (3), (5), (12) and (18)). It is therefore important to introduce such parameters, taking into account some of the major publications (carried out mainly at Stromboli, due to the ease of data collection).

3.5.1 Gas mass and overpressure

Indirect information on gas masses and overpressures involved in Strombolian explosions and puffing activity can be obtained through processing of field data (e.g., seismic signals, thermal and high-speed video, UV measurements). *Table 3.1* reports the main ranges for gas mass and, when available, gas overpressure for Strombolian explosions involved in both puffing and explosive activity.

Table 3.1 Gas masses and overpressures derived from field data at Stromboli for the range of normal Strombolian explosions and puffing activity.

Gas mass (kg)	Overpressure (MPa)	Study	Reference
90-180	0.0006	Photoballistic	Chouet et al. 1974
0.3-30	0.02-0.6	Acoustic	Vergniolle and Brandeis 1996
~3 (NE vent) ~5 m^3 (SW vent)	~0.4 ~0.05	Acoustic	Ripepe and Marchetti 2002
~1016 (Type 1) ~3000 (Type 2)	10	Seismic	Chouet et al. 2003
10-40 (puffing)	--	Thermal	Harris and Ripepe 2007a
150-1500	--	Thermal	Delle Donne and Ripepe 2012
224-612	0.1	SO_2	Mori and Burton 2009
2-55 (puffing)	--	SO_2	Tamburello et al. 2012
4-714	0.10-0.56	High-speed video	Taddeucci et al. 2012b

3.5.2 Slug ascent velocity and conduit radius

Slug ascent velocity and conduit radius can be estimated using both mathematical models, processing of field data (e.g., acoustic and seismic signals, UV measurements) and direct filed observations (e.g., thermal and high-speed videography).

Table 3.2 reports the main values for these parameters, derived by field measurements at Stromboli.

Table 3.2 Slug ascent velocities and values of conduit radius for normal Strombolian explosions measured from field data at Stromboli or modelled.

Velocity (m/s)	Conduit radius (m)	Study	Reference
--	0.5-3	Photoballistic	Chouet et al. 1974
1.6	0.5	Acoustic	Vergniolle and Brandeis 1996
1.1[a]	--	SO_2 and CO_2	Allard 2010
0.2[b]	~0.4	Seismic	Pino et al. 2011
3.7	--	Seismic and acoustic	Ripepe et al. 2001
10-70[c]	--	Seismic and acoustic	Harris and Ripepe 2007
--	2-5	Modelling	Genco and Ripepe 2010
0.11-2.6	--	Modelling	Llewellin et al. 2012
0.11-2.6	1.5-3	Modelling	Del Bello et al. 2012
--	~1.3-~1.5	SO_2	Burton at al. 2007a
--	~2	Thermal	Delle Donne and Ripepe 2012
--	0.5-2	High-speed video	Taddeucci et al. 2012
--	2.5	High-speed video	Gaudin et al. 2014

[a] considering a 1 m wide slug rising from 10 km depth in 2.7 h.
[b] for a slug rising from 10 km depth in 15.5 h.
[c] in the shallower conduit, so likely considering the near-surface acceleration due to gas expansion.

3.5.3 Rheology of the magma

Magma rheology cannot be measured directly, but it is possible to estimate it by laboratory rheometry of natural samples and rheological models. Density and viscosity depend on controlling parameters such as temperature, magmatic composition, gas and crystal content, values of which are often assumed. These parameters vary considerably depending on the nature of the events and the original magma depth within the conduit. Therefore, viscosity and density estimates can show a wide range of values (*Table 3.3*).

Table 3.3 Viscosity and density measurements for basaltic magmas

Viscosity (Pa s)	Density (kg/m^3)	Location	Reference
1900 (T<1300°C) 95-1900 (T≈1300°C)	--	Makaophuhi (Hawaii)	Shawn 1969
--	1300-2600	Columbia River Basalt	Murase and McBirney 1973
10-300	--	Stromboli	Vergniolle 1996, 1998
1.4×10^{4} [a] 15-20[b]	2700 2500	Stromboli	Métrich et al. 2001
20-30[c] 10^{4} [d]	2500 2700	Stromboli	Landi et al. 2004
2000-2600[c] 3000-5000[d]	~1300 ~2650	Stromboli	Lautze and Houghton 2006
10^{2}-10^{4} [e] $10^{1.5}$-10^{3} [f] ~5[g]	--	Stromboli	Misiti et al. 2009
100	2700	Stromboli	Allard 2010
268-4360[h]	--	Stromboli	Vona et al. 2011
50-500[i] 6640[l] $1.2\text{-}53.1\times10^{6}$ [m]	900 -- 1300	Stromboli	Gurioli et al. 2014

[a] Crystal-rich magma at a temperature between 1100-1400°C.
[b] Crystal-poor magma at a temperature of 1150°C.
[c] For a volatile-rich magma.
[d] For a degassed, crystal-rich magma.
[e] For an anhydrous HK-basaltic melt at ~5 km depth, T ≈ 1000-1200°C.
[f] For a HK-basaltic melt at ~5 km depth, T ≈ 1000-1200°C and 2.0 *wt* % H_2O.
[g] for a magma rising from a depth between 8-3 km, 3.67 *wt* % H_2O, at 1200°C.
[h] For a HK-basaltic melt at 1150-1187°C, and a crystal volume fraction ranging between 10-30%.
[i, l, m] For fresh magma, mixed region high-/low-viscosity magma and a degassed and viscous layer at the top of the conduit respectively.

A range of surface tension values for several basaltic liquids was also derived, ranging between 0.25-0.45 N/m (Muramase and McBirney 1973). For a typical basaltic magma, a surface tension value of 0.4 N/m is generally assumed (e.g., Seyfried and Freundt 2000; James et al. 2006, 2008).

3.5.4 Volcanic parameters and scaling

Until recently, most of the models and experimental investigations considered a set of standard values for Strombolian-type volcanoes, with a magma of density ρ = 2600 kg/m^3, surface tension σ = 0.3-0.4 N/m and viscosity μ = 1000 Pa s, filling a conduit 3 m in diameter (e.g., Seyfried and Freundt 2000; Chouet et al. 2003, 2008;

James et al. 2008, 2009; Del Bello et al. 2012; Lane et al. 2013). These conditions yield to N_f = 42. It lies in an intermediate zone of the flow regime, where surface tension is negligible and both inertial and viscous forces play a role in the slug behaviour (Llewellin et al. 2012), as also the modified diagram of White and Bearmore (1962) shows (*Fig. 3.10*; Seyfried and Freundt 2000).

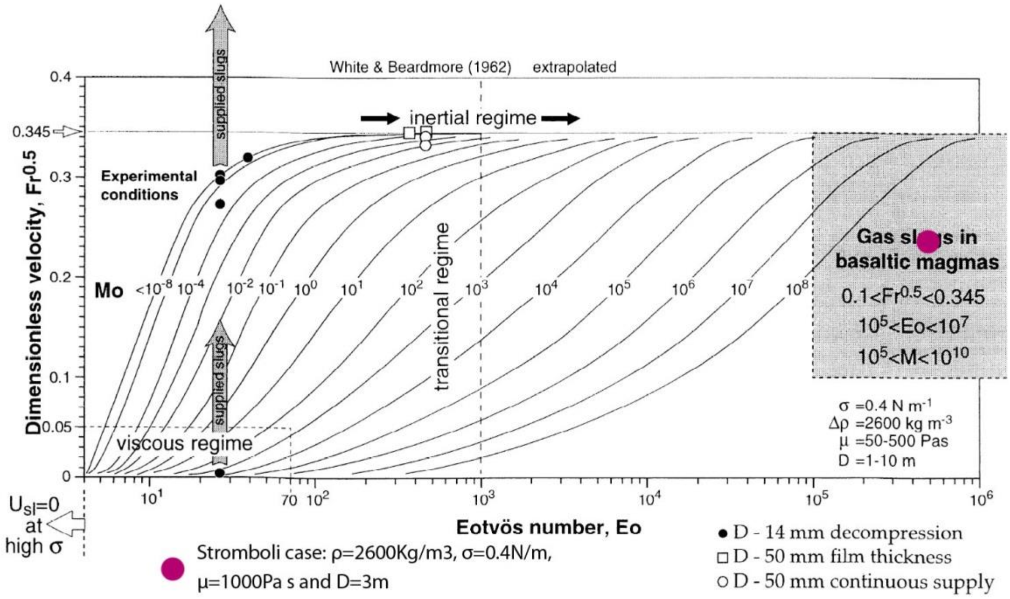

Figure 3.10 Modified diagram from White and Bearmore (1962) to scale for gas slug ascending and expanding in a conduit filled with low-viscosity magma, showing the influence of different liquid rheologies and conduit diameters on the slug ascent velocities (dimensionless) (modified from Seyfried and Freundt 2000).

However, if a layer of more viscous magma must be considered at the top of the conduit, a slug will behave differently depending if ascending in the fresh magma or in the degassed and more crystallized magma layer. For this study, viscosities between 10-50 kPa s with ρ = 1300 kg/m^3 for the viscous magma layer, and 50-500 Pa s and ρ = 900 kg/m^3 for the fresh magma are considered. These values are based on the most recent and accurate viscosity measurements on field samples collected at Stromboli in 2008, showing mingled textures resulting from the interaction of magmas with different rheological properties in the shallower part of the conduit (Gurioli et al. 2014). The considered values for the conduit radius, based on recent field measurements carried out at Stromboli (May 2014), range between 1.5-2.5 m (as also reported by Taddeucci et al. 2012a and Gaudin et al. 2014, *Table 3.2*).

These parameters give N_f~0.42 to ~4.55 for the evolved magma (plug) and ~29 to ~630 for the magma beneath the plug, for decreasing viscosities and increasing conduit radii (*Table 3.4*). This means that the slug behaviour, while ascending in the magma beneath the plug, is controlled by inertia with viscous contributions and by viscosity in the degassed and crystallized magma. However, the transition between viscous and mixed regime is around $N_f \approx 100$ (Llewellin et al. 2012); thus, depending also on conduit radius, there can be a range of viscosity for which viscous forces have a greater control on the slug flow in the fresh magma (*Table 3.4*).

Applying equations (12) and (5) to the above conditions and depending on conduit radius, slug ascent velocities are in the range ~1.09-~2.36 m/s in the fresh magma, and decrease considerably in the high-viscosity magma layer, between ~0.02-~0.31 m/s (*Table 3.4*).

Table 3.4 Summary of volcano-scale parameters covered in this study.

Conduit radius		***Underlying magma***				***Degassed and viscous magma ("plug")***		
	Density (kg/m^3)	900				1300		
	Viscosity (kPa s)	0.05	0.15	0.3	0.5	10	20	50
1.5 m	**Ascent velocity V_s (m/s)**	1.8	1.63	1.37	1.09	0.11	0.06	0.02
	Inverse viscosity N_f	293	98	49	29	2.11	1.06	0.4
2 m	**Ascent velocity V_s (m/s)**	2.1	1.98	1.78	1.53	0.2	0.10	0.04
	Inverse viscosity N_f	451	150	75	45	3.2	1.62	0.65
2.5 m	**Ascent velocity V_s (m/s)**	2.36	2.28	2.12	1.91	0.31	0.16	0.06
	Inverse viscosity N_f	630	210	105	63	4.55	2.2	0.9

3.6 Modelling volcanic slugs

The chemical-engineering literature has provided a solid basis to build on in order to investigate the dynamics of slug ascent in volcanic systems characterized by low-viscosity magma. However, being all industrial-oriented work, it focused on the prediction of the ascent velocity and the flow patterns in which the liquid organized around the bubble. The effect of, e.g., gas expansion, pipe geometry and burst dynamics has not been investigated.

The effect of gas expansion has been always corrected: e.g., in White and Bearmore, 1962, small variations of the velocity with bubble length caused by the expansion of the gas has been corrected; Bugg and Saad, 2002, sealed the experimental setup full of liquid with valves in order to hinder bubble grow during ascent. In contrast, expansion is of fundamental importance when studying volcanic slugs. The work of Sousa et al. (2006) is the only chemical engineering investigation focused mainly on the effect of gas expansion on the velocity of a slug, demonstrating how the gas expansion during the bubble ascent leads to a continuous displacement of the liquid head above the bubble and to an increase in the ascent velocity of the slug nose.

When the experimental approach is applied to volcanology we must simplify the complexity of the volcanic scenario in order to develop practical laboratory systems. Gas slugs ascending in a volcanic conduit expand, and, in a basaltic magma, the gas can achieve a significant expansion, especially in the upper few tens of metres (e.g., Seyfried and Freundt 2000; James et al. 2008). Therefore, rapid slug expansion due to gas decompression must be taken into account.

Another important assumption is the geometry of the conduit. At depth it is likely that the conduit is characterized by a complex structure comprising dykes with variations in inclination and size. Despite this, open systems including Stromboli (Italy) or Yasur (Vanuatu) are always considered as volcanoes with a vertical shallower conduit, where gas expansion occurs. This conduit region can comprise a complex system of fissures underlying the vents (e.g., Chouet et al. 2003, 2008). Unsurprisingly, the conduit cannot be considered smooth and with constant diameter, but characterized by obstacles and roughness that could influence the formation and ascent of the slugs. Vergniolle (1998) pointed out that for an open-conduit volcano like Stromboli, constantly active for at least 2000 years, the conduit wall should have been smoothed by centuries of activity.

The use of a single rheologically uniform liquid as analogue for the magma, a three-phase system (solid, liquid and gas) is a significant simplification. Rheological variations within the magma column could be addressed using more liquids with different rheological properties for sharp rheological variations, or a liquid with a temperature-dependent viscosity surrounded by a circulatory system of liquid of variable temperature to create a gradual viscosity transition. However, although likely possible and endorsed by recent field and textural evidence, such rheological variations have not been considered and experiments were mainly carried out in single viscosity systems to give first-order insights into the conduit fluid dynamics.

Considering these assumptions, it is possible to design realistic laboratory experiments to investigate processes taking place in more complex and constantly evolving volcanic systems. Early laboratory experiments demonstrated the validity of the experimental approach (e.g., Seyfried and Freundt 2000) and have been able to explain a possible mechanism behind the formation of the slugs (e.g., Vergniolle and Jaupart 1986; Jaupart and Vergniolle 1989) and how flow regimes within the conduit vary depending on gas supply (e.g., Seyfried and Freundt 2000; Pioli et al. 2012). However, the effect of gas expansion and conduit geometry was not explored until recently, with experiments designed to investigate the fluid dynamics and pressure changes induced by 1) the ascent of slugs in vertical and inclined tubes (James et al. 2004), 2) their passage through conduit geometrical changes (James et al. 2006) and 3) near-surface slug expansion (James et al. 2008, 2009; Del Bello et al. 2012; Lane et al. 2013).

Pressure variations associated with the ascent of slugs in a vertical or inclined tube (*Fig 3.11*) can represent a viable source of seismic and acoustic energy in low viscosity magmatic systems. Indeed, the ascent of a bubble leads to strong pressure variations, due to the liquid flowing around the slug, during the entire ascent time and at burst. Conduit inclination also plays an important role in the flow regime, promoting bubble coalescence and the increase of both length and velocity of the slugs, at the expense of their frequency of occurrence during continuously gas-supply two phase flow (James et al. 2004).

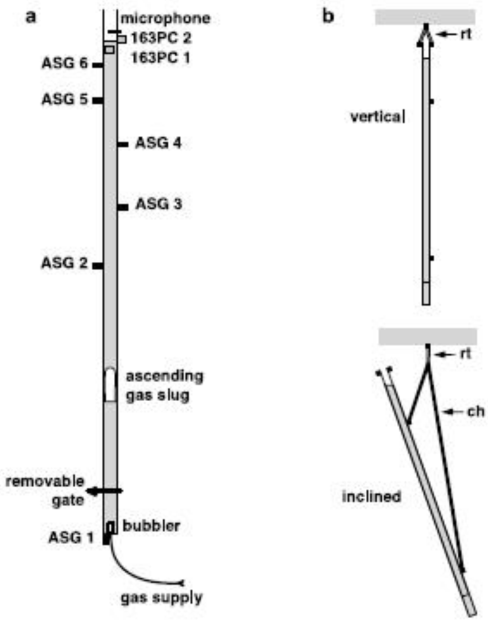

Figure 3.11 The experimental apparatus comprised of a 2.5-m-high tube with internal diameter of 38 mm where both single slugs and continuously-supplied slugs ascended in water or sugar-water solutions. Six pressure transducers, attached at various heights to cover the entire length of the tube (**a**), were used to detect pressure variations; the experiments were conducted in both vertical and inclined conditions (**b**). The gas was injected through a syringe and the slug generated through a removable gate for the single slug, while for the continuous gas supply a bubbler at the base of the tube has been used (James et al. 2004).

When a slug passes through a significant increase in conduit diameter (*Fig. 3.12*), an abrupt flow pattern change occurs due to the difference in the slug ascent velocity in a wider conduit and the resultant change in the liquid flux around the slug nose after entering the larger conduit. This leads to the disruption of the bubble in several portions, mirrored by strong variations in pressure. Systematic pressure changes vary with slug size, tube diameter, liquid viscosity and liquid depth. Indeed, changes in the net force were detected only in liquid where the flow is not controlled by viscous forces and the magnitude of the pressure changes is a function of the tube geometry, with the largest pressure transient occurring with the greater tube widening. It seems that the rapid acceleration of a small volume of downward-moving liquid, and not the upward acceleration of the large liquid volumes in the conduit as thought so far in the interpretations of volcanic seismic data, could be the source of significant pressure and forces changes. When scaled to the volcanic system, the force magnitude estimates produced in the experiments are comparable to the values obtained through seismic inversion by Chouet et al. (2003) and therefore plausibly responsible for the generation of VLP signals at Stromboli (James et al. 2006).

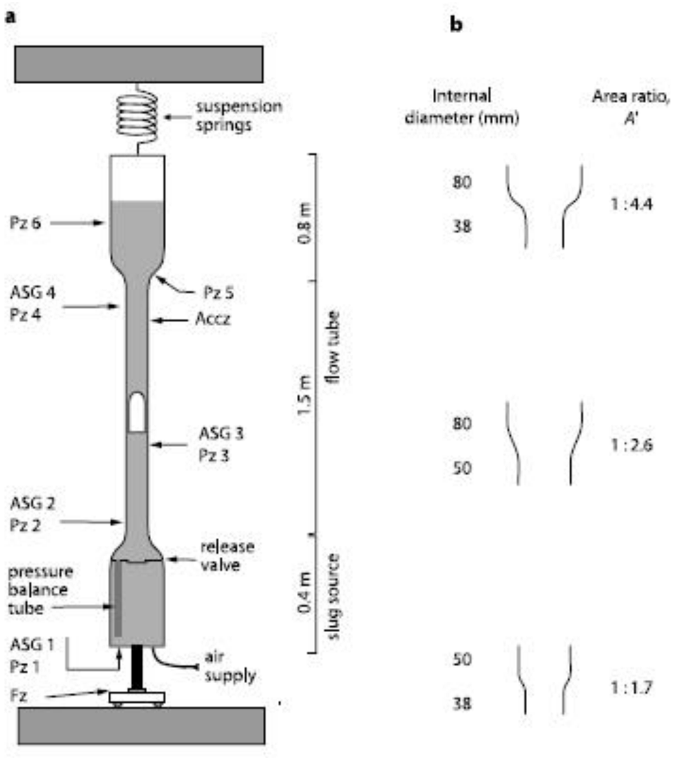

Figure 3.12 The experimental apparatus comprised vertical tubes with different diameters equipped with three different flared sections and filled with liquids with different viscosities, covering a range between 0.001-30 Pa s. (**a**) Pressure sensors are located along the tube suspended from springs attached to the ceiling. Piezo and active strain gauge pressure sensors are mounted at the bottom of the set-up. (**b**) Different geometry change ratio used in the tube (James et al. 2006).

Vergniolle (1998) and Seyfried and Freundt (2000) developed an analytical model for the expansion of a gas slug in a cylindrical, vertical volcanic conduit, considering, respectively, momentum conservation and the rate of change in the slug length due to its decompression. The model from Vergniolle (1998), in particular, considers an overpressured slug at the base of a cylindrical conduit filled with a Newtonian liquid of constant density and viscosity. Here the slug can rise and expand due to decompression, inducing a change in the magma level above the bubble. Therefore, assuming a constant velocity for the slug nose, the height of magma column decreases linearly in time while draining around the expanding bubble. The length of the bubble and of the magma column above it is calculated equating the rate of change of momentum of the liquid against the pressure, gravitational and viscous forces. However, Vergniolle (1998), implying a constant velocity for the slug nose, did not consider variations due to the near surface expansion; furthermore, the volume of liquid around the bubble is neglected. Based on including these considerations, James et al. (2008) developed a new experimentally-validated 1D model, considering the forces applied to the column of liquid above the slug. Experimental observations (*Fig. 3.13*) on slug behaviour were used to describe this dynamic model. According to these observations, both the slug base velocity and the thickness of the liquid film were constant, while the slug nose accelerated due to a rapid expansion of the gas. The acceleration of the nose led to an increase of the liquid flux past the bubble nose. Thus, a linear decrease of the height of the liquid mass above the bubble with the nose velocity cannot be considered, as previously assumed by Vergniolle et al. (1998). Therefore, the model assumes constant velocity for the base instead of the nose, which can be calculated from the Fr number, through $Fr = 0.345(1 - e^{-N_f/34.5})$. With this velocity defined, the expansion of the gas can be estimated measuring the forces exerted on the liquid above the bubble and considering the thickness of the falling film around it, obtained using the solution (15) derived by Batchelor (1967). Then, for a vertical pipe and a slug of initial length L_0 (*Fig. 3.14*), the conservation of liquid volume leads to

$$h = h_0 - V_s t - (L - L_0)(1 - A') \quad (19),$$

where $V_s t = s$ is the distance between the slug base and its initial position, V_s the slug base velocity at time t, h the height of the liquid above the slug, $A' = (r_s/r_c)^2$. In response to the increasing volume of gas, the mass of liquid above the slug accelerates. The acceleration can be expressed in terms of pressure, gravitational and viscous forces acting on the liquid: $F_p = \pi r_s^2(P - P_a), F_g = -\pi r_s^2 \rho g h$ and $F_v = -8\pi\mu h L' A'$ respectively, where P_a is the surface pressure, l_p the pipe length and U_f the mean flow velocity in the pipe. F_v for the laminar flow has been derived from the pressure drop under Poiseuille flow (Batchelor 1967) and assuming that the flux of gas and liquid are equal. Then, considering the product of mass and acceleration and the sum of the forces equals,

$$\pi\rho h r_s^2 \frac{d^2\left(V_s t + L + \frac{1}{2}h\right)}{dt^2} = F_p + F_g + F_v \qquad (20).$$

If the gas behaves as a perfect gas, in a pipe with a constant radius and with an initial gas pressure P_0,

$$\frac{1}{2}\rho(1 + A')L'' = P_0 L_0^{\gamma} L^{-\gamma} h^{-1} - \rho g - P_a h^{-1} - 8\mu L' r_c^{-2} \qquad (21),$$

with γ the ratio of specific heats (James et al. 2008).

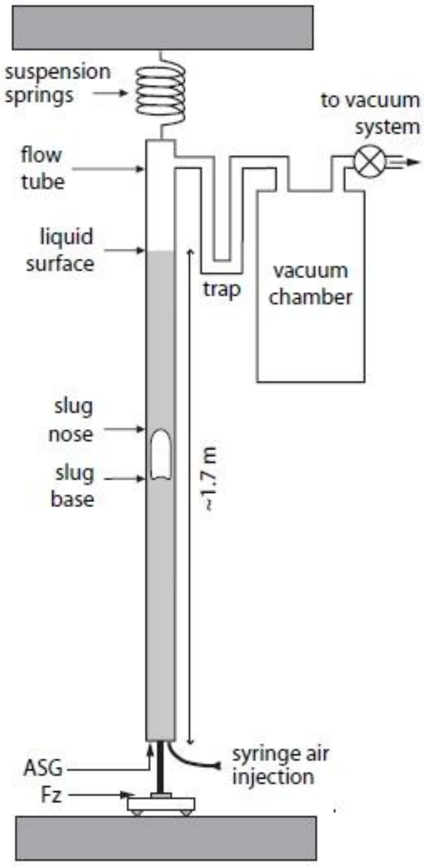

Figure 3.13 Laboratory experiments were carried out in a 2-m-high vertical pipe, sealed at the base and connected at the top to a vacuum chamber to reduce the ambient pressure and scale for gas expansion. Pressure and vertical motion were measured by means of a pressure sensor (ASG) and a force sensor (Fz) (James et al. 2008).

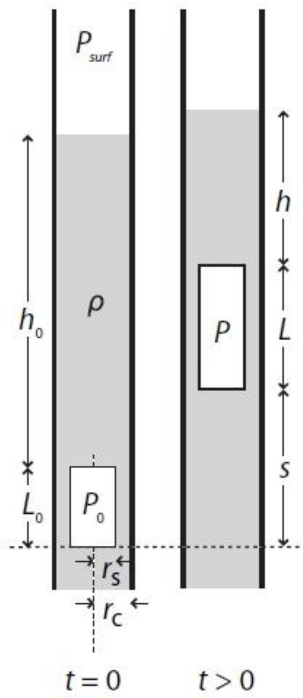

Figure 3.14 1D model for describing the final ascent of a slug without considering its burst. The white area represents a slug as a gas cylinder with constant radius r_s and initial length L_0 ascending in a vertical pipe with radius r_c and length L filled with a rheologically uniform liquid (grey areas). The parameters used in the model are showed here at starting condition t = 0 and at some subsequent time t > 0 (James et al. 2008).

To assess the accuracy of the model, the results were compared with both experimental and computational fluid dynamic (CFD) simulation data; the results agreed, reproducing the rapid expansion of the gas observed in laboratory experiments well (James et al. 2008). The 1D model reproduces quite well the behaviour of an expanding slug, and can be used to investigate the role of parameters such as magma rheology, conduit radius and initial gas volumes on slug behaviour. Furthermore, both experimental and CFD data demonstrated how the near-surface gas expansion and acceleration, the slug burst and the drainage of the liquid film surrounding the slug lead to pressure and force variations. The CFD model was applied to an ideal volcanic scenario, and the changes in the pressure and conduit forces observed were supported by the results of the laboratory experiments. The resultant forces can be correlated with those inverted from VLP seismic data acquired on Stromboli, highlighting the importance of this tool for interpreting LP and VLP signals as a function of fluid flow processes. Furthermore, the model values are in agreement with field measurements (Chouet et al. 2003), supporting the hypothesis that VLP signals are caused by instabilities in the flow regime as the slug passes through a change in conduit geometry (James et al. 2004, 2006) rather than by the expansion or the burst itself (James et al. 2008).

Following studies expanded the previous work, focusing on the determination of the gas overpressure acquired by a slug prior to burst (James et al. 2009; Del Bello et al. 2012). Gas overpressure is a fundamental parameter for studying variations in explosion vigour and for the understanding of the associated geophysical signals. Indeed, different eruptive regimes can develop, depending on the slug overpressure at burst, affecting the magnitude of the associated geophysical signals as well (James et al. 2009). Two of the key parameters controlling slug overpressure are the thickness of the falling film around it and the initial gas volume. The dimensionless film thickness can be expressed as the proportion of the cross-sectional area of the conduit occupied by the falling film, $A' = 1 - r_s^2/r_c^2$ (*Fig. 3.15*), related to the dimensionless film thickness by $A' = \lambda'(2 - \lambda')$ (James et al. 2009; Del Bello et al. 2012). The *static pressure model* (James et al. 2009) assumes a cylindrical slug (length L_s and radius r_s) rising in a pipe of radius r_c. and growing in response to the decrease in the magmastatic pressure; inertial and viscous forces are neglected. The magma remains confined in the conduit as the expanding gas bubble pushes it upwards. During its ascent, the slug pressure is in equilibrium with the pressure in the column of liquid above it. This magmastatic pressure P_h is given by: $P_h = \rho g h + P_a$, where h is the height of the magma column above the slug, ρ the density of the magma and P_a the atmospheric pressure at the vent. As the slug starts to expand, it increases its length (L) by a perturbation ΔL, and, with the magma head above the slug flowing into the falling liquid film, P_h decreases as well. The magmastatic pressure above the slug, P^*_h, decreases and becomes:

$$P_h^* = P_h - \rho g A' \Delta L \quad (22).$$

Assuming that the slug behaves isothermally, the pressure in the slug (P) decreases as well in response to the expansion and the new pressure P' is given by

$$P' = PL/(L + \Delta L) \quad (23).$$

The ratio between these two pressures, (23) and (22), will determine if the perturbation grows, $P' > P_h^*$, in which case the slug becomes unstable and continues to grow until it reaches the surface (i.e., the perturbation will grow and the slug will arrive at surface with a significant overpressure), or decays, $P_h^* > P'$, then the slug is stable (i.e., the slug will expand in equilibrium with the surrounding liquid and burst passively, with negligible dynamic overpressure). The limiting pressure below which a slug becomes unstable is given by:

$$P_{slim} = \sqrt{\rho g A' P_0 L_0} \qquad (24),$$

where P_0 and L_0 are the initial gas slug pressure and length.

Equation (24) can be re-cast in dimensionless form to compare laboratory and real volcanic systems, as P^*_{slim}, the ratio between the limiting pressure and the surface pressure: $P^*_{slim} = \frac{\sqrt{\rho g A' L_0 P_0}}{P_a}$. A gas slug with $P^*_{slim} < 1$ will arrive stable at the surface, with a pressure close to the atmospheric one, leading to eruptive events characterized by low energy (i.e., negligible dynamic overpressure). While for $P^*_{slim} > 1$, the slug will arrive at the surface with a significant overpressure and the burst will be energetic (James et al. 2009).

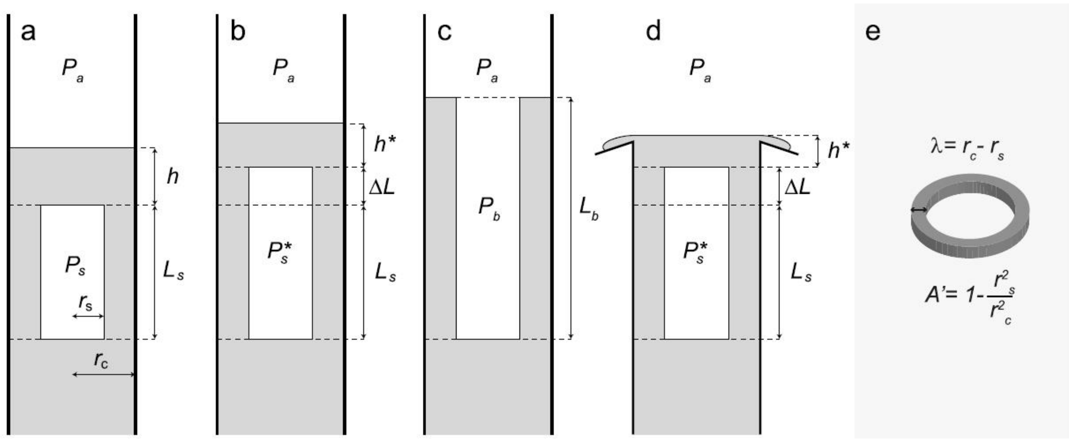

Figure 3.15 Theoretical model developed by Del Bello et al. (2012), considering a cylindrical slug of radius r_s bursting at the top of a conduit of radius r_c. In (**a**) the parameters used in the model are showed at starting condition; then a perturbation induces an increase of the slug length (**b**) and at some subsequent time, the perturbation causes the slug to burst in case of magma confined in the conduit (**c**) or if magma is allowed to overflow outside the conduit (**d**). In (**e**), schematic representation of the thickness of the liquid film around the slug and the dimensionless parameter *A'*.

This model was adopted and expanded (no pun intended!) by Del Bello et al. (2012; *Fig. 3.15*). Introducing L_a (the length a slug would have at atmospheric pressure P_a), and for $P_{slim} = P_a$ it is possible to determine the critical length, $L_{a\ lim}$, that a slug can reach without becoming unstable:

$$L_{a\ lim} = P_a / \rho g A' \qquad (25).$$

If $L_a < L_{a\ lim}$ the slug is small enough to maintain the equilibrium $P_s = P_h$ during its ascent (P_s= pressure of the gas within the slug), and it will arrive at the surface stable. Otherwise, if $L_a > L_{a\ lim}$, the equilibrium is not maintained; the slug will be unstable and burst at the surface with a significant overpressure. The critical depth at which the slug becomes unstable is $h_{lim} = P_{slim} - P_a/\rho g$. These equations can be non-dimensionalized using P_a and $P_a/\rho g$ as characteristic pressure and characteristic length-scale, so $L_{a\ \mathrm{lim}}$, $P'_{s\ lim}$ and h'_{lim} can be re-cast as $L'_a = L_a \frac{\rho g}{P_a}, P'_{s\ lim} = \frac{P_{s\ lim}}{P_a}, h'_{lim} = h_{lim} \frac{\rho g}{P_a}$ where $P'_{s\ lim} = P^*_{slim}$ from James et al. (2009).

Furthermore the product of A' and L'_a is the ratio of the slug length and the critical slug length, called the *stability index* γ_s, representing "*how much bigger a slug is than the smallest slug that will burst with an overpressure*" (Del Bello et al. 2012):

$$\gamma_s = A'L'_a = \frac{L_a}{L_{a\ lim}} \quad (26).$$

This is a key parameter: $P_{s\ lim}$ and h_{lim} can be re-cast in dimensionless form as functions of γ_s, yielding to $P'_{s\ lim} = \sqrt{\gamma_s}$ and $h'_{lim} = \sqrt{\gamma_s} - 1$, and the burst process can be described entirely as a function of the stability index. If $\gamma_s \leq 1$, the slug will expand in equilibrium with the surrounding liquid and burst passively, with negligible dynamic overpressure; if $\gamma_s > 1$, instead, the slug is unstable, and it will arrive at surface with a significant overpressure. The slug will become unstable once reaching the critical depth h'_{lim}. As an alternative of the slug length, it is possible to calculate the stability index using the volume of gas released during a slug burst V_a, easier to calculate for a real volcanic system through several monitoring techniques: $V_a = L_a \pi r_s^2$. In dimensionless form V_a becomes $V'_a = V_a \frac{\rho g}{\pi r_c^2 P_a}$ and then $V'_a = (1 - A')L'_a$.

Using this last equation, γ_s can be rewritten as a function of slug volume as:

$$\gamma_s = \frac{V'_a A'}{1 - A'} \quad (27).$$

The model demonstrates the important role that both γ_s and A' play in the behaviour of the slug: knowing the liquid properties and if it is possible to measure V_a and A', then it is possible to estimate the slug overpressure and length at the burst and the critical depth (Del Bello et al. 2012). The model also considers the possibility of magma overflowing outside the conduit as the rising slug pushes it upward, in agreement with direct observation of normal Strombolian explosions ("*overflow model*", *fig. 3.15d*). In this case, a smaller height of magma above the slug, due to the overflow during the expansion, is considered. The magmastatic pressure above the slug once the expansion begins is given by:

$$P^*_h = \rho g(h - \Delta L) + P_a \quad (28).$$

A' no longer appears in the equation because the volume of magma above the slug is no longer conserved due to the overflowing. Thus, to calculate $P_{s\ lim}$ and $L_{a\ lim}$, A' must be removed from the original equations.

Therefore, liquid rheology and gas volumes control the fluid dynamics involved in processes of slug ascent, expansion and burst and gas pressurization (James et al. 2008, 2009; Del Bello et al. 2012). These processes, in turn, can represent a viable source mechanism for the associated geophysical signals; thus, any variation in the slug behaviour will be reflected in seismic and acoustic measurements (e.g., James et al. 2006, 2008, 2009; Chouet et al. 2008, 2013; Lane et al. 2013).

Depending on the initial gas volume, three different behaviours - passive, transitional and explosive regimes - can be identified through the dimensionless ratio $\Delta P_b/\Delta P\hat{}_a$ and γ_s. ΔP_b is the ratio between the theoretical estimate of the peak dynamic overpressure in the slug at burst (James et al. 2009; Del Bello et al. 2012),

$$\Delta P_b = P_a\left((\gamma - 2\sqrt{\gamma_s} + 1)/(2\sqrt{\gamma_s} - 1)\right)$$

(29), and $\Delta P\hat{}_a$ the excess pressure peak, produced by the rapid displacement of the air above the liquid surface caused by the acceleration of the liquid head above the expanding gas. These behaviours can also be identified by visual observation of the excess pressure waveforms, ΔP_A (*Fig. 3.16*; Lane et al. 2013).

The time derivative of the experimental excess pressure ΔP_A is representative of the acoustic signal in a 3D atmosphere from a 1D source, and can be compared as synthetic infrasonic signal with real volcanic signals, produced at Stromboli from ash-free and ash-poor eruptions, ejecting pyroclasts to variable heights. This activity is likely representative of the arrival and burst of a gas slug at the magma surface. The qualitative similarity between the synthetic infrasonic and Strombolian infrasonic signals demonstrates the plausibility of the rise and expansion of slugs as first-order fluid dynamic sources mechanism for infrasonic signals generated by gas puffing and explosive eruptions at Stromboli (*Fig. 3.17*; Lane et al. 2013).

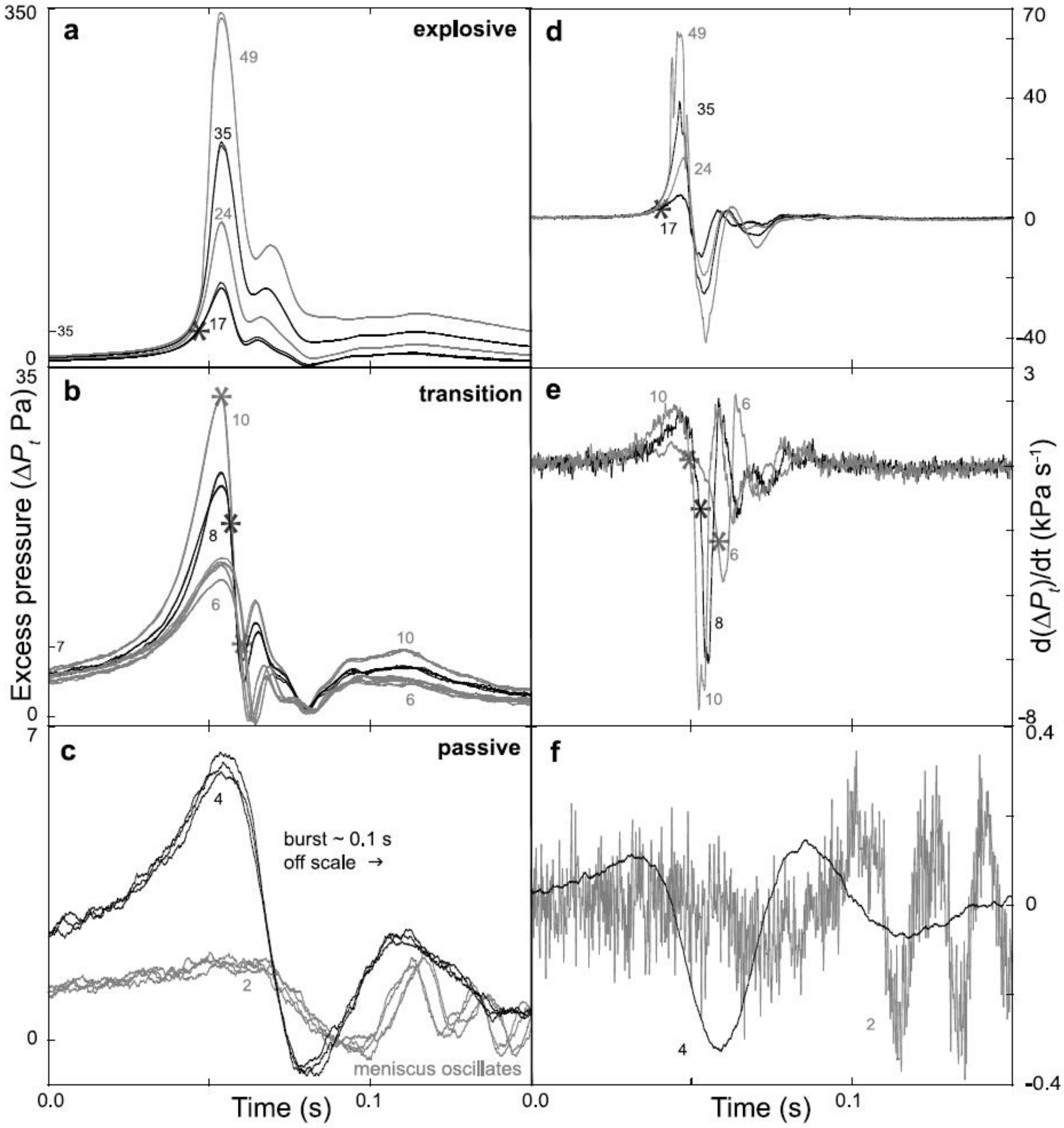

Figure 3.16 Unimodal excess pressure ΔP_A (**a**, **b**, **c**) and time derivative of pressure variations $d(\Delta P_A)/dt$ (**d**, **e**, **f**) as a function of time for initial experimental gas volumes between 2-49 ml identify the passive, transition and explosive regimes. Excess pressure peak produced by the gas flux was proportional to the initial volumes of gas generating it. Asterisks indicate the burst point of the slugs. Liquid properties are μ = 0.162 Pa s and ρ = 860 kg/m^3, ambient pressure P_a = 1 kPa (Lane et al. 2013).

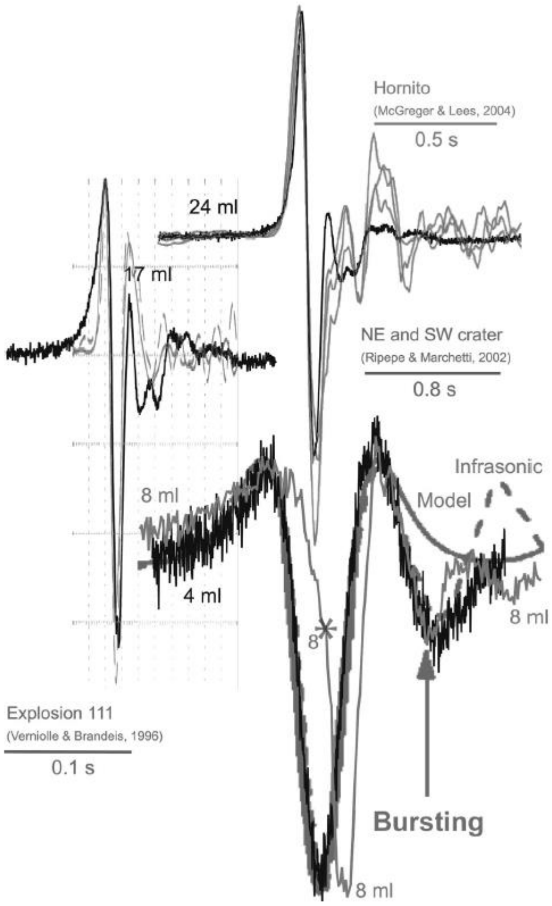

Figure 3.17 The first time derivative of excess pressure $d(\Delta P_A)/dt$, as a function of time, compared to published infrasonic signals measured at Stromboli by Vergniolle and Brandeis (1996), Ripepe and Marchetti (2002) and McGreger and Leeds (2004) (Lane et al. 2013).

3.7 Future directions

All the above investigations have been designed considering the ascent of a gas slug in the simplest possible scenario, a conduit filled with a homogeneous magma. The presence of a more viscous magma at the top of the conduit is now generally accepted, and evidenced by textural and geochemical analysis and field data. If a viscous magma layer is present at the top of the conduit, any interaction between two different magmas and the ascending slug could potentially lead to complex flow pattern changes, geometrical discontinuities, obstacles to the slug path; all complexities that could affect slug behaviour. These variations and, in turn, the evolution of gas expansion and pressurization would be then controlled by the properties of the viscous layer (e.g., Lautze and Houghton 2006; Gurioli et al. 2014; Leduc et al. 2015). Therefore, it is now imperative to investigate the role of a degassed, crystallized and more viscous magma in shallower part of the conduit on the slug behaviour.

This study seeks to investigate the missing link between the laboratory analysis and a more realistic volcanic scenario, in which a more viscous layer is present at the top of the conduit of a basaltic volcanic system. This is achieved by providing a detailed analysis of the fluid-dynamics involved during the ascent, expansion and burst of slugs in a rheologically stratified column, and the associated geophysical signals. However, the well-established dimensionless parameters have been defined for the experimental and volcanic scenario of a single-viscosity system. Thus, the possible unsteady nature of the flow in a dual-viscosity system cannot guarantee an accurate scaling and it is not possible to rely completely on the scaling arguments. This highlights the need for using 3D computational fluid dynamic (CFD) simulations and experimentally-validated numerical models to explore and support the applicability of the new laboratory results to the natural system.

Chapter 4 - Methods

The impact of a degassed, crystallized and more viscous magma at the top of the conduit on slug behaviour in basaltic volcanoes and the associated geophysical signals is addressed in this study by performing analogue laboratory experiments.

Experiments have been specifically designed to explore the fluid-dynamics and pressure variations, within the liquid and above its surface, involved in the processes of expansion and burst of a gas slug ascending first in rheologically uniform liquid, and then in a rheologically stratified liquid column.

Laboratory experiments are the core of this study. The following sections illustrate the experimental apparatus and procedures, the measurement equipment, properties of the analogue materials and how data were processed.

4.1 Experimental apparatus

The apparatus comprised a main 2-m-high transparent borosilicate glass tube, with an internal diameter of ~0.025 m, connected by flanges to an upper and lower section 0.5-m-high each, of the same diameter. Although assumed constant in all three sections, the diameter varies slightly at each pipe end, characterized by a flaring where the internal diameter gradually increases from ~0.025 m up to ~0.027 m. The main pipe was marked along its entire length every 0.1 m; each mark provided a reference scale and height for the measurements (*Fig. 4.1a*). The base of the tube was connected by a 25-40 mm adaptor (0.1-m-high) to an 80-40 mm concentric reducing glass section (0.1-m-high), to allow sufficient room for an efficient gas injection. Its wider section was sealed with an aluminium plate (0.15 m in diameter and 0.025 m thick) that served as a base for an active strain gauge pressure transducer and a flexible vacuum tube used for connecting the injection mechanism (*Fig. 4.1b*). The aluminium plate provided also stability to the system that was suspended from the concrete ceiling by means of two springs, allowing freedom of movement to the entire apparatus. The springs were attached to a second 0.1-m-high concentric reducing glass section of 80 mm to 25 mm, connected, in turn, to both the upper section of the tube and, via vacuum tubing, to a liquid trap (*Fig. 4.1c*). This was used as security measure in case of injection of an excessive volume of gas in the system while operating at low pressures. It should then prevent the liquid from reaching the vacuum system, to which the liquid trap is connected. The vacuum system comprises a rotary pump (BOC Edwards E2M40) capable of reducing the pressure above the liquid surface in the apparatus down to 5×10^{-3} mbar (~0.5 Pa), and the chamber, providing a buffer volume so that the pressure at the top of the liquid can be maintained almost constant. Two dial gauges (BOC Edwards CG 16K 0-50 mbar and 0-25 mbar; Appendix 3), one active strain gauge pressure transducer (BOC Edwards A.S.G.1000; Appendix 3) and a digital tester - directly wired to the transducer - were used to measure the pressure in the chamber.

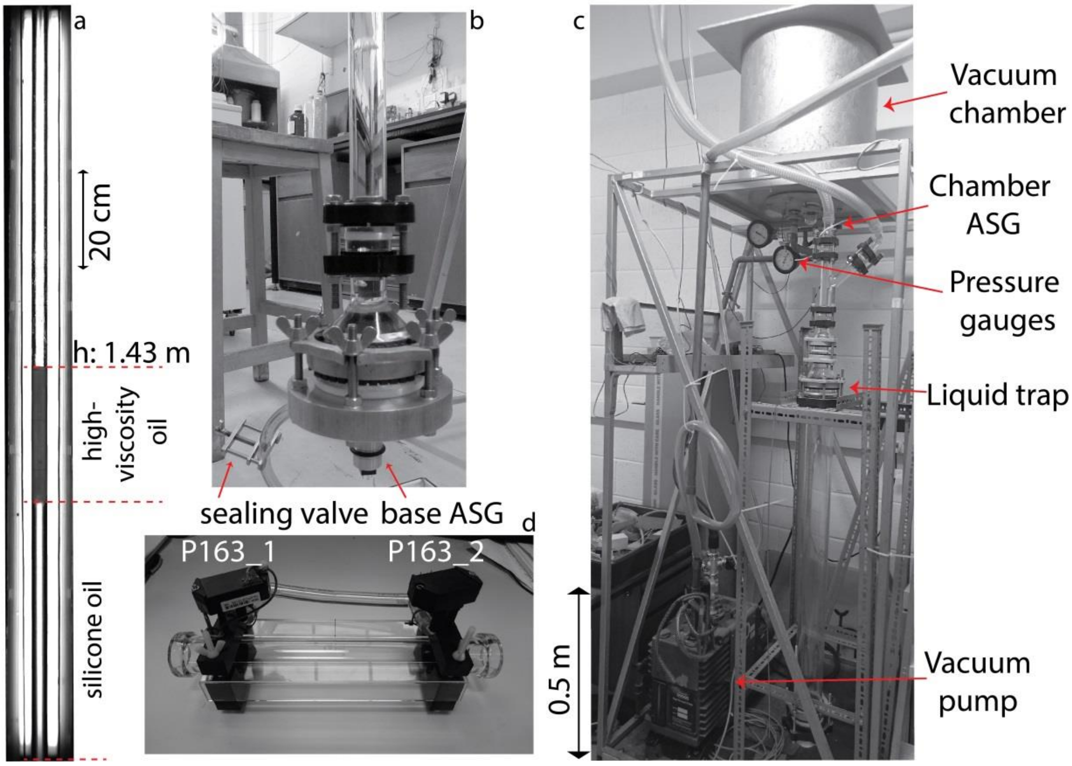

Figure 4.1 Experimental apparatus. (**a**) Main tube section, 2-m-high, filled with silicone oil overlain by a layer of more viscous castor oil, as imaged by the high-speed camera at a distance of 2.54 m; behind the tube two fluorescent lights were used as external source of light. (**b**) Lower section of the tube and the reducing glass section, sealed by an aluminium plate. An active strain gauge (base ASG), measuring pressure variations within the liquid, and a vacuum hope, connected to the injection system and sealed by a valve, were connected to the plate. (**c**) The vacuum system comprises a vacuum chamber and a vacuum pump; connected to the chamber, two pressure gauges and an active strain gauge (chamber ASG) were used to monitor the pressure. A liquid trap between the tube and the chamber avoids spillage of oil within the chamber. (**d**) The upper section of the tube (0.5-m-high) hosted two differential pressure transducers (P163_1 and P163_2) monitoring pressure variations above the liquid surface.

The upper section of the apparatus has been drilled to accommodate the two differential pressure transducers at a distance of 0.2 m from each other (*Fig. 4.1d*). For each sensor, one port monitored the pressure changes above the liquid surface, while the second port was connected directly to the vacuum chamber. The apparatus was partially filled with silicone oil only or silicone oil and a variable quantity of castor oil, up to a fixed height of h_0 ~1.43 m above the tube base.

The gas was injected using two different syringes, of maximum capacity 10 ml and 50 ml respectively, that can be connected to the apparatus by means of a hose kept closed by a valve. The plunger of the smaller syringe was drilled at intervals corresponding to 2 ml volume. For the bigger syringe, the volumes were fixed by blocking the plunger with pins of precise length corresponding to the desired volume.

4.2 Data acquisition system

Pressure changes within the liquid, at the base of the apparatus, and in the vacuum chamber were monitored through two active strain gauge pressure transducers, while two differential pressure transducers recorded pressure variations above the liquid surface. Processes within the tube (i.e., dynamics of slug ascent expansion and burst of the slug, interaction between two different liquids) were imaged with a high-speed camera. All the sensors and the camera were controlled via LabVIEW from a WorkStation Dell Precision T3600 (*Fig. 4.2*).

The workstation is powered by an Intel Xeon processor E5-1603 at 2.80 GHz and 64 GB of RAM, necessary to handle simultaneously the OS services (Windows 7 Professional SP1) and the acquisition of synchronized data from the sensors and high-speed videos, without risk of losing data or of a system crash due to memory limits. Of the 1TB hard-drive, a 500 GB partition is reserved only for the OS and the programs, while a second 500 GB partition is used for temporary storage and data acquisition. Systematic backups on several external hard-drives were performed daily to minimize the risk of data loss.

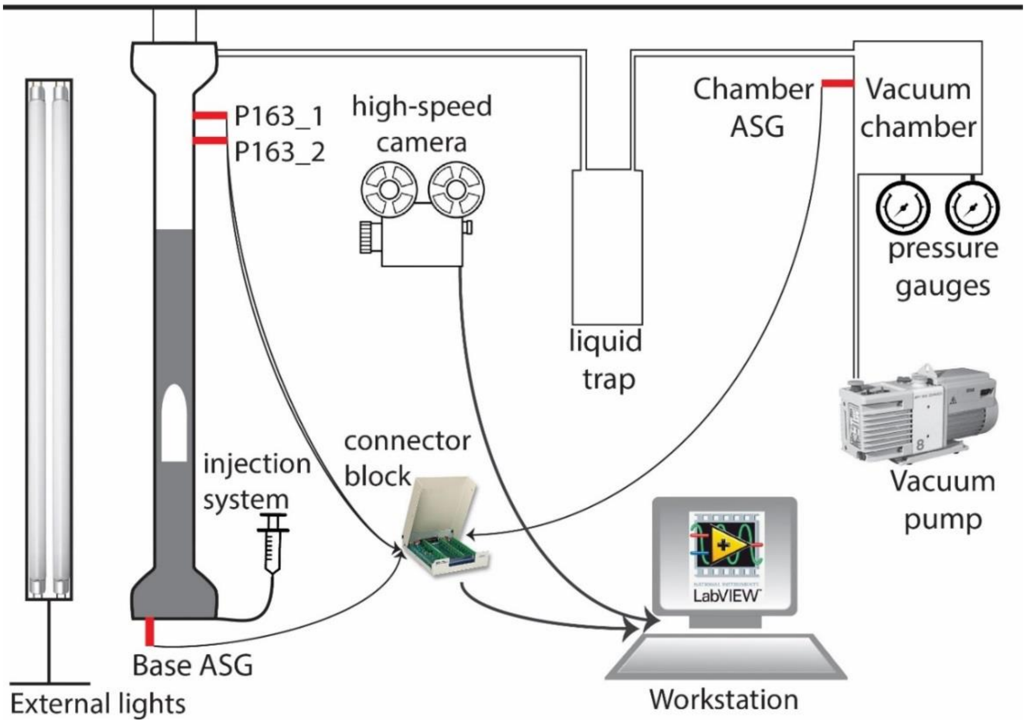

Figure 4.2 Schematic diagram of the experimental set-up and logging system. The apparatus was suspended to the ceiling by means of two springs. Its top was connected to the liquid trap and the vacuum system. Behind the apparatus, an external source of light provided sufficient illumination for the high-speed camera to operate at low exposure times, allowing acquisition up to 300 fps. The camera was connected to the frame-grabber on-board the workstation. Each sensor was wired to the connector block that, in turn, was connected to the data logger on-board the workstation. Through LabVIEW, all the instrumentation was controlled by a single interface, allowing synchronized acquisition of high-speed video and pressure variations for each experiment.

4.2.1 High-speed camera

A high frame rate was required for investigating in details the fluid dynamic processes involved in the rapid processes of near-surface slug expansion and burst; for this study all the experiments were imaged with a Basler acA2000-340km high-speed camera (Appendix 4).

This high-speed video system uses a C-MOS monochromatic sensor CMV2000, with a diagonal of 12.7 mm, full frame rate (pixel size 5.5 × 5.5 µm) and a maximum resolution of 2048 × 1088 pixel; available bit densities are 8, 10 and 12 bits. The camera interfaces with the frame grabber via the Camera Link protocol, specifically designed for real-time and high-speed video acquisition, and supports base-, medium-, and full-Camera Link configuration mode. In full-Camera Link configuration, at a resolution of 2048 × 256 pixel, bit density of 8 bits and exposure time of 0.2 ms the camera allows acquisitions up to 300 frames per second (fps).

In order to minimise parallax, the camera was positioned at a height of 1.80 m and 2.54 m distant from the apparatus. At the beginning of each experiment, the liquid surface was always at the centre of the camera field of view. Three different lenses were used, depending on the injected gas volumes and the experimental ambient pressure, each with a different vertical field of view (it always covered the entire width of the tube): ±0.58 m for the Sigma lens 50 mm, ±1.15 m for the Pentax C2514-5M 25 mm and ±1.6 m for the Pentax C1614-5M 16 mm.

During the experiments, an external lighting system (single 2 m unit with double fluorescent high-frequency and low heat output lights) was placed behind the apparatus, covering the entire length of the 2-m-high pipe, providing a light source sufficiently strong to illuminate the tube, so that the camera can operate at low exposure time, allowing the acquisition at 300 fps still maintaining a high vertical resolution.

4.2.2 Frame Grabber and cables

All Camera Link cameras require a dedicated frame grabber. For this study, the National Instrument PCIe-1433 was used in conjunction with the Basler acA2000-340km camera (Appendix 4). The NI 1433 acquires the images in real time and transfers them to system memory: thus, the maximum acquisition time depends on the amount of RAM available. The NI 1433 has an internal memory of 512 Mb, supports all the Camera Link configurations (Base, Medium, Full, and Extended Full) and up to 80-bit acquisition at 20 to 85 MHz pixel clock frequency. It supports the Power over Camera Link (PoCL) protocol, so that can be used to power the device in case of failure of the camera external power supply, avoiding data losses during the acquisition.

The camera was connected to the NI 1433 via two Camera Link shielded cables with 26-pin Miniature Delta Ribbon connectors (MDR-26). Two cables are required for using the camera in full-configuration, allowing a 64-bit wide video path that can carry 5.44 GBit/s (680 MB/s).

4.2.3 Differential pressure transducers

The upper section of the apparatus was equipped with two differential pressure transducers (Honeywell 163PC01D75), spaced 0.2 ± 0.005 m apart; this section of the tube was always above the maximum burst point of the slug, and never soaked by the oils. The purpose of these transducers was to monitor pressure variations above the liquid surface during the experiments with respect to the vacuum chamber (ΔP_A).

These are amplified differential transducers that record pressure changes by means of a silicon diaphragm. According to the official datasheet, 160PC series operates within a pressure range of ±2.5 inches H_2O, equivalent to ±623 Pa from a single, positive supply voltage ranging from 6.0 to 12 VDC (Appendix 4). The transducers have a response of 249 Pa/V, with a frequency response from DC (direct current) to 1 kHz.

4.2.4 Absolute pressure transducers

An Active Strain Gauge with a pressure range of 2000 mbar (BOC Edwards A.S.G.2000) was used to monitor pressure variations at the base of the apparatus (P_L). A similar transducer, but with a pressure range of 1000 mbar (BOC Edwards A.S.G.1000) was connected at the vacuum chamber, monitoring any variation in pressure.

These sensors have a response speed of 5 ms and a frequency response of 0-200 Hz (Appendix 4).

4.2.5 Data logger

All the four transducers were wired to the National Instrument board assembly SCB-68 with a shielded I/O connector block. This, in turn, was connected to the data logger via the proprietary National Instrument NI 68-pin I/O connector and a shielded 68-conductor cable.

The data logger is a PCI National Instrument 6034E, specific for applications involving continuous high-speed data logging (Appendix 4). It supports up to 16 channels at a resolution of 16 bits, and a maximum sampling rate of 200 kHz. With only 4 transducers connected, the maximum sampling rate for each channel is 50 kHz: for this study each channel has a logging frequency of 5000 sample per second (5 kHz).

4.2.6 Data storage

During a workday, video and sensor data were temporary stored in the internal hard-drive of the workstation. However, data from a single experiment have a size of ~5 GB (or more, depending on the acquisition time): it is impossible to store all the data only in the internal drive. More importantly, it is not safe in case of disk failure. Backups were carried out routinely on five Toshiba 3 TB external drives and a Buffalo 12TB DriveStation Quad (Appendix 4). The DriveStation provides a reliable solution for storing the entire dataset safely on four hard-drives, 3 TB each, optimized for continuous operation, and with a redundant backup. Furthermore, data are saved in

RAID 5 configuration: information is spread equally among all 4 drives, and – even in case of failure of a single drive – data can be retrieved without any loss.

4.3 LabVIEW

LabVIEW is a program development application created by National Instruments, based on a graphical programming language. By creating specific programs (Virtual Instruments, *VI*) in a block diagram form, it is possible to imitate and control actual instruments (assuming that the appropriate drivers are available for LabVIEW) through a graphical interface. The main components of a VI are the *front panel* and the *block diagram*. The front panel simulates the control panel for one or more physical instruments, and it is directly connected to the *block diagram*, where the actual coding is done. Here, it is possible to build block diagram wiring for specific objects: each object has a specific function, and it is used to send or receive data (terminals), control the flow of execution (wires) or perform specific actions (nodes), either pre-programmed or customized.

The VI developed specifically for this study simultaneously acquires high-speed video and all the transducers signals from the experiments, directly relating each image frame to the pressure data (Appendix 5). From the VI is possible to take direct control of the camera through the Vision Development Module (IMAQ) and of the set of sensors via the DAQ board (DAQ). The first version of the VI was developed in LabVIEW 2013 version 13.0f2 (64-bit); the final code was finessed in LabVIEW 2014 version 14.0f1 (64-bit).

The first step in programming the VI was to create virtual instruments mirroring the actual ones in the *Measurements & Automatic explorer*, to be recalled in the block diagram and controlled from the front panel.

4.3.1 National Instruments Measurement & Automatic Explorer

The NI *Measurement & Automatic Explorer* (MAX) provides access to the IMAQ and DAQ devices allowing configuring the hardware, testing the instrumentation and creating and editing tasks. A camera needs to be installed and named from here for the first time and in MAX it is also possible to set almost every video acquisition parameter. The same settings can be modified directly from the front panel of the VI (sending serial commands to the camera) or coded in the block diagram, without the need for accessing MAX each time. For this study, the acquisition window was set to 2040 × 256, limiting the horizontal field of view to the apparatus and reducing the size of the resulting frames.

In MAX it is also possible to create a "*Task*" for all the sensors: this is the fastest and most reliable way for recalling and activating all the four transducers from the main VI simultaneously, as soon as the acquisition starts, rather than separately. This can be done easily by adding each sensor individually in the same task. No matter what the order of addition, every instrument in the same task will be activated simultaneously without any delay as soon as the task is recalled from the VI. All the transducers send an output in voltage; the signal input for all of them ranges between +10 V and -10 V, with a continuous acquisition at a frequency of 5 kHz and 16 bit of resolution. Each channel can be named, to easily recognise each trace in the output file ("Ch_0_Base", for the base ASG, "Ch_1_Chamber" for the ASG in the vacuum chamber, "Ch_2_Lower163" and "Ch_3_Upper163" for the lower and upper differential pressure transducers respectively).

4.3.2 Logging VI

The front panel (*Fig. 4.3*) of the VI represents the graphical interface that allowed simultaneous control of the camera and transducers, and it mirrors the code in the block panel (*Fig. 4.4*). The first block of the panel is reserved for the camera: from here it was possible to set the main camera parameters, e.g., exposure time and recording time (expressed as "number of images", e.g., 30 s = 9000 images). The second block controls the DAQ (sample frequency and the number of sample per seconds to save).

Once all the parameters are set, the VI is ready. When initiated, it begins the pre-allocation process reserving all the memory needed for acquiring the selected number of images and the signals from the transducers. Then, it waits in stand-by for an input from the operator before starting the acquisition. As soon as it receives the "Start" command, the camera simultaneously starts to acquire the images and sends the start command to the DAQ board. When the acquisition stops, the VI starts to transfer the frames from the memory buffer to the hard-drive and then the program is complete. The sensor data are written in a separate TDMS (Technical Data Management Streaming) file (a proprietary format) in real time during the acquisition.

Usually the DAQ acquisition can be initiated without a command from the camera; this unusual step has been implemented due to a delay between the "Start" input and the real image acquisition. This delay is caused by the high number of images that needs to be acquired.

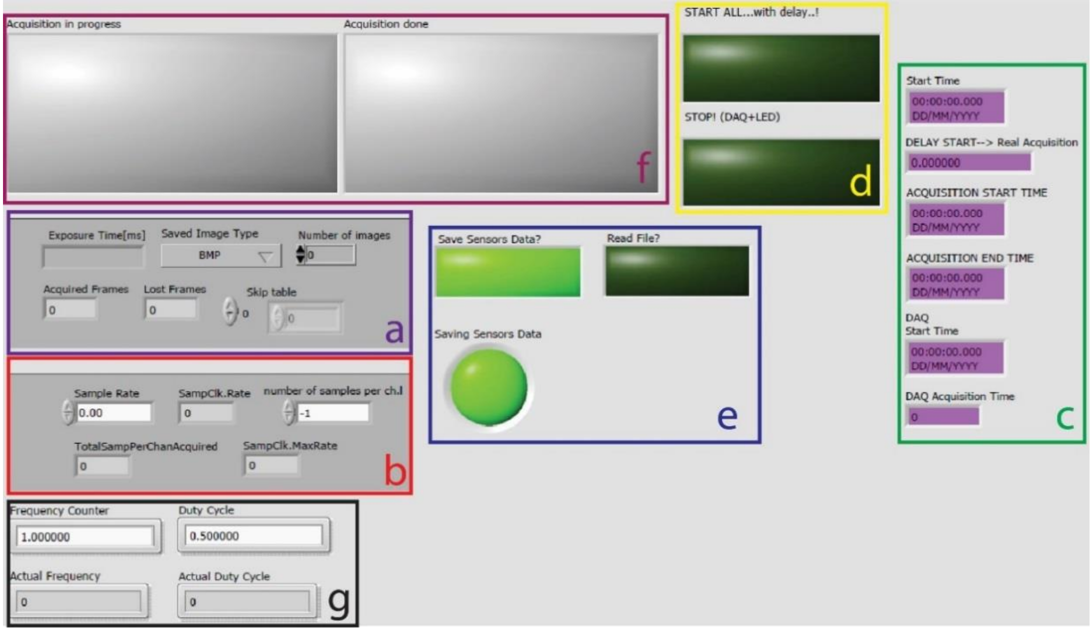

Figure 4.3 Front panel of the VI developed for acquiring synchronized high-speed video and transducers data during experiments. The camera can be controlled from the first panel on the left (**a**): from here it is possible to send serial commands to the IMAQ device, setting parameters such as exposure time, number of images to acquire (i.e., time of acquisition) and file format of the output (bitmap, tiff, jpeg). It also shows the total number of frames acquired and the number of lost frames, if any. From the panel below (**b**) is possible to select the acquisition rate for the transducers and number of sample to save for each channel (the default value -1 indicates that each second, each transducer will save a number of samples equal to the acquisition frequency); depending on the number of channels in use, the maximum sample frequency available per channel is displayed as well. Basic information can be read on the panel on the right (**c**), such as: start time and total time of acquisition for the camera and the transducers, delay between the VI initialization and the start of the real acquisition. The "Start" button in (**d**) starts the acquisition of both images and transducers data while the "Stop" button stops only the DAQ acquisition (IMAQ acquisition stops automatically once it acquires the desired number of images). It is also possible to decide to save only images, or both images and sensors data, to check if the VI is indeed saving the sensor data and if the output file from the transducers will be opened automatically for error checking or not (**e**). The LEDs on the top section (**f**) indicate if the acquisition started and when it stops. When the "Acquisition in progress" LED turns on, it indicates that the real acquisition started and the experiment can start. Additional settings (**g**) can be sent to an external counter (implemented in the VI but not used during the experimental campaign) in case a double check of the synchronization between the images and the transducers data is needed.

There are two ways in LabVIEW for coding high-speed video applications, using two proprietary VIs; each with a compromise. One option is the *IMAQ Grab Acquire*, specifically designed for high-speed images acquisition. With this VI the acquisition is instant but, for frame rates > 150 fps, there is a significant loss of frames. The higher the frame rate, the greater the number of frames lost. The second option is to use *IMAQ Start*; originally designed for low-level acquisition, this VI proved to be more reliable than the one specific to high-speed applications. Indeed, it can acquire up to 18000 images (60 s at 300 fps) without frames loss; however, even after the pre-allocation process, there is a delay between the "Start" and the real acquisition. This issue has been brought to the attention of the National Instrument Applications Engineering team; after several consultations and tests, the manufacturer confirmed that, given the high frame rate and size of each image to store, there is no solution, so far, for avoiding either frames loss or delays. The final decision to implement the *IMAQ Start VI* was based on the fact that any loss of frames can compromise the observation of the rapid processes occurring during the gas expansion and burst. As a result, a virtual LED has been added in the front panel of the VI, directly wired (in the block diagram) to the frame grabber and the DAQ board: as soon as the camera starts to buffer the frames and the DAQ to log the data, the led turns on and the experiment may start.

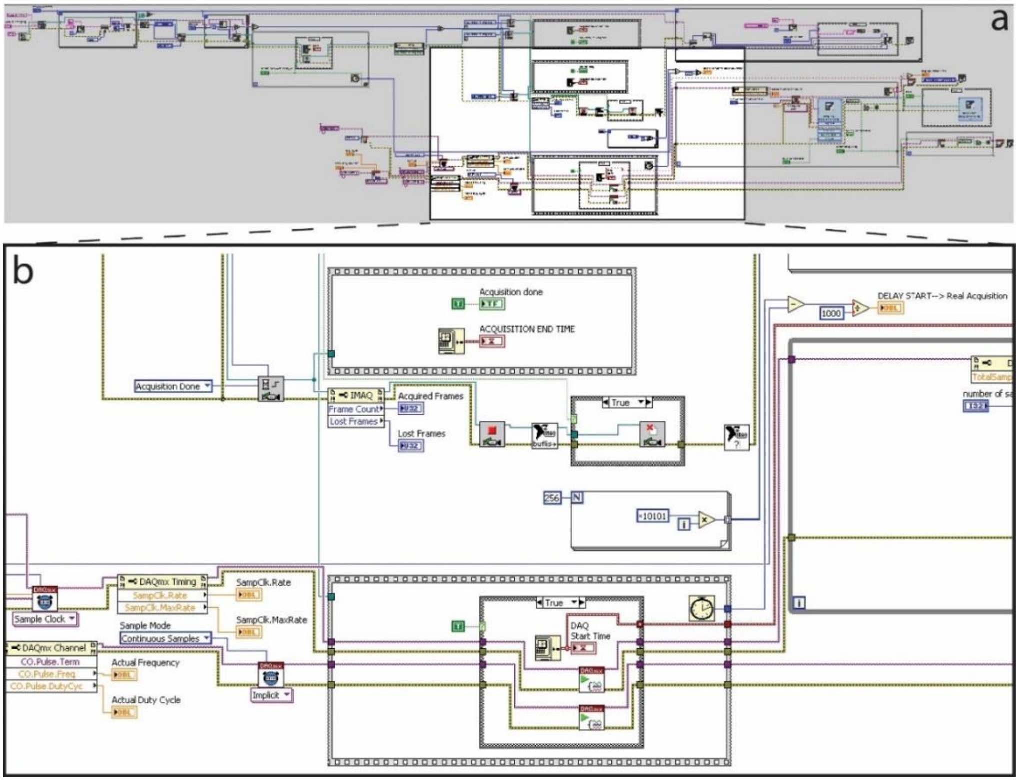

Figure 4.4 Block panel of the VI, where the actual coding is done. Overview of the code developed for this study (**a**) and (**b**) details of a section of code to illustrate the graphical programming language of LabVIEW. Any button, LED and indicator in the Front Panel is linked to the equivalent string of code in the block panel, in turn directly in communication with the related instrument. Once the program runs, the code is executed according to the dataflow dictated by how the VIs and sub-VIs in the diagram are wired (each square in the diagram represents a different VI).

4.3.3 Additional VIs

Two additional VIs were developed. A first one can be used to measure the exact frame rate of the camera, depending on exposure time and image resolution. A second one opens and reads the TDMS files, containing the transducer data. From this VI it is possible to load individual pressure traces or the entire dataset for each experiment. Of the selected traces, it is then possible to load all raw data values or to specify the number of values to show in a table or graph, and to display the properties of the specified file and the original acquisition settings.

4.4 Analogue materials and scaling

For the idealised volcanic scenario (Chapter 3, §3.5.4), fluid properties and conduit geometries give N_f ~0.42 to ~4.55 the for the plug and ~29 to ~630 for the magma beneath the plug (*Table 3.4* in Chapter 3, §3.5.4). These values lie in regions of the flow regime where the slug behaviour is controlled by viscosity in the plug, and by inertia with viscous contributions in the fresh magma (e.g., N_f = ~1.6 for a magma μ = 20 kPa s, ρ = 1300 kg/m^3 and N_f = 150 for a magma μ = 150 Pa s, ρ = 900 kg/m^3, with a conduit radius r_c = 2 m; *Table 4.1*).

Considering the N_f values for the volcanic scenario, silicone oil WACKER AS 100 (provided by *Wacker Chemie AG*), a clear, colourless, and odourless polydimethylsiloxane with a viscosity μ = 0.1 Pa s and a density ρ = 990 kg/m^3, was used as analogue for low-viscosity magma. Castor oil represented the degassed and more viscous magma layer, with a μ = 1 Pa s and ρ = 961 kg/m^3. The material properties and the apparatus geometry give the slug ascent in the viscous regime for the castor oil (N_f = ~12; *Table 4.1*) and in the mixed regime for the silicon oil (N_f = ~123 *Table 4.1*). Thus, both system lies in the same regimes during the active flow processes.

Table 4.1 Comparison between experimental and volcano-scale parameters

Parameters	Silicone oil	Castor oil	Fresh magma	Plug
Viscosity (Pa s)	0.1	1	150	20000
Density (kg/m^3)	990	961	900	1300
Conduit diameter (m)	0.025		2	
Inverse viscosity, N_f	122.57	11.89	150.34	1.62
Froude number, Fr	0.31	0.108	0.317	0.016
Film cross section A'	0.41	0.52	0.39	0.55
Dimensionless film thickness, λ'	0.41	0.527	0.394	0.544
Slug radius (m)	0.0096	0.0085	1.55	1.35

4.5 Experimental procedure

The experimental campaign comprised two sets of experiments. The first investigated the expansion and burst of slugs and the associated pressure changes in a pipe filled with a rheologically uniform liquid (single-viscosity system). The second set, in contrast, aimed to investigate the same processes but for a slug ascending, expanding and bursting in a column of low-viscosity oil overlain by a layer of variable thickness comprising higher viscosity liquid.

All experiments were carried out at experimental ambient pressures P_a of 3, 1 and 0.3 kPa, to explore a wide range of gas expansion ratios and stability index γ_s (e.g., James et al. 2008, 2009; Del Bello et al. 2012; Chapter 3, §3.6), and volumes of injected gas (V_0) of 2, 4, 6, 8, 10, 17, 24, 32, 49 ± 0.1 ml. This range of volumes non-dimensionalised through the parameter V'_a to give V'_a = 0.08-2, 0.6-14 and 6-152 for P_a of 3 kPa, 1 kPa and 300 Pa respectively (Chapter 3, §3.6). Scaled to the volcanic case, these values represent erupted gas volumes at atmospheric pressure, V_a (Chapter 3, §3.6), of ~4-~90 m^3, ~30-~700 m^3 and ~300-~8000 m^3. Hence these ranges of volumes cover those for normal Strombolian explosions, 2-2 × 10^4 m^3 (0.5-3000 kg, Chapter 3, §3.5.1), derived from processing of field data (e.g., Vergniolle and Brandeis 1996; Ripepe and Marchetti 2002; Mori and Burton 2009).

4.5.1 Single-viscosity system

For the ascent of slugs in a single-viscosity system, the apparatus was filled with silicone oil up to a height of 1.43 m. The syringe, once the desired gas volume has been selected, was connected to the base of the apparatus via the vacuum hose before lowering the pressure. Once attached, the valve sealing the vacuum hose was opened and the vacuum pump turned on. The pump was left on until all the liquid degasses and any trapped bubble was removed (in particular the ones in the tube connecting the syringe to the apparatus), allowing the pressure to slowly set to the desired value. In the meantime, the VI was initiated: the initial pre-allocation process took ~60 s (for an acquisition of 30 s at 300 fps) to complete. After that, the camera and transducers were ready to log.

When the desired pressure was reached, the pump was turned off to prevent vibrations being recorded by the transducers. The pressure inside the chamber can be read on one of the two dial gauges (or both for pressure lower than 2.5 kPa) and the tester connected to the transducer; pressure was always gauged using the dial gauges, with the tester as a contingency.

Once the pressure was set and the vacuum pump turned off, the VI was started: as soon as the acquisition commenced, the gas was released in the apparatus by removing the pin blocking the plunger in the syringe. There was no need to press the plunger to release the gas: the air was simply drawn into the apparatus due to the difference in pressure between the base of the liquid column and the atmosphere providing a controlled and consistent injection of gas.

The gas injection and slug formation were not recorded by the camera, which imaged only the entire, or part, of the main 2-m-high pipe. The experiments lasted ~20 s each, and the recording time was set to 30 s; this resulted in 9000 images and 150000 data points for each channel (for a sampling frequency of 5 kHz). Each frame was saved as bitmap (BMP) file, 2040 × 256 pixel resolution, 8 bit density and a mean size of ~575 KB; this means that for each experiment, the entire image sequence has a size on disk of ~4.94 GB. The TDMS file has a mean size on disk of ~9 MB.

As soon as the video acquisition stopped, a second virtual LED turned on, and the DAQ acquisition was stopped manually; at this point, the VI transferred all the images from the memory buffer to the hard-disk. The transfer took ~5 minutes, during which the valve at the base of the apparatus was closed, sealing the apparatus, the syringe was disconnected and the pressure was vented up to ~0.5 atm. It is fundamental to seal the valve before detaching the syringe; otherwise, as soon as the vacuum tubing is exposed to atmospheric pressure, air will be sucked into the apparatus, causing the overflow of the silicone oil into the liquid trap, with the risk of damaging the differential pressure sensors.

To test the reproducibility of the experiments, each experiment was repeated four times for all volumes and pressures explored. At least one series of experiments covering all volumes and pressures was imaged with the 16 mm lens, in order to image the ascent of the slug along the entire main section of the apparatus. This allowed a better overview of the evolution of the slugs, and tracking of variations in slug dimension and velocity as soon as it enters the main pipe section as well as the final stage of ascent.

A total of 95 experiments were carried out, providing a full dataset of synchronized data for transducer signals and high speed imagery for a single-viscosity system.

4.5.2 Viscous plug experiments

The procedures for experiments in a dual-viscosity system, once the layer of more viscous oil was settled on the less viscous one, were the same as those for the single-viscosity system. However, due the interaction between the fluids and the partial or complete disruption of the viscous layer at burst, it was necessary to wait for the liquids to settle again before running a new experiment. The waiting time can vary between 1 h up to almost a day, depending on the plug thickness, volume of injected air and pressure.

Castor oil represented the high-viscosity layer at the top of the conduit (§4.4); five different thickness (h_p) of viscous impedance, non-dimensionalized as a function of the tube diameter, D, were considered: 1D (h_p ≈2.57 cm), 2D (h_p ≈ 5.15 cm), 5D (h_p ≈12.85 cm), 10D (h_p ≈25.7 cm) and 20D (h_p ≈51.4 cm). To maintain the liquid column level at a constant height of ~1.43 m, so that each set of experiments was carried out under initial identical conditions, for each plug thickness a certain volume of silicone oil was drained through the vacuum tubing at the base of the apparatus.

The castor oil was poured from the top section of the apparatus directly on the liquid surface of the silicone oil, and left to settle for at least 24 hours. Compared to the single-viscosity experiments, the desired pressure before each experiment was reached more slowly, in order to avoid the disruption of the viscous layer due to rapid expansion of the bubbles escaping the system during the degassing process. Depending on the viscous layer thickness, this process can last up to 1 h.

The experiments lasted between ~20-~40 s each, and the recording time was set to 45 s; this resulted in 13500 images and 225000 data points for each channel.

As for the single-viscosity experiments, each run was repeated to test its reproducibility. Furthermore, an additional volume (32 ml) and pressures (5, 2, and 0.1 kPa) have been considered to better understand the control of these parameters on the pressure changes and fluid dynamic processes. A total of 410 experiments were conducted in the dual-viscosity system.

4.5.3 Data processing

Following the data acquisition, the TDMS files were first opened through Excel with an NI plug-in, and then the data were imported and processed in Kaleidagraph. The raw data values were converted to actual pressure values (Pa) using their respective calibration functions:

- *Pa= 249 × volts* (differential pressure transducers)
- *Pa = 20000 × volts* (absolute pressure gauge at the base of the apparatus).
- *Pa = 10000 × volts* (absolute pressure gauge at the vacuum chamber)

To reduce noise, P_L was smoothed with a varying moving average. For ΔP_A, first the pre-injection value was subtracted to obtain pressure variations, than a 25-point running average was applied to reduce noise (*Fig. 4.5*).

Image data were first qualitatively described, in order to evaluate the quality of the videos (e.g., sharpness, focus, exposure and field of view). Then, a thorough description for each video allowed the identification of the main fluid-dynamic processes involved in the experiments. These observations were done with *ImageJ*, a public domain Java-based image processing program (Abramoff et al. 2004), capable of handling large image stacks. Then, images were processed with *Pointcatcher*, a tracking software written in *Matlab* by Dr Mike James (http://tinyurl.com/Pointcatcher; e.g., James and Robson 2014), designed for both automatic and manual tracking through a video sequence. By tracking the slug base and nose it was possible to obtain variations over time in position, size, and ascent velocity of the slug. Tracking the liquid free surface of both the silicone oil and castor oil, instead, allowed measuring their variations in position, velocity of the viscous layer and of the low-viscosity intrusion into the high-viscosity layer (*Fig. 4.5*).

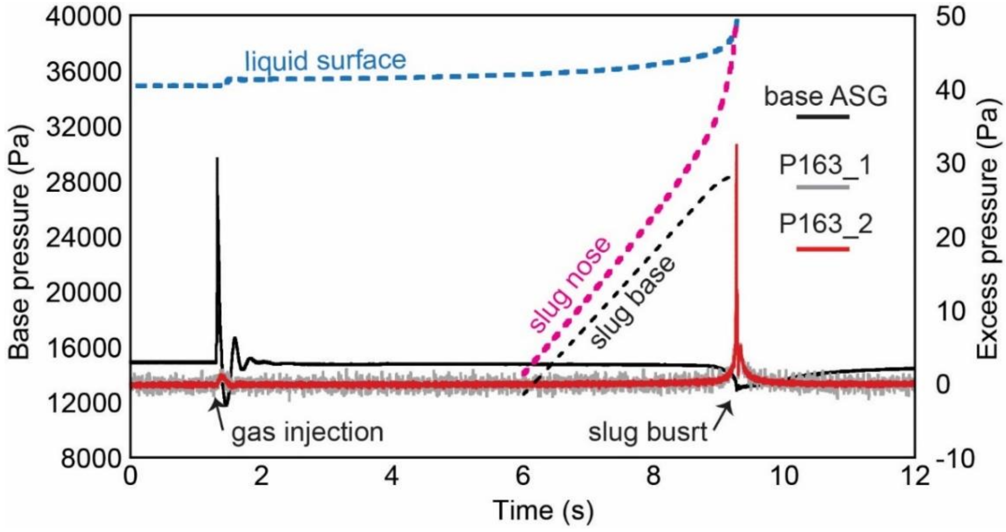

Figure 4.5 Transducers data from the base ASG (black solid line) and the two P163s (grey and red solid lines) converted in pressures (Pa) from the raw data (voltages), for a 6 ml slug ascending in a column of silicon oil overlain by a viscous layer 12.5-cm-thick. Also shown are the positional data for the liquid surface (blue broken line), the slug nose (purple broken line) and the slug base (black broken line). Positional data for the slug nose and base are not available before 6 s, and for tube heights < ~0.5 m, because of the camera field of view.

4.6 Computational fluid dynamic (CFD) simulations

3D computational fluid dynamic simulations have proven to be a powerful tool for the investigation of volcanic processes associated with the final ascent stage of a gas slug (James et al. 2008; Chouet et al. 2010). The same commercial software used in previous investigations has been used for this study, *Flow3D* (FLOW Science, release 10.0 and 11.0.1.03, http://www.flow3d.com), a CFD package specialized in free-surface flows.

Simulations were carried out both at laboratory-scale, to validate the CFD model with experimental data, and at volcano-scale, to explore the applicability of the fluid-dynamics observed in the laboratory to a real volcanic scenario (Stromboli).

In both cases, above the liquid surface there was no gas, and the gas slug was modelled as a continuous void region (i.e., contains no mass) governed by the equation $PV^{\gamma} = constant$. Thus, the internal fluid flow, and the shear stresses at boundaries, is not simulated and the interface between the gas and fluids is tracked by using the volume of fluid (VOF) method: the liquid volume fraction is calculated in each cell and the interface liquid-gas is identified in the cells only partially filled with liquid. Therefore, the interface slopes and curvatures are calculated using the liquid volume fractions in neighbouring cells, with its positions controlled by the gas and liquid static pressures, liquid dynamics and surface tension (e.g., James et al. 2008; Chouet et al. 2010).

The experimental tube and the volcanic conduit were both modelled as vertical, rigid (no elastic deformation) cylinders, closed at their base. The low-viscosity liquid and the high-viscosity layer (either magmas or silicon/castor oil) were modelled as incompressible Newtonian liquids with a temperature-dependent viscosity. The liquid column was divided in two distinct temperature regions. A high-temperature region (T = 1100°C) covered either the silicone oil or the low viscosity magma, from the base of the cylinder up to the base of the high-viscosity layer; the second region, with a T = 500°C, defined the high-viscosity layer, covering all its height. To reduce the effect of heat transfer across the magma column that could lead to a gradual variation in the viscosity, a thermal conductivity of 10^{-8} W m^{-1} K^{-1} (i.e., negligible) was imposed (Appendix 6).

Turbulence was accounted for using the Prandtl mixing length model (adequate for fully developed, nearly steady flows), which assumes that the fluid viscosity is enhanced by turbulent mixing processes in regions of high shear (e.g., near solid boundaries), also to allow implicit calculation of viscous stresses and decrease simulations run times. A no-slip condition was applied at the liquid-solid boundary. Cell pressures and velocities are calculated using an implicit solution method, with a successive over-relaxation iterative process, that each iterations dynamically self-adjusts the time step, convergence and stability criteria (e.g., maintaining the time step smaller than the Courant stability limit × a safety factor, usually 0.45, by backing up and repeating the time cycle with a smaller time-step size) to optimize solution without a loss of accuracy.

For simulations of slugs ascending in a single-viscosity system, axial symmetry was used, reducing the mesh size, calculating the flow within a 90° sector of the cylindrical conduit (James et al. 2008; Chouet et al. 2010). Here, due to the complex interaction between liquids of different rheological properties and the slug, a quarter-tube simulation was not sufficient. Thus, to avoid artefacts created from the symmetry simplifications (as observed in the first batch of simulations carried out in a dual-viscosity system), simulations were carried out in full 3D. For the laboratory scenario, the flow was solved over a Cartesian mesh of 28 × 28 × 400 in x-y-z, corresponding to a cell size of 0.1 × 0.1 × 0.5 cm. For a volcanic conduit, a mesh of 32 × 32 × 704 cells in x-y-z was considered, with a cell size of 0.1 × 0.1 × 0.4 m.

Selected laboratory experiments were modelled, covering the range of experimental pressures and gas volumes. The same experimental conditions (apparatus geometry, injected slug volumes, experimental ambient pressures and thickness of the plug) were recreated; all the laboratory simulations were carried out in 3D.

Simulations at volcano-scale represented a 300-m-high volcanic conduit, of diameter 3 m, filled with a 200-m-high column of magma. Viscosity values ranged between 20 and 1000 Pa s for the magma beneath the high-viscosity layer and between 1 and 20 kPa s for the viscous layer. The selected ranges give N_f = ~732-~14 for the low-viscosity magma, and N_f = ~2.1-~1.05 for the viscous layer (*Table 4.2*). In respect to the range of values determined by textural measurements, and generally considered for this study ($10 < \mu < 50$ kPa s, Gurioli et al. 2014), the viscosity used for the viscous magma in Flow3D was lower. However, this range was selected after an extensive testing phase considering a wide range of viscosity contrasts, and exceeding a plug viscosity of 20 kPa often resulted in simulation initialization problems for low viscosities of the liquid beneath the plug.

The simulations were initiated considering a slug, represented as a cylinder of length L_0 and radius r_s, at the bottom of the conduit (or pipe). When modelling experimental volumes, L_0 and r_s were easily derived from the mass of gas injected in the apparatus. For volcanic slugs the initial volume of the slug was scaled for the volcanic case through the dimensionless parameter V_a' (Del Bello et al. 2012; Chapter 3, §3.6). *Table 4.3* illustrates the range of erupted gas volumes at atmospheric pressure derived from the injected volumes, depending on the experimental pressures.

Simulations at laboratory scale can take up to a full day; for volcanic scale each simulation can take several days to complete (4-12 days).

Table 4.2 Summary of volcano-scale parameters considered for the CFD simulations

	Underlying magma						*Degassed magma (plug)*		
Viscosity (Pa s)[a]	20	50	150	300	500	1000	10000	15000	20000
Density kg/m³ [b]	900						1300		
Surface tension (N/m)[c]	0.4								
Conduit diameter (m)	3								
Conduit height (m)	300								
Magma column height (m)	200								
Inverse viscosity, N_f	732	293	97	49	29	14	2.11	1.41	1.05
Froude number, Fr	0.33	0.33	0.3	0.25	0.20	0.12	0.02	0.014	0.01
Dimensionless film thickness, λ	0.25	0.33	0.43	0.48	0.50	0.52	0.54	0.55	0.55
Slug radius (m)	1.29	1.22	1.13	1.08	1.05	1.03	1.01	1.01	1

[a, b] values from Gurioli et al. (2014)
[c] value from Murase and McBirney (1973)

Table 4.3 Volcanic gas volumes at atmospheric pressure scaled from the experimental injected volumes at different ambient pressure values.

Injected gas volumes (ml)	***Scaled volcanic slug volumes (m^3)***		
	3000 Pa	**1000 Pa**	**300 Pa**
2	4	31	333
4	8	63	666
6	12	94	999
8	16	126	1332
10	20	157	1665
17	34	267	2830
24	48	377	3995
32	63	503	5327
49	97	770	8157

Chapter 5 - Viscous plugging can enhance and modulate explosivity of Strombolian eruptions

Elisabetta Del Bello[a], Steve J. Lane[b], Mike R. James[b], Ed W. Llewellin[c], Jacopo Taddeucci[a], Piergiorgio Scarlato[a], Antonio Capponi[b]

[a] Istituto Nazionale di Geofisica e Vulcanologia, Via di Vigna Murata, 605, 00143, Rome, Italy

[b] Lancaster Environment Centre, Lancaster University, Lancaster LA1 4YQ, UK

[c] Department of Earth Sciences, Durham University, South Road, Durham DH1 3LE, UK

Published paper (Appendix 1):

E. Del Bello, S.J. Lane, M.R. James, E.W. Llewellin, J. Taddeucci, P. Scarlato, A. Capponi, *Viscous plugging can enhance and modulate explosivity of strombolian eruptions*, Earth and Planetary Science Letters, Volume 423, 1 August 2015, Pages 210-218, ISSN 0012-821X, http://dx.doi.org/10.1016/j.epsl.2015.04.034.

Reviewers: Sylvie Vergniolle and anonymous

Recent textural, petrological and field evidence (e.g., the ejection of mingled pyroclasts, multiple eruptive pulses within a single Strombolian eruption) suggest the presence of a degassed, crystallized and more viscous magma at the top of the conduit, through which the slugs burst. This physical situation is now generally accepted, however an experimental investigation on the effects of a possible plug on the eruption dynamics and the associated geophysical signals is still missing.

This manuscript represents the first experimental investigation of this scenario, detailing the fluid dynamics involved with the ascent, expansion and burst of a gas slug in a rheologically stratified column. Water is used as analogue for the low-viscosity magma, and castor oil represents the high-viscosity magma layer. 3D computational fluid dynamic simulations are used to explore the applicability of the processes identified in the experiments for a real volcanic system.

The results show how the presence of a viscous layer not only leads to a complex interaction between the different magmas as the slug ascends and expands, but it also increases the explosivity of the eruptions, modifying accordingly the geophysical signals. Furthermore, experimental and CFD results give insights into processes that could be responsible for the occurrence of mingled pyroclasts and the eruptive pulses observed at Stromboli volcano.

Elisabetta Del Bello: carried out the experiments, data processing, wrote the manuscript.
Steve J. Lane: contributed to discussions, reviewed the manuscript, and obtained grant funding (for Antonio Capponi).
Mike R. James: contributed to discussions, reviewed the manuscript, obtained grant funding (for Antonio Capponi), and provided the initial CFD model code.
Ed W. Llewellin: contributed to discussions, reviewed the manuscript.
Jacopo Taddeucci: contributed to discussions and initiated collaborations.
Piergiorgio Scarlato: obtained grant funding (for Elisabetta Del Bello) and initiated collaborations.
Antonio Capponi: carried out all the CFD simulations, contributed to discussions.

Abstract

Strombolian activity is common in low-viscosity volcanism. It is characterised by quasi-periodic, short-lived explosions, which, whilst typically weak, may vary greatly in magnitude. The current paradigm for a Strombolian volcanic eruption postulates a large gas bubble (slug) bursting explosively after ascending a conduit filled with low-viscosity magma. However, recent studies of pyroclast textures suggest the formation of a region of cooler, degassed, more-viscous magma at the top of the conduit is a common feature of Strombolian eruptions. Following the hypothesis that such a rheological impedance could act as a 'viscous plug', which modifies and complicates gas escape processes, we conduct the first experimental investigation of this scenario. We find that: 1) the presence of a viscous plug enhances slug burst vigour; 2) experiments that include a viscous plug reproduce, and offer an explanation for, key phenomena observed in natural Strombolian eruptions; 3) the presence and extent of the plug must be considered for the interpretation of infrasonic measurements of Strombolian eruptions. Our scaled analogue experiments show that, as the gas slug expands on ascent, it forces the underlying low-viscosity liquid into the plug, creating a low-viscosity channel within a high-viscosity annulus. The slug's diameter and ascent rate change as it enters the channel, generating instabilities and increasing slug overpressure. When the slug reaches the surface, a more energetic burst process is observed than would be the case for a slug rising through the low-viscosity liquid alone. Fluid-dynamic instabilities cause low and high viscosity magma analogues to intermingle, and cause the burst to become pulsatory. The observed phenomena are reproduced by numerical fluid dynamic simulations at the volcanic scale, and provide a plausible explanation for pulsations, and the ejection of mingled pyroclasts, observed at Stromboli and elsewhere

Keywords

plugged conduit, eruption dynamics, volcano infrasonic, slug bursting, Taylor bubble, analogue experiments

5.1 Introduction

Strombolian activity may be very long-lived, with episodes lasting years, decades, or even centuries. This longevity, coupled with the photogenic nature of the explosions, has made some persistently active Strombolian volcanoes popular tourist destinations – for instance, more than ten thousand tourists visit the summit of Stromboli itself each year. Although usually benign, Strombolian activity spans a range of magnitudes, and includes events that are much more violently explosive and may pose a significant hazard to tourists and nearby communities. It is important, therefore, to determine the factors that cause a usually mildly explosive system to generate more violent explosions.

The discrete explosions that characterise the Strombolian eruptive style are interpreted as the impulsive bursting of over-pressured gas pockets – or slugs – at the top of a magma column (Chouet et al. 1974; Blackburn et al. 1976; Burton et al. 2007). Over-pressure is a fundamental consequence of large gas bubbles rising from depth and expanding against viscous and inertial retardation as pressure decreases (James et al. 2008, 2009; Del Bello et al. 2012). This behaviour is generally restricted to basaltic or andesitic magmas, because these systems have sufficiently low viscosities to allow bubble coalescence and decoupling of gas slugs from magma over short time scales (order of seconds to hours). Experimental and numerical models within the volcanological literature consider the slug rising through a medium with uniform viscosity and density. These models provide first order explanations of the dynamics of gas expansion, overpressure, and generation of seismic and acoustic signals (e.g., Vergniolle and Brandeis 1996; Vergniolle et al. 1996; Seyfried and Freundt 2000; Parfitt 2004; O'Brien and Bean 2008; D'Auria and Martini 2011; James et al. 2009; Kobayashi et al. 2010; Del Bello et al. 2012; Gerst et al. 2013; Kremers et al. 2013; Nguyen et al. 2013; Lane et al. 2013; Sánchez et al. 2014). However, none of these approaches encompasses the presence of a region of degassed, crystalline magma with increased viscosity and strength in the shallow conduit. Such a rheological impedance – which can be termed a 'plug' – is commonly inferred, and physically plausible, at active Strombolian-type vents (e.g., Gurioli et al. 2014).

Textural data from many Strombolian-type volcanoes support the coexistence of magmas that have contrasting rheology as a result of cooling-and degassing-driven crystallisation (e.g., Taddeucci et al. 2004; Cimarelli et al. 2010; Kremers et al. 2012;

Ruth and Calder 2013). Considering Stromboli as a canonical case during its ‘normal’ activity, it is very common to find both bubble-rich, crystal-poor textures and bubble-poor, crystal-rich textures inter-mingled within a single pyroclast (e.g., Lautze and Houghton 2005, 2006; Polacci et al. 2006, 2009; Colò et al. 2010; D’Oriano et al. 2011; Gurioli et al. 2014). It has been proposed that these textures represent mingling of relatively fresh, gas-rich magma with older, completely or partially degassed magma, in the shallow conduit (e.g., Lautze and Houghton 2005). Cooling, degassing and associated crystallisation of the magma in the upper conduit cause it to have a much higher viscosity than its deeper, fresh counterpart. This rheological distinction is not to be confused with the so-called ‘high porphiricity’ (HP or ‘black’) and ‘low porphiricity’ (LP or ‘golden’) magma types (e.g., Métrich et al. 2005); these are distinguished on the basis of geochemical and isotopic analyses, with LP magma thought to occupy the system at depths greater than ∼3.5km. At the volcanic scale, rapid expansion of the gas slug associated with the burst process occurs only within the last few tens of meters of the magma column (James et al. 2008). Hence, the region of plug–slug interaction is limited to the shallowest portion of the conduit, entirely within the HP magma domain.

The presence of a plug, and its thickness, must have an important impact on eruption dynamics. For instance, we would expect the viscous plug to retard slug expansion, thereby promoting the development of overpressure within the slug as it rises. We would also expect the plug material and thickness to affect the dynamics of the bursting process. Lautze and Houghton (2006) were the first to suggest, based on field observations, that changing proportions of magma with differing viscosities influenced eruption frequency and vigour, supporting the notion that plug thickness could change over time. These factors introduce additional complexity compared with the unplugged scenario (e.g., Andronico et al. 2008). This complexity might be manifest in the seismo-acoustic signatures of the explosions (e.g., Johnson and Lees 2000; Lyons et al. 2012), and in the visual character of the explosions. We note, for instance, that recent high-speed videography studies have identified that gas escape during Strombolian explosions is typically pulsatory (Taddeucci et al. 2012a; Gaudin et al. 2014), suggesting greater complexity than simple bursting of an overpressured slug. Understanding the role that a viscous plug plays in modulating the dynamics of slug ascent and burst is, therefore, of considerable importance in the interpretation of the waveform and amplitude of generated pressure changes (Lane et al. 2013). In order to gain insight into the complex volcanic system (e.g., Gurioli et al. 2014), we use first-order laboratory experiments to evaluate the influence of a Newtonian, high-viscosity plug on gas slug ascent and burst in a vertical tube. Our experiments build on previous work carried out in single-viscosity systems (James et al. 2004, 2006, 2008, 2009; Lane et al. 2013), and we adopt a similar analogue methodology. We also use a computational fluid dynamic model (James et al. 2008; Chouet et al. 2010) to conduct numerical simulations of the same scenario at the volcano scale, in order to explore the applicability of our laboratory results to the natural system.

5.2 Experimental method

5.2.1 Scaling considerations

We model an idealised volcanic scenario in which a layer of high-viscosity magma of variable thickness overlies a column of low-viscosity magma. The behaviour of a slug ascending a vertical pipe filled with a viscous liquid may be described via a number of dimensionless groups, namely the Morton number *Mo*; the Eötvös number *Eo*; the inverse viscosity *Nf*; the Froude number *Fr*; and the Reynolds number *Re* (e.g., Viana et al. 2003; Llewellin et al. 2012). These groups are defined and calculated for the volcanic and experimental scenarios in the Supplementary Content. We show that, in both systems, surface tension plays a negligible role in slug ascent (e.g., Seyfried and Freundt 2000) hence behaviour is controlled by the inverse viscosity N_f,

$$N_f = (\rho/\mu)\sqrt{gD^3} \quad (1),$$

where ρ and μ are the density and dynamic viscosity of the liquid, g is the gravitational acceleration, and D is the tube diameter.

For a canonical representation of parameters at volcano-scale, we choose a viscosity of 5×10^4 Pa s for the plug based on recent estimations for magma in the shallowest part of Stromboli's conduit (e.g., Gurioli et al. 2014) and 50 Pa s for the underlying magma based on minimum accepted values for basaltic melts (*Table 5.1*). Although density differences are observed among pyroclasts that tap the uppermost conduit (e.g., Lautze and Houghton 2005), we exclude density stratification from our analysis and assume that the volcanic system is dynamically stable (or that gravitational instability develops on timescales much longer than that needed for plug formation). Based on values in Table 5 of Gurioli et al. (2014), we estimate a density of approximately 1000 kg/m^3 for the plug and underlying magma during the active flow process. The respective values of the inverse viscosity in the plug and underlying magma in a 5-m-diameter conduit are then $N_f \approx 0.7$ and $N_f \approx 700$ putting slug behaviour in the viscous and inertial regimes respectively (e.g., White and Beardmore 1962). The dimensionless thickness (λ') of the falling film of magma around the rising slug is essentially independent of N_f in these regimes (Llewellin et al. 2012), with values of 0.33 and 0.14 respectively. We also calculate the fraction of the tube cross-section occupied by the falling film $A' \approx 0.55$ if magma viscosity is that of the plug, and $A' \approx 0.25$ if viscosity is that of the underlying magma (see Supplementary Content for derivation). Consequently, a gas slug is predicted to narrow substantially when entering the plug zone (occupying ~60% of the cross sectional area it occupies in the underlying liquid).

Table 5.1 Summary of experimental parameters and scaling to the volcanic case.

Materials	**Experimental parameters**		**Volcanic conditions**		**CFD simulations**	
	Water	Castor	Underlying magma	Plug	Underlying magma	Plug
Density ρ (kg/m^3)	1000	970	1000		1000	1000
Viscosity μ (Pa s)	0.001	0.986	50	50000	20	20000
Surface tension[c] σ (N/m)	0.07	0.03	0.4	0.4	0.4	0.4
Gravity g (m/s^2)	9.81		9.81		9.81	
Conduit diameter *D* (m)	0.025		5		3	
Inverse viscosity N_f	12381	12.18	700	0.70	815	0.81
Dimensionless film[a] λ'	0.09	0.31	0.14	0.33	0.13	0.33
Film cross section[b] A'	0.16	0.53	0.25	0.55	0.24	0.55
Slug radius r_s (m)	0.01	0.01	2.16	1.68	1.30	1.01
Viscosity contrast μ*	986		1000		1000	
Slug cross section ratio	0.56		0.61		0.60	

[a] Calculated from equation 4.2 in Llewellin et al. (2012).
[b] Calculated from equation 28 in Del Bello et al. (2012).
[c] Data for the volcanic case are from Murase and McBirney (1973).

In the laboratory we use castor oil (viscosity 0.986 Pa s; density 970 kg/m^3) and water (viscosity 0.001 Pa s; density 1000 kg/m^3) as respective analogues for the plug and underlying magma (see *Table 5.1*). Given a pipe diameter of 2.5 cm, this gives us values of $N_f \approx 12$ and $N_f \approx 12000$ in the plug and underlying liquid respectively. Although these values are somewhat higher than their counterparts in the volcanic system (i.e., the experiments are relatively less viscous), they lie in the same viscous and inertial regimes respectively; the divide between the regimes was found to be around $N_f \approx 100$ by Llewellin et al. (2012). Consequently, the fractions of the pipe cross-section occupied by a falling film of oil or water ($A' \approx 0.53$ and $A' \approx 0.16$ respectively) are similar to those in the volcanic scenario. The experimental N_f values also lie in the same regions where λ' is almost constant, and the viscosity ratio is of order 1000 for both experimental and volcanic scenarios.

5.2.2 Experimental apparatus

The experimental apparatus (*Fig. 5.1*) comprises a vertical glass tube 0.025 ± 0.001m in diameter (D), filled with liquid to a height of 1.80 ± 0.01 m, and with a nominal ambient pressure above the liquid P_a of 3.0 ± 0.1 kPa to scale for gas expansion during ascent (James et al. 2008). Experiments were carried out by injecting a known volume of air (V_0) equilibrated to the same pressure as the base of the tube.

Slug rising and bursting were filmed at 299.7 ± 0.1 frames per second with a Casio Exilim FX1 camera. Pressure in the air above the liquid (P_A) was measured at 1 kHz (NI PCI 6034E data-logger, with 16 channels) with two Honeywell differential 163PC01D75 transducers, and within the liquid at the base of the tube (P_L), with one BOC Edwards A.S.G. 1000 sensor. Pressure variation (ΔP_A and ΔP_L) is then obtained by subtracting measured pre-injection values from the recorded pressure. To reduce noise, ΔP_A is smoothed by taking the mean of the two transducers and a 5-point running average, and ΔP_L is smoothed with a varying running average corresponding to the apparatus resonant 'bounce' frequency (James et al. 2008).

Air volumes (V_0) of 2, 4, 6, 8 and 10 ± 0.1 ml were injected into a water column (single-liquid 'control' experiments) or into a water column whose top was replaced with a layer of castor oil of thickness h equal to either 2D (i.e., h = 0.05 m of oil above 1.75 m of water), or 7D (h = 0.18 m of oil above 1.62 m of water). Each experiment was repeated to assess both reproducibility and variability under nominally identical conditions. The injected volumes non-dimensionalise to give V'_a = 0.09, 0.18, 0.28, 0.37 and 0.45 respectively (Del Bello et al. 2012; see Supplementary Content for methodology). For the volcanic system, these experiments represent erupted gas volumes of 7–37 m^3 (1.2 to 6 kg) and plugs 0, ~10, and ~35m thick (Video V01). In both systems, V'_a is calculated based on the properties of the liquid underlying the plug, and in a single liquid system would result in passive expansion with slug overpressure only becoming significant at the largest bubble size (Lane et al. 2013).

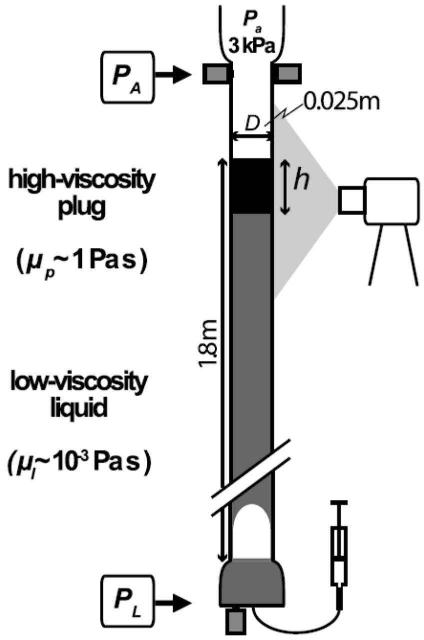

Figure 5.1 Experimental apparatus. Known volumes of air were injected into the base of a water-filled tube overlain with a high-viscosity 'plug' of thickness *h*. Pressure above the plug was held at 3 kPa. Gas slug ascent, expansion and burst were imaged, and pressure variation was measured in the liquid at tube bottom (P_L) and in air above the free surface (P_A).

5.3 Experimental results

5.3.1 Control experiments without viscous plug

The injected air forms a slug that ascends and expands within the tube, surrounded by a falling film of water that shows no discernible ripples (*Fig. 5.2a*, Video V01). As noted in previous experimental studies, base pressure ΔP_L decreases during slug ascent (*Fig.5.3a*), because an increasing water mass in the falling film is dynamically supported on the tube wall (e.g., James et al. 2004). Slug expansion, which accelerates during ascent, displaces the liquid's free surface upwards. The slug bursts when its nose catches the liquid surface. After burst, the water film drains back, developing ripple structures, and ΔP_L increases to the pre-injection value.

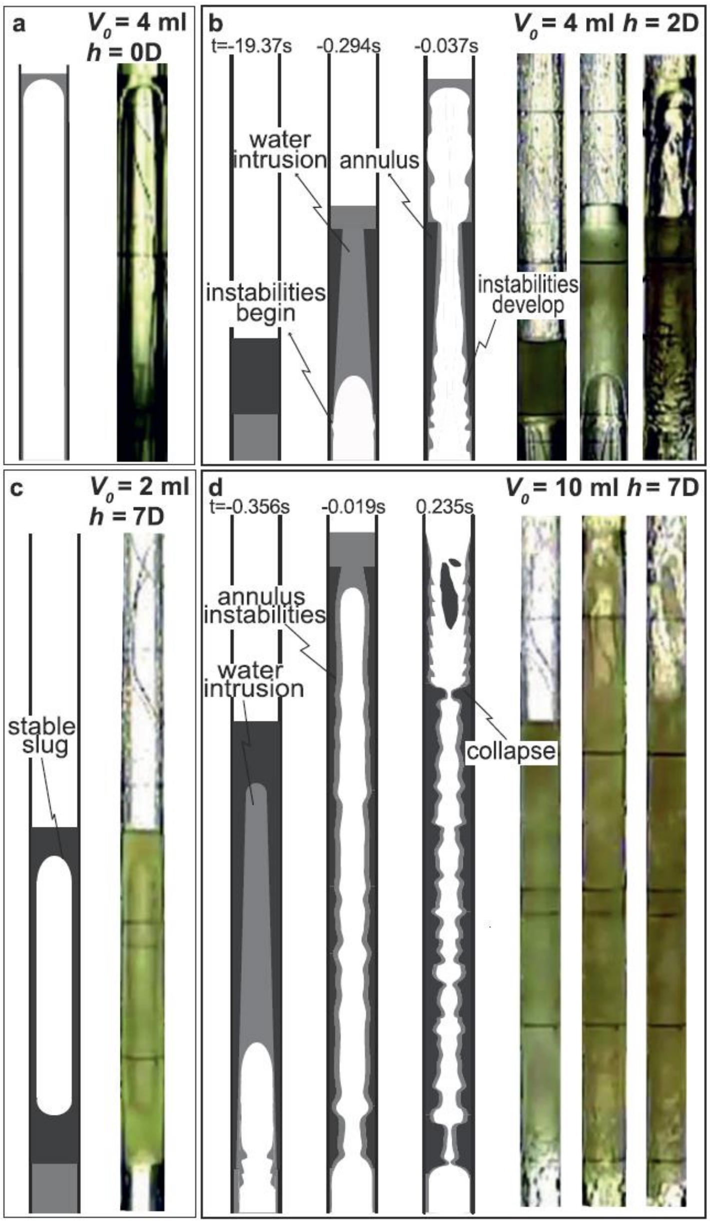

Figure 5.2 Still frames and interpretive sketches from selected experiments. **a**) Control experiment without plug (h = 0D) and 4 ml slug. Note smooth slug walls. **b**) Thin plug experiment (h = 2D). Slug rise and expansion forces water through the plug, forming an oil annulus (−0.294 s relative to burst). The slug rises through the annulus into water extruded above it, and film instabilities develop along the annulus (−0.037 s). **c**) A thick plug (h = 7D) is deep enough to fully accommodate a 2 ml slug. **d**) A 10 ml slug rising into the partially water-intruded oil plug causes rippling of the water film (−0.356 s), then its rapid expansion disrupts the upper reaches of the annulus (−0.019 s). At burst, the oil/water mixture slumps down, hindering or blocking the escaping gas flux (0.235 s).

Acceleration of the liquid's free surface and air liberation during the burst process generate a reproducible pulse (*Fig. 5.3a*) in the pressure above the liquid ΔP_A (Lighthill 1978). The resulting waveforms are similar to those observed in experiments conducted with oil ∼100 times more viscous than water (Lane et al.

2013) indicating insensitivity to absolute viscosity under inertial conditions. The peak excess pressure $\Delta P_A\hat{}$ scales linearly with dimensionless slug volume (*Fig. 5.4*) as also observed by Lane et al. (2013).

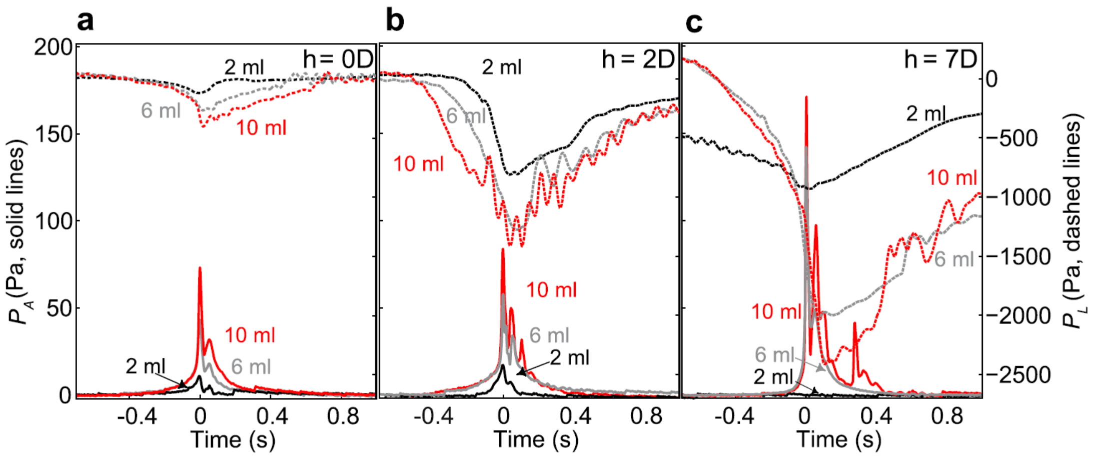

Figure 5.3 Pressure changes in the liquid at the base of the tube (ΔP_L, dashed lines) and in the air above the free surface (ΔP_A, solid lines), as a function of time and injection gas volume, for **a**) no plug (h = 0D), **b**) thin (h = 2D), and **c**) thick (h = 7D) plug experiments.

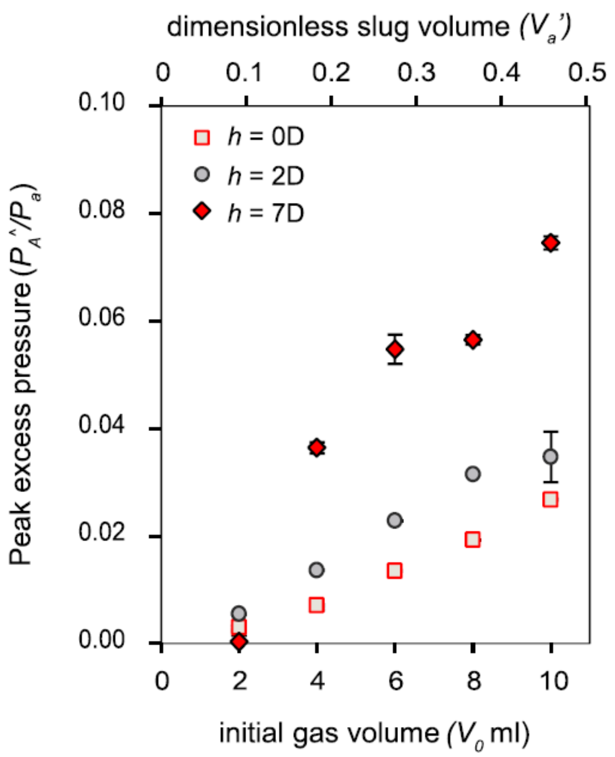

Figure 5.4 Peak excess pressure $\Delta P\hat{}_A$ normalised to P_a is reported as function of volume (V_0). Equivalent V'_a is also reported.

5.3.2 Thin viscous plug experiments

The presence of a thin viscous plug (plug thickness h =2D) slightly retards slug expansion during ascent. A smaller initial decrease in ΔP_L compared with the control experiments, or even a slight ΔP_L increase for the smallest V_0, was observed (*Fig. 5.3b*). Slug expansion drives an intrusion of water into and through the plug (*Fig. 5.2b*, Video V02). The intruding water core displaces and spreads oil along the tube wall to form a high-viscosity annulus, longer than the initial plug, enclosing a low-viscosity channel of water. The radial thickness of the oil annulus averages ~3 mm, and increases slightly from bottom to top, forming a dynamic, partial constriction of the effective tube cross-section. Once the water core breaches the plug, extruded water accumulates above it, the accumulated volume increasing as the slug expands.

When the slug reaches the base of the annulus, it exploits the low-viscosity pathway provided by the water core to ascend through it. A three-layer, axi-symmetric flow configuration is formed, with the ascending slug surrounded by a falling film of water, all enclosed within the oil annulus, which appears to be stationary (*Fig.5.2b*) on this time-scale. As the slug rises through the annulus, ΔP_L rapidly decreases by a factor of 2 to 4 compared with the control experiment (*Fig. 5.3b*). As the slug encounters the dynamic geometry change created by the high-viscosity annulus, instabilities form in the falling water film below the annulus. We suggest this could be caused by a reduction in the flux of water into the falling film below the annulus caused by the narrowing of the ascending slug within the annulus. As the slug ascends through, and emerges from the high-viscosity annulus, further instabilities begin to develop within the annulus. These are caused by the emergence of the slug from the dynamic geometry of the annulus (James et al. 2006) and the rapid waning of the flow processes that generated both the falling water film and the oil annulus. As both liquids drain back after burst and ΔP_L increases to the pre-injection value large downward ripples develop along the pipe walls (*Fig. 5.2b*). The ripples induce ΔP_L fluctuations 5 to 10 times larger than observed in the control experiments (*Fig. 5.3b*).

$\Delta P^{\wedge}_A$ is slightly greater than in the control experiments (*Fig. 5.4*). The ΔP_A waveform has a similar initial pulse, but lasts longer and becomes more complex and variable (*Fig. 5.3b*). The Video (V02) suggests ripples in the draining liquids cause significant and variable impedance of air escape rate from the slug, modulating ΔP_A.

5.3.3 Thick viscous plug experiments

A thick viscous plug (plug thickness h = 7D) retards slug expansion during ascent more strongly than a thin one, producing a higher maximum ΔP_L (*Fig. 5.3c*, maximum ΔP_L for the 2 ml slug is out of figure to the left). Small and large slugs display contrasting behaviour. The 2 ml slugs expand modestly, intrude minimal water into the oil, and are fully accommodated in the oil plug (*Fig. 5.2c*), passing slowly through it without developing any instability. Bursting is visible as a rupturing of an oil meniscus (Video V03), concomitant with a minimum in ΔP_L (*Fig. 5.2c*). Negligible acceleration of the free surface is observed and no ΔP_A signal is detected. This rupture dynamics is typical of the 'quiescent' regime experimentally identified by Lane et al. (2013), and is analogous to the bursting process observed by Kobayashi et al. (2010).

Expansion of the 4–8 ml slugs intrudes water significantly into the plug, with instabilities within the falling water film observed below the annulus as the slug ascends. Only the 10 ml slugs intrude sufficient water to accumulate it atop the oil annulus (*Fig. 5.2d*, Video V04). In this case, rapid slug expansion through the long, narrow, water-filled annulus causes a dramatic ΔP_L drop, as the entire plug mass becomes dynamically supported by the tube wall (*Fig. 5.3c*). The rapid change in flow structure caused by slug expansion strongly destabilises the annulus causing its upper reaches to disrupt into mixed water/oil globs. The bursting process is complex, involving transient restriction and blockage of the tube by the collapsing annulus and draining water (*Fig. 5.2d*). At burst, the slug base is still below the base of the annulus, leaving it fully supported by the tube wall. As the slumping annulus, mixed with water, encounters the water surface at the slug base, a reproducible step increase in ΔP_L occurs (*Fig. 5.3c*), unique for the 10 ml slug.

A thick high-viscosity plug increases $\Delta P\wedge_A$ by a factor of ∼3 to5 compared with the control (*Fig. 5.4*). ΔP_A waveforms also become more complex as V_0 increases (i.e., increasing initial injected volumes; *Fig. 5.3c*), with: a) negligible signal at 2 ml; b) some similarity to control experiments at 4–8ml; and c) large secondary peaks at 10 ml, some of them appearing up to 0.5 s after the primary peak. The ΔP_A peaks at 0.23, 0.27, and 0.47 s in Fig. 5.3c represent secondary pulses of air escaping temporary blockages of the tube caused by unstable slumping oil and globs of oil descending after being previously ejected up-ward. These peaks are observed in each 10 ml run, but their timing varies.

5.4 The impact of viscous plugging on slug burst dynamics

Our experimental results demonstrate that the presence of a viscous plug impacts strongly on slug ascent and burst. The viscous plug retards slug growth during ascent, implying an increase in slug overpressure (Bagdassarov 1994), which drives more vigorous bursting. Slug expansion during ascent causes the underlying liquid to penetrate the viscous plug, creating an annular constriction through which the slug must pass. The annulus increases the fraction of the pipe cross-section occupied by the liquid, creating a dynamic narrowing in the conduit geometry. The area occupied by the slug reduces by nearly half when entering the annulus, decreasing from 0.84 to 0.47 of the pipe cross section. The slug expansion rapidly accelerates as it passes through the constriction as a result of this decrease in its cross-sectional area. Increasing slug expansion enhances free surface acceleration, causing excess pressure $\Delta P^{\wedge}_A$ to increase accordingly (Lighthill 1978). Plotting $d(\Delta P_A)/dt$, representing synthetic infrasonic waveforms resulting from the experimental fluid-dynamic source mechanism (Lane et al. 2013), also illustrates positive correlation of the main peaks with hand V_0, and also shows that secondary oscillation pulses are more prominent when the viscous plug is present (*Fig. 5.5*). The two-layer liquid flow, generated by slow intrusion of water into and through the oil plug as the ascending gas slug expands, becomes dynamically unstable on rapid change to a three-layer fluid flow as the gas slug expands through the water core. The resulting instabilities cause transient blocking of the slug's narrow path, adding significant complexity to the burst process. As a result, the slug pinches into shorter gas pockets, causing pulsatory bursting that modulates the associated ΔP_A signal after the main pulse. Finally, the fluid-dynamic instabilities cause the two liquids to inter-mingle; this effect is strongest when a large slug ascends through a thick viscous plug.

5.5 Volcano-scale simulation

A three-dimensional numerical simulation of the final ascent stage of a slug of gas at volcano scale (as in James et al. 2008; Chouet et al. 2010) was carried out using the FLOW-3D fluid dynamics simulation package (Video V05). The simulation was performed with a conduit diameter of 3 m, a plug thickness h = 2D (~6 m), an underlying magma thickness of 194 m (simulating a total 200 m thick magma column), viscosities of 20000 and 20 Pa s, respectively, and a non-dimensional slug volume V'_a = 0.28 (equivalent to ~22 m^3 of gas). This gave N_f values of ~0.8 and

~800 for the viscous plug and the underlying magma respectively. Although slightly lower than the ‘canonical’ volcanic system, these N_f values represent the minimum acceptable values for basaltic melts (e.g., Vergniolle and Jaupart 1986); these were the highest values we could use without encountering numerical instabilities.

The CFD simulation shows a phenomenology similar to that observed experimentally (*Fig. 5.6*). Low viscosity liquid intrudes into and above the high viscosity plug, causing it to form an annulus as the gas bubble expands on ascent (*Fig. 5.6a, b*); gas follows the low viscosity intrusion through the high viscosity annulus, with the slug narrowing in the annulus and ‘ponding’ below the annulus (*Fig. 5.6c*). Ripples of instability form within the falling film below the annulus, and collapse of the low viscosity liquid above the annulus segments the ascending slug (*Fig. 5.6d*). This detailed level of similarity between our scaled experiment and the modelled volcanic scenario supports the applicability of the observed analogue phenomena to the natural volcanic case.

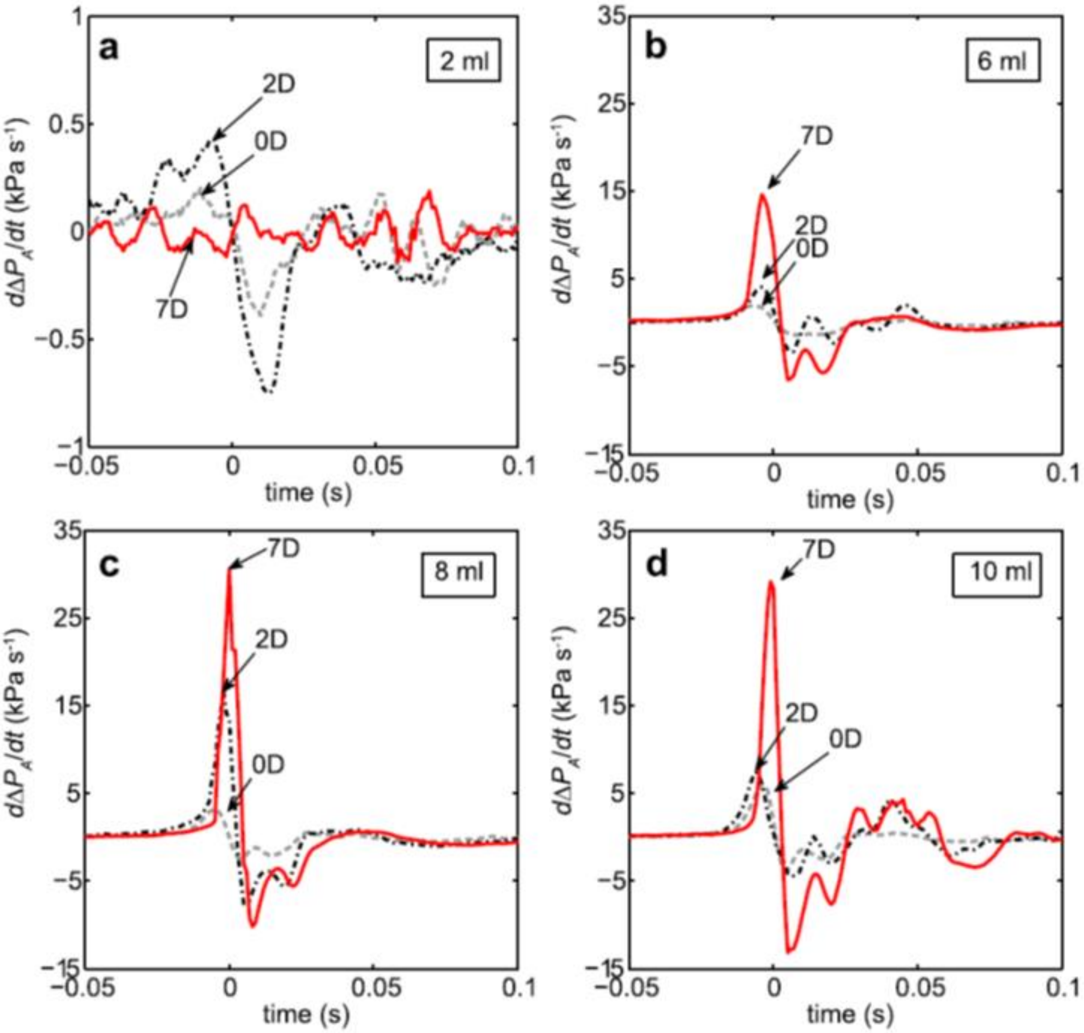

Figure 5.5 Time derivative of pressure variation $d(\Delta P_A)/dt$ as a function of time for initial air volumes (V_0) of: **a**) 2 ml (V'_a = 0.09), **b**) 6 ml (V'_a = 0.28), **c**) 8 ml (V'_a = 0.37) and **d**) 10 ml (V'_a = 0.45) ascending through different plug thicknesses. Such quantities would be equivalent to gas volumes of 7, 22, 29 and 37 m^3 at the volcanic scale, respectively. Note that ~80 Hz oscillations emerge on calculation of $d(\Delta P_A)/dt$ and that these plausibly represent high frequency but low amplitude half-wave resonance of gas above the flow in the experimental tube.

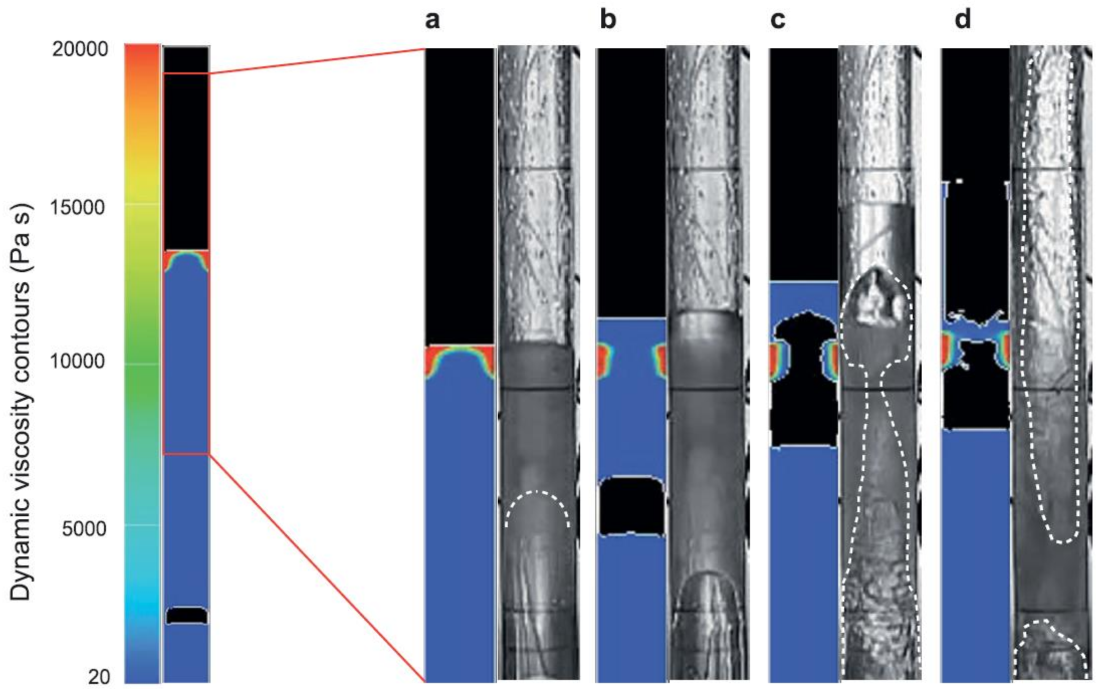

Figure 5.6 Results from CFD simulation at the volcanic scale. The parameters of the simulation are V_0 = 22 m^3 (V'_a = 0.28), P_a = 105Pa, μ_1=20 Pa s, μ_2 = 20 000 Pa s; h = 6 m (2D), D = 3 m, magma column height 200 m. Still frames (**a**, **b**, **c**, **d**) extracted from the simulation (see Video V05), show good comparison with experiments at the same scaled conditions V_0 = 6 ml (V'_a = 0.28) and h = 2.5 cm (2D), in terms of burst dynamics and liquid film perturbations, supporting the experimental procedures. Dashed lines indicate the low-viscosity intrusion profile (frame **a**), the slug profile (frame **c**), the bursting slug and the slug nose of the newly formed bubble profiles (frame **d**).

5.6 Implications for Strombolian volcanic eruptions

Our laboratory experiments allow us to develop a general conceptual model for slug ascent and burst through a viscous plug (*Fig. 5.7*) that could give insight into key phenomena observed in natural Strombolian eruptions. Firstly, several authors have described the simultaneous eruption, during a single Strombolian explosion, of pyroclasts from magmas with contrasting textural and rheological properties, sometimes mingled within a single pyroclast (e.g., Taddeucci et al. 2004; Lautze and Houghton 2005, 2006; Gurioli et al. 2014). Our experiments open a new possible scenario, in which mingling results from the fluid dynamic instabilities that develop when a slug expands through the self-organising geometry of a core of low-viscosity magma within an annular plug of high-viscosity magma. The instabilities cause the two magmas to mingle in the slug burst region, scavenging both into pyroclasts.

Secondly, high-speed videography has revealed the presence of ejection pulses – highly variable in duration and pyroclast velocity – within individual strombolian explosions (Taddeucci et al. 2012a). Experimentally, these pulses are caused by transient blocking of the conduit by the same instabilities, supporting the hypothesis, proposed by Taddeucci et al. (2012a), that “transient gas pockets formed by the repeated collapse of the liquid film lining conduit walls during the bursting of long slugs”. We observe a semi-quantitative similarity between pyroclast ejection velocity at Stromboli and air pressure in the scaled experiments. The experimental timescale of the individual pressure pulses (~0.05 s) is about a factor of ten shorter than the duration of the whole bursting process (~0.5 s), matching well the scaling factor for the timescale of ejection pulses (~0.1–1s) to that of strombolian explosions (a few seconds to tens of seconds).

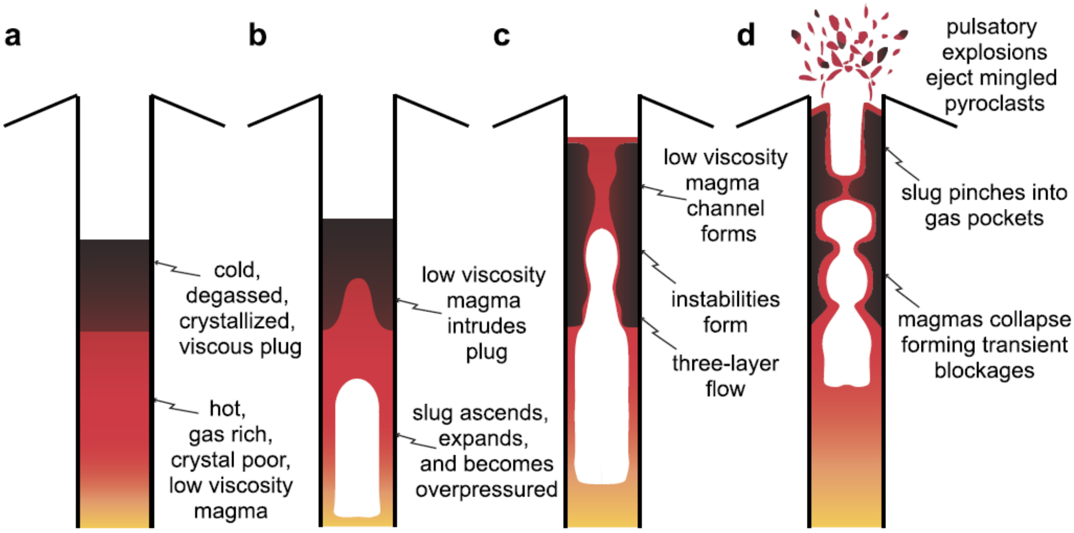

Figure 5.7 A model illustrating the effect of viscous plugging on a Strombolian eruption. **a**) Before slug ascent, degassing and cooling of a magma stagnating atop the conduit forms a high viscosity plug. **b**) Expansion of the slug, impeded by viscous resistance of the plug, causes low viscosity magma to intrude the plug. **c**) A three-layer flow forms as the slug enters the low viscosity channel, developing dynamic instabilities. **d**) Instabilities grow causing mingling of the two magmas, channel collapse, and slug disruption into smaller pockets. Accelerated slug expansion culminates in pulsatory bursting and ejection of mingled pyroclasts. The system then resets to a during the quiescence period before the next slug burst.

Our experimental findings provide a new reference for understanding, interpreting, and modelling Strombolian volcanic eruptions. The instabilities that cause pulsations in the eruption are only observed in experiments that include a viscous plug (compare control experiments and previous studies, e.g., James et al., 2009; Lane et al., 2013), suggesting that the presence of a plug could be a plausible pre-requisite for the generation of complex multi-pulse behaviour, as may be observed from infrasound and videography. Furthermore, the formation of an annulus of higher-viscosity magma in our experiments advocates the existence of a ‘dynamic’ conduit geometry, which changes cyclically in response to the passage of slugs. The balance of timescales of plug-forming and plug-consuming processes (i.e., magma degassing, cooling, crystallisation, and entrainment of fall-back material, vs. the return time and volume of passing slugs) will create a complex feedback controlling the generation and recovery of the dynamic and effective conduit geometry (James et al. 2006), explosion dynamics, and the linked frequency and intensity of explosions.

Finally, our results indicate that the increase in explosivity and complexity of Strombolian eruptions related to the presence of a viscous plug are mirrored by differences in the first time derivative of pressure variation $d(\Delta P_A)/dt$, i.e., atmospheric infrasound. In our experiments, a ‘thick’ plug increases peak pressure of the main ‘burst’ by a factor of 3 to 5 compared with no plug, and is associated with the development of more prominent secondary peaks. Extrapolating the observed trends in natural volcanic eruptions requires care and is beyond the intention of this work. However, a quick by-eye comparison with infrasonic signals generated by eruptions from the ‘Hornito’ vent at Stromboli (*Fig.6E* in McGreger and Lees 2004), shows remarkable similarity to the $d(\Delta P_A)/dt$ synthetic waveform from the 10 ml, 7D experiment (*Fig.5.8*). Qualitatively the first pulse is well matched, in similarity to single viscosity systems (Lane et al. 2013); however, in contrast to the single viscosity system, the subsequent secondary oscillations are also well matched, suggesting that slug interaction with a thick viscous plug could provide a plausible first-order mechanism for such infrasonic signals. Thus, we expect that, during volcanic eruptions, the presence and thickness of a viscous plug introduces another degree of freedom to the system, which may act to increase variability and reduce the certainty of interpretation of air and ground motion signals. This ultimately bears on the importance of multiple monitoring, during eruptions, of parameters such as erupted gas masses, and magma rheology, for a more accurate interpretation of infrasonic signals.

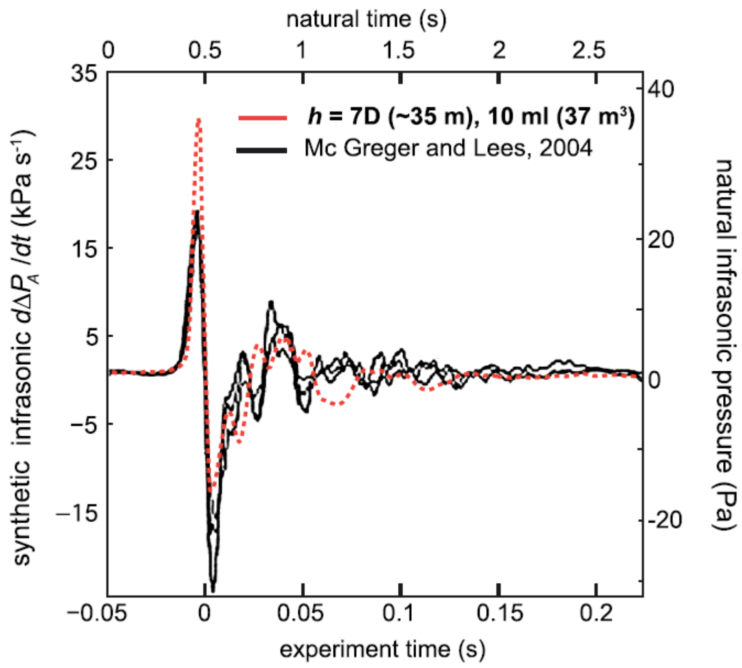

Figure 5.8 The first time derivative of experimental excess pressure $d(\Delta P_A)/dt$, as a function of time, for the 10 ml, 2D experiment (dashed line) was compared to measured infrasonic signals at Stromboli reprinted from McGreger and Lees (2004 with permission from Elsevier, solid lines). Both time axis and pressure axis are adapted to best fit the experimental to the measured data.

5.7 Conclusions

The presence of a viscous plug at the top of a volcanic conduit can play a major role in modifying the nature of Strombolian explosions. A viscous plug increases the explosivity of Strombolian eruptions by enhancing slug overpressure. The plug introduces complexities by modulating the slug expansion and burst process, explaining observed eruption pulses and secondary acoustic signals. The presence of a plug also explains the commonly observed eruption of mingled-texture pyroclasts. The key fluid-dynamic mechanism is the expansion of the ascending gas slug driving intrusion of low viscosity magma into the overlying plug. The resulting annulus of plug material surrounds an intrusion of low-viscosity magma through which the slug then rises to the free surface. The 'rapid' expansion of the gas slug through the low-viscosity intrusion destabilises the liquid annulus, which acts as a dynamic constriction of the conduit, modulating gas escape and strongly affecting the geophysical signals, such as infrasound, associated with the expansion and burst of the slug. For the same gas volume, a viscous plug leads to the generation of different types of pressure signals. Thus, our experimental results reveal some important aspects of the explosivity of basaltic systems. In particular, they evidence that besides gas volume, the presence and extent of viscous plugging must be considered for the interpretation of infrasonic measurements of Strombolian eruptions. In this study, viscous plugs are modelled as discrete bodies, whereas in real volcanic systems, plugs are likely to be gradational features, i.e., it is likely that a plug is characterized by a gradual transition between the lower viscosity magma and the higher viscosity one. Despite continuous monitoring of Stromboli volcano these features are still not predictable or fully understood. Further work is required to determine the impact that this has on our first order findings.

5.8 Video description

Videos **V01**, **V02**, **V03**, and **V04** contain video sequences and synchronised pressure variations acquired during the following experiments: **V01**) control experiment (no viscous cap, h = 0D), 4 ml slug; **V02**) thin viscous cap (h = 2D), 4 ml slug; **V03**) thick viscous cap (h = 7D), 2 ml slug; **V04**) thick viscous cap (h = 7D), 10ml slug. Unfiltered and filtered pressure variations are reported for both ΔP_A (pink and red lines, respectively) and ΔP_L (grey and black lines). Predicted atmospheric acoustic pressure (yellow line, $d(\Delta P_A)/dt$) is also reported for the three experiments in the movies that show P_A signals. Video **V05** contain the result of the CFD simulation at the volcanic scale (V_0 = 22 m^3, P_a = 105 Pa, μ_1 = 20 Pa s, μ_2 = 20000 Pa s; h = 6 m, D =3 m, magma column height 200 m) described in Section 5.

5.9 Acknowledgements

This work was partly supported by E.D. PhD project grant (University of Bologna) funded by INGV. A.C. received funding from the People Programme (Marie Curie Actions) of the European Union’s Seventh Framework Programme (FP7/2007–2013) under the project NEMOH, REA grant agreement No. 289976. We thank Sylvie Vergniolle and an anonymous reviewer for their constructive comments, which helped improve the manuscript. We also thank Tamsin Mather for her editorial handling of the manuscript.

Supplementary Content

5.10 Scaling considerations

Here we provide the details on the scaling relationships between our experimental setup and the volcanic scenario.

The dimensional quantities that are relevant to slug ascent in a vertical pipe are: the liquid density ρ (kg/m^3); liquid viscosity μ (Pa s); surface tension σ (N/m); pipe radius r_c (m); gravitational acceleration g (m/s^2); and slug ascent velocity v_s (m/s). Five dimensionless combinations of these parameters are commonly used to describe the system: the Morton number *Mo*; the Eötvös number *Eo*; the inverse viscosity *Nf*; the Froude number *Fr*; and the Reynolds number *Re* (e.g, James et al. 2004, 2009; Seyfried and Freundt 2000; Llewellin et al. 2012).

The Morton number represents the ratio of viscous and surface tension forces,

$$Mo = \frac{g\mu^4}{\rho\sigma^3}\,. \tag{S1}$$

The Eötvös number represents the ratio of buoyancy and surface tension forces,

$$Eo = \frac{4\rho g r_c^2}{\sigma}\,. \tag{S2}$$

The inverse viscosity, sometimes called the buoyancy Reynolds number, is given by (Wallis 1969),

$$N_f = \frac{\rho}{\mu}\sqrt{gD^3}\,. \tag{S3}$$

The slug Reynolds number represents the ratio of inertial and viscous forces,

$$Re = \frac{2\rho v_s r_c}{\mu}\,. \tag{S4}$$

The Froude number is a dimensionless measure of slug ascent velocity,

$$Fr = \frac{v_s}{\sqrt{2gr_c}}\ . \qquad \text{(S5)}$$

Since we have six dimensional parameters, and three dimensions (mass, length and time), we expect to only require three dimensionless parameters to describe the system. Consistent with this, the following relationships exist amongst the five parameters above ($N_f = \sqrt[4]{Eo^3/Mo}$; and $Re = N_f Fr$) reducing the number of *independent* parameters to three. Furthermore, Llewellin et al. (2012) show that, when surface tension can be neglected (which holds for $Eo > 40$; Viana et al. 2003), Fr is a function of N_f only, so Re and N_f are uniquely related, and can be considered cognate.

At basaltic volcanoes, typical density (800-2600 kg/m^3), viscosity (10-50000 Pa s), surface tension (0.2-0.4 N/m), conduit diameter (2-5 m) and slug ascent velocity (1-2 m/s) ranges provide values of dimensionless parameters for volcanic slugs in the range $10^2 < Mo < 10^{17}$, $10^5 < Eo < 10^6$, and $10^0 < N_f < 10^4$, $10^{-2} < Fr < 10^{-1}$, $10^{-1} < Re < 10^2$. The high values of *Eo* indicate that surface tension plays a negligible role for volcanic slugs in basaltic magmas, hence their morphology and ascent velocity are predominantly controlled by inertial and viscous forces. Consequently, we can neglect *Eo* and *Mo* and the system is adequately described by the inverse viscosity N_f (from which *Fr* and *Re* can be derived).

Material properties and scaling relationships for experiments and 'canonical' volcanic scenario are reported in Table 5.1. Notably, the smaller diameter of our laboratory-scale pipe, and the use of low viscosity analogues, results in much smaller *Eo* and *Mo* numbers than in basaltic systems. Consequently, surface effects will be relatively enhanced in our experiments, especially in the case of slugs ascending through water. However, for all experiments, $Eo > 40$ so this difference should not represent a controlling factor. The calculated inverse viscosities indicate that both volcanic and experimental slugs will be viscously controlled in the plug region ($N_f <$ ~10) and inertially controlled in the low-viscosity liquid region ($N_f >$~1000).

The dimensionless thickness of the falling film λ' (film thickness divided by pipe radius) can be determined empirically from N_f (Llewellin et al. 2012):

$$\lambda' = 0.2014 + 0.123\tanh(2.66 - 1.15\log_{10} N_f)\ , \qquad \text{(S6)}$$

From this, we can determine the fraction of the conduit's cross sectional area that is occupied by the falling film A' (James et al. 2009)

$$A' = \lambda'(2-\lambda') \text{ (hence also } \lambda' = 1-\sqrt{1-A'}\text{).} \tag{S7}$$

This, in turn, allows us to calculate how much the slug narrows when entering the plug zone.

Slug volumes are non-dimensionalized following Del Bello et al. (2012). They define a characteristic volume $V_c = \pi r_c P_a / \rho g$ where P_a is the ambient pressure above the liquid. The dimensionless slug volume is then

$$V_a' = \frac{V_a}{V_c} \tag{S8}$$

where V_a is the volume that the slug would have at ambient pressure.

Chapter 6 - Gas slug ascent in a stratified magma: implications of flow organisation and instability for Strombolian eruption dynamics

Antonio Capponi, Mike R. James, Steve J. Lane
Lancaster Environment Centre, Lancaster University, Lancaster LA1 4YQ, UK

Published paper (Appendix 2):

A. Capponi, M.R. James, S.J. Lane, *Gas slug ascent in a stratified magma: Implications of flow organisation and instability for Strombolian eruption dynamics*, Earth and Planetary Science Letters, Volume 435, 1 February 2016, Pages 159-170, http://dx.doi.org/10.1016/j.epsl.2015.12.028.

Reviewers: Katie Cashman and Sylvie Vergniolle

Chapter 5 gave the first insights on how the presence of a plug modifies the nature of Strombolian explosions, increasing the explosivity of the eruptions and modifying the properties of the ejecta.

Motivated by this evidence, work was carried out to detail the range of fundamental flow configurations that can develop in association with slug flow through a rheologically stratified conduit, by combining laboratory experiments, numerical modelling and 3D CFD simulations. Silicone oil was used as analogue for low-viscosity magma and, compared to the previous investigation (Del Bello et al. 2015), a wider range of plug thickness, slug volumes and experimental ambient pressures have been considered, to cover all possible flow configurations and to better scale for gas expansion ratio.

A 1D model (Appendix 6) was developed to illustrate the relevance of the identified flow configurations to Strombolian-type volcanoes. These configurations are also supported by 3D CFD simulations carried out at volcano-scale, considering eruptive parameters valid for Stromboli volcano. Then the implications for Strombolian eruptions of each flow configuration have been explored; results show

how the synergy between initial gas slug volume and plug properties (viscosity and thickness) controls the transition in flow configurations. Each configuration encompasses a variety of processes such as, for example, magma mingling, leading to the ejection of mingled pyroclasts, generation of instabilities within the falling liquid film and dynamic geometrical changes, resulting in eruptive pulses, and variations in the degree of slug pressurization, modifying eruption magnitude.

Antonio Capponi: carried out the experimental campaign and data processing, developed the 1D model, wrote the Matlab (1D model; Appendix 6) and LabVIEW (data logging; Appendix 5) codes, carried out 3D CFD simulations and wrote the manuscript.

Mike James: contributed to discussions, reviewed the manuscript, gave assistance in Matlab and Flow3D, provided the initial CFD model code, proposed the original idea for the experiments and obtained grant funding.

Steve Lane: contributed to discussions, reviewed the manuscript, gave assistance in the laboratory, proposed the original idea for the experiments and obtained grant funding.

Abstract

The canonical Strombolian paradigm of a gas slug ascending and bursting in a homogeneous low-viscosity magma cannot explain the complex details in eruptive dynamics recently revealed by field measurements and textural and geochemical analyses. Evidence points to the existence of high-viscosity magma at the top of the conduit of Strombolian-type volcanoes, acting as a plug. Here, new experiments detail the range of flow configurations that develop during the ascent and burst of a slug through rheologically-stratified magma within a conduit. End-member scenarios of a tube fully filled with either high- or low-viscosity liquid bracket three main flow configurations: (1) a plug sufficiently large to fully accommodate an ascending gas slug; (2) A plug that can accommodate the intrusion of low-viscosity liquid driven by the gas expansion, but not all the slug volume, so the slug bursts with the nose in the plug whilst the base is still in the low-viscosity liquid; (3) Gas expansion is sufficient to drive the intrusion of low-viscosity liquid through the plug, with the slug bursting in the low-viscosity layer emplaced dynamically above the plug. We show that the same flow configurations are viable at volcanic-scale through a new experimentally-validated 1D model and 3D computational fluid dynamic simulations. Applied to Stromboli, our results demonstrate that the key parameters controlling the transition between each configuration are gas volume, plug thickness and plug viscosity. The flow processes identified include effective dynamic narrowing and widening of the conduit, instabilities within the falling magma film, transient partial and complete blockage of the conduit, and slug disruption. These complexities influence eruption dynamics and vigour, promoting magma mingling and resulting in pulsatory release of gas.

Keywords

plugged conduit; magma mingling; slug dynamics; conduit geometry; flow configurations; analogue experiments; flow modelling

6.1 Introduction

Strombolian eruptions are characterised by short impulsive events. These typically occur in basaltic or andesitic magmas where viscosity is sufficiently low to allow gas segregation over short time scales (Blackburn et al. 1976; Parfitt 2004; Houghton and Gonnermann 2008). Explosions are interpreted as representing the arrival and burst of over-pressured large gas pockets (slugs) at the surface (Chouet et al. 1974; Blackburn et al. 1976). The slugs can form either by coalescence of smaller bubbles at geometrical discontinuities in the conduit (Vergniolle and Jaupart 1986; Jaupart and Vergniolle 1988) or by differential ascent rate of the bubbles with respect to the magma column (Parfitt and Wilson 1995; Parfitt 2004). Either way, the ascent, expansion and burst of slugs have almost always been considered in rheologically uniform media (e.g., Vergniolle and Brandeis 1996; Vergniolle et al. 1996; Seyfried and Freundt 2000; James et al. 2006, 2008; Kobayashi et al. 2010; Del Bello et al. 2012; Lane et al. 2013).

However, an increasing body of evidence (e.g., Lautze and Houghton 2005, 2006; Polacci et al. 2009; D'Oriano et al. 2011; Colò et al. 2010; Gurioli et al. 2014) suggests that the cooling, degassing and crystallisation of the uppermost part of the magma column, along with mixing with recycled material from collapses of the conduit wall, re-entrained pyroclasts and lithics, could generate an evolved magma region at the top of the conduit. Gas slugs must ascend and burst through this stratified rheological heterogeneity. The rheological properties and thickness of this region may influence explosion intensity and style (Lautze and Houghton 2005, 2006), while textural and geochemical variations in the ejecta may reflect mingling of magmas with different physical properties in the shallow conduit (Polacci et al. 2009; D'Oriano et al. 2011; Colò et al. 2010; Gurioli et al. 2014). Textural features observed in samples collected at Stromboli seem to correlate with explosion frequency and magnitude, with a broader mingling promoted by increased magma and gas flux (i.e., greater explosion frequency and vigour). In contrast, a lower flux (i.e., low level of activity) leads to more restricted mingling (Lautze and Houghton 2006). Complexities in eruptive dynamics, such as pulses within a single Strombolian eruption (Taddeucci et al. 2012a; Gaudin et al. 2014), are also difficult to explain with simplified models of slug burst in a rheologically uniform fluid, although conduit discontinuities could play a role (James et al. 2006).

Such evidence motivated initial experimental work on the effects of a viscous upper layer (or ‘plug’) on eruptive dynamics (Del Bello et al. 2015). In this scenario, a gas slug ascending and expanding in a column of low-viscosity liquid overlaid by a plug drives an intrusion of low-viscosity liquid into the plug. The plug liquid thus creates a viscous annulus that, in turn, encloses the intrusion (*Fig. 6.1*). As the slug arrives at the plug base, it uses the low-viscosity intrusion to rise through the plug. The slug can burst in two different flow configurations: 1) whilst fully accommodated into the plug volume, or 2) whilst in a low-viscosity layer emplaced by the intrusion above the plug. Each configuration encompasses apparent dynamic narrowing and widening of the conduit for the slug, instabilities within the falling film surrounding the slug, transient partial blockages of the conduit, and slug disruption (Del Bello et al. 2015). These complexities gave insight into the generation of eruptive pulses and mingled pyroclasts, together with enhancement of slug overpressure with respect to a single-viscosity system (Del Bello et al. 2015); however, accurate scaling for slug expansion and viscosity contrast was not achieved.

Here, we build on the experimental foundation of Del Bello et al. (2015) to fully define the rich range of fundamental fluid configurations that can develop in association with slug flow through a viscous plug at the top of a volcanic conduit. We used comprehensively scaled laboratory experiments to identify flow organisation and instability within different fluid configurations expressed by varying relative plug and slug sizes. We developed a model to determine these configurations for a given set of parameters, and validated it against the laboratory data and, at volcano-scale, against the results of 3D computational fluid dynamics simulations. Finally, we explored the implications of flow richness in the shallow conduit for interpretation of Strombolian eruptive processes.

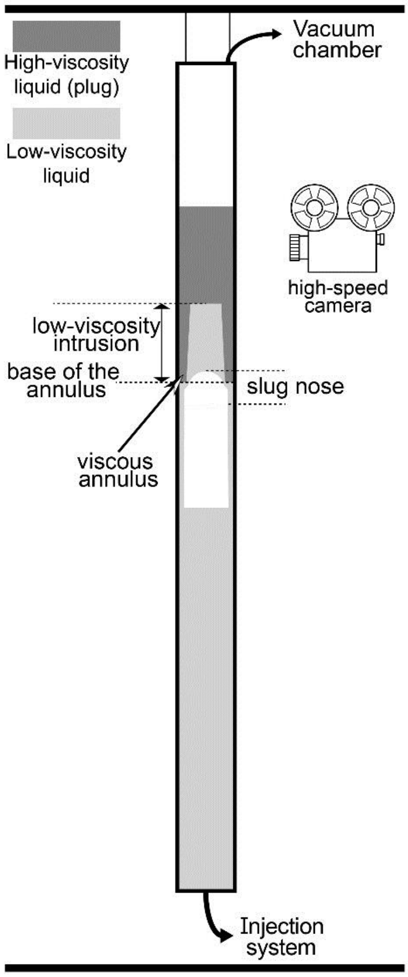

Figure 6.1 The experimental apparatus comprised a 3-m-high vertical tube, with a diameter *D* of 0.025 m, connected to a vacuum chamber and a gas injection system. Scaling considerations dictated that experimental ambient pressure was varied between 3 kPa, 1 kPa and 300 Pa. Slug ascent, expansion and burst through the experimental liquids were imaged with a high-speed camera at 300 *fps*. As a slug ascended and expanded in the tube, it drove an intrusion of the underlying low-viscosity liquid into the plug, forming a low-viscosity channel (low-viscosity intrusion). The intrusion displaced and spread the high-viscosity liquid along the tube wall, creating a high-viscosity annulus (viscous annulus) that, in turn, enclosed the intrusion.

6.2 Methods

The complex volcanic system was simplified to explore the effect of a vertical rheology contrast on the behaviour of the slug during its ascent, expansion and burst in a constant-geometry tube filled with Newtonian liquids. The experimental apparatus (*Fig. 6.1*) comprised a vertical 3-m-high glass tube with internal diameter D of 0.025 m. The base of the tube was sealed, with the exception of the gas injection system. The top was connected to a vacuum chamber in order to reduce the ambient pressure, P_a, and enable slug expansion processes to be scaled (James et al. 2008). We used *AS100* silicone oil (viscosity μ = 0.1 Pa s, density ρ = 990 kg/m^3, Wacker

Chemie AG) as analogue for low-viscosity magma (*Table 6.1*), improving on the experiments of Del Bello et al. (2015) by (a) providing more accurate scaling of viscosity contrast, and (b) enabling access to the explosive region of slug expansion (James et al. 2009; Del Bello et al. 2012). Immiscible castor oil (μ = ~1 Pa s, ρ = 961 kg/m^3) represented the high-viscosity plug with a density less than that of the silicone oil and a suitably high viscosity. At both laboratory and volcanic scales, surface tension plays a negligible role (e.g., Seyfried and Freund 2000), and the inverse viscosity N_f controls the ascent of a slug:

$$N_f = (\rho/\mu)\sqrt{gD^3} \tag{1},$$

where g is the gravitational acceleration. For the tube geometry, we obtain N_f values of ~12 and ~122 for the castor oil and silicone oil respectively (*Table 6.1*). These values lie in regions of the flow regime where the slug behaviour is controlled by viscosity in the plug, and by inertia with viscous contributions in the silicone oil (e.g., White and Beardmore 1962).

Table 6.1 Comparison of experimental parameters from this study and from Del Bello et al. (2015) and scaling to the volcanic case

Materials	Water[a]	Silicone oil[b]	Castor oil[a-b]	Underlying magma[e]	Plug[e]
Conduit radius, r_c (m)		0.0125		2.5	
Density (kg/m^3)	1000	990	961	900	1300
Viscosity (Pa s)	0.001	0.1	1	50-300	10000-50000
Inverse viscosity, N_f	12380	122	12	630-105	4.5-0.91
Film cross section, A'[c]	0.16	0.41	0.52	0.26-0.36	0.53-0.54
Dimensionless film, λ'[d]	0.08	0.23	0.31	0.14-0.24	0.32-0.32
Film thickness, λ (m)	0.001	0.0029	0.0039	0.35-0.60	0.80-0.81
Slug radius, r_s (m)	0.011	0.0095	0.0085	1.89-2.14	1.67-1.68
Viscosity contrast	1000	10		33-1000	

[a] used in Del Bello et al. (2015).
[b] used in this study.
[c] calculated from equation (28) in Del Bello et al. (2012).
[d] calculated from equation (4.2) in Llewellin et al. (2012).
[e] viscosity and density data reported in Gurioli et al. (2014).

The apparatus was filled to a height of ~1.43 m with either silicone oil only, or with silicone oil overlain by a layer of castor oil. Layer thickness of the plug was non-dimentionalised as a function of the tube diameter, D: ~2.5 (1D), ~5 (2D), ~12.5 (5D), ~25 (10D) and ~50 (20D) cm plugs, widening the range of Del Bello et al. (2015), which only considered ~5 (2D) and ~17.5 (7D) cm layers. In addition to the gas volumes (2, 4, 6, 8 and 10 ± 0.1 ml) and P_a (P_a = 3 kPa, limited by water boiling point) used in Del Bello et al. (2015), we injected volumes of air (V_0) of 17, 24, 32 and 49 ± 0.1 ml, with P_a reduced to 1 ± 0.1 kPa and 300 ± 0.1 Pa, greatly extending the range of gas expansion ratios.

The injected gas volumes non-dimensionalise through the parameter V_a' (Del Bello et al. 2012; Supplementary Content), giving V_a' = 0.08–2, 0.6–14 and 6–152 for experimental P_a of 3 kPa, 1 kPa and 300 Pa respectively. Scaled to the volcanic case, these values represent erupted gas volumes at atmospheric pressure of 4–90 m^3, 28–690 m^3 and 300–7300 m^3, and cover the range of gas volumes estimated for normal strombolian activity (Vergniolle and Brandeis 1996; Vergniolle et al. 1996; Ripepe and Marchetti 2002; Chouet et al. 2003; Harris and Ripepe 2007; Mori and Burton 2009) i.e., 2–2 × 10^4 m^3 (0.5–3000 kg), and for gas puffers, 50–190 m^3 (10–30 kg). Each experiment was imaged at 300 ± 0.1 frames per second with a Basler acA2000-340km high-speed camera.

To extend our 1D numerical model to volcanic-scale, we considered an idealised system with a 200-m-high magma column within a conduit of radius 1.5, 2 or 2.5 m, covering the range of values appropriate to Stromboli (Taddeucci et al. 2012a; Gaudin et al. 2014). Magma viscosities range between 10–50 kPa s and 50–500 Pa s, with densities of 1300 kg/m^3 and 900 kg/m^3, for the plug and the underlying magma respectively (Gurioli et al. 2014). These parameters give N_f values ~4.55 to ~0.42 for the plug and ~630 to ~29 for the underlying magma. Slug ascent is under dominant viscous control in the plug, but with a significant degree of inertial contribution within the underlying magma, a condition mimicked experimentally.

6.3 Results

The experiments revealed a rich set of flow configurations, reflecting variation in the ratio of the lengths of the high-viscosity plug and gas slug. The flow configurations can be conceptually considered within a spectrum of relative plug lengths, ranging from infinite (i.e. a conduit fully filled with the high-viscosity liquid, *fig. 6.2a*) to zero (i.e. a conduit filled with the low-viscosity liquid, *fig. 6.2e*). These single-viscosity end-members bracketed three distinct intermediate and more complex flow configurations (*Fig. 6.2b*, *c*, *d*). The transitions between these configurations were not sharp, and included intermediate behaviours. However, they encompassed the same processes observed in the main configurations and, thus, are not detailed here (see Supplementary Content for more information).

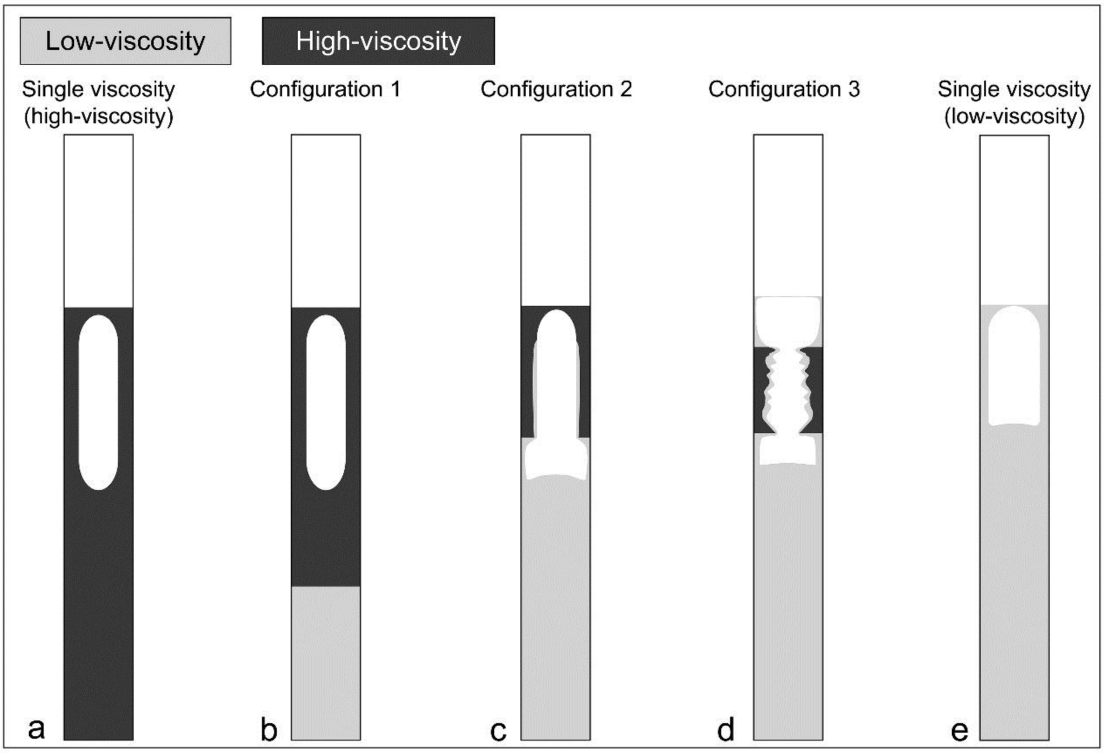

Figure 6.2 Experimentally informed conceptual sketches of tubes filled with (**a**) high-viscosity and (**e**) low-viscosity liquid represent the configuration end-members that sandwiched three main flow configurations for the two-layer system. (**b**) Configuration 1: the viscous plug volume fully accommodates the gas slug. (**c**) Configuration 2: the plug volume cannot accommodate both the low-viscosity intrusion and the slug. At burst, the slug nose and main body are in the plug, whilst the base is still in the low-viscosity liquid. (**d**) Configuration 3: slug expansion drives the intrusion of low-viscosity liquid through the plug, extruding a low-viscosity layer above the plug in which the slug burst. Instabilities develop as the slug passes through the annulus into the extruded low-viscosity layer.

6.3.1 Single viscosity

We define infinitely thick and infinitely thin plugs as end-member configurations (*Fig. 6.2a*, *e*) in which slug ascent is effectively within a single-viscosity system. In the experiments, the injection of air at the base of the apparatus formed a slug (James et al. 2008; Lane et al. 2013; Del Bello et al. 2015) that rose, expanded and elongated surrounded by a falling liquid film. The slug burst when all the liquid head above it has flowed into the falling film, except for a thin layer forming a meniscus. When ascending in a low-viscosity liquid (*Fig. 6.2e*), the slug occupied almost all the cross sectional area of the tube, surrounded by a thin falling film of liquid (*Fig. 6.3*); for gas volumes larger than 17 ml, film instabilities developed with time. At burst, the meniscus ruptured, and its remnants were dragged upward by the released gas before falling or draining back on the liquid surface (Video V01). Small volumes of gas (2-8 ml) produced pre-burst oscillation of the slug nose at surface.

For slug ascent in high-viscosity liquids (*Fig. 6.2a*), the slug ascended with a lower velocity, surrounded by a thicker falling film, thus the fraction of the tube cross-section occupied by the film, *A'* (Del Bello et al. 2012; Supplementary Content), increased from ~0.41 to ~0.52 (*Table 6.1*, *Fig. 6.3*). Consequently the area of the tube occupied by the slug decreased, while its length increased. The rate of gas expansion was slower, driving a slower acceleration of the liquid surface. When at the liquid surface, the slug burst with a slow rupture of a thick viscous meniscus, which completely drained to the tube wall just above the burst point and without the ejection of any droplets or observable pre-burst oscillation.

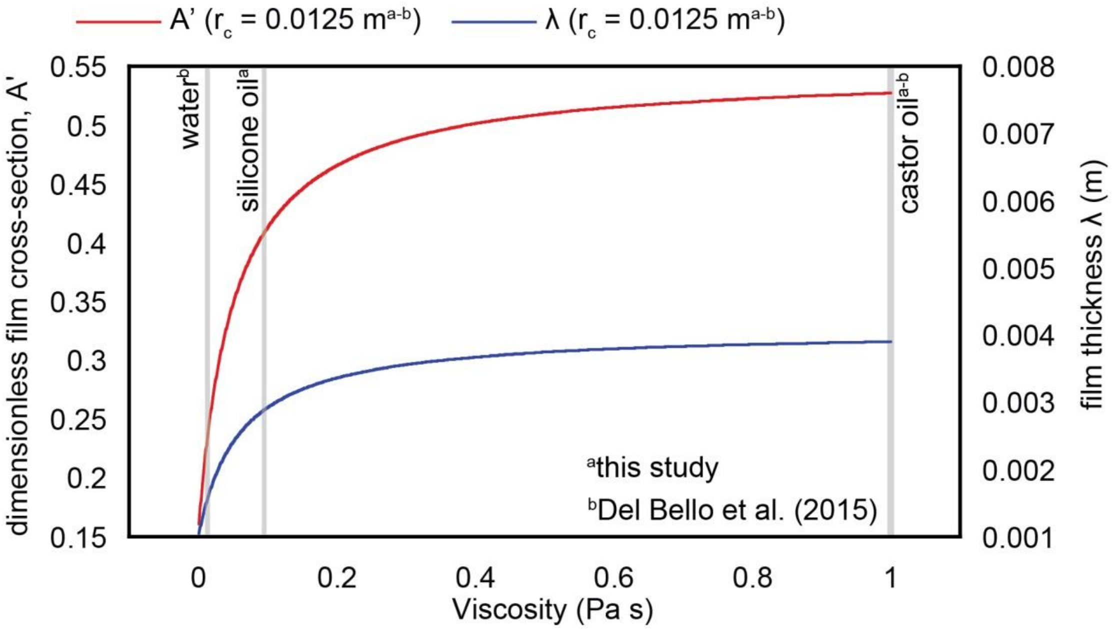

Figure 6.3 Variations of the dimensionless film cross section *A'* (calculated from equation (28) in Del Bello et al. 2012) and thickness of the falling liquid film (m), λ, as a function of viscosity for a tube radius of 0.0125 m; shaded areas highlight the values for water (μ = 0.001 Pa s, ρ = 1000 kg/m^3; used in Del Bello et al. 2015), silicone oil (μ = 0.1 Pa s, ρ = 990 kg/m^3; this study) and castor oil (μ = 1 Pa s, ρ = 961 kg/m^3; both this study and Del Bello et al. 2015).

6.3.2 Configuration 1

In a layered system in which the plug volume was significantly greater than the slug volume, a steady slug flow was established in both the low- and high-viscosity liquids (*Fig. 6.2b*), with a transitional period as the slug moved between the fluids (Video V02, 8-13 s). At the onset of an experiment the slug rose in the low-viscosity liquid. As it ascended, gas expansion drove an intrusion of low-viscosity oil into the plug, the extent of which depended on the relative volumes of the slug expansion and the plug. Around the intrusion, the high-viscosity liquid represented a viscous annulus, with an average radial thickness ∼4 mm, thinnest at the plug base (*Fig. 6.3*).

When the nose of the ascending slug reached the base of the annulus, the annulus acted as a dynamic change in the confining geometry. This forced the slug to ascend through a diameter reduction and into the intrusion (*Fig. 6.4a*, sketch II; Video V02, 8 s). For all configurations the intrusion volume must equal the slug volume expansion; therefore the intrusion was always smaller than the slug itself. Thus, at some point, the slug transited from ascending within the intrusion to within the main body of the plug itself, defining Configuration 1. Once this was complete, the high-viscosity plug liquid fully accommodated the bubble within it (*Fig. 6.4a*, sketch III). Ascent rate and slug morphology became more viscously dominated and burst processes reflected those in high-viscosity fluids (Video V02).

6.3.3 Configuration 2

For experiments in which the plug volume was insufficient to fully accommodate the slug, slug burst occurred with the slug nose within the plug liquid, and the slug base still in the low-viscosity liquid (*Fig. 6.2c*). As for Configuration 1, when the slug arrived at the base of the annulus, it used the intrusion as a pathway through the plug (*Fig. 6.4b*, sketch II; Video V03, 13-16 s) with, at some point, the slug nose entering the high-viscosity plug liquid (*Fig. 6.4b*, sketch III; Video V03, 16 s). At burst, the high-viscosity meniscus disrupted into small droplets (Video V03, 17 s). If the nose of the intrusion had almost reached the plug surface when the slug burst (mainly for 5*D* and 10*D* plugs and 10, 17 and 24 ml slugs), then the burst involved droplets of a mixture of low/high viscosity oil, ejected up the tube.

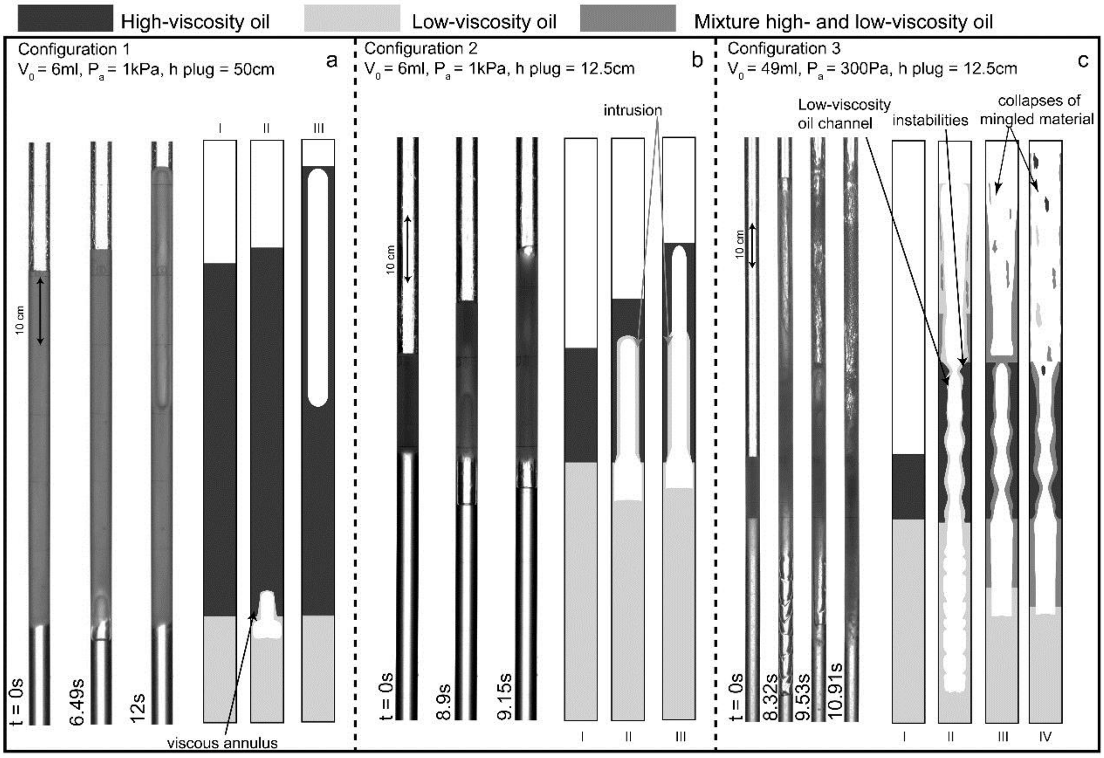

Figure 6.4 Still frames and interpretative sketches from selected experiments representative of the identified flow configurations are shown. (**a**) Configuration 1: as the slug rose, gas expansion drove the intrusion of low-viscosity liquid into the plug (6.49 s); once the transition between the liquids was complete, the slug was fully accommodated within the plug (12 s). (**b**) Configuration 2: the slug exploited the low-viscosity intrusion, enclosed within the viscous annulus, to ascend through the plug (8.9 s). This tri-axial flow comprises ascending gas, descending low-viscosity liquid and, at flow timescale, relatively stationary high-viscosity liquid. At burst: (i) the slug nose was within the viscous plug, (ii) the low-viscosity film and the viscous annulus surrounded the slug main body (tri-axial flow), and (iii) the slug base remained in the low-viscosity liquid below the plug (annulus) base (9.15 s). (**c**) Configuration 3: the low-viscosity intrusion breached the plug top, and the slug burst into the extruded low-viscosity layer (8.32 s); instabilities formed and propagated along the falling film, leading to bubble break-up, partial blockage of the conduit and mixing between liquids (9.53 s). At burst, globules of this mixture fell back on the liquid surface (10.91 s).

6.3.4 Configuration 3

Configuration 3 represents the scenario in which slug expansion is sufficiently large that the low-viscosity intrusion breaches the plug top and emplaces a layer of low-viscosity liquid above the annulus (*Fig. 6.2d*; Video V04, from 5 s onwards). Experimentally, the viscous annulus effectively generated two regions of geometry change for ascending slugs; at the base of the plug, the annulus created a dynamic restriction, whilst at the top, slugs passed back into the low-viscosity liquid only – effectively a dynamic widening (*Fig. 6.4*c, sketch II). The widening enabled the slug nose to accelerate and the abrupt change led to rapid draining of the liquid head around the slug (James et al. 2006). As the increased downward flux of liquid past the slug nose converged at the top of the annulus, the falling film thickened within the annulus, creating a narrowing neck around the slug. If this closed, the gas flow may be temporarily halted as the gas slug was broken into two (*Fig. 6.4c*, sketch III; Video V04, 16-18 s) or, if the processes were repeated, more offspring bubbles. The break-up process, always taking place in < 1 s after the main bubble burst, generated up to 4 offspring bubbles in the experiments, bursting sequentially. We observed also partial restrictions of the gas escape pathway, at a mean frequency of 2 per second.

When the slug nose within the intrusion ascended above the top of the annulus, instabilities formed in the falling film around the slug body due to the dynamic geometry change; these instabilities propagated down the low-viscosity film within the annulus and continuously disrupted the boundary between the two liquids, initiating mingling (*Fig. 6.4c*, sketch II-III). Sometimes, for large gas volumes and thin plugs (1*D* and 2*D*), gas expansion caused rapid intrusion of low-viscosity liquid breaking through the plug: some of the high-viscosity annulus was detached, dragged upward within the low-viscosity liquid above and surrounding the slug body, and mixed into the low-viscosity liquid. As burst progressed, pockets of this mingled mixture were ejected (*Fig. 6.4c*, sketch IV). The burst process was highly variable: it involved bubble oscillations and detachment of the entire meniscus, or bubbles burst without any oscillation, with a complete disruption of the meniscus and droplets ejected high in the tube and followed by several collapses of the film lining the tube wall (Video V04).

6.4 Determination of flow configurations at volcano-scale

To determine the flow configuration (e.g., 1 to 3) for a specific set of parameters, we developed a first-order 1D model to describe slug ascent, expansion and intrusion of liquid into the plug. The model is based on previously used geometrical representations of slug morphology (Vergniolle 1998; Seyfried and Freundt 2000; James et al. 2008, 2009; Del Bello et al. 2012) and, for simplicity, we neglected inertial forces on the liquid above the slug. Such inertial effects can be important when large rates of gas expansion are involved (James et al. 2008, 2009), but expansion rates will be generally reduced by the presence of the plug. Thus although the model will slightly overestimate gas expansion, this simplification is suitable for a model aimed only at estimating the active flow configurations. Furthermore, to retain the first-order approach and avoid the complexities involved with transitional behaviour and slug ascent within the intrusion, the model determines the active configuration no later than the point at which the slug nose reached the original plug base, without considering the full ascent up to slug burst.

The slug is represented as a cylinder of length L and constant radius r_s, ascending in a vertical tube of radius r_c (*Fig. 6.5*). Above the slug, we consider three different sections; the lowest filled by the low-viscosity liquid only, viscosity μ_1 and density ρ_1, of height h_1. The uppermost section represents the viscous plug, with viscosity μ_2, density ρ_2, radius r_c and height h_3. The middle section represents the intrusion of low-viscosity liquid into the high-viscosity plug to form the annulus, with viscosity μ_1 and density ρ_1, length h_2 and radius r_ϕ. The radius r_ϕ is the result of $r_\phi = r_c - r_p$, where r_p is the thickness of the high-viscosity layer against the tube wall which forms the high-viscosity annulus. Due to the evolving nature of the annulus, r_p will vary in space and time. Consequently, in order to provide a characteristic first-order estimate in our straightforward model we assume a thickness as for a falling film surrounding a slug, which can be given as a function of the inverse viscosity, N_f (Llewellin et al. 2012; Supplementary Content):

$$r_p = \left(0.204 + 0.123 \tanh\left(2.66 - 1.15 \log_{10} N_f\right)\right) r_c \qquad (2).$$

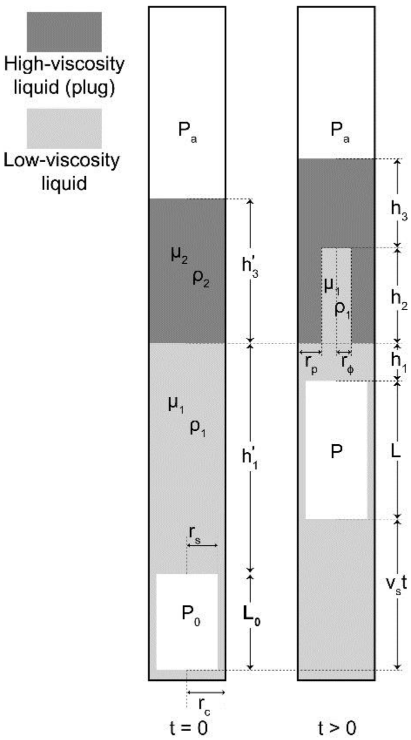

geometrical parameters	
P P_a	ambient pressure
P_0	initial bubble pressure
P	bubble pressure
L_0	initial bubble length
L	bubble length
h_1'	initial height of low-viscosity liquid above the slug
h_3'	initial height of the plug
h_1	height of low-viscosity liquid above the bubble
h_2	height of low-viscosity intrusion
h_3	depth from the plug top to the intrusion
$v_s t$	depth from the bubble base to the tube base
r_c	tube radius
r_s	bubble radius
r_p	viscous annulus radius
r_Φ	intrusion radius
μ_1	viscosity of the liquid beneath the plug
μ_2	plug viscosity
ρ_1	low-viscosity liquid density
ρ_2	plug density

Figure 6.5 The 1D model geometry for a gas slug ascending in a low-viscosity liquid overlaid by a high-viscosity liquid is shown. White regions represent the gas bubble, while grey-scale regions the liquids.

Initial conditions are the height of the low-viscosity liquid above the slug nose, h_1', the height of the plug, h_3', the initial (magmastatic) bubble pressure, $P_0 = \rho g(h_1' + h_3') + P_a$, the slug length, L_0, and radius, $r_s = r_c - \lambda$, where λ is the thickness of the low-viscosity falling liquid film, determined by using equation (2) for the low-viscosity liquid (*Fig. 6.3*).

We assume constant velocity v_s for the slug base, thus, at any time, t, the height of the low-viscosity liquid column h_1 above the slug nose is given by:

$$h_1 = (L_0 - L) - v_s t + h_1' \qquad (3).$$

Equating the intrusion volume to the gas expansion, the height of the low-viscosity liquid intrusion h_2 can be expressed as:

$$h_2 = -A(L_0 - L) \qquad (4),$$

where $A = \frac{r_s^2}{r_\phi^2}$. Conservation of volume for the plug liquid yields:

$$\pi r_c^2(h_3 + h_2) - \pi r_\phi^2 h_2 = \pi r_c^2 h_3' \qquad (5),$$

where h_3 is the distance between the plug top and the intrusion (h_2) top. Simplifying and substituting for h_2, h_3 can be expressed as:

$$h_3 = h_3' + (L_0 - L)(A - B) \qquad (6),$$

where $B = \frac{r_s^2}{r_c^2}$.

The force on the liquid column above the slug due to the pressure difference between the slug and the surface is given by $F_p = \pi r_s^2(P - P_a)$. If the slug behaves like a perfect gas and adiabatic expansion, then $PV^\gamma = constant$ (where γ is the ratio of specific heat), and the slug pressure, with constant radius and pressure P_0 at $t = 0$, F_p can be expressed as:

$$F_p = \pi r_s^2\left(P_0 L_0^\gamma L^{-\gamma} - P_a\right) \qquad (7).$$

The gravitational force is given by $F_g = -\pi r_s^2 \rho h g$, where ρ and h are respectively the density and the height of the involved liquid, and g is the acceleration due to gravity. Finally, assuming no-slip conditions at the wall, the Poiseuille law gives the viscous force for a laminar flow in a cylindrical pipe:

$$F_v = -8\pi\mu h V_f \qquad (8),$$

where μ is the viscosity of the liquid and V_f the flow velocity. If we assume that the liquid flow is equal to the volume flux controlled by the gas expansion, we obtain:

$$F_v = -8\pi\mu h \dot{L} B \qquad (9).$$

Equating the pressure force with the sum of the gravitational and viscous forces for the low-viscosity liquid column above the slug, the low-viscosity liquid intrusion, and the plug, we obtain:

$$\pi r_s^2\left(P_0 L_0^{\gamma} L^{-\gamma} - P_a\right) = -\pi r_s^2 \rho_1 g(h_1 + h_2) - \pi r_s^2 \rho_2 g h_3 - 8\pi \dot{L} \frac{r_s^2}{r_c^2}(\mu_1 h_1 + \mu_2 h_3) - 8\pi \dot{L} \frac{r_\phi^2}{r_c^2} \mu_1 h_2 \qquad (10).$$

Simplifying and substituting for both h_2 and h_3 yields:

$$(P_0 L_0^{\gamma} L^{-\gamma} - P_a) = -g[\rho_1(h_1 - A(L_0 - L))] - g[\rho_2(h_3' + (L_0 - L)(A - B))] - 8\dot{L} r_c^{-2}[\mu_1 h_1 + \mu_2[h_3' + (L_0 - L)(A - B)]] - 8\dot{L} r_\phi^2 \frac{r_c^{-2}}{r_s^2} \mu_1[-A(L_0 - L)] \qquad (11),$$

and finally:

$$\dot{L} = \{-g[\rho_1(h_1 - A(L_0 - L))] - g[\rho_2\left(h_3' + (L_0 - L)(A - B)\right)] + (P_0 L_0^{\gamma} L^{-\gamma} - P_a)\}/\{8 r_c^{-2}\,[\mu_1 h_1 + \mu_2\,[h_3' + (L_0 - L)(A - B)]] + 8 r_\phi^2 \frac{r_c^{-2}}{r_s^2} \mu_1\,[-A(L_0 - L)]\} \qquad (12).$$

The first order differential is solved numerically in *Matlab*, using a Runge-Kutta formula. Due to the imposed initial conditions (in particular, $L = L_0$ at $t = 0$), instabilities may arise in the initial solutions using the Runge-Kutta method. However any initial instabilities, if develop, rapidly dissipate after few iterations without affecting the model solution (for details on the model validation with experimental measurements, see next section). With the focus of the model being to determine flow configurations within the parameter space of a system, it is sufficient to consider the values determined when either the intrusion breaches the plug surface, $h_3 = 0$ (indicating Configuration 3) or when the slug reaches the plug base, $h_1 = 0$. In this latter case, Configuration 1 is identified if there is sufficient plug material to fully encompass the volume of the gas slug, otherwise Configuration 2 is determined.

6.4.1 Model validation

To verify the suitability of equation (12), we compared modelled slug ascent to experimental data representative of each configuration (*Fig. 6.6*). For model inputs, we measured the ascent velocity of the base from the laboratory video, derived the initial slug length directly from the experimental gas volumes, and, to calculate the intrusion radius, assumed the value of the annulus radius equal to a falling film surrounding a slug. For Configuration 1 (*Fig. 6.6a*) and 2 (*Fig. 6.6b*), the model accurately reproduced the variations in position of the slug nose, base and the liquid surface, with the intrusion level always below the plug surface. For Configuration 3

(*Fig. 6.6c*), the model accurately predicted both the timing and position of the plug breach.

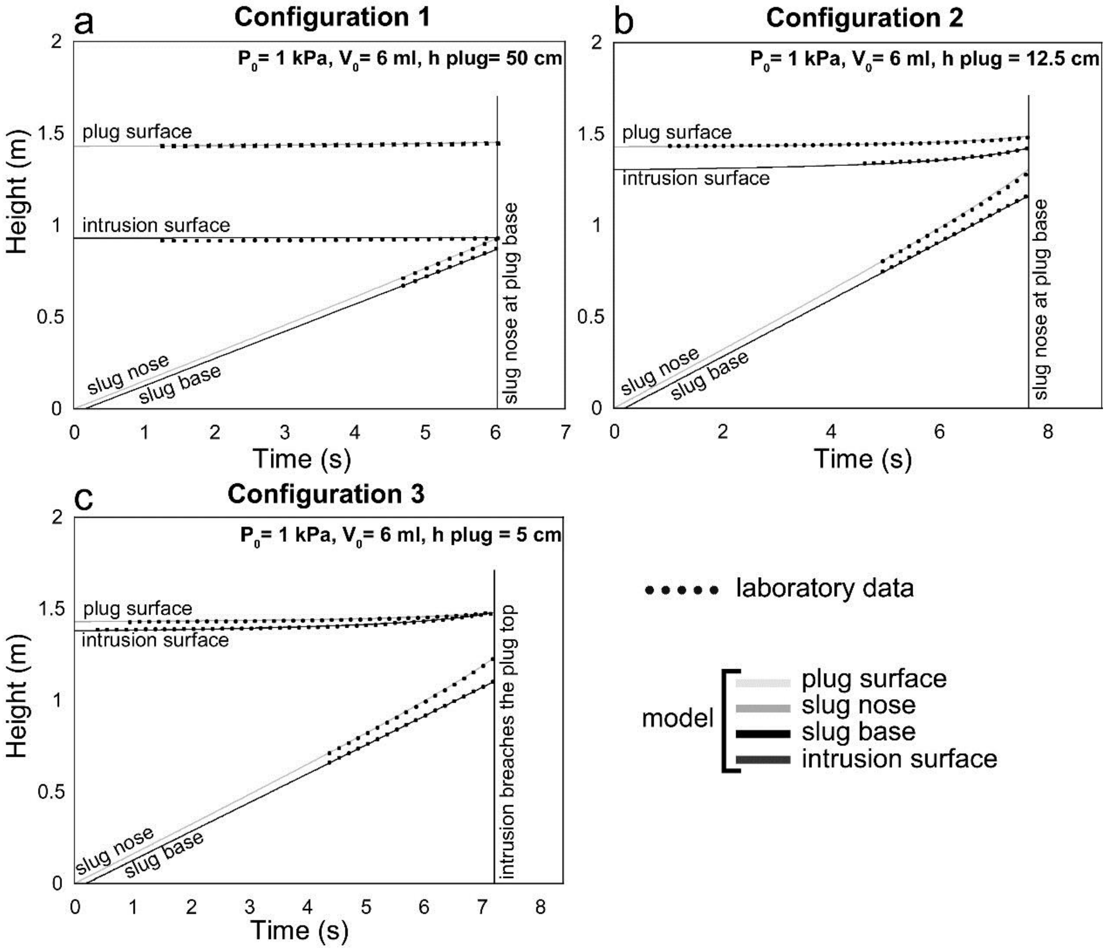

Figure 6.6 Comparison of slug ascent profiles measured from laboratory video (symbols) and the 1D model (lines) for each flow configuration. A 6 ml slug ascends in a liquid column overlain by a plug of 50 cm (Configuration 1; **a**), 12.5 cm (Configuration 2; **b**) and 5 cm (Configuration 3; **c**) with a P_a = 1 kPa. In all cases the variations in position of the plug surface, intrusion surface, slug nose and slug base are well reproduced. For Configuration 3 (**c**), the intersection between the plug and intrusion curves indicates that the low-viscosity liquid breached the plug surface. The comparison with the experimental data is limited up to the moment the simulation stopped. Note that video data for the slug ascent are not available for heights < ~0.5 above the apparatus base, because of the camera field of view.

We neglected the inertial forces in the formulation of equation (12), so gas expansion is slightly overestimated by the model, as well as the intrusion volume, leading to small discrepancies between the laboratory experiments and model results (*Fig. 6.7a*). Larger slugs and rapid gas expansion, resulting in greater intrusion of low-viscosity liquid, cause the model prediction of Configuration 3 or 2 instead of Configuration 2 or 1 respectively. For a conduit filled with two fluids of different densities, a horizontal pressure gradient will develop as soon as the low-viscosity liquid starts to intrude the plug. This has been neglected as there is incomplete understanding of the relationship between fluid exchange and development of horizontal pressure gradients, with no way of parameterising the pressure gradients in terms of the properties of the system (e.g., Becket et al. 2011). However, considering these simplifying assumptions, when compared with the experimental data the model results are in good agreement with the experimental measurements (*Fig. 6.6*) and the model successfully identifies the dominant areas of parameter space for Configuration 1 and 3, separated by Configuration 2.

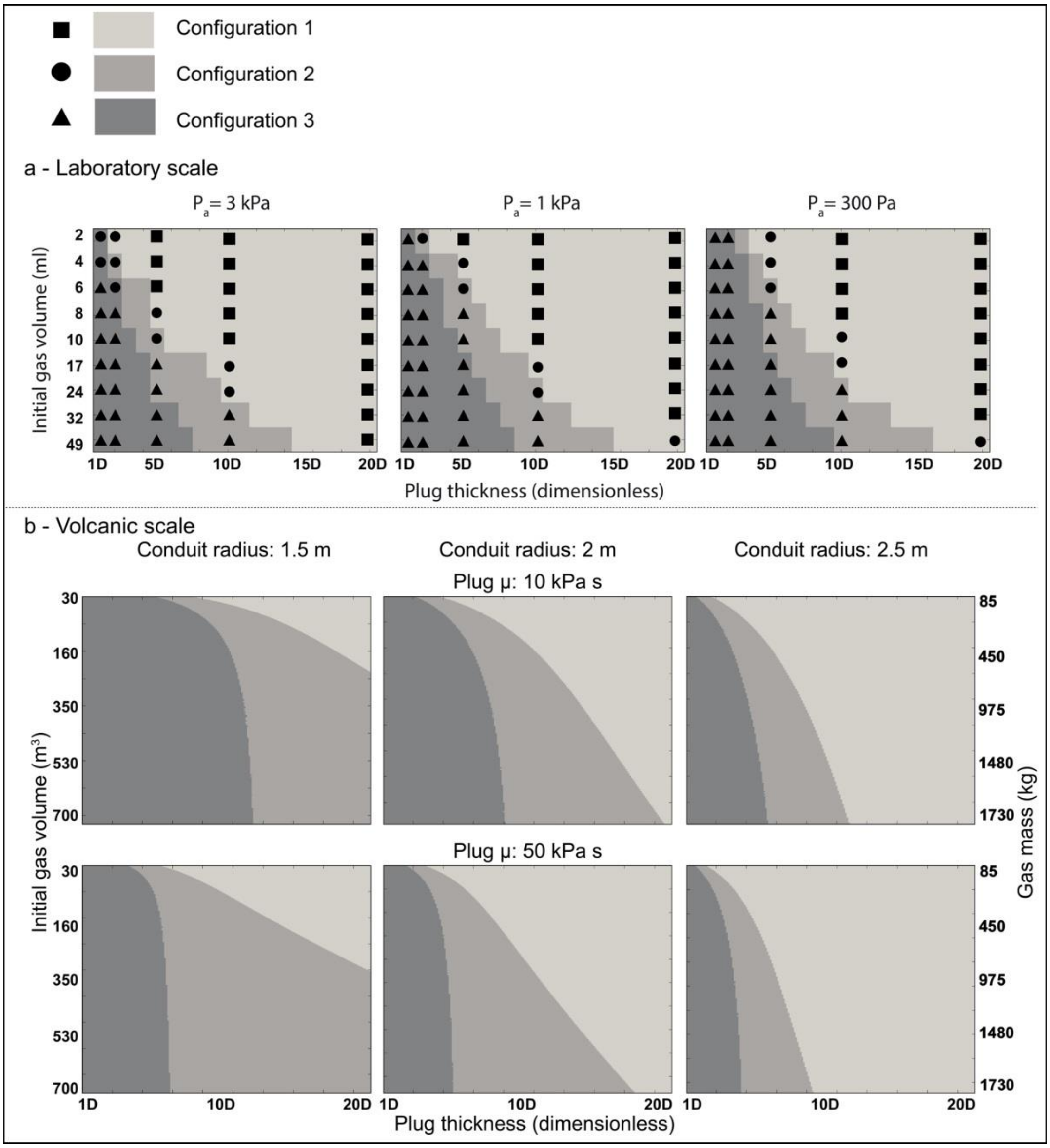

Figure 6.7 (**a**) Comparison between experimental fluid configurations (symbols) and configurations determined by the 1D model (shaded regions) is shown as a function of initial gas volume (ml) and plug thickness (dimensionless), for ambient gas pressures of 3 kPa (left), 1 kPa (middle) and 300 Pa (right). (**b**) Flow configurations determination by the 1D model for an idealised volcanic scenario are shown, for a plug viscosity of 10 kPa s (upper row) and 50 kPa s (lower row), and as a function of initial gas volume (m^3), or gas mass (kg; right axis), plug thickness (dimensionless) and volcanic conduit radii of 1.5 (left), 2 (middle) and 2.5 (right) m; the configuration distribution is insensitive to the viscosity of magma beneath the plug within the limit 50-500 Pa s.

Applying the model to an idealised volcanic-scale scenario (*Fig. 6.7b*) indicated that a similar pattern of flow configurations could be relevant at Stromboli. To corroborate this, we carried out 3D computational fluid dynamics (CFD) simulations using the commercial software Flow3D (James et al. 2008; Chouet et al. 2010; Del Bello et al. 2015).

First, we modelled selected laboratory experiments to validate the CFD model against experimental data, recreating the same experimental conditions (apparatus geometry, injected slug volumes, experimental ambient pressures and plug thickness). The CFD simulations produced results similar to those observed in the laboratory in terms of both flow processes and slug and intrusion shapes (*Fig. 6.8a*, *b*; Video V05). The generation of the viscous annulus and the complex interaction between the two liquids were also accurately reproduced, together with the disruption of the slug and the generation of offspring bubbles and partial blockages of the conduit (*fig. 6.8c*, *d*; Video V05).

Together with the qualitative comparison between observed and modelled processes, to validate the CFD model we also compared modelled to experimental slug ascent velocity, ascent profiles and thickness of the falling liquid film. For laboratory-scale simulations, Flow3D underestimated slug ascent velocities, with a mean value for low-viscosity liquid of ~0.136 m/s against a measured mean value from the laboratory video of ~0.155 m/s. This issue, also reported in James et al. (2008), occurs for Froude number larger than 0.25 (for our silicone oil, Fr = 0.31), and confirmed by the publisher of Flow3D (see James et al. 2008 for details). The curves in figure 6.9 illustrate the ascent of a gas slug – expanding into an experimental ambient pressure of 1 kPa and with a 5D plug – as shown by laboratory data (circles) model data (crosses) and CFD simulation (solid lines). To allow a graphical comparison between the dataset, the CFD velocity was scaled by the ratio of modelled to observed velocities. Figure 6.9 shows that the experimental slug nose, base and liquid surface positions are reproduced accurately by both the 1D configuration model and the 3D flow model.

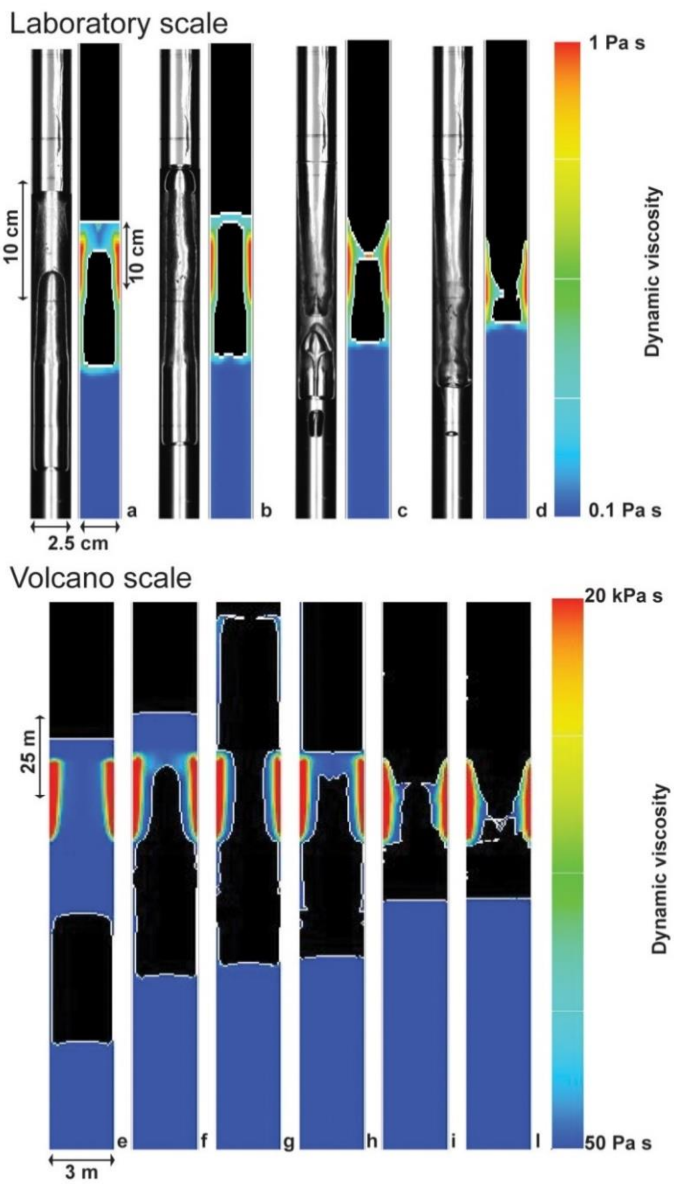

Figure 6.8 (**upper panel**) Still frames from a laboratory experiment and 3D CFD simulation for a 10 ml slug, expanding in a P_a = 3 kPa and a plug h = 12.5 cm (Configuration 3). The CFD simulation reproduced experimental observation well, including the variations in slug shape, intrusion dynamics, burst dynamics and bubble breakup process (see also Video V05). Note the asymmetry in panels **c** and **d** that demonstrate the requirement for full 3D simulation. (**lower panel**) Still frames from a 3D CFD simulation at volcanic-scale. Input parameters are V_0 = 140 m^3, P_a = 10^5 Pa, μ magma = 50 Pa s, μ plug = 20 kPa s, r_c = 1.5 m, column h = 200 m, conduit radius r_c = 1.5 m, conduit h = 300 m, and plug h = 15 m. Note the visible asymmetry that develops once instabilities arise from panel **g** onward, underscoring the requirement for a 3D approach once dynamic instability develops.

Finally, we used equation 2 to calculate the theoretical thickness of the falling film surrounding a slug, λ to be compared with measurements for λ derived from the video and from CFD simulations (for different V_0, P_a and plug thickness). The comparison shows good agreement between results (*Table 6.2*), both at laboratory (comparison between theoretical, modelled and measured λ) and volcanic-scale (comparison between theoretical and modelled λ), further highlighting the good agreement between modelled and experimental results.

Table 6.2 Comparison between theoretical (using equation 2), modelled (measured form 3DCFD simulations) and experimental (measured from videos) falling liquid film thickness, λ

	Laboratory scale		**Volcanic scale**[a]	
λ^b (m)	Laboratory λ (m)	Flow3D λ (m)	λ (m)	Flow3d λ (m)
0.0039	0.0037	0.0036	0.488	0.46
	0.0035	0.0038		0.48
	0.0038	0.0040		0.51
	0.0040	0.0041		0.49

[a] for a plug μ = 20 kPa, ρ = 1300 kg/m^3, conduit radius = 1.5 m.
[b] calculated from equation 4.2 in Llewellin et al. (2012).

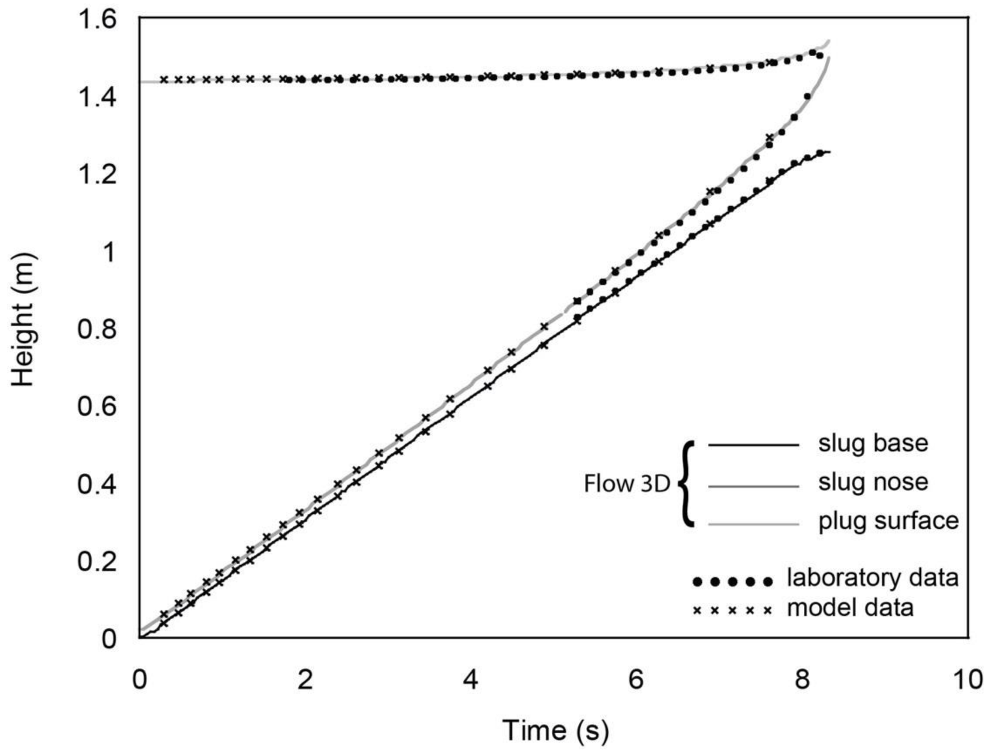

Figure 6.9 Comparison of ascent profiles shown by a laboratory experiment (circles), the 1D model (crosses) and 3D CFD simulation (solid lines) for a 6 ml slug expanding into P_a = 1 kPa, with a plug h = 12.5 cm. Both modelling approaches agree well with the experimental validation data.

For the volcanic scenario, a 300-m-high vertical cylinder with a radius of 1.5 m (for CFD simulations, only this conduit radius was used), closed at the lower boundary, represented the conduit. Although a closed condition was not realistic and more representative of the experimental condition, once a stable slug flow was established in the conduit, this boundary condition did not affect the flow (e.g., James et al. 2008; Chouet et al. 2010). The 200-m-high magma column was modelled as an incompressible Newtonian liquid with a temperature-dependent viscosity and divided into two temperature regions. The first region covered the low-viscosity magma, while the second region defined the plug. Viscosity values ranged between 10-1000 Pa s for the magma beneath the plug and between 1-20 kPa s for the plug, lower than the typical value of Stromboli (1-50 kPa s, Gurioli et al. 2014): exceeding that range resulted in simulation initialisation problems. The gas slug was modelled as a continuous void region (contains no mass) governed by the equation $PV^{\gamma} = constant$.

The volcano-scale simulations, for plug thickness and gas volumes of 3–60 m and 30–250 m^3 respectively, showed changes in slug shape as it enters the annulus (*Fig. 6.8e, f*), and reproduced the generation of instabilities and slug disruption (*Fig. 6.8g-l*). As predicted, the slug transition from a low-viscosity magma to a viscous plug caused a sudden decrease in the slug ascent velocity.

As for the burst process, different dynamics can be associated with the different configurations. Based purely on visual observation of the burst dynamics, Configuration 1 involved a slow fragmentation of the viscous meniscus above the slug, with almost no pyroclast ejection. In Configuration 2 the fragmentation of the magma meniscus was fast and its particles were ejected up to tens of meters above the burst point (note this is a minimum inertial height since no drag from expanding gas is applied). Configuration 3 explosions ranged in style depending on slug volumes, plug thickness, generation of secondary bubbles and blockages of the conduit. In general the burst process seemed characterised by dynamics common to both Configuration 1 and 2, with ejection of material above the burst point but at heights inferior to Configuration 2. Furthermore, most of the ejecta appeared to be mingled and collapsed back in the conduit, creating partial blockages that forced the slug into smaller pockets of gas.

The simulations, showing flow processes similar to those observed in the scaled laboratory experiments, support the applicability of the 1D model and endorse the main roles played by slug volume and plug properties in determining the prevailing flow configuration. The computational fluid dynamics simulations also enabled investigation of the role of the underlying magma viscosity on the complex syn- and post-burst dynamics involved in Configuration 3. A lower viscosity magma drained faster along the conduit/annulus walls, accumulating at the top of the annulus. This promoted the fast and cyclic creation of narrowing necks around the slug. Every time a neck closed, the slug was disrupted, generating offspring bubbles and secondary bursts (pulses). Magma clots were also ejected at greater heights and their collapse produced partial blockages of the conduit, trapping the slug gas into smaller pockets and leading to sub-pulses. For each pulse and sub-pulse, burst depth gradually increased (Video V06, 21-34 s). With increasing magma viscosity, drainage along the conduit walls slowed, with the generation of fewer, or no, pulses but only partial blockages due to collapse of material back into the conduit (Video V06).

6.5 Implications for Strombolian eruptions

Our experiments characterised the spectrum of flow configurations for a set of liquid parameters, tube geometry and for single slug ascent in a rheologically stratified conduit. In our idealised volcanic scenario, both configuration model and CFD simulations indicate the sensitivity of configurations to initial gas volumes and plug properties (*Fig. 6.7b*). For a particular conduit radius, the distribution of configurations in parameter space was insensitive to the viscosity of the magma beneath the plug, which can be considered mainly as a means of delivering the slug into the plug (*Fig. 6.7b*, Video V06). In contrast, conduit radius had a strong influence on configuration transitions. The Configuration 1 domain increased with increasing radius (*Fig. 6.7b*) implying that, for identical magmatic conditions, vents of different radius could erupt with different style.

Under plugged conditions, it appeared both experimentally and numerically that the burst vigour was always greater when compared to an unplugged scenario. As previous models in single-viscosity systems demonstrated, slug overpressure varies with the thickness of the falling film, controlled by magma viscosity (James et al. 2009; Del Bello et al. 2012). Hence, the same initial gas volume burst with a lower overpressure in a low-viscosity liquid (thin film, *Fig. 6.2e*) compared to in a higher viscosity liquid (thick film, *Fig. 6.2a*). This effect occurred in Configuration 1; however, because the slug was initially ascending in a low-viscosity magma, its overpressure also increased due to pressurisation of the conduit below the plug. The greater the plug thickness and viscosity, the more pressure can be retained to be released during a more vigorous burst.

Within Configuration 2, gas expansion intruded a substantial volume of low-viscosity liquid into the plug; the further the intrusion penetrated, the higher the slug can ascend within the low-viscosity channel enclosed within the viscous annulus. The greater thickness of the complex “double” falling film resulted in increased slug lengthening to accommodate gas expansion, opposed by the presence of the un-intruded plug above, and enhancing the generation of overpressure. In Configuration 3, the full development of an open low-viscosity channel through the plug removed the 'capping' effect, allowing the slug to expand more freely and, compared to the other two configurations, reducing slug overpressure. Furthermore, the partial constriction of the tube and the gas slug break-up into smaller pockets produced multiple bursts and modulation of the gas release within Configuration 3.

In support of the role of different flow configurations on slug overpressure, Del Bello et al. (2015) quantified similar effects for their experiments, that can be now categorised as Configurations 1 and 3 (Configuration 2 was not identified). All of their plugged experiments, regardless plug thickness, showed a greater acoustic amplitude and an increase in slug overpressure with respect to the single-viscosity experiments (Figs. 5.3 and 5.4 in Ch. 5, Del Bello et al. 2015). In Configuration 1, Del Bello et al.'s slugs showed a greater increase in both conduit pressurisation during slug ascent and acoustic amplitude at burst compared to slugs bursting in Configuration 3. In Configuration 3, slugs were characterised by a lower overpressure but also by highly variable gas release rates, both in terms of magnitude and time, and generated a range of pressure pulses (burst of offspring bubbles) and sub-pulses (conduit constriction) (Del Bello et al. 2015).

Therefore, for volcanoes where multiple vents are constantly active (e.g., Stromboli and Yasur, Vanuatu), each active vent may be characterised by plugs with different properties, controlling both burst dynamics and explosion magnitude, thus affecting acoustic amplitudes. However, a unique explanation of a particular acoustic amplitude is further complicated because the same gas mass can lead to different flow configurations sensitive to conduit width (*Fig. 6.7b*). Slug parameterisation and the linking of field results and fluid dynamic models, so far based on single-viscosity scenarios suggesting a positive correlation for the burst pressure with both initial slug volume and magma viscosity (e.g., Vergniolle and Brandeis 1996; James et al. 2009; Del Bello et al. 2012; Lane et al. 2013), becomes more poorly constrained with the added degrees of freedom provided by rheological complexity.

6.5.1 Magma mingling

As a result of interactions between the different viscosity magmas, the textural and geochemical properties of the ejected pyroclasts will also depend on the flow processes occurring within the plug. Our experiments reveal that mingling of material may occur in two ways. If the low-viscosity magma intrudes the plug deep enough but without breaching it, the slug approaches the surface surrounded by a low-viscosity magma film, enclosed in turn by the high-viscosity annulus forming a tri-axial flow (Del Bello et al. 2015), i.e., at the boundary of Configuration 2 with 3. At burst, the fragmenting meniscus will comprise layers of both low- and high-viscosity magma, promoting mingling and ejection of mingled pyroclasts. However, with only the meniscus region involved, mingling is expected to be a relatively localised process. A more extended mingling occurs within Configuration 3 (*Figs. 6.2d* and *6.4c*), where: (a) globules of the annulus are mixed into the low-viscosity liquid during rapid intrusion and (b) flow instabilities (also observed by Del Bello et al. 2015) produce cyclic collapses of the low-viscosity film which, in turn, initiate a broader mingling with the high-viscosity liquid of the annulus within the tri-axial flow. The same instabilities are responsible for slug break-up and for creating partial blockages in the conduit that force the slug into smaller pockets. The effect is a pulsatory bursting with these processes coexisting. Both laboratory observations (Video V04, V07) and, particularly, CFD simulations for Stromboli (Video V06) showed that the secondary burst depths changed with time. Initially, the slug burst in the low-viscosity magma above the plug. Slug break-up then occurred at the top of the viscous annulus and secondary bubbles and transient gas pockets burst inside a region of mingled material or within the plug, with the burst depth gradually increasing. Ejected material was, therefore, scavenged at increasing depth with time, sampling different regions of the complex collapsing liquid structure. Physical changes in magma should then occur at two different scales, and the level of mingling could help in determining the flow configurations. If mixing occurs mainly during slug ascent (Configuration 3), mingling is a predominant process, likely showing, e.g., the coexistence of different vesicle populations. In contrast, the lower the mingling in the ejecta, the more restricted is the process, reflecting a possible mingling only at burst, during magma fragmentation (Configuration 2). Analysis of the mingling textures within ejecta from a Strombolian eruption could, therefore, provide evidence of the near-surface flow dynamics within the conduit.

6.5.2 Pulsatory behaviour

At Stromboli, Gaudin et al. (2014) related individual pyroclast ejection pulses to successive pressure release pulses and sub-pulses of duration between 0.05–2 s and an average pulse rate of 7 per second, with a minimum of 3 up to 120 pulses per eruption. As a general trend, with some exceptions, the greater the number of pulses and sub-pulses, the longer the explosions, with greater gas masses involved (Gaudin et al. 2014). In our experiments, secondary bursts (pulses), followed by several partial blockages (sub-pulses) of the gas path, were achieved only in Configuration 3, with their larger number resulting from the disruption of larger gas volumes (24–49 ml). Smaller volumes (8–17 ml) generated offspring bubbles, without any sub-pulses, and shorter burst times. With these volumes scaled to the volcanic-case, CFD simulations showed the same positive correlation between volumes and number of pulses and sub-pluses as measured in the experiments. Although no formal scaling exists for these processes at laboratory-scale, the trend observed in both laboratory and CFD simulations is similar to the one derived from field observations, also suggesting the presence of a plug as a pre-requisite for pulsatory behaviour. Furthermore, CFD simulations showed that greater initial gas volume and lower viscosity of the underlying magma favour secondary bursts from offspring bubbles and sub-pulses generated by partial blockages of the conduit, while a higher viscosity led mainly to sub-pulses (restriction of gas escape pathway), with the generation of fewer, or no, secondary bubbles (blockage of gas escape pathway; Video V06). Hence, while not measurably affecting the pre-burst processes, the viscosity of the underlying magma can noticeably influence syn- and post-burst dynamics and therefore any measured geophysical signals.

6.6 Conclusions

Based on scaled laboratory experiments we define a framework to describe the characteristic styles of the flow organisation involved with the ascent and burst of slugs in a rheologically stratified conduit, where a high-viscosity plug overlies a low-viscosity magma. Conduits that are fully filled with either high- or low-viscosity magma represent end-member scenarios that can be considered as infinitely thick or thin high-viscosity plugs respectively. In between, our experiments demonstrated three fundamental flow configurations, determined by the ratio of plug size and slug gas volume. In Configuration 1, the plug was sufficiently large to fully accommodate the ascending slug. In Configuration 2, a smaller plug was sufficient to accommodate the volume change due to expansion of the slug on ascent, but not the full volume of the slug. Consequently, when the slug burst at the surface of the plug, its base was still in the low-viscosity liquid. Finally, in Configuration 3, slug expansion drove an intrusion of low-viscosity liquid right through the plug, enabling slug burst to occur within the low-viscosity liquid, with the plug acting only as a region of effectively reduced conduit diameter.

We developed a model, validated with the laboratory experiments and by 3D CFD simulations at volcano-scale, to explore configuration parameter space. Our results showed how gas volume, plug thickness and plug viscosity were the key parameters controlling the transitions between different configurations; transitions were much less sensitive to properties of the underlying magma. Each configuration encompassed a variety of processes: dynamic narrowing and widening of the effective conduit, generation of instabilities along the falling liquid film, transient blockages of the slug path and slug break-up. These complexities influenced the slug ascent dynamics and gas overpressure at burst, and thus also the resulting eruptive style and, by implication, geophysical signals.

The complex flow processes can also promote magma mingling, not only by fragmentation of a rheologically layered meniscus but also through instabilities in the falling film and surrounding fluid annulus, leading to more localised or distributed regions of mingling respectively. In Configuration 3, flow instabilities cause a narrowing of the gas escape pathway causing sub-pulses within the eruption process. The flow instabilities can be sufficient to seal the gas escape pathway and cause slug break-up through the creation of transient blockages, resulting in a pulsatory, multi-bubble burst process. A widening of the conduit was needed for the slug break-up and falling film collapses, and both the viscosity of the underlying magma and the gas volume seemed to determine the frequency of pulses and sub pluses.

Our results showed how these flow configurations can influence eruption vigour, style and pyroclast properties. The configuration framework should be considered when interpreting slug-burst related geophysical signals, and points the way to more detailed links between fluid dynamic models and acoustic signals.

6.7 Video description

Videos **V01**, **V02**, **V03** and **V04** show the flow processes occurring during slug ascent, expansion and burst in the following experiments: (**V01**) Single and low-viscosity system, plug h = 0 cm (0D), P_a = 1 kPa, V_0 = 6 ml; (**V02**) Configuration 1, plug h = 50 cm (20D), P_a = 1 kPa, V_0 = 6 ml; (**V03**) Configuration 2, plug h = 12.5 cm (5D), P_a = 1 kPa, V_0 = 6 ml. (**V04**) Configuration 3, plug h = 12.5 cm (5D), P_a = 300

Pa, V_0 = 49 ml. Video **V05** shows the comparison between a laboratory experiment and a CFD simulation for a 10 ml slug, P_a = 3 kPa and plug h = 5 cm (2D); frame rate of the laboratory video has been accelerated to allow an easier video comparison. Video **V06** shows the comparison between three different CFD simulations at volcanic-scale, for the same gas volume, V_0 = 140 m^3, ascending in a 300-m-high volcanic conduit of radius 1.5 m, filled with magma beneath the plug (plug h = 15 m [5D]) of viscosities 50 (left), 150 (middle) and 300 (right) Pa s. Video **V0**7 contains a sequence of the bubble break-up process from an experiment of a 24 ml slug, P_a = 3 kPa and plug h = 12.5 cm (5D).

6.8 Acknowledgments

This research is part of A.C. PhD at Lancaster University, funded by the People Programme (Marie Curie Actions) of the European Union's Seventh Framework Programme (FP7/2007-2013) under the project NEMOH, REA grant agreement n° 289976. We thank Kathy Cashman and Sylvie Vergniolle for thorough and constructive comments that greatly improved the manuscript, and the editor Bernard Marty.

Supplementary Content

In the supplementary material, we provide additional details on the scaling relationships between the volcanic scenario, laboratory experiments and CFD model.

6.9 Scaling considerations

A well-established parameterization exists for describing the behaviour of an ascending, constant-length slug in a tube filled with a liquid, through a series of dimensionless numbers: the Morton (*Mo*), Eötvös (*Eo*), Froude (*Fr*), Reynolds (*Re*) numbers and the inverse viscosity N_f (e.g., White and Beardmore 1962; Wallis 1969; Viana et al. 2003; Llewellin et al. 2012; Del Bello et al. 2012). At volcanic scale, surface tension plays a negligible role (e.g., Seyfried and Freund 2000; Llewellin et al. 2012), and the ascent of a slug is controlled by the balance of inertia and viscosity, parameterized through the inverse viscosity N_f

$$N_f = \frac{\rho}{\mu}\sqrt{gD^3} \qquad \text{(S1)},$$

where ρ and μ are the density and viscosity of the liquid, g is the gravitational acceleration and d is the tube diameter.

For an idealised volcanic scenario, we considered magma viscosities between 10–50 kPa s and density of 1300 kg/m^3, and between 50–500 Pa s and 900 kg/m^3 for a possible plug and the underlying magma respectively (e.g., Gurioli et al. 2014). This gives N_f values ~4.5 to ~0.91 for the plug and ~630 to ~63 for the fresh magma, for a 2.5 m volcanic conduit (*Table 6.3*). For a diameter of the experimental tube of d = 0.025 m, we obtain N_f values of ~12 and ~122 for the optimised experimental liquids of castor oil (μ = 1 Pa s, ρ = 961 kg/m^3) and silicone oil (μ = 0.1 Pa s, ρ = 990 kg/m^3) respectively. In both cases, these values lie in regions of the flow regime where the slug ascent is under dominant viscous control in the plug, but with a significant degree of inertial contribution within the low viscosity liquid, with the transition between regimes around $N_f \approx 100$ (Llewellin et al. 2012).

The dimensionless thickness of the falling liquid film, $\lambda' = \lambda/r_c$, can be expressed as an empirical function of N_f (Llewellin et al. 2012):

$$\lambda' = \left(0.204 + 0.123\tanh\left(2.66 - 1.15\log_{10} N_f\right)\right)r_c \qquad \text{(S2)}.$$

For the 1D model, the value of the annulus radius, r_p, used to calculate the intrusion radius, was assumed equal to a falling film surrounding a slug, λ. This first-order approximation was supported by the agreement – within measurements error –

between measurements for r_p derived from the video and from CFD simulations (for different V_0, P_a and plug thickness) and the prediction of λ, derived from equation (S2) from Llewellin et al. (2012); this also applied for the volcanic case (*Table 6.2*).

From equation (S2), we can then determine the fraction of the tube cross-section occupied by the falling film, *A'* (James et al. 2009; Del Bello et al. 2012)

$$A' = \lambda'(2 - \lambda') \quad \text{(S3).}$$

Table 6.3 Summary of volcano-scale parameters

Conduit radius		***Underlying magma***				***Plug***		
	Column height (m)	200						
	Density (kg/m^3)	900				1300		
	Viscosity (kPa s)	0.05	0.15	0.3	0.5	10	20	50
1.5 m	**Ascent velocity v_s (m/s)**	1.8	1.63	1.37	1.09	0.11	0.06	0.02
	Inverse viscosity N_f	293	98	49	29	2.11	1.06	0.4
	Slug radius (m)	1.22	1.13	1.08	1.05	1.013	1.011	1.01
2 m	**Ascent velocity v_s (m/s)**	2.1	1.98	1.78	1.53	0.2	0.10	0.04
	Inverse viscosity N_f	451	150	75	45	3.2	1.62	0.65
	Slug radius (m)	1.68	1.55	1.48	1.43	1.355	1.35	1.347
2.5 m	**Ascent velocity v_s (m/s)**	2.36	2.28	2.12	1.91	0.31	0.16	0.06
	Inverse viscosity N_f	630	210	105	63	4.55	2.2	0.9
	Slug radius (m)	2.15	1.99	1.9	1.83	1.696	1.689	1.685

6.9.1 Slug Ascent velocity

Slug base ascent velocity, v_s, required for the 1D model, was evaluated using the well-established dimensionless relationship from Wallis (1969), where v_s is expressed as:

$$v_s = Fr\sqrt{gD} \quad \text{(S4),}$$

where *D* is the internal diameter of the conduit and *Fr* the dimensionless Froude number, expressed with the simplified equation of Viana et al. (2003) from Llewellin et al. (2012):

$$Fr = 0.34\left[1 - \left(\frac{31.08}{N_f}\right)^{1.45}\right]^{-0.71} \quad \text{(S5).}$$

Applying equations (S4) and (S5) to our experimental condition, with N_f ~122 for the low-viscosity oil, gives us v_s of 0.153 m/s, in agreement – within measurement errors – with the measured values from the video of ~0.155 m/s. For the considered volcanic parameters and depending on conduit radius, slug ascent velocities are in the range ~0.7 – ~2.4 m/s, while velocity decreases considerably in the high-viscosity plug, ranging between ~0.02 – ~0.31 m/s (*Table 6.2*).

Table 6.4 Comparison between laboratory measurements for the annulus radius, r_p, and thickness of the liquid film for the plug liquid, λ.

Laboratory scale			**Volcanic scale**[a]	
λ^b (m)	Laboratory r_p (m)	Flow3D r_p (m)	λ (m)	Flow3d r_p (m)
0.0039	0.0037	0.0036	0.488	0.46
	0.0035	0.0038		0.48
	0.0038	0.0040		0.51
	0.0040	0.0041		0.49

[a] for a plug μ = 20 kPa, ρ = 1300 kg/m^3, conduit radius = 1.5 m.
[b] calculated from equation 4.2 in Llewellin et al. (2012).

6.9.2 Slug volumes

Erupted gas volumes at atmospheric pressure for a typical Strombolian eruption have been estimated through several field methods. Vergniolle and Brandeis (1996) estimated volumes between 2 and 200 m^3, by fitting synthetic acoustic waveforms to real signals from 36 eruptions at Stromboli. Following the same approach, Ripepe and Marchetti (2002) measured gas volumes between 20–35 m^3 for a series of eruptions at the NE and SW crater zone respectively. Chouet et al. (2003) inferred volumes of 6.8 × 10^3–21 × 10^3 m^3 from seismic signals measurements. SO_2 measurements conducted by Mori and Burton (2009) yield volumes of 1.5–4.1×10^3 m^3.

For the experimental injected volumes, the dimensionless number V_a' is expressed as:

$$V_a' = V_a \frac{\rho g}{\pi r_c^2 P_a} \quad \text{(S6),}$$

(equation 18 in Del Bello et al. 2012), where V_a is the volume that the slug would have at ambient pressure. This gives us V_a' = 0.08–2, V_a' = 0.6–14 and V_a' = 6–152 for experimental P_a of 3 kPa, 1 kPa and 300 Pa respectively. Scaled to the volcanic case, these values represents erupted volumes at atmospheric pressure of 4–90 m^3, 28–690 m^3 and 300–7300 m^3, covering the range of erupted gas volumes at atmospheric pressure involved during normal Strombolian activity. Note that the dimensionless parameter V_a' is derived from a model developed in a single-viscosity system (Del Bello et al. 2012).

6.10 Transitional behaviours

We considered, as end-members of the identified flow configurations, a conduit fully filled with either high- or low-viscosity liquid (*Fig. 6.10a*, *e*). Between these single-viscosity end-members, three main configurations existed (Configuration 1-3; *fig. 6.10b-d*), occasionally separated by transitional behaviours.

The extent of the low-viscosity intrusion was controlled by the slug expansion and the plug thickness. A transitional case between Configuration 1 and 2 existed for large gas volumes, where gas expansion can be sufficiently large to drive the low-viscosity intrusion deep enough into the plug, but without breaching it. Once the slug moved into the plug, the plug volume was barely sufficient to accommodate both the slug and the intrusion volumes. At burst, the bubble was surrounded for almost its entire length by a low-viscosity film enclosed by the annulus, with its base at the same depth of the base of the annulus (*Fig. 6.10f*).

Similarly, between Configuration 2 and 3, the low-viscosity intrusion can reach the top of the plug. Then, the intrusion: 1) breached the plug top just before the burst, without spilling any low-viscosity liquid above it, or 2) breached the plug starting to emplaced liquid above it, but without being able to create a fully developed layer before the burst. At burst, the slug body was completely surrounded by low-viscosity film and by the viscous annulus, with the base still in the low-viscosity liquid (*Fig. 6.10g*)

As for Configuration 3, when large volumes and thin plugs (1*D* and 2*D*) were involved, the intrusion can break through the plug, detaching some of the high-viscosity annulus and mixing it into the low-viscosity liquid (*Fig. 6.10h*) or - rarely – a thin plug (1*D*) can be completely torn apart and its remnants dragged on the top of the low-viscosity liquid within both the liquid surrounding its body and the liquid head above its nose.

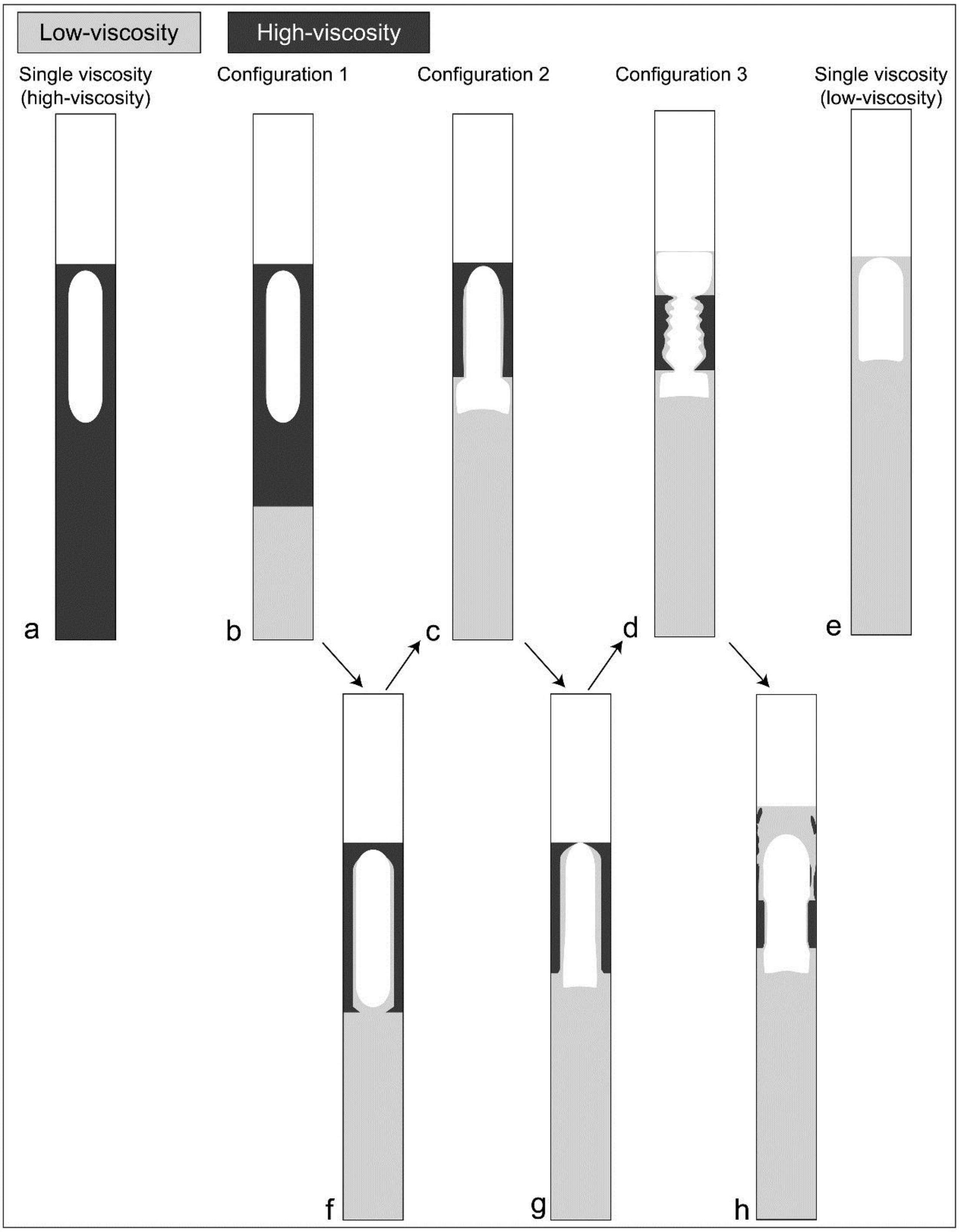

Figure 6.10 Conceptual sketches for single high- (**a**) and low-viscosity (**e**) end-members, Configurations 1 (**b**), 2 (**c**) and 3 (**d**), and transitional behaviours. Transition between Configuration 1 and 2 (**f**) may involve a deep intrusion of low-viscosity liquid, with the plug volume barely able to accommodate both slug and intrusion volumes. If the intrusion breached the plug top just before the burst, we were in between Configuration 2 and 3 (**g**). For Configuration 3, part of the viscous annulus can be detached by the intrusion, and brought to surface within the liquid surrounding and above the slug (**h**).

6.11 CFD model

3D computational fluid dynamic simulations were carried out using the commercial software Flow3D. A 200-m-high column of magma filled a 300-m-high vertical, rigid conduit. The low-viscosity magma and the viscous plug were modelled filling the conduit with an incompressible Newtonian liquid column with a temperature dependent viscosity, divided in two temperature regions. The first region defined the low viscosity magma, from the base of the conduit up to the desired plug base height; the second region defined the plug, covering all its height. To reduce the effect of heat transfer across the magma column, a thermal conductivity of 10^{-8} W m^{-1} K^{-1} (i.e., negligible) was imposed. To avoid artefacts that were created from the symmetry simplifications required for 2D modelling, simulations were carried out in full 3D, solving the flow over a Cartesian mesh of 32 × 32 × 704 cells in *x*-*y*-*z*.

For the volcanic scenario, viscosity values ranged between 10 and 1000 Pa s for the magma beneath the plug and between 1 and 20 kPa s for the plug. These values give us N_f of ~1460 down to ~14 for the low-viscosity magma, and ~21 down to ~1.05 for the plug. For modelling purposes, the initial volume of the slug was scaled for the volcanic case using the non-dimensional parameter V_a' (Del Bello et al. 2012, 2015).

Chapter 7 - Gas slug ascent in a stratified magma: implications of acoustic and seismic source mechanism in Strombolian eruption

Antonio Capponi, Steve J. Lane, Mike R. James

Lancaster Environment Centre, Lancaster University, Lancaster LA1 4YQ, UK

Paper in preparation

Chapter 6 (Capponi et al. 2016a) illustrated how, for a gas slug ascending through a rheologically stratified magma column, the flow can be organized in three main flow configurations. Each configuration encompasses processes that affect slug expansion and burst, potentially leading to variations in eruption magnitude and, therefore, in any measured geophysical signal.

This manuscript seeks to explore the link between the fluid-dynamics processes identified for each flow configuration on pressure variations, and the possible implications for the interpretation of Strombolian explosions.

The results show that a plug, regardless of its thickness, always hinders gas expansion. Each configuration leads to distinct rates of change of gas slug growth and volumetric expansion, also reflected on the subsequent magma acceleration. Changes in the inflation-deflation sequences observed at the vents of Strombolian-type volcanoes may then depend on how the properties of the magmas and initial gas volumes (i.e., flow configurations) control gas expansion and ascent.

Acoustic amplitudes are also strongly dependent on the flow configuration in which the slugs burst. Both acoustic peak amplitudes and waveforms seem to reflect different burst dynamics. Laboratory waveforms compare well with measured infrasonic signals from Stromboli, suggesting that a slug expanding and bursting through a plug could represent a plausible source mechanism for infrasonic signals. Furthermore, the presence of a plug seems to be a pre-requisite for the pulsatory behaviour recently observed at Stromboli.

Antonio Capponi: carried out the experimental campaign, data processing, 3D CFD simulations and wrote the manuscript.

Steve J. Lane: contributed to discussions, reviewed the manuscript, proposed the original idea for the experiments and obtained grant funding.

Mike R. James: contributed to discussions, reviewed the manuscript, proposed the original idea for the experiments and obtained grant funding.

Abstract

Strombolian activity is explained in terms of large pockets of gas ascending and bursting at the surface of a low-viscosity magma. However, field measurements and textural analyses suggest that a region of degassed and more viscous magma exists at the top of the conduit, acting as a plug. Based on this hypothesis, recent experimental and numerical investigations showed that the flow within a rheologically stratified conduit can be organised in three main flow configurations depending on the ratio of plug size and slug volume. Each configuration encompasses processes affecting in different degree gas ascent, expansion and burst, which represent the main source mechanisms for infrasonic and seismic signals. Here we investigate the link between these flow processes and pressure changes, which occur in two main phases. (1) The slug ascent within the low-viscosity liquid and its transition from the low-viscosity liquid into the high-viscosity one generate distinct sequences of pressurization-depressurization, related to different rates of changes of gas bubble growth and volumetric expansion. This suggests that, in a volcanic system, localized ground-deformations may depend on how the flow configurations control the slug growth and magma acceleration. (2) At burst, flow configurations control burst dynamics and acoustic peak amplitudes. The rate of change of the excess pressure within the experimental tube can be used to generate synthetic infrasonic signals. The same gas volume for different flow configurations produces synthetic waveforms resembling infrasonic waveforms acquired at different vents at Stromboli, characterized by different eruptive activity. Thus, the slug-plug interaction may represent a viable first-order mechanism for infrasonic signals at Stromboli. Furthermore, the variability observed in the infrasonic waveforms and eruptive activity may not be caused only by variations in gas volumes and overpressure but also by variations in slug frequency. High-frequency slug ascents could favour the generation of a pathway within the plug, resulting in complex eruptions characterized by longer and more complex infrasonic signals, reflecting a longer mass discharge process and variable gas release rates. A slower slug frequency, instead, can allow the formation of a uniform plug, which thickness and, thus, flow configuration and resulting infrasonic signal, depends on the interval time between each slug.

Keyword
Eruption dynamics; slug flow; plugged conduit; volcano infrasonic; volcano seismicity; analogue experiments

7.1 Introduction

Acoustic and seismic surveillance is regularly performed at Stromboli and several Strombolian-type volcanoes worldwide, providing data to constrain fluid-dynamic processes in the conduit and physical parameters of large gas pockets (*slugs*). Gas slug rise, expansion and burst at the surface provide a plausible explanation for Strombolian explosions (Chouet et al. 1974; Blackburn et al. 1976). Slug expansion is the main source mechanism generating pressure pulses that propagate in the atmosphere as infrasonic signals, with amplitude being a function of slug volume and overpressure (e.g., Vergniolle and Brandeis 1996; James et al. 2009; Lane et al. 2013). At Stromboli, different vents have characteristic infrasonic signatures (Ripepe et al. 2001, 2002; McGreger and Lees 2004), reflecting different eruption mechanisms, with magma viscosity and gas overpressure controlling the transition between passive, transitional or explosive regimes (James et al. 2009; Lane et al. 2013). Seismic signals seem to relate to perturbations in the flow pattern when slugs pass through discontinuities in the conduit, e.g., changes in conduit geometry or inclination (Chouet et al. 2003, 2008; James et al. 2004, 2006). Ground displacements also occur, showing a sequence of inflation-deflation cycles associated with pressure variations in the conduit related to gas bubble growth and magma acceleration prior the explosion and following release of the gas-pyroclast mixture to the atmosphere (e.g., Genco and Ripepe 2010; Lyons et al. 2012).

Interpretation of the geophysical signals associated with explosive activity has often relied on models of a gas slug ascending and bursting in a rheologically uniform low-viscosity magma, in line with the canonical Strombolian paradigm. Nowadays, such simplified models cannot explain new field and textural evidence (e.g., Lautze and Houghton 2005, 2006; Colò et al. 2010: D'Oriano et al. 2011; Taddeucci et al. 2012; Gurioli et al. 2014; Gaudin et al. 2014) that points to the coexistence in the shallower conduit of two rheologically distinct melts, with the higher viscosity magma acting as a plug atop the low-viscosity one (e.g., Gurioli et al. 2014). Recent experimental and numerical investigations (Del Bello et al. 2015; Capponi et al. 2016a) revealed that, as the gas slug ascended, expanded and burst within a rheologically stratified magma column, the flow can be organized in three distinct and complex configurations depending on the relative slug and plug sizes. A slug can burst (1) after being fully accommodated within the plug volume (Configuration 1), (2) at the surface of the plug, whilst its base is still in the low-viscosity liquid (Configuration 2) or (3) within a low-viscosity layer emplaced above the plug (Configuration 3; Capponi et al. 2016a). Each configuration encompasses a variety of processes: dynamic narrowing and widening of the conduit, instabilities within the falling liquid films, transient partial blockages of the slug path and slug disruption. These complexities can influence slug expansion, burst dynamics and explosion vigour (Del Bello et al. 2015; Capponi et al. 2016a), and thus potentially affect the resulting eruptive style and geophysical signals (e.g., Johnson and Lees 2000; Lyons et al. 2012).

Previous laboratory investigations of slug ascent, expansion and burst in single-viscosity systems provided a plausible first-order mechanism for the generation of seismic and acoustic signals (e.g., Vergniolle and Brandeis 1996; James et al. 2004, 2009; Kobayashi et al. 2010; Lane et al. 2013). Initial experimental work in a layered system showed how the presence of a plug can increase eruption explosivity and the variability of infrasonic signals (Del Bello et al. 2015). Now, to better understand the link between flow processes in a rheological stratified conduit and pressure variations, and how a viscous plug transforms geophysical signals, a more detailed comparison between geophysical and experimental data is needed. Here, we build on the description of the fluid dynamics involved in each flow configuration detailed by Capponi et al. (2016a) and extend our analysis to link the effects of the processes encompassed by each configuration on pressure variations within liquid and gaseous phases. We then explore the possible implications for Strombolian eruptions.

7.2 Methods

The experiments described in Capponi et al. (2016a) detailed the fluid dynamic processes of a gas slug ascending, expanding and bursting in a 3-m-high tube filled with a column of Newtonian oil (silicone oil *AS100*, viscosity μ = 0.1 Pa s, density ρ = 990 kg/m^3) overlain by a layer of greater viscosity oil (castor oil, μ = 1 Pa s, ρ = 961 kg/m^3), varied in thickness (*Fig 7.1*; Capponi et al. 2016a).

Experiments were carried out under reduced ambient pressure P_a (3 ± 0.1 kPa, 1 ± 0.1 kPa and 300 ± 0.1 Pa) in order to scale for gas expansion (James et al. 2008).

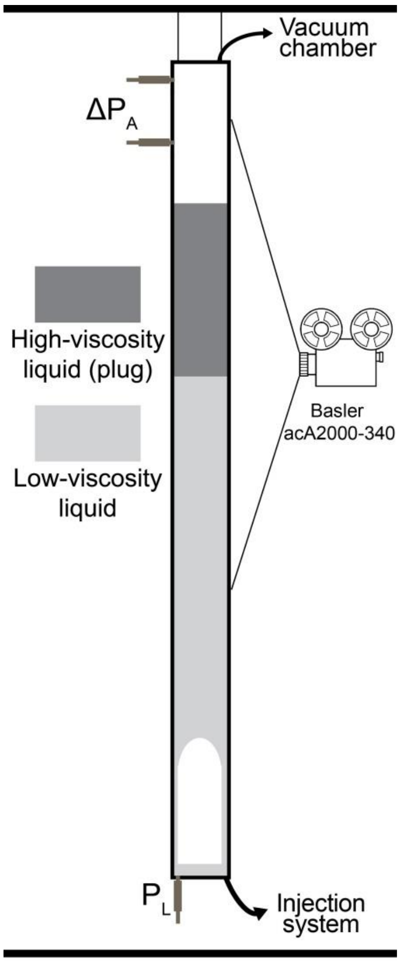

Figure 7.1 The experimental apparatus comprised a 3-m-high vertical tube, with a diameter D = 0.025 m, connected to a vacuum chamber and a gas injection system. Pressure variations were measured within the liquid, at the bottom of the apparatus, by a pressure sensor (P_L) and above the liquid in the ambient air by two differential pressure transducers (ΔP_A). Slug ascent, expansion and burst through the experimental liquids were imaged with a high-speed camera at 300 fps.

Known volumes of gas (ranging between 2 ± 0.1 ml and 49 ± 0.1 ml) were injected at the base of the apparatus. Plug thickness was non-dimensionalised as a function of the tube diameter (D = 0.025 m), and ranged between ~2.5 (1D) cm up to ~50 (20D) cm (Capponi et al. 2016a). For the prevailing liquid parameters and apparatus geometry, slug ascent is mainly controlled by viscous forces for the plug and by viscous forces with a significant degree of inertial contribution for the silicone oil. A BOC Edwards ASG 2000 sensor measured the pressure within the liquid at the base of the apparatus (P_L). At the top, the apparatus was connected to a vacuum chamber and pressure changes in the air above the liquid surface with respect to the vacuum chamber pressure (ΔP_A) were measured with two Honeywell differential pressure transducers 163PC01D75. Each experiment was imaged with a Basler high-speed camera acA2000-340km at 300 ± 0.1fps. All sensors were logged at 5 kHz by a 16-bit National Instrument DAQ board. All the transducer data and high-speed video were recorded through LabVIEW 2014 software, which directly relates each image frame to the pressure data.

7.3 Flow configurations

The experiments revealed three main flow configurations, bracketed between end-member scenarios of a tube fully filled with either high- or low-viscosity liquid (*Fig. 7.2a*, *e*). The transition between configurations was a function of the lengths of the high-viscosity plug and gas slug. Here we summarise the main process involved with each flow configuration (for details, see Capponi et al. 2016a).

7.3.1 Configuration 1

As the slug ascended in the low-viscosity oil, gas expansion drove an intrusion of low-viscosity liquid into the plug. The intrusion distributed the plug liquid along the tube, forming a viscous annulus around it that acted as a dynamic diameter reduction. As the slug nose entered the annulus, the area of the tube occupied by the slug decreased and its length increased. First, the slug used the intrusion as a pathway through the plug; then, at some point, it moved from within the low-viscosity intrusion to within the plug liquid. As soon as the slug base was in the plug, the plug fully accommodated the entire slug volume (*Fig. 7.2b*).

7.3.2 Configuration 2

If the plug was not sufficiently large to accommodate both the intrusion and the slug volumes, the slug burst with its nose within the plug, whilst its base was in the low-viscosity liquid. Gas expansion drove a greater amount of liquid into the plug compared to Configuration 1, and as a result, a low-viscosity falling liquid film was enclosed within the annulus surrounded the slug body, further reducing the area of the tube occupied by the slug (*Fig. 7.2c*).

7.3.3 Configuration 3

For sufficiently large gas expansions, the low-viscosity intrusion breached the plug emplacing a layer of low-viscosity liquid above the annulus. The base of the annulus represented a dynamic restriction while its top created a dynamic widening. As the slug nose passed through the widening, it accelerated causing a rapid drainage of the liquid head above the slug that converged at the top of the annulus. Here, the falling film thickened and created a narrowing neck around the slug. If this closed, the gas flow was temporarily halted and the slug broken into two or more offspring bubbles. Due to the change in geometry, instability formed in the falling liquid film around the slug body, creating partial restrictions of the gas escape pathway (*Fig. 7.2c*).

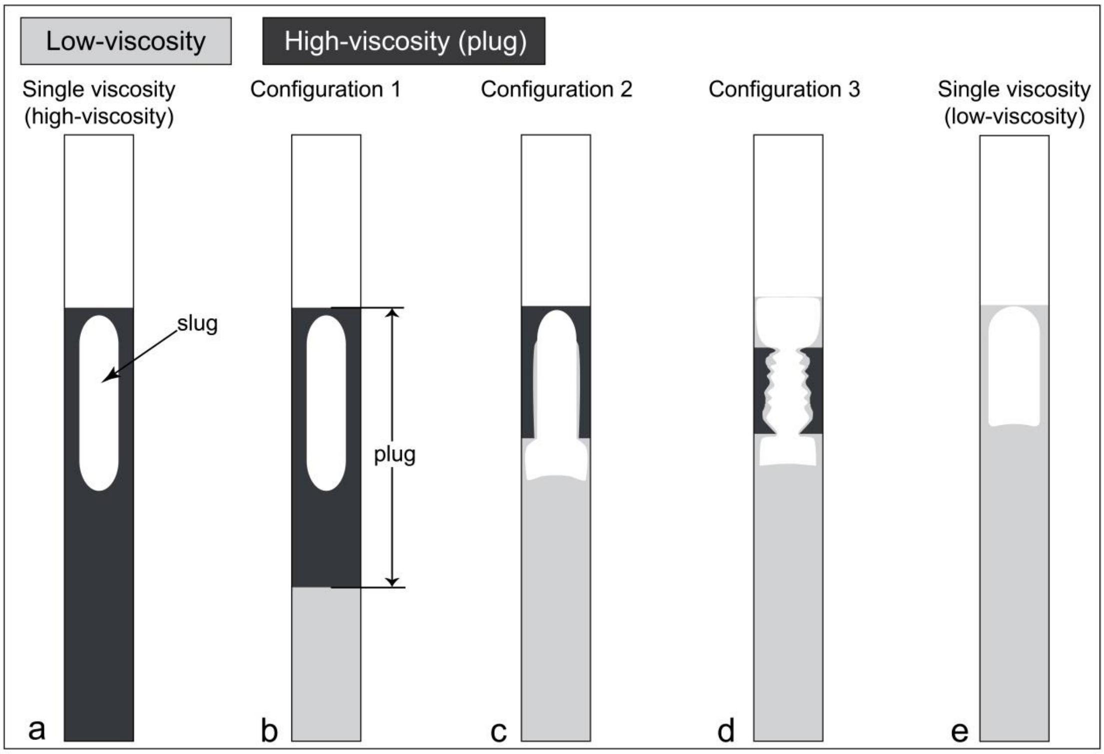

Figure 7.2 Conceptual sketches of tubes filled with (**a**) high-viscosity and (**e**) low-viscosity liquid representing end-member configurations that sandwiched three main flow configurations. (**b**) In Configuration 1, the high-viscosity plug volume is sufficiently large to fully accommodate the gas slug. (**c**) In Configuration 2, a plug can accommodate the intrusion but not all the gas volume: the slug burst whilst within the plug with the slug base still in the low-viscosity liquid. (**d**) In Configuration 3, slug expansion is sufficiently large to drive the low-viscosity intrusion through the plug, extruding a low-viscosity layer above the plug from which the slug burst (see Capponi et al. (2016a) for details).

7.4 Experimental results and interpretation

We identified two main phases during which pressure variations took place: (1) as the slug ascended through the low-viscosity liquid and moved, partially or completely, from within the low-viscosity liquid to within the plug liquid, and (2) during the burst process.

7.4.1 Slug ascent

In a single-viscosity system, an increasing mass of oil surrounding the slug within the falling liquid film was dynamically supported on the tube wall as the slug elongated on decompression, leading to a gradual decrease in P_L (*Fig. 7.3*). Gas expansion accelerated during ascent, causing a pressure drop to burst. After burst, the oil drained back to the liquid surface re-pressurizing the system (*Fig. 7.3*) and P_L increased to pre-injection values (e.g., James et al. 2008; Del Bello et al. 2015).

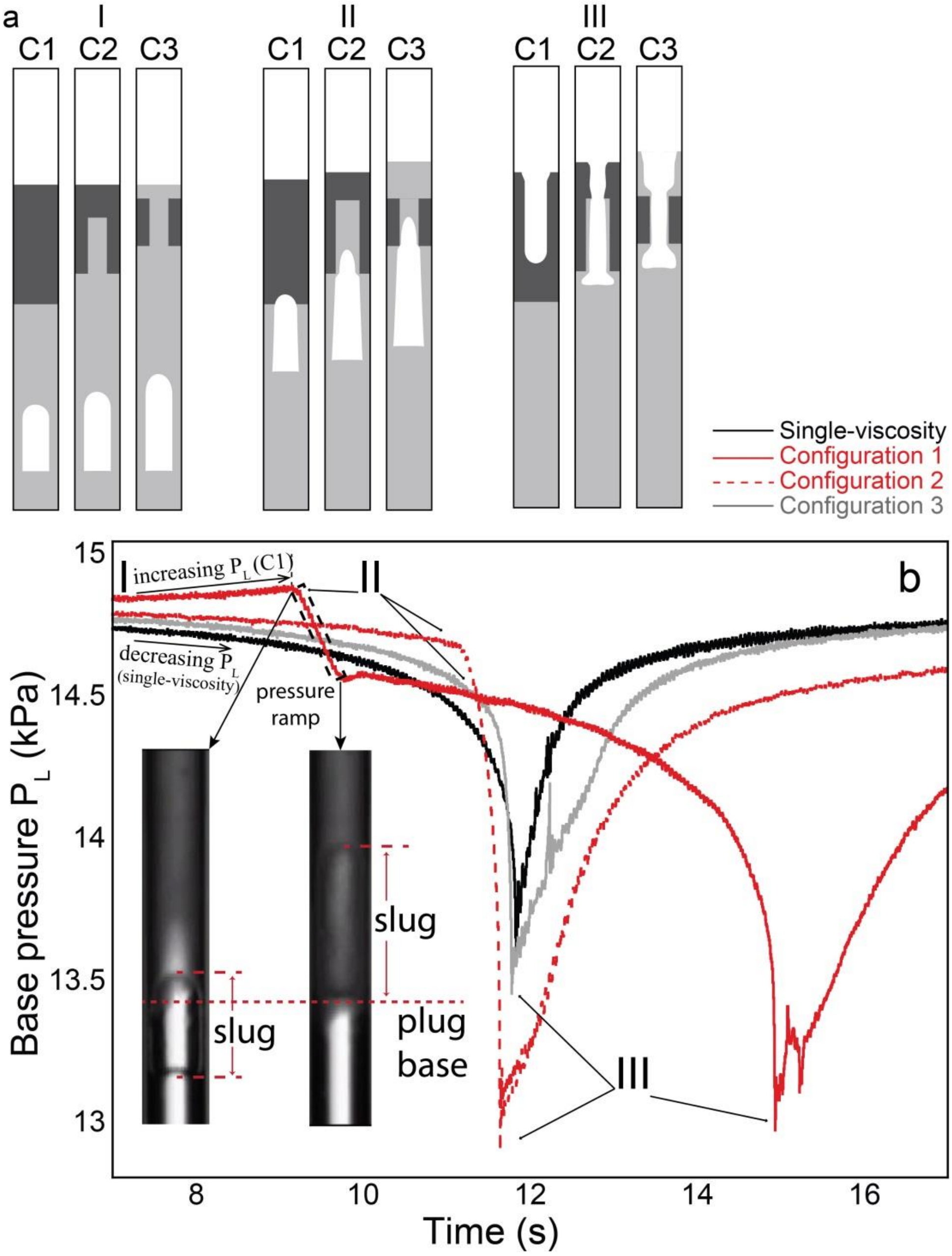

Figure 7.3 Pressure within the liquid at the tube base (P_L) varies with flow process and time. (**a**) Sketches of the flow processes observed for each configuration (C1, C2, C3) as: (I) the slug ascended in the low-viscosity liquid beneath the plug, (II) as the slug nose entered the viscous annulus and (III) at burst. (**b**) Resulting pressure variations within the liquid are shown for a 6 ml slug (P_a = 1 kPa) ascending through a single-viscosity system (black line), Configuration 1 (red line), Configuration 2 (dashed red line) and Configuration 3 (grey line). Note the greater maximum in P_L for Configuration 1 with respect to the single-viscosity control system, followed by a decreasing pressure ramp (II), developed during the transition of the slug from within the low-viscosity liquid to within the plug and ending as soon as the entire slug length is fully accommodated by the plug. The timing for the processes II and III differed between configurations due to different plug thickness and variations in slug ascent mechanism within the plug.

In a layered system, a slug still rose due to its buoyancy but its expansion was hindered and pressure retained due to the presence of a plug. The greater the plug thickness, the less the slug was able to accommodate its expansion through intruding low-viscosity liquid into the plug, resulting in an increase in slug overpressure. This led to variations in P_L strongly dependent on the initial slug volume and the plug size (i.e., the flow configuration), with smaller decreases in P_L for Configuration 3 and 2 compared to a single-viscosity scenario (*Fig. 7.3*), and an absolute pressure increase for Configuration 1. The same initial gas volume, with respect to the single-viscosity system, always showed the highest maximum in P_L for Configuration 1 when the slug reached the plug base (*Fig. 7.3*), mirrored by a decrease in slug length of up to ~15%. In Configuration 2, the more liquid intrusion was driven by the gas expansion through the plug, the faster P_L decreased compared to Configuration 1, but still the rate of pressure decrease was substantially smaller than the single-viscosity scenario (*Fig. 7.3*). Configuration 3 showed a pressure decrease closer to that of the single-viscosity control, but again clearly smaller during the slug ascent in the low-viscosity liquid. Pressure decrease then accelerated once the liquid intrusion breached the plug, removing its capping effect and allowing the slug to expand freely, feeding the low-viscosity liquid layer emplaced above the plug (*Fig. 7.3*).

When the slug nose reached the base of the viscous annulus, it started to ascend through the intrusion. As the slug nose moved from the low-viscosity intrusion to within the main body of the plug itself, P_L rapidly started to decrease (*Fig. 7.3*). This was evident especially for Configuration 1, which showed a decreasing pressure ramp whose onset corresponded to the slug nose entering the plug and ended as soon as the slug base was accommodated by the plug (*Fig. 7.3*). This ramp represented the pressure loss around the slug beginning as the supply of low-viscosity liquid draining into the falling liquid film declined and an increasing volume of high-viscosity liquid (thicker falling film) was supported by viscous shear forces along the tube wall. The area of the tube occupied by the slug consequently decreased and the slug length increased. The transition from the low-viscosity liquid to the plug led to pressure drops ranging between ~95 Pa and ~3570 Pa, depending on the slug volume and plug thickness. A similar pressure drop was observed during the passage of a slug through a region of tube narrowing (James et al. 2006), generated here by the dynamic viscous annulus. Defining an equivalent aspect ratio for the slug size, L', as $L' = L/D = 4V/\pi D^3$, where L is the length of the bubble and assuming a static cylindrical gas volume (V) with the same diameter as the pipe, the overall pressure drop was expressed as

$$-\Delta P_L \approx \rho g L_i' D_w (1 - A') \tag{1},$$

where L_i' is the equivalent aspect ratio of the slug in the lower tube, D_w is the diameter of the wider tube (slug in low-viscosity liquid) and A' is the ratio of the cross sectional area of the wider tube to the narrower tube (slug in high-viscosity liquid; equation 6 in James et al. 2006). The length of the slug for calculating L' and the radii for the wider and narrower fluid pathways (i.e., tube radius minus the thickness of the high-viscosity falling liquid film) to obtain A' were measured directly from video images. Estimation of the pressure drop using equation (1) for 6, 24 and 49 ml slugs, yields $-\Delta P_L$ of 478 Pa, 1520 Pa and 2390 Pa respectively. This agrees, within error, with measured values of pressure drop of ~450 Pa, ~1340 Pa and ~2800 Pa respectively.

The decreasing pressure ramp developed only for a slug fully accommodated by the plug (i.e., Configuration 1, *Fig. 7.3*). For Configuration 2, only the onset of the ramp was detected when thick plugs were involved (10*D* and 20*D*), with the slug nose moving into the high-viscosity region before the accelerated near-surface expansion. Then, as soon as the slug approached the surface, the decrease in P_L blended with the faster non-linear pressure drop driven by the very rapid near-surface expansion of the slug. For Configuration 3 it was not possible to detect the slug transition in the plug; however, once the low-viscosity intrusion breached the plug, the entire high-viscosity liquid volume was supported by viscous shear forces along the tube wall, together with the low-viscosity film surrounding the slug body as it passed through it. This led to a much greater overall pressure drop compared to the other two configurations. Instabilities developed in the falling film around the slug body when the slug nose within the intrusion ascended above the top of the annulus; these propagated downward within the low-viscosity film enclosed within the annulus. The greater the gas volume, the more these oscillations were pronounced, disrupting the boundary between the two liquids (Capponi et al. 2016a). This was reflected by oscillations in P_L, with frequencies of ~25-~50 Hz.

7.4.2 Slug burst

During slug ascent, no pressure changes in ΔP_A were detected. As the slug approached the liquid surface, gas expansion resulted in the acceleration of the liquid surface above it, which caused a rapid displacement of the air above the liquid resulting in an increase in ΔP_A.

7.4.2.1 Single, low-viscosity control system

Within a single-viscosity system, the peak excess pressure, $\Delta P\hat{}_A$, produced by the gas flux was proportional to the gas mass generating it (*Fig. 7.4a*), thus related to the initial injected gas volume, V_0 (Lane et al. 2013). For the range of V_0, with P_a = 1 kPa, three different behaviours have been identified through the dimensionless ratio $\Delta P_b/\Delta P\hat{}_A$ (Lane et al. 2013), where ΔP_b is a theoretical estimate of the peak dynamic overpressure in the slug at burst (James et al. 2009; Del Bello et al. 2012; Lane et al. 2013), and the dimensionless stability index (Del Bello et al. 2012; Lane et al. 2013), γ_s, which predicts if a slug will expand in equilibrium with the surrounding liquid and burst passively with negligible dynamic overpressure ($\gamma_s < 1$) or not ($\gamma_s > 1$). Similar behaviours were identified, for the same range of volumes and P_a, in a liquid slightly more viscous (μ = 0.162 Pa s) and less dense (ρ = 860 kg/m^3), by Lane et al. (2013), classified as passive, transitional and explosive regimes (Lane et al. 2013). $\Delta P_b/\Delta P\hat{}_A$ plotted against γ_s (*Fig. 7.4b*) identifies the passive regime for injected volumes 2–4 ml ($\gamma_s < 1$), and the transitional and explosive regimes for 6–10 ml and 17–49 ml ($\gamma_s > 1$) respectively (*Fig. 7.4b*). The same regimes can be identified by visual observation of the excess pressure ΔP_A waveforms (*Fig. 7.4c*).

7.4.2.2 Rheologically plugged system

In a layered system, the scaling arguments derived from geometrical considerations (James et al. 2008; Del Bello et al. 2012) cannot be rigorously applied; however, it is possible to identify a trend based on the flow configuration within which the slugs burst. For the same plug thickness, $\Delta P\hat{}_A$ scaled with V_0 (*Fig. 7.5a*); for constant V_0 (i.e., for the same initial injected gas volume) and varying plug size $\Delta P\hat{}_A$ was a function of flow configurations (*Fig. 7.5b*). Smaller V_0 (2–10 ml), bursting in Configuration 3, showed a $\Delta P\hat{}_A$ increase as function of plug thickness (1*D*, 2*D* and 5*D*). Larger V_0 (17–49 ml) showed more variability in $\Delta P\hat{}_A$ values. For this range of volumes, the generation of offspring bubbles and partial blockages of the tube strongly affected the gas release (Capponi et al. 2016). For each gas volume, maximum $\Delta P\hat{}_A$ value was usually reached within Configuration 2, followed by a decrease in $\Delta P\hat{}_A$ for transition to Configuration 1 (*Fig. 7.5b*). In the absence of Configuration 2, the greater peak was usually associated with Configuration 1.

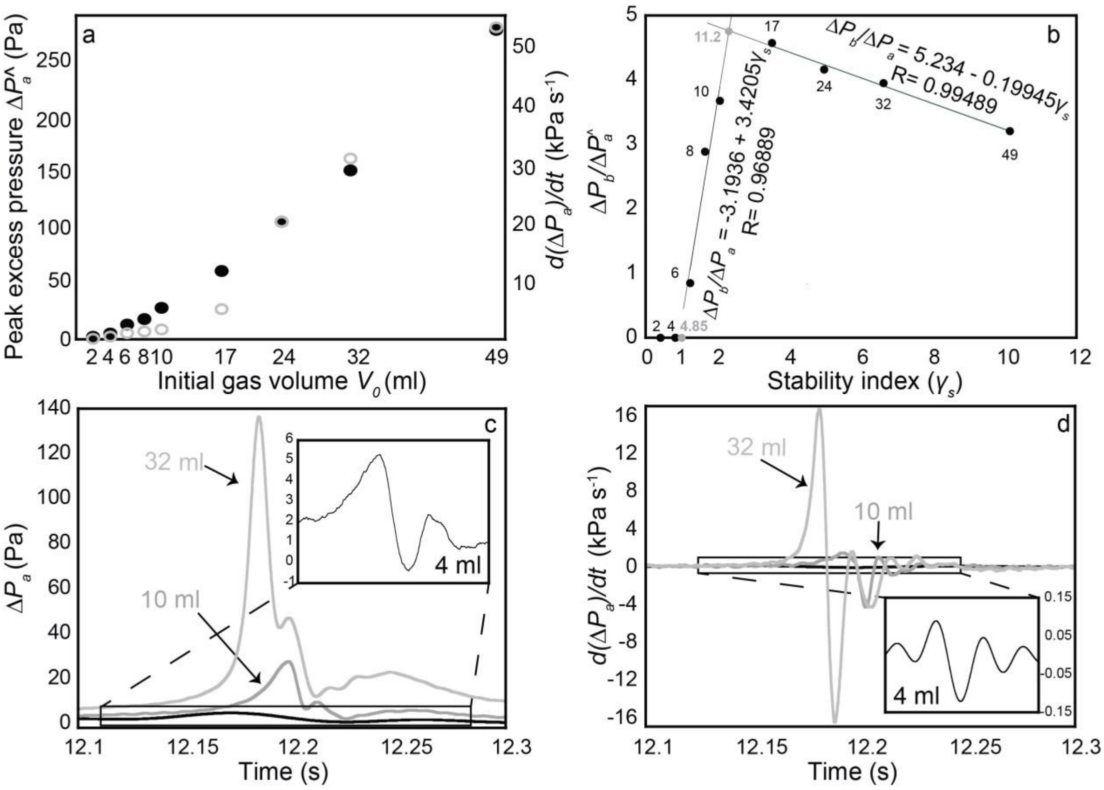

Figure 7.4 shows change in gas pressure above the liquid for the single (low) viscosity control system. (**a**) Peak excess pressure $P^{\wedge}_A$ (black symbols) is reported as function of experimental injected volumes (V_0). Peak amplitudes of the time derivative of pressure variations $d(\Delta P_A)/dt$ (grey symbols) are also reported. (**b**) Dimensionless ratio between theoretical slug overpressure at burst (ΔP_b) to measured peak excess pressure ($\Delta P^{\wedge}_A$) plotted against the dimensionless slug stability index (γ_s) for all the experimental volumes (ml, black dots; P_a = 1 kPa). The transition between passive and transitional regimes is identified by γ_s = 1 (for an empirical V_0 = 4.85 ml) and between transitional and explosive regimes by the intersection of the linear empirical curves at γ_s = 2.31, corresponding to V_0= 11.2 ml. Waveform shapes of (**c**) excess pressure variations (ΔP_A) and (**d**) time derivative of pressure variations $d(\Delta P_A)/dt$, as function of time (P_a = 1 kPa) for initial slug volumes of 4 ml, 10 ml and 32 ml, are representative of the passive, transitional and explosive regimes respectively. The insets in (**c**) and (**d**) show details of ΔP_A and $d(\Delta P_A)/dt$ respectively, for the 4 ml slug.

Figure *7.6a* illustrates the above relationships, showing ΔP_A variations for the same slug volume ascending through a plug of 0*D* (single-viscosity), 2*D*, 5*D* and 20*D*. All the plugged experiments were characterized by a greater $\Delta P^{\wedge}_A$, with Configuration 2 clearly featuring the greater maximum value, followed by Configuration 1 and Configuration 3, which is characterized by a longer coda. The passive, transitional and explosive regimes in the single-viscosity system were identified also by differences in waveform shape generated by increasing gas volumes (*Fig. 7.4c*); in a layered system, similar classes of waveform shapes can still be identified, but in signals produced by the same gas volume for different flow configurations (*Fig. 7.6a*).

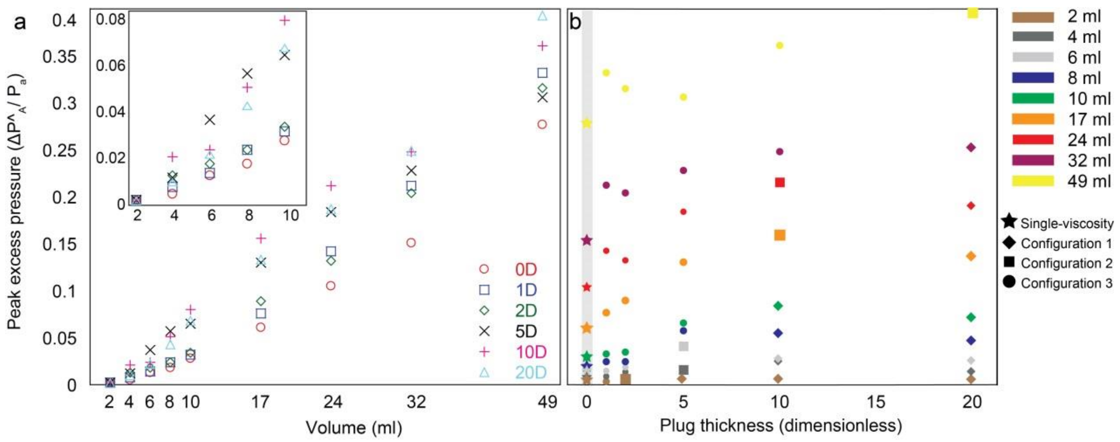

Figure 7.5 (**a**) Peak excess pressure *ΔP^A* normalised for P_a of 1 kPa show (for the same plug thickness) a dependence on initial gas volume V_0; (**b**) as function of plug thickness (dimensionless), for the same gas volume (colours) and varying plug thickness, *ΔP^A* is dependent on the flow configurations (symbols). The grey band identifies *ΔP^A* for the single-viscosity control system.

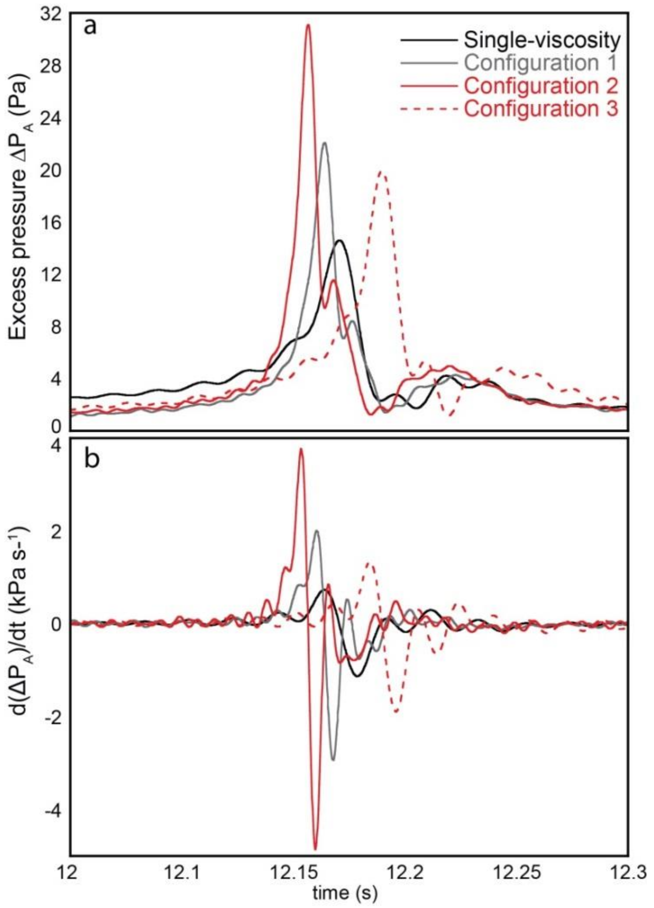

Figure 7.6 (**a**) Excess pressure variations (ΔP_A) and (**b**) time derivative of pressure variations $d(\Delta P_A)/dt$ as function of time for a 6 ml slug (P_a = 1 kPa) ascending through a single-viscosity system (black line, 0*D*), Configuration 1 (grey line, *h* plug = 50 cm, 20*D*), Configuration 2 (red line, *h* plug = 12.5 cm, 5*D*) and Configuration 3 (dashed red line, *h* plug = 5 cm, 1*D*) show the dependence of pressure variations on flow configurations.

By using both peak excess pressure and waveform shape variation, we were able to identify features reflecting different burst dynamics depending on the flow configuration. Configuration 1 and 2 share a similar pulse shape. However, the slower compressional acoustic pulse in Configuration 1 was the result of 1) the slower gas expansion and acceleration of the liquid free surface caused by the ascent of a slug in a high-viscosity liquid, and 2) the slower rupture of the viscous meniscus and release of the gas (*Fig. 7.6a*). In contrast, the greater increase in ΔP_A and the narrowest acoustic pulse width in Configuration 2 reflected a rapid acceleration of the liquid surface and a faster disruption of the meniscus and release of the gas (*Fig. 7.6a*). A higher overpressure is expected with a slug surrounded by a thicker falling film, as previous models in single viscosity systems also demonstrated (James et al. 2009; Del Bello et al. 2012). This was always the case for Configuration 2, where both a falling film of intruded low-viscosity oil and the viscous annulus enclosing the intrusion surrounded the slug. By contrast, when in Configuration 1, only the high-viscosity annulus surrounded the slug, resulting in less energetic bursts (Capponi et al. 2016a). Configuration 3 was characterized by a longer, lower amplitude signal compared to the other configurations (*Fig. 7.6a*). This was due to the combined effect of 1) a less over-pressurized slug compared to Configuration 1-2, with gas expansion sufficiently large to intrude the low-viscosity liquid through and above the plug, and 2) the gas flow was temporarily halted during the slug break-up process, or impeded by partial blockages of the gas escape pathway, leading to progressive gas release and reduced peak pressure (Capponi et al. 2016a).

The burst of offspring bubbles and the gas escaping temporary blockages led to secondary pulses and sub-pulses respectively, following the main pressure pulse (*Fig. 7.7a*). Both secondary pulses and sub-pulses shared a similar and reproducible waveform but showed a progressive decrease in amplitude. In order to verify that the observed pulses related to the original injected mass of gas, *M*, we used ΔP_A to estimate the variations in the mass flux, q, through:

$$\Delta P_A = \frac{c}{A}\frac{dM}{dt} = \frac{c}{A}q \qquad (2),$$

where *c* is sound speed and *A* the tube cross sectional area (Lighthill 1978; Lane et al. 2013). The definite time integral of ΔP_A across the excess pressure peak is proportional to the injected mass of air generating the peak (Lane et al. 2013). When it was possible to visually relate pressure pulses to the main and secondary bursts, integrating around the slug expansion and burst data showed that the sum of the derived air masses for each pulse was indeed consistent, within measurement error, with the value of the original injected mass: e.g., derived masses M of ~6.5×10^{-6} and ~1×10^{-5} kg for initial gas masses of 5.6×10^{-6} and 8.7×10^{-6} kg (32 and 49 ml) respectively.

For each secondary bubble that was generated, P_L showed pressure drops that occurred while the system was already re-pressurizing as the oil film drained back to the liquid surface following the main burst (*Fig. 7.7a*). These pressure drops share a similar waveform to the one produced by the main burst, with a gradual decrease in magnitude; once all the bubbles burst, the system continues re-pressurizing. The entire process can be described as a sequence of pressurization-depressurization-repressurization, with duration a function of the total number of secondary bubbles.

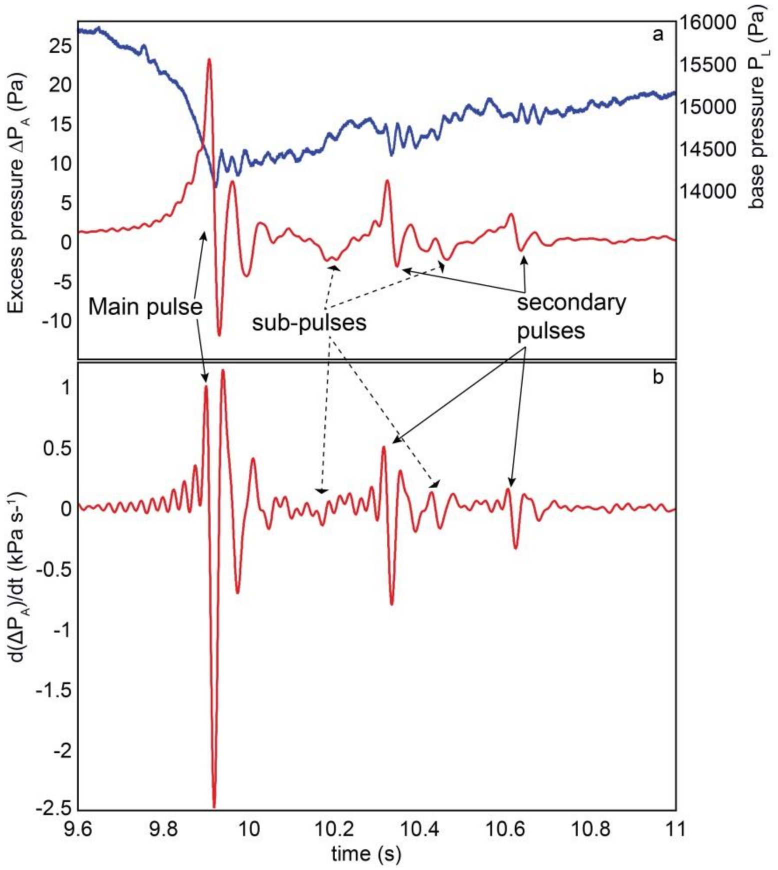

Figure 7.7 (**a**) Pressure variations above (ΔP_A) and within (P_L) the liquid and (**b**) time derivative of pressure variations $d(\Delta P_A)/dt$ as function of time for a 24 ml slug and Pa = 3 kPa, showing the effect of highly variable gas release rates during burst. The main compressional pulse is followed by two secondary pulses related to the burst of two offspring bubbles, interspaced by sub-pulses generated by transient partial restriction of the slug pathway. Note the progressive decrease in the acoustic amplitudes associated with the secondary pulses.

7.5 Volcanic implications

The key fluid-dynamic source mechanism responsible for pressure changes within and above the liquid in the tube, and, by similarity, in a volcanic conduit (Lane et al. 2013), is gas expansion driven by reducing pressure during slug ascent. A viscous layer atop the liquid column adds further complexities to the expansion process, modifying pressure variations. We identified two distinct phases for the source mechanism: pre-burst and burst.

7.5.1 Volcano deformation considerations

Figure *7.3* summarises the pressure measured at the base of the experimental tube in response to the ascent, expansion and burst of a gas slug through a homogeneous liquid and the three configurations identified for gas escape through a plugged system. Bubble burst is followed by liquid drainage of variable complexity to return to the starting condition.

Prior to burst, pressure changes within the liquid began as soon as the experimental slug formed and ascended in the low-viscosity liquid. The presence of a viscous plug hindered gas expansion and, compared to an unplugged system, relative pressure at the tube base increased (*Fig. 7.3*) as the gas slug buoyantly ascended from release point to the plug base. Experimentally, a small absolute pressure increase was observed for Configuration 1. The partial or complete transition of the slug into the plug then led to a gradual depressurization. Configuration 3 showed a lesser degree of pressurization but a greater number of high-frequency oscillations reflecting the development of pressure instabilities, which became larger with time and continued even after the bubble burst. At Stromboli, the passage of the slug through geometrical discontinuities represents a plausible source of VLP seismic events located at 220–330 m below the crater (Chouet et al. 2003, 2008). The shallow transient geometrical discontinuities induced by a possible plug cannot explain these depths and, thus, cannot be responsible for VLP signals; however, the shallow geometry still controlled flow disturbances and can represent a place where fluid pressure changes can be coupled to the conduit and be responsible for short-term and localized ground displacements. Ground displacement can be detected by filtering broadband seismic measurements as short-time sequences of ground inflation-deflation cycles, with the inflation related to conduit pressurization prior the explosion (i.e., bubble expansion and consequent magma acceleration), followed by deflation associated with the gas-and-fragments release into the atmosphere (e.g., Genco and Ripepe 2010; Lyons et al.

2012). During the ascent in the low-viscosity liquid, slug expansion is hindered and the greater the plug thickness and viscosity, the more pressure can be retained within the slug. Thus, each configuration is characterized by a different degree of decrease in gas expansion rate and, consequently, in volumetric expansion triggering different conduit responses to the flow processes. This would result in slower temporal changes in ground-deformation for Configuration 1 and faster for Configuration 3. As the slug starts to transit from the low-viscosity liquid to the plug, the configurations would also control any change in ground inflation: within the plug (i.e., Configuration 1), the gas slug slowly expands, leading to a slow acceleration of, the magma volume above it. If the slug uses the low-viscosity intrusion to ascend through the plug (i.e., Configuration 2-3), slug expansion is faster, as the acceleration of the fluid above it. When the slug pass through a shallow widening in the conduit (i.e., Configuration 3), the sudden acceleration of the slug nose lead to rapid draining of the liquid head around the slug, and the slumping liquid generates further oscillations and changes in the velocity field of the liquid around the slug and at the top of the widening. This variability may help explain, for example, the observed inflation processes of vent covers preceding Strombolian explosions (Capponi et al. 2016b). Indeed, field observations showed how cover inflation can last from few seconds up to tens of minutes and always accelerated nonlinearly in the few seconds preceding an explosion, followed by subsequent deflation (Capponi et al. 2016b). These processes likely result from volumetric changes within the conduit, and the variable inflation timescales and trends may reflect rheological variations in the shallower part of the conduit, whose extent would hinder gas slug expansion and reduce its ascent velocity to different degrees, thus affecting the rates of change in both magma acceleration and in-vent ground deformation.

Hence, distinct locations at which the flow undergoes dynamic change exist for each configuration, leading to a different degree of pressure changes and liquid acceleration through the entire gas expansion process and, thus, in the resulting forces exerted on the conduit by pressure. Such changes can potentially show a sequence of conduit pressurization-depressurization associated with a shallow source where the flow organisation and plug properties control expansion dynamics and, thus, the rates of change in ground displacement. However, due to the very shallow source, it is likely for the deformation cycles to be dominant only in the vent area and may not be detected by broadband seismic signals, unless ground-based instruments are deployed in the immediate vicinity of the vent (e.g. Genco and Ripepe 2010).

7.5.2 Volcano acoustic considerations

Gas expansion and release are responsible for variations in the pressure within the tube above the liquid surface, ΔP_A. The time derivative of ΔP_A is a theoretical representation of the acoustic signal in a 3D atmosphere from a 1D source (Lighthill 1978), thus obtaining a synthetic infrasonic waveform to be compared with measured volcanic signals (Lane et al. 2013). The qualitative similarity between $d(\Delta P_A)/dt$ and Strombolian infrasonic signals demonstrated the plausibility of the rise and expansion of slugs as first-order fluid dynamic sources mechanism for infrasonic signals generated by gas puffing and explosive eruptions at Stromboli (Lane et al. 2013).

Peak amplitudes of $d(\Delta P_A)/dt$ in the single-viscosity system scaled with V_0, particularly for the explosive regime (17-49 ml; *Fig. 7.4a*, *d*). In a layered system, the flow configurations control both acoustic amplitudes and waveform shapes (*Fig. 7.6b*) for otherwise similar eruption conditions. The comparison of experimental $d(\Delta P_A)/dt$ with the volcanic case requires care, due to both the first-order laboratory approach and path effects during field measurement. The experiments are scaled to the source mechanism of gas expansion and the complexities of a natural system (e.g., ash production and topography) are not reproduced. Thus, for comparison we chose infrasonic signals produced at Stromboli from ash-free or ash-poor eruptions, with ejection of pyroclasts to various heights, likely representative of the arrival and burst of a gas slug at some depth in the conduit (Lane et al. 2013). The comparison was made by scaling both time and pressure axis by the same factor to best fit "by eye" the experimental to the measured data, considering that natural acoustic signals are ~10 times the period of the experimental system, and qualitatively comparing the first pulse and the secondary oscillations (taking into account that high frequency oscillations may emerge calculating $d(\Delta P_A)/dt$, plausibly representing resonance of the gas within the experimental tube).

Experimentally, the same gas volumes bursting in different configurations produce waveforms that resemble infrasonic signals recorded at different vents at Stromboli. For the same conditions (V_0 = 6 ml, P_a = 1 kPa) bursting both in a single low-viscosity system and within Configuration 1 (essentially a single high-viscosity system), the synthetic waveforms showed considerable similarity with the infrasonic waveform of explosion 95 of Vergniolle et al. (1996), recorded from the eastern vents

(*Fig. 7.8a*, *b*). However, the waveform resulted from Configuration 1 was the closest match to the natural one (*Fig. 7.8b*). Indeed, in contrast to a single low-viscosity system, the secondary oscillations following the main pulse were better represented and the experimental burst point matched the bubble bursting of Explosion 95, marked by high frequencies in the acoustic pressure (Vergniolle et al. 1996). The waveform produced by the same gas volume but within Configuration 2 can be compared to the ones for the northeast crater zone, NEC (McGreger and Lees 2004): once again, the main pulse was well reproduced, with some similarities within the following secondary oscillations (*Fig. 7.8c*). Finally, the waveform for the slug bursting within Configuration 3 was remarkably similar to the waveform from Hornito (*Fig. 7.8d*), matching the main pulse (McGreger and Lees 2004). Furthermore, this synthetic waveform for a 6 ml gas volume escaping a plugged system provided a better match for the Hornito than the unplugged 24 ml volume from Lane et al. (2013), with a better match of the secondary oscillations.

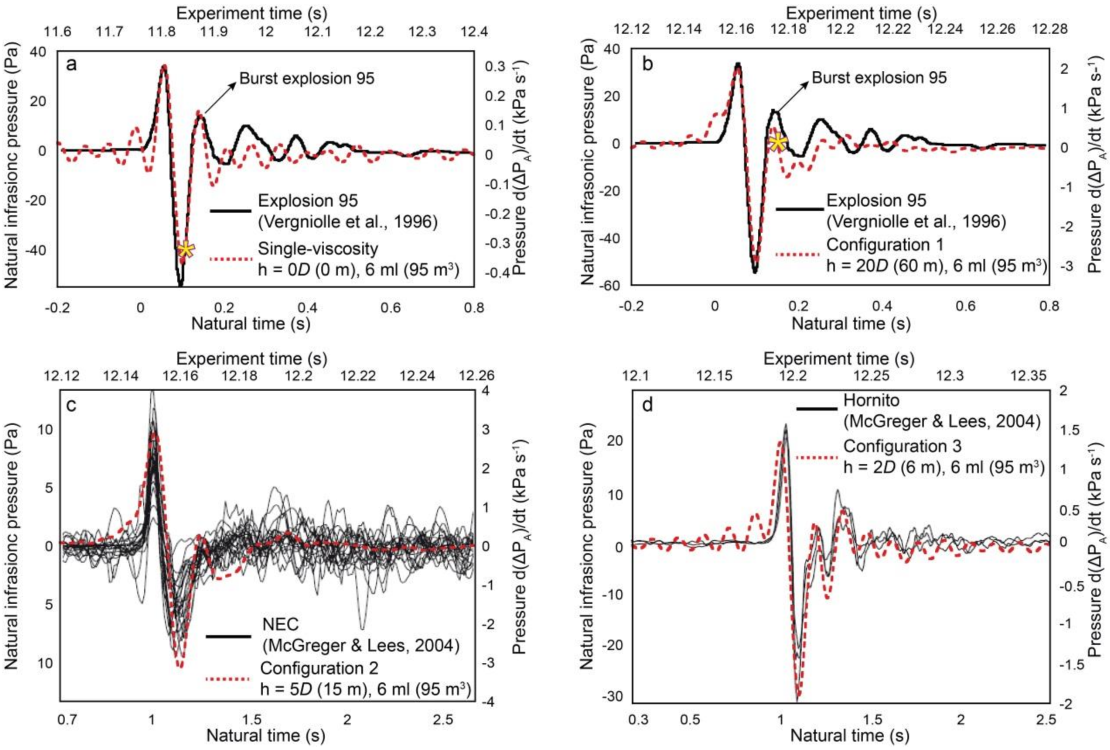

Figure 7.8 The time derivative $d(\Delta P_A)/dt$ for an experimental 6 ml slug ascending through (**a**) single low-viscosity system, (**b**) Configuration 1, (**c**) Configuration 2, and (**d**) and Configuration 3, was compared to infrasonic signals measured at Stromboli from (**a**, **b**) Vergniolle et al. (1996, reprinted with permission from AGU) and from (**c**, **d**) McGreger and Lees (2004, reprinted with permission from Elsevier). Both time and pressure axis were scaled by the same factor to best fit the experimental to the measured data. The asterisk in (**a**) and (**b**) indicated the burst of the 6 ml experiment.

A 6 ml experimental slug (P_a = 1 kPa) scales to an erupted volcanic gas volume of 95 m^3 at atmospheric pressure (Del Bello et al. 2015; Capponi et al. 2016a). In order to identify possible differences in burst dynamics resulting from the expansion and burst of such volume for each flow configuration at volcanic scale, we used 3D CFD simulations carried out by Capponi et al. (2016a). Configuration 1 (*h* plug = 60 m) underwent a slow fragmentation of the viscous meniscus above the slug, with few pyroclasts ejected and may be compared (*Fig. 7.8b*) to Explosion 95 (Vergniolle et al. 1996), from the eastern vents, which consisted of the arrival and burst of bubbles of several sizes at the surface, with the ejection of pyroclasts within the gas jet up to a few metres above the vent, and sound emissions. Configuration 2 (*h* plug = 15 m) involved a vigorous burst with the fast fragmentation of the meniscus, and ejection of pyroclasts to much higher heights above the burst point, compare (*Fig. 7.8c*) to the Northeast Crater (NEC) that produced well-collimated, gas-rich eruptions, 10 to 20 s in duration, ash-free or -poor, and with minor bombs reaching heights up to 300 m (McGreger and Lees 2004). Configuration 3 (*h* plug = 6 m) produced the ejection of material above the burst point but both their amount and heights were inferior to Configuration 2 (Capponi et al. 2016a), whilst The Hornito produced loud jet-like acoustic noise, with minimal associated ejecta (McGreger and Lees 2004).

Thus, the same gas volume bursting in different configurations generates laboratory waveforms resembling infrasonic signals typical of specific vents at Stromboli. When scaled to the volcanic case, and modelled via 3D CFD simulations (Capponi et al. 2016a), distinct burst dynamics are simulated that are similar to those observed from vents at the time of the infrasound acquisition. This suggests that slug expansion and burst through a rheologically stratified liquid can provide a viable first-order source mechanism for infrasonic signals at Stromboli and justify the variable explosive activity observed at Stromboli. However, it also casts a shadow on the actual interpretation of infrasonic signals, where variations in amplitude are usually related to variations in the bubble overpressure and volume, without considering changes in magma rheology and conduit geometry. Models of gas slugs ascending in a rheologically stratified conduit revealed how the same range of gas volumes, depending on plug thickness and viscosity, can lead to different flow configurations promoting different eruptive styles (Capponi et al. 2016a) and, as the pressure variations demonstrate, modifying the geophysical signals accordingly. This implies that the variability in eruptive style inferred by infrasonic signals for each vent cannot be attributed only to variation in slug metrics, but may also depend to variations in the magmatic condition (i.e., in flow configurations) and supply of slugs, which may control the configuration transition.

If initially a viscous layer can form at the top of the magma column (*Fig. 7.9a*) and slugs start to form and rise more frequently, an open path within a plug is likely to be created over time and kept open (i.e., rapid transition from Configuration 1-2 to Configuration 3, *fig. 7.9c*). If such activity remains steady in time generating a semi-permanent path through the plug, it is also possible that a circulatory system develops. The continuous and frequent arrival of slugs could favour a constant influx of low-viscosity magma in the central part of the conduit feeding the intrusion, while the degassed dense material comprising the viscous annulus sinks at depth, descending in the region surrounding the low-viscosity intrusion and clearing the shallower part of the conduit over time. Conversely, a lower frequency of slug formation would favour the generation of a uniform plug, whose thickness and, thus, flow configuration, will depend on how much time the magma has to cool down before the next explosion (*Fig. 7.9a*, *b*). Thus, for volcanoes where multiple vents are constantly active (e.g., Stromboli and Yasur, Vanuatu), each vent may be characterized by an open path through the plug to the surface or by variable plug thickness, producing different eruptive styles and, ultimately, distinct infrasonic signatures depending on the timescale of slug formation interacting with the timescale of viscous layer formation and resetting after an event. Therefore, in parallel with infrasonic monitoring, knowledge of variations in magma rheology, slug volume and supply rate will help in better understanding and strengthening the link between conduit dynamics, variations in explosion styles and intensity, and geophysical signals (e.g., Ripepe et al. 2009; Taddeucci et al. 2013).

Slug break-up and the partial restrictions of the slug path, characterizing Configuration 3 (Capponi et al. 2016a), led to highly variable gas release rates (*Fig. 7.7a*) with the main strong compressional pulse followed by pulses (burst of offspring bubbles) and sub-pluses (transient restriction). The gradual decrease in the acoustic amplitudes associated with the secondary pulses mirror a decrease in the overpressure within each gas pocket bursting at the surface; amplitude of the sub-pulses is always lower than the pulses. Both processes have been observed at volcanic-scale in 3D CFD simulations, with a greater frequency of pulses and sub-pluses favoured by a lower viscosity of the underlying magma (Capponi et al. 2016a).

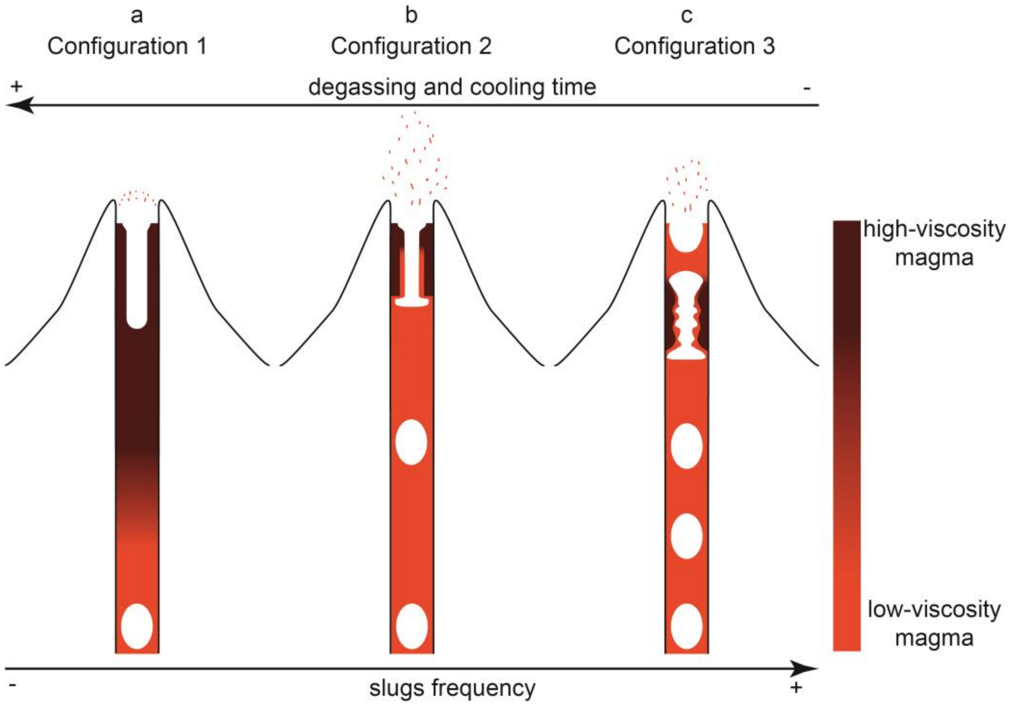

Figure 7.9 Conceptual sketches illustrating the effect of slug frequency on conduit dynamics. (**a**) For a low slug release frequency, the time interval between explosions is large enough to allow the generation of a degassed and viscous layer of magma at the top of the conduit, large enough to accommodate the ascending slug. The quiescent time preceding the next explosion allows the viscous layer to settle again. (**b**) An increase in the slug generation frequency reduces the cooling time of the magma, and, as a result, the thickness of the viscous layer is reduced. If reduced sufficiently, the plug will not be large enough to accommodate both the liquid intrusion and the ascending slug. The slug will then burst in the plug, with its base still in the low-viscosity magma. (**c**) Higher-frequency slug release creates an open path right through the plug, kept open by the train of ascending slugs. Each time a slug passes through the geometrical discontinuities, the slug break-up process may be triggered, and instabilities along the liquid film may create partial blockages of the slug path, resulting in longer and complex eruption and highly variable gas release rates.

The successive release of increasingly less overpressured gas pockets would result in eruptive pulses characterized by decaying pyroclast ejection pulses (assuming pyroclast velocity is related to gas overpressure); this has been demonstrated volcanically by high-speed and thermal video imagery (Taddeucci et al. 2012b; Harris et al. 2012). Second-order velocity fluctuations between the main ejection pulses (Taddeucci et al. 2012a; Gaudin et al. 2014) could be related to the same pressure fluctuations responsible for the partial restriction of the gas escape pathway. The acoustic signal ($d(\Delta P_A)/dt$) also showed a complex waveform (*Fig. 7.7b*), with multiple pulses of variable amplitude, interspaced by high-frequency oscillations. These are the most heterogeneous waveforms and with longer duration, reflecting a longer volume discharge process. At Stromboli, the South-West vents often produced the longer and more complex infrasonic signals, with a low-amplitude compressional pulse followed a longer coda, modelled as the bursting of smaller gas bubbles at surface or longer mass discharge process (McGreger and Lees 2004; Ripepe et al. 2008). Thus, the slug break-up mechanism, together with the generation of transient partial blockages of the conduit, is not only likely to be operative at Stromboli being responsible for the longer and more complex eruptions mirrored by distinct infrasonic signals, but also demonstrates the need for a plug as a pre-requisite for such behaviour.

7.6 Conclusions

The ascent of a gas slug through a rheologically stratified liquid column produced a variety of pressure changes, whose magnitude was strongly dependent on the flow configuration in which the slug burst.

During slug ascent in the low-viscosity liquid, pressure changes within the fluid involved, compared to an unplugged system, an absolute pressurization of the tube below the plug, followed by a gradual depressurization as the slug moved from the low-viscosity liquid into the high-viscosity one. The greater level of slug pressurization and subsequent depressurization was achieved in Configuration 1, followed by Configuration 2 and 3. Ground deformation at volcanoes is often a response to pressure change and fluid flow within the volcanic conduit before, during and after eruption. Therefore, any variation in pressure within the conduit and liquid surface acceleration reflecting different degree of volumetric expansion induced by different flow configurations could be detected at the surface. This is because variations in the rate of temporal changes of ground-deformations at the vent show a cycle of inflation of the vent area, whose magnitude reflects the degree of slug growth and magma acceleration, which is then followed by deflation as response to the pressure release at burst.

At burst, for constant gas mass each flow configuration produced distinct peak amplitudes and waveform shapes, reflecting different burst processes. Similarities between infrasonic measurements acquired at different vents at Stromboli and synthetic waveforms associated with different flow configurations demonstrated that infrasonic signals can be interpreted in terms of gas slug expanding and bursting through a viscous layer. At Stromboli, each vent is characterized by a distinct infrasonic signature that can be related to different rheological conditions, with the size and frequency of the slugs dictating the configuration transition. High-frequency slug ascents favour the generation of a pathway within the plug, leading to longer and more complex eruption featuring multiple burst and pressure fluctuations, as both natural and experimental infrasonic signals showed. A slower slug frequency can allow the formation of a more uniform plug, which thickness and, thus, flow configuration and associated infrasonic signal, depend on the time interval between each slug or on variations in slug size.

Ultimately a possible link between slug frequency, flow configurations and eruption intensity highlights the need of multiple monitoring of parameters such as gas volumes and magma rheology to better interpret geophysical signals and integrate the complexities of flow organisation in models of eruption dynamics.

7.7 Acknowledgments

The research leading to these results is part of A.C. PhD at Lancaster University and has received funding from the People Programme (Marie Curie Actions) of the European Union's Seventh Framework Programme (FP7/2007-2013) under the project NEMOH, REA grant agreement n° 289976

Chapter 8 - Recycled ejecta modulating Strombolian explosions

Antonio Capponi[a,b], Jacopo Taddeucci[b], Piergiorgio Scarlato[b], Danilo M. Palladino[c]

[a]Lancaster Environment Centre, Lancaster University, Lancaster LA1 4YQ, UK

[b]Istituto Nazionale di Geofisica e Vulcanologia, Via di Vigna Murata, 605, 00143, Rome, Italy

[c]Dipartimento di Scienze della Terra, Sapienza Università di Roma, Rome, Italy

***Published paper* (Appendix 3)**:

A. Capponi, J. Taddeucci, P. Scarlato, D.M. Palladino, *Recycled ejecta modulating Strombolian explosions*, Bulletin of Volcanology, Volume 78:13, 2016, DOI 10.1007/s00445-016-1001-z.

Reviewers: Matt Patrick, Andy Harris, Pierre-Simon Ross

Chapters 5, 6 and 7 illustrate the importance of a degassed and more viscous magma layer at the top of the conduit in controlling the slug behaviour and changes in the flow patterns. Each identified flow configuration encompasses a variety of processes including, e.g., dynamic narrowing and widening of the conduit, generation of instabilities along the falling liquid film, transient blockages of the slug path and slug break-up. All these complexities, in turn, lead to different degrees of slug overpressure, reflected in variations in conduit pressurization and distinct infrasonic signatures that also relate to different eruptive styles. Furthermore, the interaction between an ascending slug and the liquids promotes magma mingling, therefore controlling the ejecta properties.

However, experimental insights and numerical models alone cannot fully unveil the link between variations in the flow patterns, slug behaviour and how the gas is physically released from the underground into the atmosphere. It is therefore important to have a detailed overview also of the processes taking place at the vent - where the only activity directly observable during eruptions occurs - in order to better understand the link between the conduit dynamics and field observations.

This manuscript seeks to investigate how the vent conditions affect the style of explosive activity at Stromboli volcano through analysis of high-speed and thermal videos of Strombolian explosions. Vent processes have been detailed, and two main eruptive regimes identified based on vent conditions: open vent vs. debris-covered vent. Explosions through debris covers, depending on the on the grain size and amount of the debris, range between ash-free or ash-poor and ballistic-rich, with relatively cold bombs and lapilli, eruptions to ash-rich and ballistic-poor or ballistic-free eruptions. Both fine and coarse debris both fall back into the vent after each explosion and gravitationally accumulate in between the explosions, generating the debris cover. In contrast, open-vent eruptions are mostly ash-free and involve the ejection of hotter and plastically deforming pyroclasts at a higher exit velocity.

The pre-explosion displacement of the debris mirrors the rise and expansion of a pressurized gas slug. Furthermore, the debris seems to interact thermally and mechanically with the magma; this interaction may lead to an increase in magma viscosity in the shallower part of the conduit. The ejection of partially molten clasts indeed suggests the presence of a transitional zone in which magma surface and debris blocks interact, with the clasts potentially being assimilated by the magma leading over time to the generation of a rheological impedance.

Antonio Capponi: collected field data during several field campaigns at Stromboli, carried out data processing of high-speed and thermal videos, and wrote the manuscript.

Jacopo Taddeucci: contributed to discussions, reviewed the manuscript, and collected field data at Stromboli.

Piergiorgio Scarlato: collected field data, obtained funding for field instrumentation.

Danilo M. **Palladino**: reviewed the manuscript.

Abstract

Two main end-members of eruptive regimes are identified from analyses of high-speed videos collected at Stromboli volcano (Italy), based on vent conditions: one where the vent is completely clogged by debris, and a second where the vent is open, without any cover. By detailing the vent processes for each regime, we provide the first account of how the presence of a cover affects eruptive dynamics compared to open vent explosions. For clogged vents, explosion dynamics are controlled by the amount and grain size of the debris. Fine-grained covers are entirely removed by explosions, favouring the generation of fine ash plumes, while coarse-grained covers are only partially removed by the explosions, involving minor amounts of ash. In both fine- and coarse-grained cases, in-vent ground deformation of the debris reflect variations in the volumetric expansion of gas in the conduit, with rates of change of the deformation comparable to ground inflation related to pre-burst conduit pressurization. Eruptions involve the ejection of relatively slow and cold bombs and lapilli, and debris is observed to both fall back into the vent after each explosion and to gravitationally accumulate between explosions by rolling down the inner crater flanks to produce the cover itself. Part of this material may also contribute to the formation of a more degassed, crystallized and viscous magma layer at the top of the conduit. Conversely, open-vent explosions erupt hotter pyroclasts, with higher exit velocity and with minor or no ash phase involved.

Keywords

Strombolian eruptions; vent processes; eruption dynamics; plume dynamics; ejection velocity; high-speed video

8.1 Introduction

Strombolian eruptions are characterized by relatively mild, impulsive releases of gas and pyroclasts that typically last a few to tens of seconds and eject a gas-particle mixture to several tens to hundreds of meters in height (e.g., Houghton and Gonnermann 2008; Cashman and Sparks 2013; Taddeucci et al. 2015). Eruptions result from the arrival and burst of overpressured gas pockets (slugs) at the free-surface (Chouet et al. 1974; Blackburn et al. 1976; Parfitt 2004; Houghton and Gonnermann 2008). This widely accepted scenario is supported by a large body of literature focused on understanding the mechanism behind explosions at Stromboli volcano (Aeolian Islands, Italy) via, for example, interpretation of seismic and infrasonic data (e.g., Vergniolle et al. 1996; Chouet et al. 2003, 2008; Marchetti and Ripepe 2005), experimental studies (e.g., James et al. 2004, 2006, 2008; Lane et al. 2013), and field observations (e.g., Chouet et al. 1974; Blackburn et al. 1976; Ripepe et al. 1993, 2008, 2009; Patrick et al. 2007; Harris et al. 2012; Taddeucci et al. 2012a, b; Gaudin et al. 2014; Bombrun et al. 2015). However, none of these studies have focused on detailing how the gas is physically released into the atmosphere, i.e., the vent processes.

Increasing textural, experimental and field evidence suggests that the Strombolian paradigm of slugs ascending and bursting in a rheologically uniform melt is too simplistic, pointing instead to the coexistence of melts with different rheological properties in the shallower conduit (Gurioli et al. 2014; Leduc et al. 2015). Cooling and degassing of the uppermost part of the magma column may lead to the generation of a more viscous and evolved magma layer in which a gas pocket bursts (Gurioli et al. 2014). The properties and thickness of this layer may have an impact on the eruptive dynamics, to cause variations in explosion intensity and style (Lautze and Houghton 2005, 2006). Textural and geochemical analyses of ejected pyroclasts at Stromboli support the coexistence of melts with contrasting rheologies (Lautze and Houghton 2005; D’Oriano et al. 2011; Colò et al. 2010), leading to magma mingling during the ascent and burst of a slug (Gurioli et al. 2014; Leduc et al. 2015).

Recent experimental investigation endorses the presence of a plug (*Fig. 8.1*), demonstrating how the interaction of an ascending slug with a high-viscosity plug heavily affects fluid dynamic processes in the conduit and explaining some of the key phenomena observed at Stromboli, such as the eruptive pulses and sub-pulses and the occurrence of mingled pyroclasts (Del Bello et al. 2015). The presence of a plug also affects the degree of slug overpressurization, leading to an increase in the explosivity of strombolian eruptions (Del Bello et al. 2015).

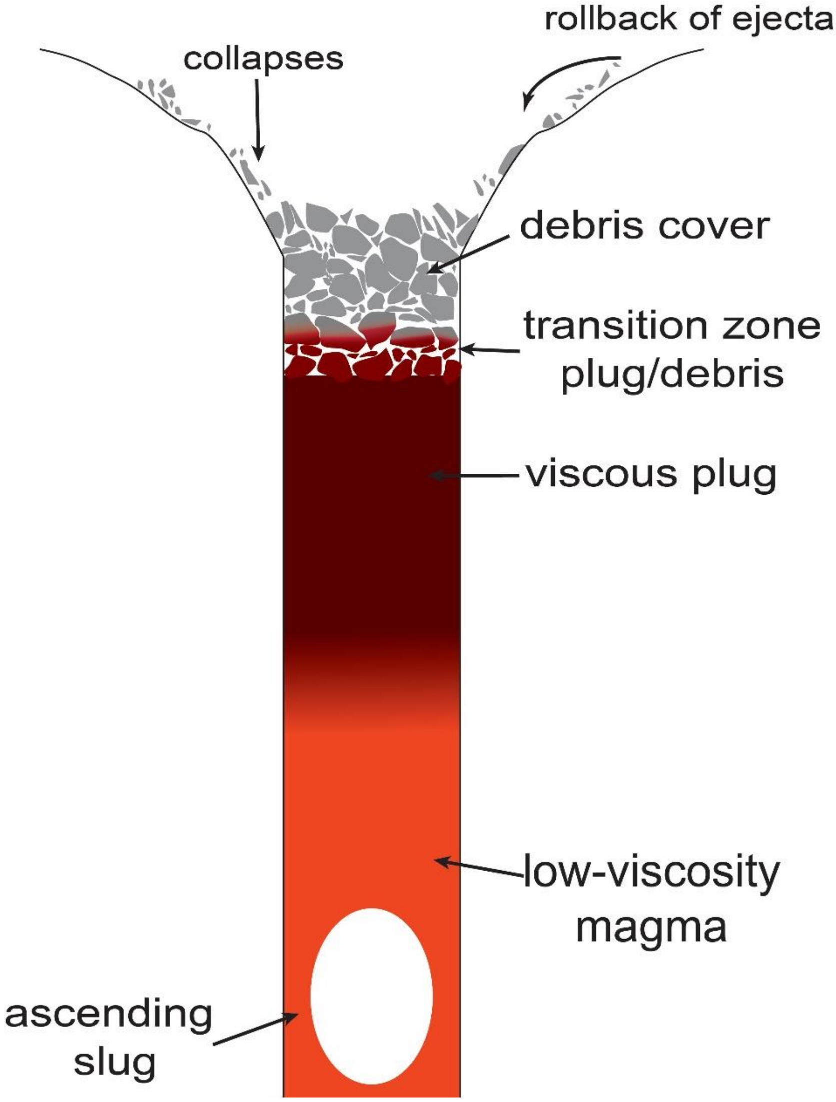

Figure 8.1 Conceptual sketch of the volcanic conduit, in which a gas slug ascends through a rheologically stratified magma column, and the vent clogged by debris. The debris cover is generated by fall-back of pyroclasts into the vent and collapses of the conduit wall; a transition zone exists between the degassed layer at the top of the magma column (plug) and the debris cover filling the vent

A second surficial layer may be also present due to temporary blockage of the vent due to backfilling of the conduit (*Fig. 8.1*). This has been proposed to result from collapses and slumping of the conduit wall, by rollback of erupted pyroclasts and lithic clasts into the vent (McGetchin et al. 1974), or magma draining back into the conduit, favouring the generation of ash plumes due to grinding of the back-fill clasts during the explosive event (Patrick et al. 2007). In light of these new findings, understanding the dynamics and evolution of vent processes during explosions at

Stromboli has gained more importance if we are to unravel the complete mechanism responsible for the persistent but extremely variable explosive activity, such as that classically observed at Stromboli. In this paper, we investigate how the presence of a debris cover affects the style of Strombolian eruptions through analysis of high-speed videos acquired at Stromboli. We identify two main eruptive regimes depending on the vent conditions (i.e., open vent vs. clogged vent) and show how the nature and amount of a debris cover strongly modify the vent processes and, eventually, explosion dynamics, magnitude and pyroclasts ejection velocity.

8.2 Terminology

Explosions at Stromboli, although relatively mild and of short duration, can be very complex in terms of both dynamics and evolution. An individual "*explosion*" is characterized by multiple, second-long "*pulses*" and sub-second-long "*sub-pulses*", each pulse being characterized by the ejection of particles at similar velocities which then decrease in time (Taddeucci et al. 2012a; Gaudin et al. 2014; Bombrun et al. 2015). In addition we can observe multiple emission points during a single event. Thus we use the term "*vent*" to indicate an area of emission points active during a single event.

8.3 Eruptions at Stromboli

Stromboli is the northernmost island of the Aeolian arc. It covers an area of ~12.2 km^2, with its summit at 924 m above sea level (a.s.l.). The current volcanic activity has persisted for at least 1400 years (Rosi et al. 2000) in the constantly evolving crater terrace located at ~800 m a.s.l. (Washington 1917; Rosi et al. 2000; Harris and Ripepe 2007), comprising three vent areas within the North-East (NEC), Central (CC) and South-West (SWC) craters (*Fig. 8.2*). This typical state of explosive activity at Stromboli is usually classified as "normal activity" and consists of recurrent mild explosions and continuous degassing (Barberi et al. 1993; Harris and Ripepe 2007a; Burton et al. 2007b), with inter-explosion time intervals of 10-10^3 seconds, and ejecting a gas-pyroclast mixture at a few tens to hundreds of meters of height (e.g., Houghton and Gonnermann 2008; Cashman and Sparks 2013; Taddeucci et al. 2013a). The "normal activity" is characterized by three main types of explosions: *Type 1* are ballistic-dominated events, with minor occurrence or absence of an ash plume; *Type 2* events involve a noticeable ash plume and can be either ballistic-rich

(*Type 2a*) or ballistic-poor (*Type 2b*) (Patrick et al. 2007). Recently, this classification has been expanded by the introduction of a new eruption type, *Type 0*, which involves gas dominated jets, characterized by the ejection of few and small juvenile pyroclasts, together with recycled material at high velocities (Leduc et al. 2015).

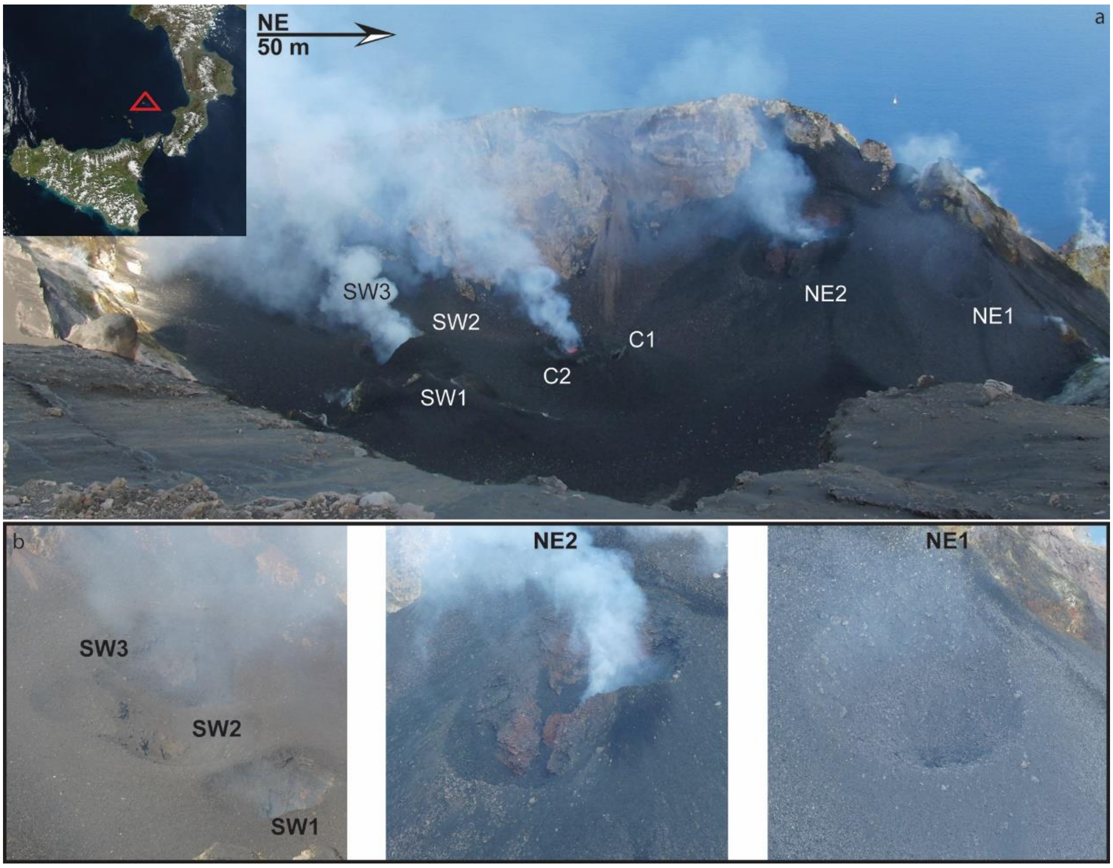

Figure 8.2 (**a**) View of the crater terrace at Stromboli from Pizzo Sopra la Fossa on September 2, 2008. SW, C, and NE mark the South-West, Central and North-East vent areas, respectively, while numbers mark individual vents in each vent area. (**b**) Close-up of the active vents imaged during the data acquisition at the North-East (NE) and South-West (SW) vent areas (satellite image courtesy of Jeff Schmaltz, MODIS Rapid Response Team, NASA GSFC, NASA Earth Observatory)

8.4 Methods

8.4.1 Equipment and data collection

Data presented here were obtained using a high-speed camera NAC HotShot 512SC. This self-contained high-speed video system records videos using a C-MOS monochromatic sensor sensitive into the near-infrared spectral region (down to about 0.1 μm), so that hot particles can be distinguished visually from cold particles by their lighter tone. At Stromboli the camera was operated at variable frame rates from 250 to 500 frames per second (fps), a resolution of 512 × 512 pixels with an 8-bit greyscale, bit density of 10 bits, and variable exposure times. The 4 GB on-board memory allowed 32.6 s of recording time at 500 fps, and 65.2 s at 250 fps.

The camera was tripod-mounted at Pizzo Sopra la Fossa, from where a complete view of the crater terrace is available (*Fig. 8.2*). This location was 288 m away and 165 m above the NE crater, 293 m away and 182 m above the SW crater, and the camera was tilted downward towards the vent of interest at an angle of 32°. The distance from the vents at the time of filming was determined by a laser telemeter (with a resolution of ± 0.5 m) and used to scale image size. A 300 mm professional lens was used, with a resulting field of view of 1.5°. Depending on the vent involved, each pixel had a width between 1.52 and 1.60 cm. All videos were acquired during daylight.

The high-speed camera data used in this study were collected during three field missions for a total of six days of shooting at the NE and SW craters zone: 4 and 5 September 2008, 17-18-19 June 2009 and 27 October 2009. A total of 49 explosions were recorded: 21 were from the NE crater and 28 from the SW crater. These covered a wide range of eruption styles, i.e.: ballistic-poor, ash-free and gas-dominated explosions (Type 0), ballistic-rich and ash-free explosions (Type 1), ash- and ballistic-rich explosions (Type 2a), ash-rich ballistic-free explosions (Type 2b). Each video covers a single vent, but occasionally – depending on the camera position – multiple active vents were involved simultaneously. In both of the crater zones several vents were active, which we refer to as NE1, NE2 and SW1, SW2, SW3 (*Fig. 8.2*, *Table 8.1*).

In addition, we use one example from the SW crater obtained on May 20, 2013, using a FLIR SC640 thermal camera (7.5-13 μm) recording at 50 fps with a 640 × 480 pixel resolution. We also include four examples from NE crater activity filmed on September 4, 2008, at 300 fps with a 512 × 384 pixel resolution using a Casio Exilim camcorder. A few visual observations from other field campaigns are also referred to in the text.

8.4.2 Analysis

The first analysis step was a qualitative description of the videos. This initial analysis allowed us first to evaluate the overall quality of the videos in terms of visibility, sharpness, focus, and disturbances from vents active outside of the camera field of view. Among all of the videos, two were discarded because the files were corrupt, and two because the erupting vent was outside of the field of view. We next described each explosion in terms of: 1) overall particle size and velocity trends, 2) variations in jet orientation, 3) multiple ejection pulses within a single explosion, 4) the presence or absence of plumes, 5) the abundance of juvenile *vs*. accidental pyroclasts, and 6) any additional processes observed.

8.4.3 Explosion duration

Explosion duration was measured using the onset of the explosion as defined by the time at which the first particle is observed in the ballistic-rich explosions, or the first ash emission in the ash-rich events. The on-board memory and the fps settings of the camera limit the maximum recording time. Thus, only for 10 cases it was impossible to define the end of the explosion, due to the memory limit or the view of the vent being obscured by the presence of ash.

8.4.4 Ejection velocities

Quantitative measurements were performed using ImageJ, a public domain Java-based image processing program (Abramoff et al. 2004), and the MTrackJ plug-in (Meijering et al. 2012). The MTrackJ plugin allows manual tracking of moving objects within an image stack, and was used for parameterizing the ejection velocity of pyroclasts. Velocities were manually measured for centimetre-sized clasts, where selected particles exiting the vent were tracked for 4-10 frames. One or more new trajectories were initiated every 2-4 frames, covering the fastest visible pyroclasts. For each trace we measured the mean velocity (m/s) over all traced points forming the trajectory (and standard deviation, σ). All the measurements were made as close as possible to the vent. The ejection velocity was measured for all explosions ejecting clearly traceable particles. Out of 45 videos, 15 were selected as the most representative of the overall variability and were processed for their entire duration so as to be used as reference models, and covered each vent in each of the measurement day. For the remaining videos, velocity measurements focused on the onset of the explosion and key moments, selected based on qualitative observations (e.g., peak of activity, onset of multiple pulses). For each explosion, we measured a minimum of 37 up to a maximum of 4001 pyroclasts (*Table 8.1*).

event	date	GMT	vent	duration (s)	fps	v max (m/s)	vent condition	N
1	04/09/08	12:20	NE1	>30 s	500	62.94 ± 3.3	coarse-grained	284
2	04/09/08	12:33	NE1	4 s	500	50.07 ± 3.7	coarse-grained	286
3	04/09/08	13:30	NE1	>30 s	500	69.15 ± 12.6	coarse-grained	606
4	04/09/08	11:00	NE2	15 s	500	188.74 ± 10.3	open	398
5	04/09/08	11:20	NE2	6 s	500	323.14 ± 74	open	336
6	04/09/08	11:36	NE2	>30 s	500	256.45 ± 10.1	open	949
7	04/09/08	14:37	SW3	13 s	500	37.87 ± 10.4	coarse-grained	232
8	04/09/08	16:55	SW1	>30 s	500	--	coarse-grained	--
9	05/09/08	10:20	SW1+2	10 s	500	19.28 ± 1.7	fine-grained	131
10	05/09/08	10:39	SW1+2	8 s	500	19.12 ± 0.9	fine-grained	37
11	05/09/08	10:45	SW1+2	20 s	500	16.58 ± 0.8	fine-grained	237
12	05/09/08	11:13	SW1+2	12 s	500	21.1 ± 2.6	fine-grained	117
13	05/09/08	11:51	SW1+2+3	25 s	250	19.07 ± 3.3	fine-grained + open	167
14	05/09/08	12:03	SW1+2+3	>56 s	250	28.6 ± 1.1	fine grained + open	656
15	05/09/08	12:20	SW1+2+3	25 s	250	17.18 ± 2.05	fine-grained + open	466
16	17/06/09	09:xx	SW1	~60 s	250	388.02 ± 70.7	open	1887
17	17/06/09	09:57:23	NE1	>30 s	500	--	--	--
18	17/06/09	11:16:30	SW1	>30 s	500	152.21 ± 11.3	open	478
19	17/06/09	11:35:42	SW1	>30 s	500	205.81 ± 4	partially covered	821
20	17/06/09	12:02:20	SW1	>30 s	500	259 ± 6.6	partially covered	3370
21	17/06/09	12:25:13	SW1	>30 s	500	230 ± 2.2	open	4001
22	17/06/09	13:05:17	SW1	~32 s	500	172 ± 13.7	open	2425
23	17/06/09	13:17:39	SW1+2	22 s	500	26.08 ± 1	open + coarse-grained	116
24	17/06/09	13:36:55	SW1+2	7 s	500	--	coarse-grained	--
25	17/06/09	14:14:58	SW1	>30 s	500	224.84 ± 12.8	partially covered	667
26	17/06/09	14:30:28	SW1	~32 s	500	181.96 ± 12.9	open	1089
27	17/06/09	14:41:44	SW1	20 s	500	138.76 ± 17.4	open	538
28	17/06/09	15:26:50	SW1	26 s	250	409.82 ± 6.9	open	1802
29	18/06/09	11:xx	NE2	20 s	500	74.7 ± 9	coarse-grained	283
30	18/06/09	10:34:50	NE2	7 s	500	120.85 ± 2.6	coarse-grained	129
31	18/06/09	10:59:20	NE2	10 s	500	53.9 ± 2.5	coarse-grained	174
32	18/06/09	12:06:xx	NE2	7 s	500	--	--	--
33	19/06/09	09:30:xx	NE1	17 s	500	367.90 ± 1.2	open	351
34	19/06/09	10:48:29	NE1	10 s	500	226.22 ± 17	open	599
35	19/06/09	11:04:46	NE1	25 s	500	365.49 ± 12.1	open	599
36	19/06/09	11:26:08	NE1	20 s	500	316.93 ± 29.6	open	477
37	19/06/09	12:04:41	NE1	18 s	500	168.89 ± 6.5	open	2706
38	19/06/09	12:15:30	NE1	12 s	500	197.09 ± 1.6	open	708
39	19/06/09	12:39:57	NE1	12 s	500	166.46 ± 13.5	open	644
40	19/06/09	13:01:34	NE1	15 s	500	268.71 ± 7.8	open	624
41	19/06/09	13:18:38	NE1	11 s	500	127.44 ± 2.2	open	1616
42	19/06/09	13:32:34	NE1	20 s	500	324.24 ± 10.2	open	769
43	27/10/09	11:38:37	SW1	?	500	--	--	--
44	27/10/09	11:53:21	SW1	11 s	500	370 ± 3	open	1250
45	27/10/09	12:03:35	SW1	8 s	500	199.12 ± 2.5	open	873
46	27/10/09	12:23:15	SW1	9 s	500	337 ±	open	494
47	27/10/09	12:40:02	SW1	5 s	500	190.47 ± 17.7	open	411
48	27/10/09	13:32:51	SW1	6 s	500	367 ± 18.2	open	1405
49	27/10/09	13:58:55	SW1	13 s	500	405 ± 28.2	open	1479

Table 8.1 Parameters (vent location, duration, maximum ejection velocity, vent condition and number [N] of measured pyroclasts) for each explosion imaged by the high-speed camera

8.5 Activity description

Based on specific vent conditions at the time of the video acquisition, we identified two end-members of eruptive regimes, depending on the state of the vent before an explosion: one where the vent was completely obstructed by debris (ranging from blocks to ash in size), and a second where the vent was open, without any cover. In between, explosions featuring processes common to both groups occurred.

8.5.1 Activity at clogged vents

In the first regime, all explosions were preceded by the uplift of the debris cover, but the type of debris comprising the vent infill resulted in remarkably different processes. With coarse debris, once the cover reached a critical degree of inflation (*Fig. 8.3a, b*), several breaches between the blocks were formed, from which jets of relatively cold, fine particles started to propagate. Ash emission from the breaches produced an ash plume (*Fig. 8.3c, d*), whose height often exceeded the camera field of view (9 m, *Fig. 8.3e*), followed closely by the ejection of juvenile pyroclasts (*Fig. 8.3f*). In some cases, this initial pulse managed to remove only part of the debris from the vent. The following jets managed to make their way through the remaining blocks and to propagate from a small localized point of emission. These were collimated jets that reached a height exceeding the limit of the camera field of view, alternating with poorly collimated ones (Video 1).

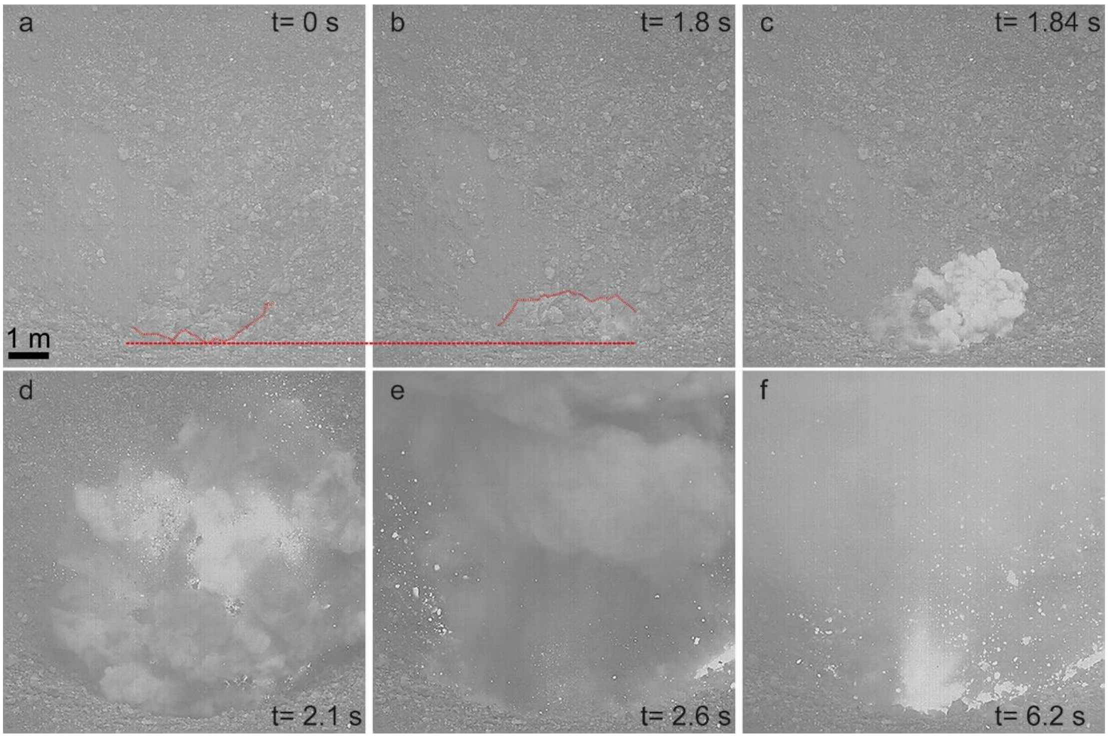

Figure 8.3 Vents with a coarse-grained debris cover: representative still-frames of an explosion at the NE1 vent. Red polylines highlight the debris profile before (**a**) and after (**b**) the ground inflation preceding the explosion (**c**), with the dashed line representing the initial lowest position. An ash plume, accompanied by ejection of juvenile (brighter tones) and few accidental (darker tones) pyroclasts (**d-e**), is followed by collimated jets of pyroclasts (**f**)

Slumping of the inner crater walls and rollback of ejecta down the inner crater slopes toward the vent was evident. In a few cases we observed the formation of a new, very small and localized emission point near the main one, characterized by continuous gas and pyroclast emission reaching heights well within the camera field of view (≤ 9 m). Initial ejection velocities reached up to 63 ± 3 m/s, with few velocity fluctuations, followed by rapid velocity pulses with occasional fluctuations and increasing velocities. Emissions from secondary points reached velocities up to ~70 m/s, while the shortest and weakest pulses had an average velocity of <30 m/s, featuring several velocity peaks up to 50 ± 4 m/s. In contrast, when the initial pulse was energetic enough to entrain and clear-out all the debris in the vent, the explosions involved the ejection of a mixture of juvenile and recycled, ash- to block-sized, pyroclasts (Video 2). The inflation process that preceded these explosions lasted for up to tens of minutes, and was followed by subsequent deflation (Video 3). These vent cover motions reach vertical displacements up to 1.9 m, with velocities up to 0.91 m/s where debris doming accelerated nonlinearly in the few seconds preceding an explosion (*Figs. 8.3a, b* and *8.4*).

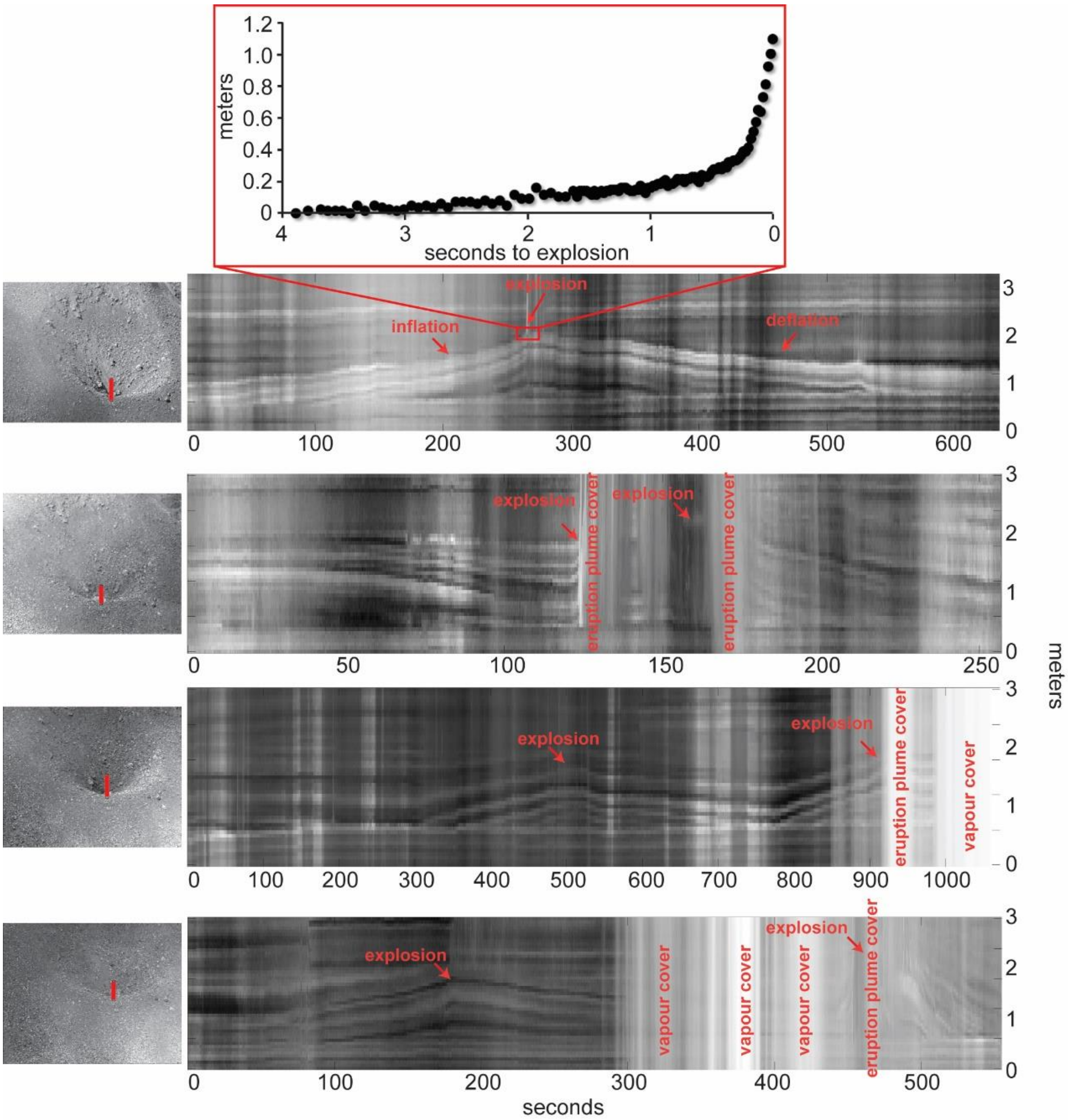

Figure 8.4 Ground deformation of the NE1 vent shows that cycles of inflation-deflation may last several minutes. Each plot displays the temporal evolution of grey levels in the videos along a vertical line crossing the vent (red line, about 3 m long, on the left-hand still frames). Inflation accelerates nonlinearly a few seconds before an explosion (top inset)

For vents covered by fine particles, explosions were preceded by a slow and uniform expansion of the cover, until a sudden increase in the expansion velocity led to a breach in its central section from which jets began to propagate (*Fig. 8.5a, b*). These jets involved gas, ash and lapilli-sized pyroclasts emission, with few block-sized pyroclasts, and the development of a conspicuous ash plume, which often visually obscured many of the lapilli-sized pyroclasts. Occasionally, the fine-grained debris was displaced en-masse and its collapse triggered a pyroclastic density current that travelled for some tens of meters away from the vent (*Fig. 8.6*, Video 4). The explosions continued with an initial gas thrust phase and the ejection of juvenile pyroclasts and lithics, but the high-concentration of ash made it difficult to impossible to discern pulses, except for powerful ones when hot material overtook the front of the plume. Sometimes, falling of veils of ash seemed to mark the end of the explosion (*Fig. 8.5c*), only for ejection of juvenile and lithic clasts to resume from the same emission point, often along with the emission of a conspicuous ash plume from a new emission point within the vent or from a nearby vent (*Fig. 8.5d*, Video 5). Despite a vigorous gas thrust phase, these explosions were characterized by low ejection velocities, with a maximum of 21 ± 3 m/s, and lasted from a minimum of ~8 s up to ~20 s. All explosions were preceded, and followed, by rolling of blocks and sliding of finer material down the inner crater slopes and towards the vent.

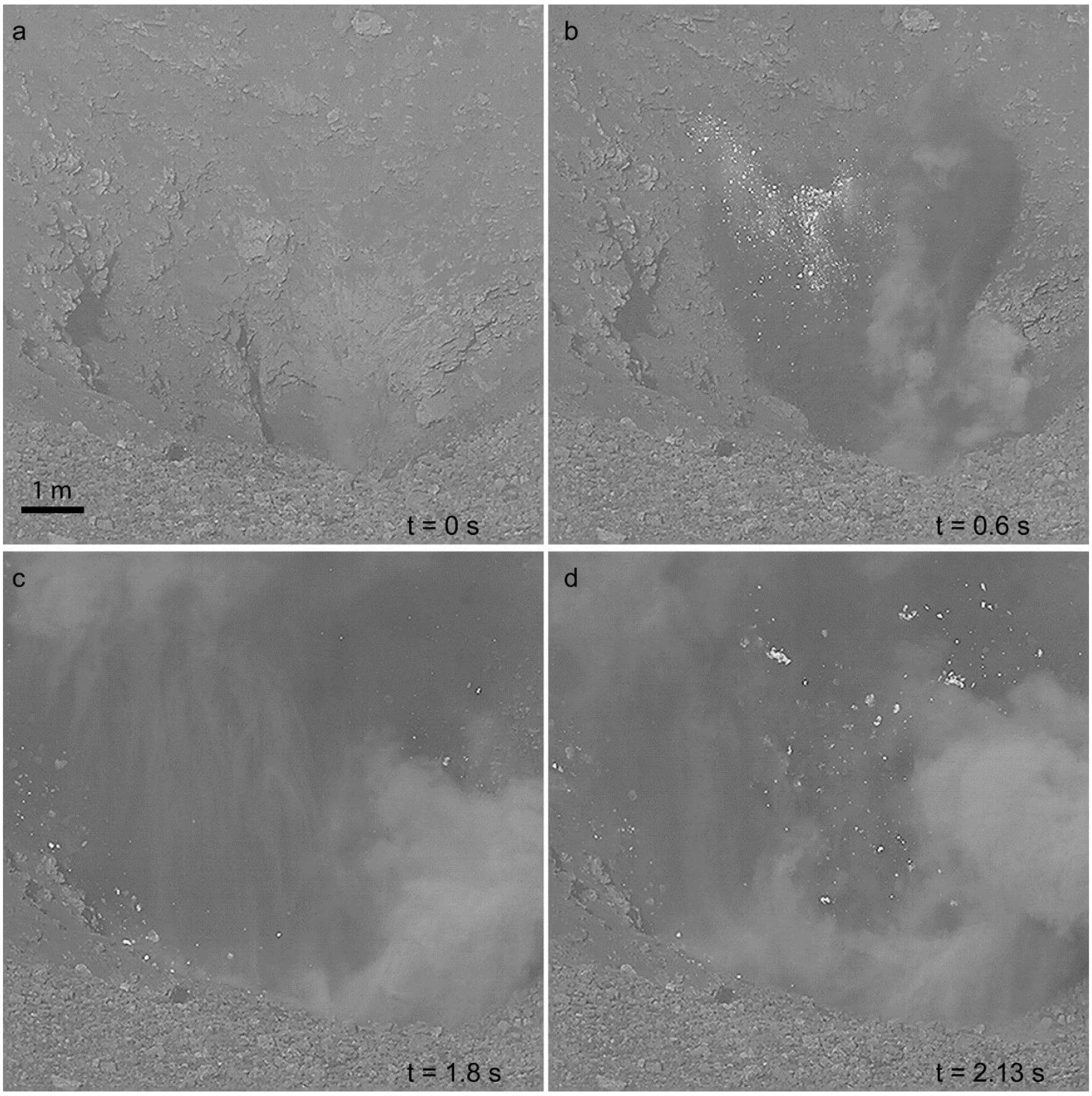

Figure 8.5 Vents with a fine-grained debris cover: explosion at the SW1 vent (**a**). When a fine-grained debris cover is breached, a mixture of ash and coarse pyroclasts is released (**b**). A substantial amount of fine material falls back into the vent (**c**), followed by a new, weaker emission of ash and coarse pyroclasts (**d**)

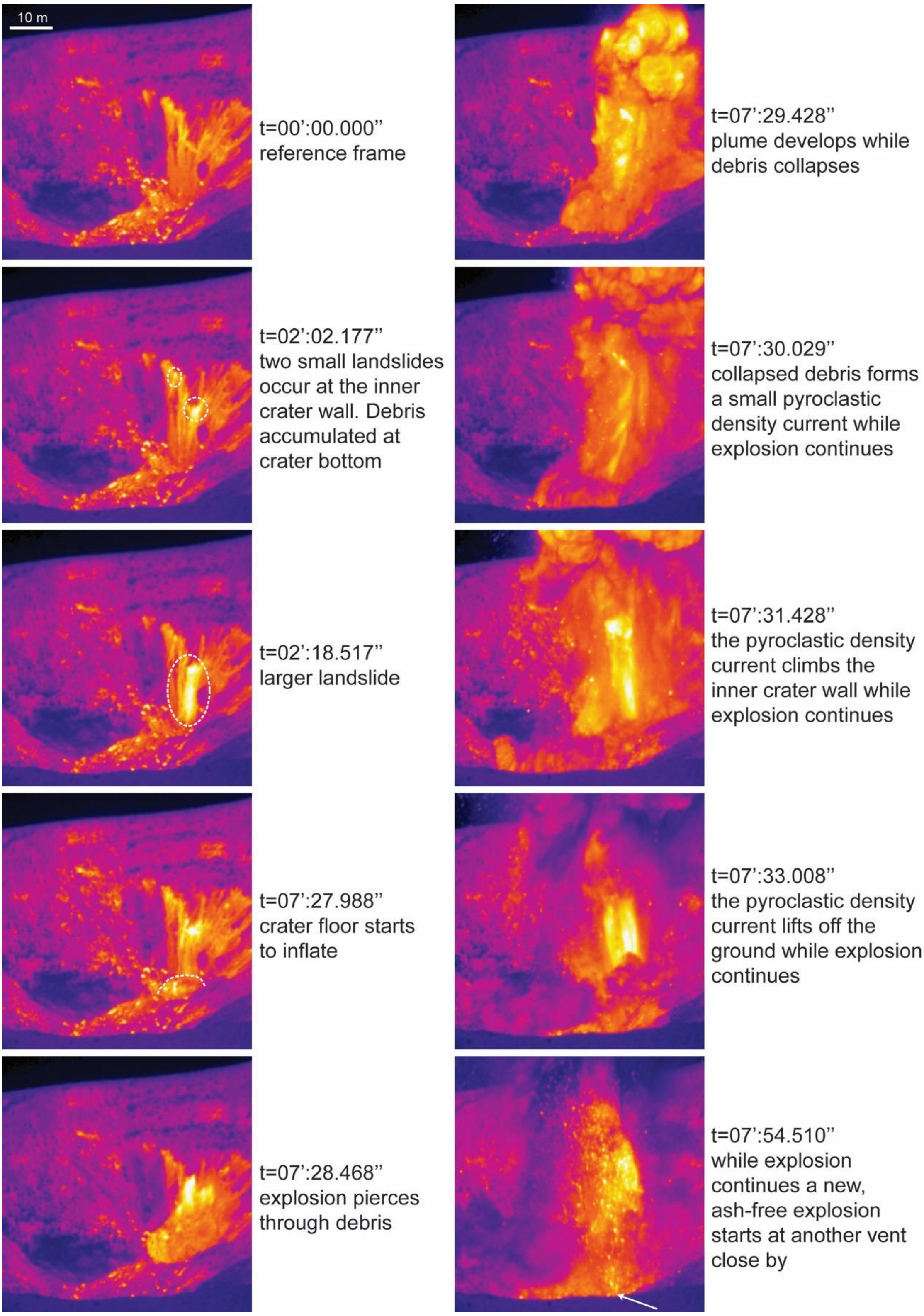

Figure 8.6 Selected frames of a thermal video from the SW vent, covering the first 7':55'' of the explosion: landslides (dashed circles, 02':02.177" and 02':18.517") and ground deformation (dashed line, 07':27.988") precede an initial ash emission breaking through the debris cover. Debris collapse triggers a small-scale pyroclastic density current (07':30.029"). While the explosion continues, a new ash-free explosion starts from a nearby vent (white arrow, 07':54.510")

8.5.2 Activity at open vents

Vents that were clear of debris displayed a faint glow and the emission of fumes. In these cases, ballistic-dominated (Type 1) explosions occurred, with minor or no associated ash phase. All explosions began with a diffuse spray of a few hot pyroclasts, exiting the vent and followed by more heavily loaded pulses of coarser pyroclasts (a similar behaviour for Type 1 explosions was also observed by Harris et al. 2012), occasionally interspersed by sub-pulses (*Fig. 8.7*). Often, the ejection of meter-sized spatter also occurred. These molten clots were flattened on landing on the inner crater walls. Often, ejecta fell back around and into the vent, and then seemed to be re-worked and ejected again in the following sub-pulses.

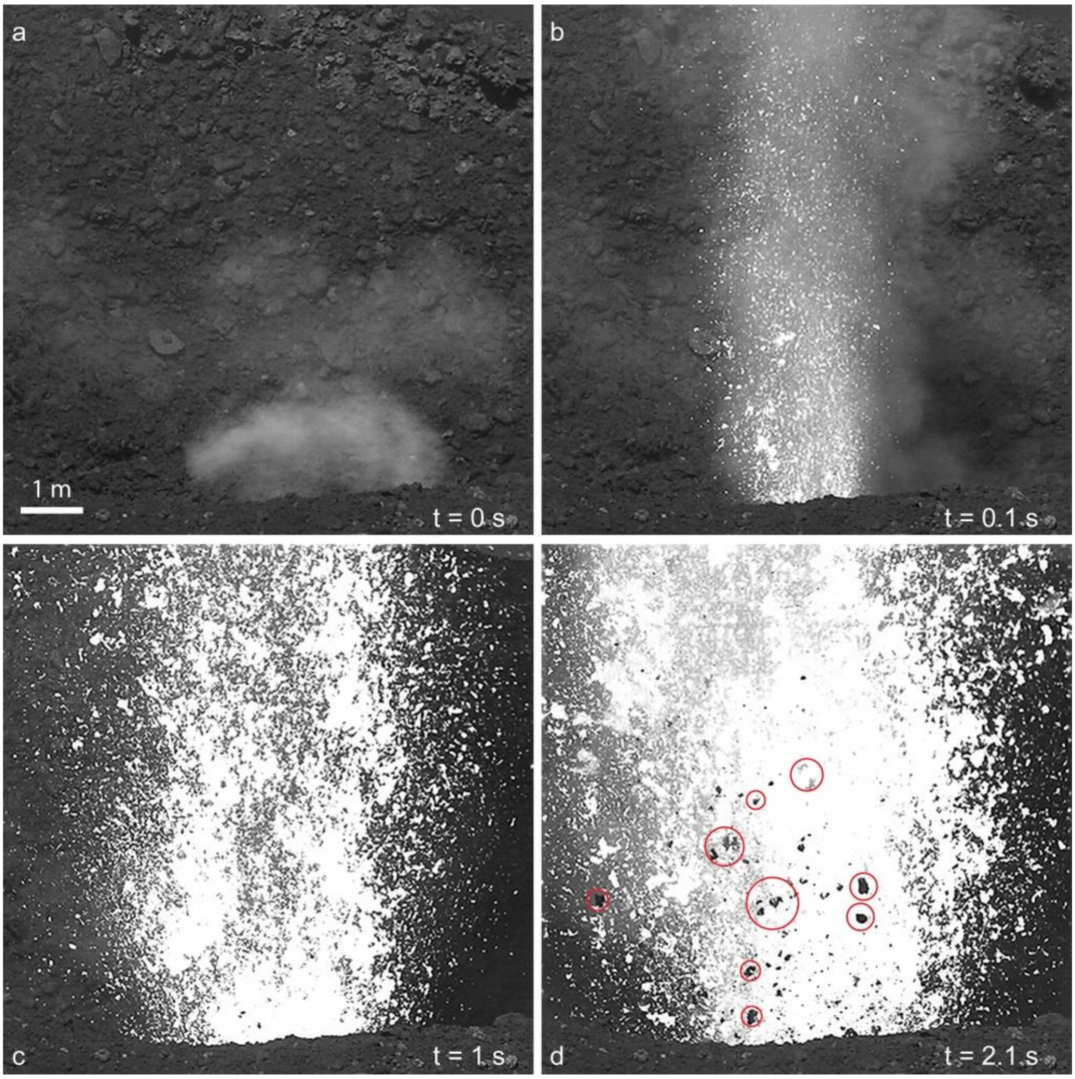

Figure 8.7 Open vent: at the NE1 vent (**a**), a dominant, well-collimated jet of fast pyroclasts (**b**) decays rapidly, followed by tens of pulses and sub-pulses that evolve quickly with wider exit angle (**c**). Concomitant to the peaks of activity, decimetre-sized, colder recycled clasts (red circles) are ejected (**d**) and, at the same time, both the eruption rate and exit angle increase

The explosions lasted between 5 s and >33 s. When it was possible to observe the whole explosions, a gradual decrease in the amount of ejected material over time was evident, mirrored by a well-defined coda of decreasing pyroclast velocity (Video 6). The average velocities ranged between 20 m/s and 50 m/s, featuring tens of high velocity peaks: usually <250 m/s (*Fig. 8.8a, b*), but in some cases exceeding 300 m/s, with an observed maximum of 410 ± 7 m/s (Explosion 28). These pulses and sub-pulses occurred so frequently that their individual velocity decay trends merged together. This explosive behaviour was characteristic of the SW vents during two working days in June 2009. As an extreme example of this type of behaviour, a *Type 0* explosion occurred on May 24, 2013, from a meter-sized, glowing, round hole in the SW vent area, with the ejection of relatively few lapilli-sized ejecta, and attained pyroclast velocities of 498 ± 19 m/s.

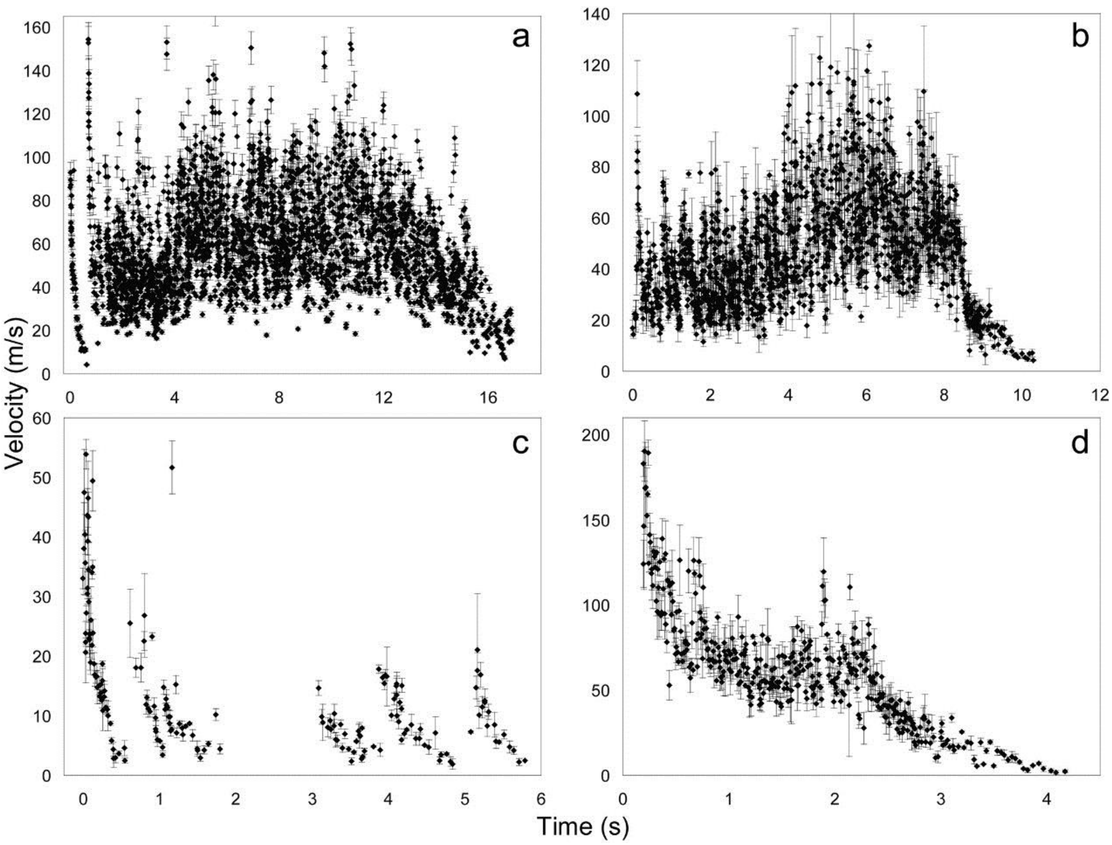

Figure 8.8 Examples of ejection velocity of pyroclasts over time for explosions at open vent NE1 (**a**, **b**), coarse-cover vent NE2 (**c**) and fine-cover vent SW1 (**d**) vent. Each point represents the velocity of a single centimeter-sized pyroclast, averaged over 4–10 frames. Time = 0 corresponds to the time at which the first pyroclast is observed

8.5.3 Intermediate and transitional cases

In several cases, the incandescent surface of the top of the magma column was visible in the vent partially covered by blocks and lapilli from previous explosions. In the very first seconds of an explosion, this surface would be disrupted by the bursting of variable sized gas bubbles, which re-worked the debris without cleaning-out the vent, until - but not always - a more energetic pulse cleared the vent (Video 7). Individual reworked blocks, when finally ejected, often showed coexisting hot and cold surfaces. In the study cases, bubbling of the surface lasted from ~ 4 to ~ 7 s. The first pulse was followed by an increase in the bubble-burst number and occurrence rate, until pyroclast ejection became almost continuous with multiple pulses and sub-pulses. As in previous cases, spatter was ejected and fell back into the vent, or become plastered onto the inner crater walls, to be recycled by the following pulses. The angles of the jet axes in the main pulses varied widely, between ~ 90º and ~ 45 º.

In several cases, two adjacent vents in the SW crater (SW1 and SW2) were observed to erupt simultaneously (*Figs. 8.6, 8.9*): one was clearly covered by fine particles and was characterized first by degassing (*Fig. 8.9b*), then by ash emission (*Fig. 8.9c*); the second was partially obscured and involved ballistic-dominated and ash-free emission (*Fig. 8.9b-c*). Explosions lasted from ~15 s up to 56 s and were characterized by low peak velocities, with a maximum just of 29 ± 1 m/s. In all cases, velocity time series showed several distinct decay trends lasting 0.2-1 s.

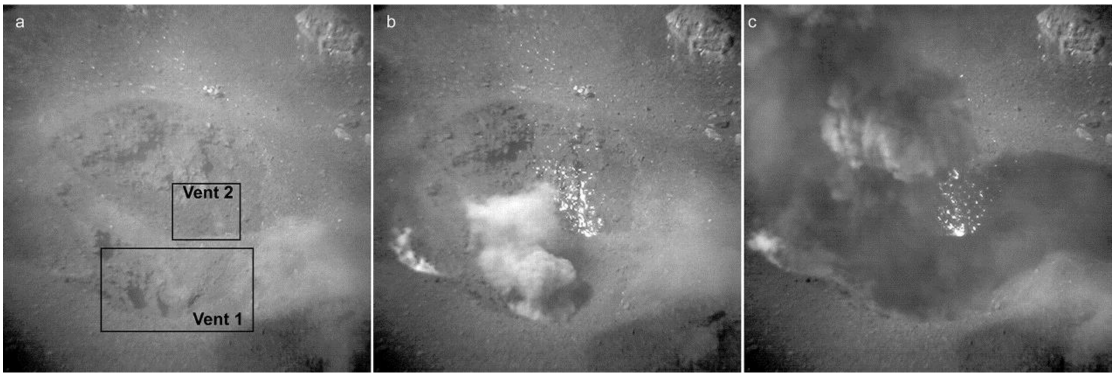

Figure 8.9 SW1 and SW2 vents (**a**), showing different eruptive styles during simultaneous activities: SW1 is characterized by degassing (**b**) and ash emission (**c**), while SW2 shows ballistic-rich and ash-free explosions (**b-c**)

8.6 Discussion

Based on visual features, we identified two end-member conditions of the volcanic vents producing Strombolian explosions, i.e. clogged *vs*. open vents, which seem to have affected both the style and vigour of the eruptions.

8.6.1 Effect of the cover

The presence and nature of vent cover has been hypothesized to influence explosion style at Stromboli by Patrick et al. (2007), and more recently by Leduc et al.

(2015). Our observations provide the first direct confirmation to this hypothesis. Within our limited number of observations, *Type 0* explosions invariably occurred through open vents, *Type 1* through open or sparsely covered vents, and *Type 2* through heavily covered vents. The dynamics of vent cover incorporation in the erupted gas/pyroclasts mixture controlled the explosion style (and type). A weak explosion through a coarse-grained debris cover (*Fig. 8.3*) would be classified as a bomb-free *Type 2b* explosion according to Patrick et al. (2007). In this case, weakly overpressured gas may have effectively elutriated only the finer particles from the overall coarse-grained cover. A stronger explosion at the same vent would also mobilize coarser pyroclasts in a bomb-rich *Type 2a* explosion. Fine-grained covers were usually entrained entirely into the plume. A thick, fine-grained cover in a narrow vent can be ejected en-masse, resulting in a small-scale pyroclastic density current (*Fig. 8.6,* Video 4) preceding the main explosion.

Several lines of evidence suggest that covered vent explosions are less energetic than open vent explosions. Covered vent explosions have lower pyroclasts ejection velocity and are never associated with visible shock or pressure waves (Taddeucci et al. 2014). Likewise, ash-rich (*Type 2*) explosions at Mt. Yasur (Vanuatu) are associated with lower acoustic amplitudes than ash-free (*Type 1*) events (Spina et al. 2015). The presence of a debris cover in the vent may affect the gas behaviour both before its release from the magma (i.e., at fragmentation), when the gas has to lift and dislodge the cover, as well as after fragmentation, when the gas has to either accelerate the debris or percolate through it. Recent experimental investigation shows how the presence of a viscous plug at the top of the magma column acts to increase the pressure at burst of slugs (Del Bello et al. 2015). We found no evidence for such an increase in the presence of cover, which apparently did not affect the growth and pressurization of the gas slugs. This is probably because the debris cover is too weak – as it is unconsolidated – to hinder gas expansion and, thus, increase slug overpressure at burst. Conversely, the presence of cover acted to dampen the energy of the event, because part of the energy stored in the gas overpressure dissipated through percolation and was used in debris acceleration. The final outcome of an explosion thus results from the competition between the amount, coherence and size of the clogging material, and the volume and pressure of the gas slug arriving at the base of the plug. In analogy to other explosive processes, we propose that this competition can be expressed by the scaled depth concept (the thickness of the debris cover divided by the cube root of the stored energy), which has been shown experimentally to control ejecta velocity and pressure wave amplitude (Taddeucci et al. 2013b).

The vertical motion of the debris cover (*Fig.8.4*) could be linked to volumetric changes in the conduit before and after an explosion. These changes occurred in the timescale of hundreds of seconds, which is comparable to the timescale of pre-explosion conduit pressurization recorded by ground motion (Genco et al. 2010), and is also compatible with time scales of bubble rise and growth in a basaltic magma (Nishimura 2009). The accelerating trend of inflation of the debris that we observed in the seconds before an explosion also matched the surface motion of a liquid column hosting a rising, pressurized gas slug (James et al. 2008, 2009). We conclude that, before an explosion, the vent-filling debris is pushed upward by the magma head which, in turn, is rising under the effect of the ascending and expanding gas slug. After the explosion, the remaining debris cover subsides back into the vent. The rate of subsidence could be controlled by the gravitational collapse of the debris into an empty conduit or the gradual sinking of the magma head. Our observations do not allow a conclusive discrimination between the two cases. However, the similar rates of debris inflation and deflation seem more readily explained by gradual magma sinking rather than debris collapse.

8.6.2 Origin of the cover

Fall-back of pyroclasts into the vent is the prime process for the formation of the debris cover. Pyroclasts were observed to fall back directly from the plume, during or after an explosion, and from the inner flanks of craters, by rolling and sliding (also, ejecta from the NEC have been observed to fall into open vents in SWC: thus, one vent may produce clog material for another one; Andy Harris, personal communication, 2015). Central to the formation of the cover is the relationship between energy and dynamics of the explosions on the one hand, which controls the size, range and trajectory of the pyroclasts, and the morphology of the vent area on the other, which controls pyroclast accumulation and distribution. At the timescale of weeks-months, the two factors are not independent at Stromboli, where periods of more frequent activity are also marked by stronger activity (Taddeucci et al. 2013a). A stronger and more frequent activity implies a wider dispersal of products and higher emission rates, promoting the growth of positive landforms around vent areas and limiting fall back (up to the formation of hornito structures). On the contrary, weaker and less frequent activity implies smaller dispersal of pyroclasts and negligible variations in the vent settings, both favouring debris accumulation, as also speculated by Patrick et al. (2007). At the timescale of hours-days a positive feedback may arise between debris accumulation resulting in weaker explosions, causing reduced ejecta range and, consequently, increasing clast fall back toward the vent. The feedback may be broken by an occasional explosion strong enough to clean the vent. The extreme sensitivity of this feedback to local conditions is well illustrated by cases of two neighbour vents erupting simultaneously but with different styles (*Figs. 8.6* and *8.9*), where minor variations result in different degrees of vent cover and explosion types even at two interconnected vents.

The mechanical and thermal state of the vent cover is open to speculations. For instance, the source of ash in *Type 2* explosions could be milling from repeated collisions among coarser clasts over multiple explosions or brittle fragmentation of cooled and crystallized magma, as argued by Patrick et al. (2007). We directly observed milling and fall back of ash into the vents (*Figs. 8.3* and *8.6*). However, we also note that, with respect to coarser pyroclasts, ash was easily wind-advected outside the vent areas, suggesting that an internal source of ash (i.e., magma fragmentation) may be required for prolonged *Type 2* activity periods. The presence of degassed and crystallized magma at the top of the Stromboli conduits is well established (e.g., Lautze and Houghton 2006; Gurioli et al. 2014), along with the potential role of clast recycling on its formation (D'Oriano et al. 2014). Indeed, there must be an interface, or transition zone, between the degassed layer at the top of the magma column and the debris cover filling the vent (*Fig. 8.1*). Direct evidence for this zone is provided by the observed partially molten clasts, and by the high temperature of the ash filling the vent (*Fig. 8.6*). The mixing with fallen back debris, due to pre- and post-explosion disruption of the debris cover, would increase the viscosity of the magma residing in the topmost part of the conduit, by enhanced cooling and addition of solids (crystals and cold scoria fragments), thus promoting its brittle behaviour and fine fragmentation.

8.7 Conclusions

High-speed observations of vent activity at Stromboli show how open vent *vs.* debris-clogged vent conditions affect the style of explosive activity. The debris cover forms by accumulation of pyroclasts into the vent by fall-back and rolling/sliding along the inner crater walls, controlled by the interplay of frequency and intensity of the explosions. The effects of the vent cover can be summarized as follows:

1) with respect to explosions at open vents, clogged vents feature the ejection of slower (and colder) pyroclasts, the presence of a debris cover effectively dampening and slowing down the gas expansion process;

2) for debris-covered vents, explosion dynamics are sensitive to the amount and grain size distribution of the debris: while *Type 2a* explosions are observed mainly from vents with fine-grained cover, weaker *Type 2b* explosions occur through vents with a coarse-grained cover. This observation confirms previous hypothesis on the origin of different explosion types (e.g., Patrick et al. 2007; Leduc et al. 2015);

3) meter-scale vertical motions of the debris cover precede (inflation) and follow (deflation) explosions on a timescale of tens of minutes, paralleling motions of the magma head. The rise rate of the debris cover is compatible with that expected for the rise and expansion of a pressurized gas slug toward the top of the magma column;

4) the debris cover is observed to thermally and mechanically interact with the magma at the top of the conduit, possibly resulting in cooling and increased viscosity, in turn promoting brittle, finer fragmentation of the top magma layer.

The observed phenomena show how the presence and nature of a debris cover may lead to complex eruptive dynamics, by affecting gas expansion, eruption intensity, grain size distribution and ejection velocity of erupted material. These findings need to be considered and integrated in future models to better understand how the interaction between arriving gas slugs, a possible viscous plug and a near-surface debris cover controls explosion style and vigour.

8.8 Video description

Video 01 A slight inflation of the coarse-grained debris cover precedes a weak explosion at the NE1 vent: the impulse is not energetic enough to clear the vent, and only a small jet of pyroclasts makes its way through the debris, followed by a slow deflation of the cover.

Video 02 A significant inflation of the coarse-grained debris cover precedes the ash-rich explosion at the NE1 vent. The initial impulse is powerful enough to remove most of the debris from the vent, with the following jets making their way through the remaining blocks. Note the fallback of pyroclasts in the vent by rolling along the inner crater walls.

Video 03 Vertical ground motions of the NE1 vent covered by a coarse-grained debris cover show that the cycles of inflation-deflation can last several minutes. The ellipse highlights the area where the cycles occur.

Video 04 Montage of the most representative parts of an explosion at the SW vent from a thermal video showing some of the processes preceding an ash-rich explosion, comprising landslides and ground deformation. As the ash plume develops, the collapse of the debris triggers a pyroclastic density current. The initial explosion is followed by an ash-free one form a nearby vent.

Video 05 Inflation of the fine-grained debris cover precedes an ash-rich explosion at the SW1 vent. Most of the fine material falls back into the vent, while a new explosion starts from the SW2 vent ejecting a mixture of ash and coarse pyroclasts. Note the ejection of several clasts showing the coexistence of hot and cold surfaces.

Video 06 Explosion at the NE1 open vent comprises an initial jet of fast pyroclasts, followed by several pulses and sub pulses showing an increase in both eruption rate and clast size.

Video 07 The bursting of variable sized bubbles disrupts the magma surface partially covered by blocks, re-working the debris, until a powerful impulse clears the vent followed by a series of pulses. Note the presence of clasts showing the coexistence of hot and cold surfaces.

8.9 Acknowledgements

A.C. was funded by MIUR (Ministry of Education, University and Scientific Research of Italy) grant “Parameterizing the Dynamics of Strombolian Eruptions through High-Speed Video Analysis” and, as part of his PhD at Lancaster University, from the People Programme (Marie Curie Actions) of the European Union's Seventh Framework Programme (FP7/2007-2013) under the project NEMOH, REA grant agreement n° 289976. We are indebted with U. Kueppers, E. Del Bello, Zazà, and all other colleagues, friends, and scecchi who helped us in the many field campaigns at Stromboli. We thank journal reviewers Matt Patrick and Andy Harris, and associate editor Pierre-Simon Ross for thorough and constructive comments that greatly improved the manuscript.

Chapter 9 - Discussion and Conclusions

This study challenges one of the main simplifications in current modelling of Strombolian eruptions, the assumption of a rheologically uniform magma column. The experimental and numerical approaches presented here allowed identification of (1) a plausible spectrum of slug flow configurations possible within a rheologically stratified column, (2) configuration relevance to Strombolian-type volcanoes, with an emphasis on Stromboli volcano, (3) constraints on the parameters controlling configuration transition and (4) the effects of each flow configuration on eruption dynamics and geophysical signals.

For each identified flow configuration, the extent and viscosity of the plug strongly affected the gas expansion that is the main plausible source mechanism for both seismic and acoustic signals. Furthermore, different degrees of slug overpressure lead to a range of burst processes at the surface, resulting in variations of explosive activity. Thus, it is crucial to understand which parameters control the changes in the conduit dynamics affecting the slug overpressure and, ultimately, eruption metrics and geophysical signals.

One of the main open questions regarding Strombolian eruptions concerns the extreme variability in style, magnitude and, therefore, detectable geophysical signals. This variability is interpreted as variations in gas slug size, but it is also often explained in terms of variations in the rheological properties of the magma in the shallower part of the conduit (e.g., Taddeucci et al. 2004; Lautze and Houghton 2006; Gurioli et al. 2014) or interaction between the gas and a possible in-vent debris cover (e.g., Patrick et al. 2007; Leduc et al. 2015). The results of this study illustrate how both scenarios have an important role in modulating Strombolian explosions and modifying gas overpressure.

Volcanoes such as Stromboli can have open- or covered-vents. In both cases, the magma column may be capped by a viscous plug generated by cooling- and degassing-driven crystallization of the magma in the shallower part of the conduit (e.g. Taddeucci et al. 2004; Cimarelli et al. 2010). However, viscosity can further increase from addition of solids due to wall collapses and their partial assimilation (e.g., D'Oriano et al. 2014; Ch. 8, Capponi et al. 2016b) and a second, more superficial, debris cover can form due to fall back of material into the vent (e.g., Patrick et al. 2007; Leduc et al. 2015; Ch. 8, Capponi et al. 2016b). Therefore, slug overpressure and eruption dynamics will depend on (1) the extent and viscosity of a plug, controlling (together with gas mass and conduit radius) which flow configuration operates in the conduit and (2) whether the gas/pyroclasts mixture is released at burst directly into the atmosphere or first the gas interacts with a vent cover, further affecting its release and the nature of the explosion.

Previous models of single-viscosity systems demonstrated how slug overpressure varies with the thickness of the falling film, λ, controlled in turn by magma viscosity (James et al. 2009; Del Bello et al. 2012). Film thickness plays an important role in a plugged conduit as well, where it strongly depends on which flow configuration operates in the conduit. Furthermore, the presence of the plug itself modifies gas overpressure during slug ascent in the lower viscosity liquid, by hindering gas expansion. Therefore, the final overpressure at burst will also depend on how much the plug hinders slug expansion during ascent and how thick is the film surrounding the slug at burst (Ch. 6, Capponi et al. 2016a).

A first effect of the different flow configurations may concern the ground deformation associated with the near-surface expansion of an ascending slug (e.g., Genco and Ripepe 2010). Despite the difficulties of measuring near-vent deformation in Strombolian-type volcanoes, due to the nature of the event leading to relatively minor displacements, ground deformation has been observed prior the explosions using seismic data and tilt-meters. The initial inflation is consistent with the increase in conduit pressurization and consequently with the magma acceleration prior to burst, and it is followed by an in-vent deflation, associated with the release of the gas-pyroclasts mixture at burst (e.g., Genco and Ripepe 2010; Lyons et al. 2012). A similar trend is shown by inflation of the vent cover at Stromboli, showing vertical displacement characterized by timescales of up to tens of minutes, and a non-linear acceleration a few seconds before an explosion, in agreement with the magma surface acceleration driven by the near-surface expansion and acceleration of a slug (Ch. 8, Capponi et al. 2016b). Magma acceleration is then driven by the volumetric expansion of the slug as it approaches the surface and, for a plugged conduit, gas expansion is affected by the plug properties, and the active flow configuration in the conduit. Thus, each flow configuration is potentially reflected at the surface by variations in ground displacement during the entire ascent of the slug (Ch. 7, 8). For a conduit of 1.5 m of radius filled with rheologically uniform magma of viscosity μ = 500 Pa s and a slug ascending in the last 200 m of conduit, the theoretical slug ascent velocity is ~1.1 m/s. Thus, the timescale associated with gas ascent and expansion up to burst is ~115 s, with a sudden non-linear acceleration a few seconds before burst (e.g., James et al. 2008). This is comparable with some of the shorter inflation timescales and trends observed at Stromboli (Ch. 8, Capponi et al. 2016b). For a rheologically stratified magma column, the higher viscosity in the shallower part of the conduit will hinder gas expansion and reduce its ascent velocity. Thus, the rates of change in magma acceleration and ground deformation will be affected as well. Dependant on the viscosity and thickness of the plug, the slug could take additional ~100 s ascending, e.g., the last 20 m of column with a magma viscosity of 6640 Pa s (minimum viscosity value for a plug, as reported in Gurioli et al. 2014) up to additional ~300 s for a 60 m viscous impedance. The presence of such an impedance will result in (1) a drop in slug ascent velocity (from a theoretical velocity of ~1.1 m/s to ~0.2 m/s), (2) hinderance of gas expansion and a slower acceleration of the magma free-surface, (3) a non-linear but slower (compared to a single-viscosity system) near-surface acceleration of the gas expansion a few seconds before burst. These timescales are also in agreement with the observed longer inflation timescales at Stromboli (Ch. 8, Capponi et al. 2016b). But estimates of viscosity can be greater, up to 50 kPa s (Gurioli et al. 2014), further increasing the ascent time and rates of change in ground deformation.

Thus plug properties affect the slug overpressure as slugs ascend in the low-viscosity magma and the rising of the magma head above it. Once an ascending slug transits partially, or completely, into the plug, its overpressure is a function of the falling liquid film. Film thickness is highly variable, depending if it is formed purely by plug liquid (Configuration 1) or by a complex double falling film of both low-/high-viscosity magma (Configuration 2), with the slug nose surrounded only by a low-viscosity film in case of extrusion above the plug (Configuration 3). In general, these different scenarios result in an increase of slug overpressure, with respect to a single and low-viscosity system. In details, the properties of the film affect the pressurization of a slug and ultimately, with the infrasonic signal amplitude being a function of gas mass and overpressure (e.g., Vergniolle and Brandeis 1996; James et al. 2009), each configuration results in its own infrasonic signature at burst.

Variations in the amplitude of acoustic signals for the same gas mass illustrate how Configuration 2 leads to more energetic explosions, followed by Configuration 1 and 3, highlighting the important role of a possible plug on explosion vigour (Ch. 4, Del Bello et al. 2015; Ch. 7).

For Strombolian-type volcanoes, any change in magnitude of the acoustic signals is assumed to be associated with changes in the discrete volume of the gas slug involved in an eruption (e.g., Vergniolle and Brandeis 1996; Ripepe and Marchetti 2001; Harris and Ripepe 2007; Colò et al. 2010). The results of this study (Ch. 7) illustrated how the same gas mass, depending on the flow configuration, can generate different pressure changes and infrasonic waveforms at burst in the laboratory. The similarity between these laboratory waveforms and real infrasonic signals from Stromboli demonstrated that the interaction and burst of a slug through a viscous plug can indeed provide a first-order mechanism for the generation of infrasonic signals at Stromboli. Furthermore, the same gas mass in different flow configurations not only generates different waveforms, it is also associated to a different eruptive style (Ch. 6, Capponi et al. 2016a; Ch. 7). Thus, any change in the flow pattern is reflected in both explosion style and associated geophysical signals.

Therefore, a new correlation between acoustic signals and the properties of the rheological impedance at the top of the conduit arises. Consequently, observed transitions between eruptive regimes such as, for example, between puffing and explosive degassing regimes observed at Stromboli (e.g., Harris and Ripepe 2007; Colò et al. 2010), as well as variations within the spectrum of the "normal activity" (e.g., Patrick et al. 2007; Leduc et al. 2015) could result from rheological changes leading to a specific flow configuration within the conduit, and not necessarily only from variations in the amount of discrete gas erupted. If multiple vents are active simultaneously (e.g., Stromboli, Yasur) variations at different vents may be linked, according to the model proposed in this study, to different plugging conditions of the uppermost portion of the conduits (Ch. 7). However, it is not uncommon for a vent to either be characterized by the same activity for long periods of time (e.g., hours to weeks; Patrick et al. 2007) or to show high variability in the activity over similar intervals (e.g., Taddeucci et al. 2013a). These two opposite behaviours may depend not only on variations in the gas volumes (Taddeucci et al. 2013a), but also on the frequency of the slugs. Indeed, a slow slug frequency means that the time interval between explosions can be sufficiently large to allow the generation of a degassed and viscous layer of magma at the top of the conduit, capable of accommodating an ascending slug (i.e., Configuration 1). An increase in slug frequency would reduce the time available for the magma to cool; as a result the thickness of the viscous layer is reduced. If reduced sufficiently, the extent of the degassed and viscous magma layer generated between explosions will not be sufficient to accommodate both the liquid intrusion and the ascending slug (i.e., Configuration 2). The higher the slug frequency the greater is the chance to create an open low-viscosity path through the high-viscosity plug, kept open by the train of ascending slugs and forming a semi-permanent geometrical discontinuity. Each time a slug passes through a geometrical discontinuity the slug break-up process may be triggered (i.e., Configuration 3). Longer and steady periods of slow or high frequency of occurrence of slugs, however, are needed respectively for the generation of either a layer thick enough to accommodate the slug or to keep the low-viscosity channel within the plug open.

The variability in Strombolian eruptions does not seem to depend only on conduit dynamics and magmatic conditions, but also from the interaction between the gas and any obstacles in its path. Indeed, the effect of a vent cover on eruptive style has previously been theorized (e.g. Patrick et al. 2007; Leduc et al. 2015) but, to date, never observed directly. Chapter 8 (Capponi et al. 2016b) provides the first detailed field evidence of this control, investigating how the vent conditions (open-vent vs. covered-vent) affect the style of explosive activity at Stromboli volcano. Two main eruptive regimes have been identified based on vent conditions, and for each regime frequency and intensity of the explosions control the amount and grain size of the cover: i.e., weaker explosions favour debris accumulation within the vent, and a higher explosion frequency results in the formation of fine-grained covers through collisions and milling among debris over time. Grain size and amount of the debris, in turn, affect (1) explosion dynamics, vigour and pyroclasts ejection velocity and (2) the thermal and mechanical interaction between the debris cover and the magma, eventually contributing to increase magma viscosity. Thus, a debris cover adds another degree of freedom to the system, further increasing the variability of explosions. Indeed, whether a slug burst through a viscous plug or at the top of uniform low-viscosity magma, the presence of a cover seems to significantly affect the post-fragmentation expansion of the gas.

Furthermore, explosions involving thick covers seem to be of lower intensity compared to open-vent ones (Ch. 8, Capponi et al. 2016b). This may suggest that the explosion magnitude, regardless the slug overpressure at burst, is further affected by vent covers. The cover could act as a dampening field between the pressurized gas and the atmosphere and eventually slowing down gas (and pyroclasts) expansion, because part of the energy stored in the gas overpressure is dissipated through percolation and acceleration of the debris. Indeed, explosions through covered vents, with respect to open vent explosions, are characterized by lower pyroclasts ejection velocity, with the pyroclasts exiting through breaches between the blocks formed during the pre-burst inflation of the cover, and do not show visible shock waves pre- and syn-eruption (Ch. 8, Capponi et al. 2016b).

Evidence of this effect on infrasonic signals can be observed at Mt Yasur (Vanuatu) characterized, as Stromboli, by a persistent but variable Strombolian activity from different vent areas. The activity is categorized into minor events, continuous bursting of small overpressurized bubbles (similar to the puffing/spattering activity observed at Stromboli), and major events. The latter can be further divided into emergent events, ash-rich and long-lasting explosions (with covered vents), and impulsive events, short and impulsive ash-free events (with open vents; Spina et al. 2015). Compared to the impulsive events, featuring short and high-amplitude acoustic signals, the emergent events are associated with longer and lower amplitude signals (Spina et al. 2015). Thus, with respect to open-vent, ash-free and ballistic rich explosions, longer and ash-rich eruptions produced at covered vents are the less energetic ones.

A similar characterization linking infrasonic signals with explosive activity at open and clogged vents is still missing at Stromboli. However, the similarities between the acoustic signatures of Yasur’s explosive activity with those of Stromboli (Spina et al. 2015) does not rule out the possibility that different vent conditions further affect the acoustic efficiency of explosions at Stromboli. Thus, the presence of a superficial cover, likely coexisting with a viscous plug, adds yet another degree of uncertainty in the interpretation of the geophysical signals.

9.1 Future directions

The scenario of a viscous plug capping the magma column has often been theorized and supported by petrological studies, but a proper investigation has been lacking. This study filled this gap, providing insights into the role of a plug on conduit dynamics, eruption styles and how it can transform geophysical signals. However, more needs to be done in order to fully understand the mechanism behind the persistent but variable Strombolian activity.

In a real volcanic system it is likely that a possible plug is characterized by both a gradual transition between the lower viscosity magma and the higher viscosity one and variable crystal content. Unlike the transition zone observed in the high-speed videos between the magma surface and the debris cover (Ch. 8, Capponi et al. 2016b), we cannot have direct evidence of a deeper transition zone between the two magmas from direct field observation. However, petrological and textural data may help in better constraining the physical condition within the conduit. Indeed, the presence of a plug triggers a complex interaction between magmas and expanding slugs, leading to magma mingling and modifying the properties of the ejecta involved in the explosion. In particular, Chapters 5 and 6 illustrate how the mingling process can be relatively localized (Configuration 2) or broader (Configuration 3); as a result, the properties of the ejecta will change depending on the level of mingling (Del Bello et al. 2015; Capponi et al. 2016a). More detailed work focused on linking the observed and modelled flow processes with variations in textural features may help to better constrain the magmatic condition within the conduit, the flow configurations modelled, and the design of future analogue laboratory experiments and numerical models to investigate the role played by a rheological gradient in the magma column and crystal contents on slug behaviour, flow patterns and the overall eruptive dynamics.

The increasing use of high-speed, thermal and SO_2 cameras is allowing new insights into explosion dynamics and measurements of gas emissions, providing robust datasets of key parameters controlling the eruptions (e.g., gas mass, pyroclasts ejection velocities, mass and size distribution), and strengthening the link between field observations and conduit dynamics. Indeed, in light of the new framework of flow configurations for rheologically stratified conduits presented here, detailed observations of the pre- and syn-eruptive processes would help in better understand how a plug leads to the observed dynamics. Thus, now more than ever, integration of experimental and numerical methods with field observation is needed to better link the eruptive dynamics to the source process, eventually producing a more detail picture of the physical conditions in the shallower volcanic conduit.

Appendix 1 – Del Bello et al. 2015

Earth and Planetary Science Letters 423 (2015) 210–218

Contents lists available at ScienceDirect

Earth and Planetary Science Letters

www.elsevier.com/locate/epsl

Viscous plugging can enhance and modulate explosivity of strombolian eruptions

E. Del Bello [a,*], S.J. Lane [b], M.R. James [b], E.W. Llewellin [c], J. Taddeucci [a], P. Scarlato [a], A. Capponi [b]

[a] Istituto Nazionale di Geofisica e Vulcanologia, Via di Vigna Murata 605, 00143, Rome, Italy
[b] Lancaster Environment Centre, Lancaster University, Lancaster LA1 4YQ, UK
[c] Department of Earth Sciences, Durham University, South Road, Durham DH1 3LE, UK

ARTICLE INFO

Article history:
Received 13 January 2015
Received in revised form 27 April 2015
Accepted 28 April 2015
Available online xxxx
Editor: T.A. Mather

Keywords:
plugged conduit
eruption dynamics
volcano infrasonic
slug bursting
Taylor bubble
analogue experiments

ABSTRACT

Strombolian activity is common in low-viscosity volcanism. It is characterised by quasi-periodic, short-lived explosions, which, whilst typically weak, may vary greatly in magnitude. The current paradigm for a strombolian volcanic eruption postulates a large gas bubble (slug) bursting explosively after ascending a conduit filled with low-viscosity magma. However, recent studies of pyroclast textures suggest the formation of a region of cooler, degassed, more-viscous magma at the top of the conduit is a common feature of strombolian eruptions. Following the hypothesis that such a rheological impedance could act as a 'viscous plug', which modifies and complicates gas escape processes, we conduct the first experimental investigation of this scenario. We find that: 1) the presence of a viscous plug enhances slug burst vigour; 2) experiments that include a viscous plug reproduce, and offer an explanation for, key phenomena observed in natural strombolian eruptions; 3) the presence and extent of the plug must be considered for the interpretation of infrasonic measurements of strombolian eruptions. Our scaled analogue experiments show that, as the gas slug expands on ascent, it forces the underlying low-viscosity liquid into the plug, creating a low-viscosity channel within a high-viscosity annulus. The slug's diameter and ascent rate change as it enters the channel, generating instabilities and increasing slug overpressure. When the slug reaches the surface, a more energetic burst process is observed than would be the case for a slug rising through the low-viscosity liquid alone. Fluid-dynamic instabilities cause low and high viscosity magma analogues to intermingle, and cause the burst to become pulsatory. The observed phenomena are reproduced by numerical fluid dynamic simulations at the volcanic scale, and provide a plausible explanation for pulsations, and the ejection of mingled pyroclasts, observed at Stromboli and elsewhere.

1. Introduction

Strombolian activity may be very long-lived, with episodes lasting years, decades, or even centuries. This longevity, coupled with the photogenic nature of the explosions, has made some persistently active strombolian volcanoes popular tourist destinations – for instance, more than ten thousand tourists visit the summit of Stromboli itself each year. Although usually benign, strombolian activity spans a range of magnitudes, and includes events that are much more violently explosive and may pose a significant hazard to tourists and nearby communities. It is important, therefore, to determine the factors that cause a usually mildly explosive system to generate more violent explosions.

The discrete explosions that characterise the strombolian eruptive style are interpreted as the impulsive bursting of overpressured gas pockets – or slugs – at the top of a magma column (Chouet, 1974; Blackburn et al., 1976; Burton et al., 2007). Overpressure is a fundamental consequence of large gas bubbles rising from depth and expanding against viscous and inertial retardation as pressure decreases (James et al., 2008; 2009; Del Bello et al., 2012). This behaviour is generally restricted to basaltic or andesitic magmas, because these systems have sufficiently low viscosities to allow bubble coalescence and decoupling of gas slugs from magma over short time scales (order of seconds to hours). Experimental and numerical models within the volcanological literature consider the slug rising through a medium with uniform viscosity and density. These models provide first order explanations of the dynamics of gas expansion, overpressure, and generation of seismic and acoustic signals (e.g., Vergniolle and Brandeis, 1996; Vergniolle et al., 1996; Seyfried and Freundt, 2000; Parfitt, 2004;

* Corresponding author. Tel.: +39 0651860744.
E-mail address: elisabetta.delbello@ingv.it (E. Del Bello).

http://dx.doi.org/10.1016/j.epsl.2015.04.034

Table 1
Summary of experimental parameters and scaling to the volcanic case.

	Experimental parameters		Volcanic conditions		CFD simulations	
Materials	Water	Castor	Underlying magma	Plug	Underlying magma	Plug
Density ρ (kg/m^3)	1000	970	1000		1000	1000
Viscosity μ (Pa s)	0.001	0.986	50	50 000	20	20 000
Surface tension σ[c] (N/m)	0.07	0.03	0.4	0.4	0.4	0.4
Gravity g (m/s^2)	9.81		9.81		9.81	
Conduit diameter D (m)	0.025		5		3	
Inverse viscosity N_f	12381.68	12.18	700.36	0.70	814.74	0.81
Dimensionless film[a] λ'	0.09	0.31	0.14	0.33	0.13	0.33
Film cross section A'[b]	0.16	0.53	0.25	0.55	0.24	0.55
Slug radius r_s (m)	0.01	0.01	2.16	1.68	1.30	1.01
Viscosity contrast μ^*	986		1000		1000	
Slug cross section ratio	0.56		0.61		0.60	

[a] Calculated from equation 4.2 in Llewellin et al. (2012).
[b] Calculated from equation 28 in Del Bello et al. (2012).
[c] Data for the volcanic case are from Murase and McBirney (1973).

O'Brien and Bean, 2008; D'Auria and Martini, 2011; James et al., 2009; Kobayashi et al., 2010; Del Bello et al., 2012; Gerst et al., 2013; Kremers et al., 2013; Nguyen et al., 2013; Lane et al., 2013; Sánchez et al., 2014). However, none of these approaches encompasses the presence of a region of degassed, crystalline magma with increased viscosity and strength in the shallow conduit. Such a rheological impedance – which can be termed a 'plug' – is commonly inferred, and physically plausible, at active strombolian-type vents (e.g., Gurioli et al., 2014).

Textural data from many strombolian-type volcanoes support the coexistence of magmas that have contrasting rheology as a result of cooling- and degassing-driven crystallisation (e.g., Taddeucci et al., 2004; Cimarelli et al., 2010; Kremers et al., 2012; Ruth and Calder, 2013). Considering Stromboli as a canonical case during its 'normal' activity, it is very common to find both bubble-rich, crystal-poor textures and bubble-poor, crystal-rich textures intermingled within a single pyroclast (e.g., Lautze and Houghton, 2005; 2007; Polacci et al., 2006, 2009; Colò et al., 2010; D'Oriano et al., 2010; Gurioli et al., 2014). It has been proposed that these textures represent mingling of relatively fresh, gas-rich magma with older, completely or partially degassed magma, in the shallow conduit (e.g., Lautze and Houghton, 2005). Cooling, degassing and associated crystallisation of the magma in the upper conduit cause it to have a much higher viscosity than its deeper, fresh counterpart. This rheological distinction is not to be confused with the so-called 'high porphiricity' (HP or '*black*') and 'low porphiricity' (LP or '*golden*') magma types (e.g., Métrich et al., 2005); these are distinguished on the basis of geochemical and isotopic analyses, with LP magma thought to occupy the system at depths greater than ~3.5 km. At the volcanic scale, rapid expansion of the gas slug associated with the burst process occurs only within the last few tens of meters of the magma column (James et al., 2008). Hence, the region of plug–slug interaction is limited to the shallowest portion of the conduit, entirely within the HP magma domain.

The presence of a plug, and its thickness, must have an important impact on eruption dynamics. For instance, we would expect the viscous plug to retard slug expansion, thereby promoting the development of overpressure within the slug as it rises. We would also expect the plug material and thickness to affect the dynamics of the bursting process. Lautze and Houghton (2007) were the first to suggest, based on field observations, that changing proportions of magma with differing viscosities influenced eruption frequency and vigour, supporting the notion that plug thickness could change over time. These factors introduce additional complexity compared with the unplugged scenario (e.g., Andronico et al., 2008). This complexity might be manifest in the seismo-acoustic signatures of the explosions (e.g., Johnson and Lees, 2000; Lyons et al., 2012), and in the visual character of the explosions. We note, for instance, that recent high-speed videography studies have identified that gas escape during strombolian explosions is typically pulsatory (Taddeucci et al., 2012; Gaudin et al., 2014), suggesting greater complexity than simple bursting of an overpressured slug. Understanding the role that a viscous plug plays in modulating the dynamics of slug ascent and burst is, therefore, of considerable importance in the interpretation of the waveform and amplitude of generated pressure changes (Lane et al., 2013). In order to gain insight into the complex volcanic system (e.g., Gurioli et al., 2014), we use first-order laboratory experiments to evaluate the influence of a Newtonian, high-viscosity plug on gas slug ascent and burst in a vertical tube. Our experiments build on previous work carried out in single-viscosity systems (James et al., 2004, 2006, 2008, 2009; Lane et al., 2013), and we adopt a similar analogue methodology. We also use a computational fluid dynamic model (James et al., 2008; Chouet et al., 2010) to conduct numerical simulations of the same scenario at the volcano scale, in order to explore the applicability of our laboratory results to the natural system.

2. Experimental method

2.1. Scaling considerations

We model an idealised volcanic scenario in which a layer of high-viscosity magma of variable thickness overlies a column of low-viscosity magma. The behaviour of a slug ascending a vertical pipe filled with a viscous liquid may be described via a number of dimensionless groups, namely the Morton number *Mo*; the Eötvös number *Eo*; the inverse viscosity N_f; the Froude number *Fr*; and the Reynolds number *Re* (e.g., Viana et al., 2003; Llewellin et al., 2012). These groups are defined and calculated for the volcanic and experimental scenarios in the Supplementary Content. We show that, in both systems, surface tension plays a negligible role in slug ascent (e.g., Seyfried and Freundt, 2000) hence behaviour is controlled by the inverse viscosity N_f,

$$N_f = \frac{\rho}{\mu}\sqrt{gD^3}, \tag{1}$$

where ρ and μ are the density and dynamic viscosity of the liquid, g is the gravitational acceleration, and D is the tube diameter.

For a canonical representation of parameters at volcano-scale, we choose a viscosity of 5×10^4 Pa s for the plug based on recent estimations for magma in the shallowest part of Stromboli's conduit (e.g., Gurioli et al., 2014) and 50 Pa s for the underlying magma based on minimum accepted values for basaltic melts (Table 1). Although density differences are observed among pyroclasts

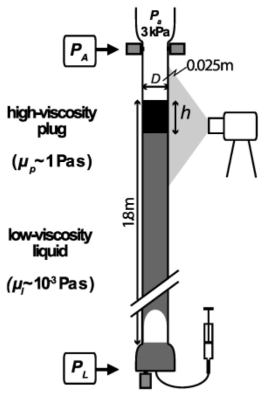

Fig. 1. Experimental apparatus. Known volumes of air were injected into the base of a water-filled tube overlain with a high-viscosity 'plug' of thickness h. Pressure above the plug was held at 3 kPa. Gas slug ascent, expansion and burst were imaged, and pressure variation was measured in the liquid at tube bottom (ΔP_L) and in air above the free surface (ΔP_A).

that tap the uppermost conduit (e.g., Lautze and Houghton, 2005), we exclude density stratification from our analysis and assume that the volcanic system is dynamically stable (or that gravitational instability develops on timescales much longer than that needed for plug formation). Based on values in Table 5 of Gurioli et al. (2014), we estimate a density of approximately 1000 kg m^{-3} for the plug and underlying magma during the active flow process. The respective values of the inverse viscosity in the plug and underlying magma in a 5-m-diameter conduit are then $N_f \approx 0.7$ and $N_f \approx 700$ putting slug behaviour in the viscous and inertial regimes respectively (e.g., White and Beardmore, 1962). The dimensionless thickness (λ') of the falling film of magma around the rising slug is essentially independent of N_f in these regimes (Llewellin et al., 2012), with values of 0.33 and 0.14 respectively. We also calculate the fraction of the tube cross-section occupied by the falling film $A' \approx 0.55$ if magma viscosity is that of the plug, and $A' \approx 0.25$ if viscosity is that of the underlying magma (see Supplementary Content for derivation). Consequently, a gas slug is predicted to narrow substantially when entering the plug zone (occupying ~60% of the cross sectional area it occupies in the underlying liquid).

In the laboratory we use castor oil (viscosity 0.986 Pa s; density 970 kg/m^3) and water (viscosity 0.001 Pa s; density 1000 kg/m^3) as respective analogues for the plug and underlying magma (see Table 1). Given a pipe diameter of 2.5 cm, this gives us values of $N_f \approx 12$ and $N_f \approx 12\,000$ in the plug and underlying liquid respectively. Although these values are somewhat higher than their counterparts in the volcanic system (i.e., the experiments are relatively less viscous), they lie in the same viscous and inertial regimes respectively; the divide between the regimes was found to be around $N_f \approx 100$ by Llewellin et al. (2012). Consequently, the fractions of the pipe cross-section occupied by a falling film of oil or water ($A' \approx 0.53$ and $A' \approx 0.16$ respectively) are similar to those in the volcanic scenario. The experimental N_f values also lie in the same regions where λ' is almost constant, and the viscosity ratio is of order 1000 for both experimental and volcanic scenarios.

2.2. Experimental apparatus

The experimental apparatus (Fig. 1) comprises a vertical glass tube 0.025 ± 0.001 m in diameter (D), filled with liquid to a height of 1.80 ± 0.01 m, and with a nominal ambient pressure above the liquid P_a of 3.0 ± 0.1 kPa to scale for gas expansion during ascent (James et al., 2008). Experiments were carried out by injecting a known volume of air (V_0) equilibrated to the same pressure as the base of the tube. Slug rising and bursting were filmed at 299.7 ± 0.1 frames per second with a Casio Exilim FX1 camera. Pressure in the air above the liquid (P_A) was measured at 1 kHz (NI PCI 6034E data-logger, with 16 channels) with two Honeywell differential 163PC01D75 transducers, and within the liquid at the base of the tube (P_L), with one BOC Edwards A.S.G. 1000 sensor. Pressure variation (ΔP_A and ΔP_L) is then obtained by subtracting measured pre-injection values from the recorded pressure. To reduce noise, ΔP_A is smoothed by taking the mean of the two transducers and a 5-point running average, and ΔP_L is smoothed with a varying running average corresponding to the apparatus resonant 'bounce' frequency (James et al., 2008).

Air volumes (V_0) of 2, 4, 6, 8 and 10 ± 0.1 ml were injected into a water column (single-liquid 'control' experiments) or into a water column whose top was replaced with a layer of castor oil of thickness h equal to either 2D (i.e., $h = 0.05$ m of oil above 1.75 m of water), or 7D ($h = 0.18$ m of oil above 1.62 m of water). Each experiment was repeated to assess both reproducibility and variability under nominally identical conditions. The injected volumes non-dimensionalise to give $V_a' = 0.09, 0.18, 0.28, 0.37$ and 0.45 respectively (Del Bello et al., 2012; see Supplementary Content for methodology). For the volcanic system, these experiments represent erupted gas volumes of 7–37 m^3 (1.2 to 6 kg) and plugs 0, ~10, and ~35 m thick (Video V01). In both systems, V_a' is calculated based on the properties of the liquid underlying the plug, and in a single liquid system would result in passive expansion with slug overpressure only becoming significant at the largest bubble size (Lane et al., 2013).

3. Experimental results

3.1. Control experiments without viscous plug

The injected air forms a slug that ascends and expands within the tube, surrounded by a falling film of water that shows no discernible ripples (Fig. 2a, Video V01). As noted in previous experimental studies, base pressure ΔP_L decreases during slug ascent (Fig. 3a), because an increasing water mass in the falling film is dynamically supported on the tube wall (e.g., James et al., 2004). Slug expansion, which accelerates during ascent, displaces the liquid's free surface upwards. The slug bursts when its nose catches the liquid surface. After burst, the water film drains back, developing ripple structures, and ΔP_L increases to the pre-injection value.

Acceleration of the liquid's free surface and air liberation during the burst process generate a reproducible pulse (Fig. 3a) in the pressure above the liquid ΔP_A (Lighthill, 1978). The resulting waveforms are similar to those observed in experiments conducted with oil ~100 times more viscous than water (Lane et al., 2013) indicating insensitivity to absolute viscosity under inertial conditions. The peak excess pressure $\Delta \hat{P}_A$ scales linearly with dimensionless slug volume (Fig. 4) as also observed by Lane et al. (2013).

3.2. Thin viscous plug experiments

The presence of a thin viscous plug (plug thickness $h = 2$D) slightly retards slug expansion during ascent. A smaller initial decrease in ΔP_L compared with the control experiments, or even a slight ΔP_L increase for the smallest V_0, was observed (Fig. 3b). Slug expansion drives an intrusion of water into and through the plug (Fig. 2b, Video V02). The intruding water core displaces and spreads oil along the tube wall to form a high-viscosity annulus, longer than the initial plug, enclosing a low-viscosity channel of

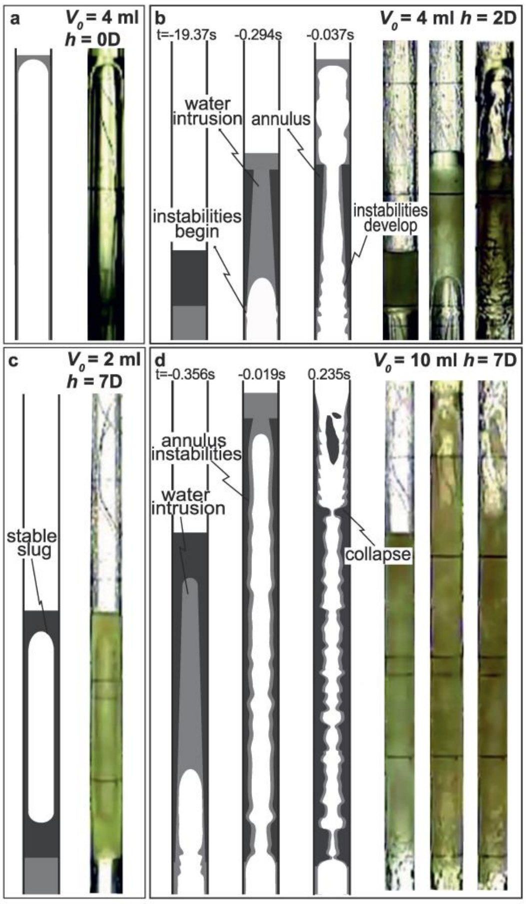

Fig. 2. Still frames and interpretive sketches from selected experiments. a) Control experiment without plug ($h = 0D$) and 4 ml slug. Note smooth slug walls. b) Thin plug experiment ($h = 2D$). Slug rise and expansion forces water through the plug, forming an oil annulus (−0.294 s relative to burst). The slug rises through the annulus into water extruded above it, and film instabilities develop along the annulus (−0.037 s). c) A thick plug ($h = 7D$) is deep enough to fully accommodate a 2 ml slug. d) A 10 ml slug rising into the partially water-intruded oil plug causes rippling of the water film (−0.356 s), then its rapid expansion disrupts the upper reaches of the annulus (−0.019). At burst, the oil/water mixture slumps down, hindering or blocking the escaping gas flux (0.235 s).

water. The radial thickness of the oil annulus averages ∼3 mm, and increases slightly from bottom to top, forming a dynamic, partial constriction of the effective tube cross-section. Once the water core breaches the plug, extruded water accumulates above it, the accumulated volume increasing as the slug expands.

When the slug reaches the base of the annulus, it exploits the low-viscosity pathway provided by the water core to ascend through it. A three-layer, axi-symmetric flow configuration is formed, with the ascending slug surrounded by a falling film of water, all enclosed within the oil annulus, which appears to be stationary (Fig. 2b) on this time-scale. As the slug rises through the annulus, ΔP_L rapidly decreases by a factor of 2 to 4 compared with the control experiment (Fig. 3b). As the slug encounters the dynamic geometry change created by the high-viscosity annulus, instabilities form in the falling water film below the annulus. We suggest this could be caused by a reduction in the flux of water into the falling film below the annulus caused by the narrowing of the ascending slug within the annulus. As the slug ascends through, and emerges from the high-viscosity annulus, further instabilities begin to develop within the annulus. These are caused by the emergence of the slug from the dynamic geometry of the annulus (James et al., 2006) and the rapid waning of the flow processes that generated both the falling water film and the oil annulus. As both liquids drain back after burst and ΔP_L increases to the pre-injection value large downward ripples develop along the pipe walls (Fig. 2b). The ripples induce ΔP_L fluctuations 5 to 10 times larger than observed in the control experiments (Fig. 3b).

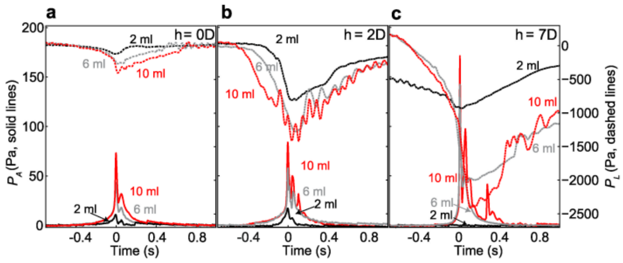

Fig. 3. Pressure changes in the liquid at the base of the tube (ΔP_L, dashed lines) and in the air above the free surface (ΔP_A, solid lines), as a function of time and injection gas volume, for a) no plug ($h = 0$D), b) thin ($h = 2$D), and c) thick ($h = 7$D) plug experiments.

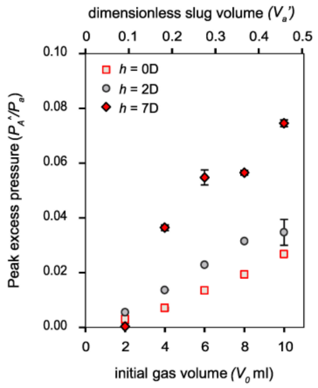

Fig. 4. Peak excess pressure $\Delta\hat{P}_A$ normalised to P_a is reported as function of volume (V_0). Equivalent V_a' is also reported.

$\Delta\hat{P}_A$ is slightly greater than in the control experiments (Fig. 4). The ΔP_A waveform has a similar initial pulse, but lasts longer and becomes more complex and variable (Fig. 3b). The Video (V02) suggests ripples in the draining liquids cause significant and variable impedance of air escape rate from the slug, modulating ΔP_A.

3.3. Thick viscous plug experiments

A thick viscous plug (plug thickness $h = 7$D) retards slug expansion during ascent more strongly than a thin one, producing a higher maximum ΔP_L (Fig. 3c, maximum ΔP_L for the 2 ml slug is out of figure to the left). Small and large slugs display contrasting behaviour. The 2 ml slugs expand modestly, intrude minimal water into the oil, and are fully accommodated in the oil plug (Fig. 2c), passing slowly through it without developing any instability. Bursting is visible as a rupturing of an oil meniscus (Video V03), concomitant with a minimum in ΔP_L (Fig. 2c). Negligible acceleration of the free surface is observed and no ΔP_A signal is detected. This rupture dynamics is typical of the 'quiescent' regime experimentally identified by Lane et al. (2013), and is analogous to the bursting process observed by Kobayashi et al. (2010).

Expansion of the 4–8 ml slugs intrudes water significantly into the plug, with instabilities within the falling water film observed below the annulus as the slug ascends. Only the 10 ml slugs intrude sufficient water to accumulate it atop the oil annulus (Fig. 2d, Video V04). In this case, rapid slug expansion through the long, narrow, water-filled annulus causes a dramatic ΔP_L drop, as the entire plug mass becomes dynamically supported by the tube wall (Fig. 3c). The rapid change in flow structure caused by slug expansion strongly destabilises the annulus causing its upper reaches to disrupt into mixed water/oil globs. The bursting process is complex, involving transient restriction and blockage of the tube by the collapsing annulus and draining water (Fig. 2d). At burst, the slug base is still below the base of the annulus, leaving it fully supported by the tube wall. As the slumping annulus, mixed with water, encounters the water surface at the slug base, a reproducible step increase in ΔP_L occurs (Fig. 3c), unique for the 10 ml slug.

A thick high-viscosity plug increases $\Delta\hat{P}_A$ by a factor of ~3 to 5 compared with the control (Fig. 4). ΔP_A waveforms also become more complex as V_0 increases (Fig. 3c), with: a) negligible signal at 2 ml; b) some similarity to control experiments at 4–8 ml; and c) large secondary peaks at 10 ml, some of them appearing up to 0.5 s after the primary peak. The ΔP_A peaks at 0.23, 0.27, and 0.47 s in Fig. 3c represent secondary pulses of air escaping temporary blockages of the tube caused by unstable slumping oil and globs of oil descending after being previously ejected upward. These peaks are observed in each 10 ml run, but their timing varies.

4. The impact of viscous plugging on slug burst dynamics

Our experimental results demonstrate that the presence of a viscous plug impacts strongly on slug ascent and burst. The viscous plug retards slug growth during ascent, implying an increase in slug overpressure (Bagdassarov, 1994), which drives more vigorous bursting. Slug expansion during ascent causes the underlying liquid to penetrate the viscous plug, creating an annular constriction through which the slug must pass. The annulus increases the fraction of the pipe cross-section occupied by the liquid, creating a dynamic narrowing in the conduit geometry. The area occupied by the slug reduces by nearly half when entering the annulus, decreasing from 0.84 to 0.47 of the pipe cross section. The slug expansion rapidly accelerates as it passes through the constriction as a result of this decrease in its cross-sectional area. Increasing slug expansion enhances free surface acceleration, causing excess pressure $\Delta\hat{P}_A$ to increase accordingly (Lighthill, 1978). Plotting $d(\Delta P_A)/dt$, representing synthetic infrasonic waveforms resulting from the experimental fluid-dynamic source mechanism (Lane et al., 2013), also illustrates positive correlation of the main peaks with h and V_0, and also shows that secondary oscillation pulses are more prominent when the viscous plug is present (Fig. 5). The two-layer liquid flow, generated by slow intrusion of water into and through the oil plug as the ascending gas slug expands, becomes dynamically unstable on rapid change to a three-layer

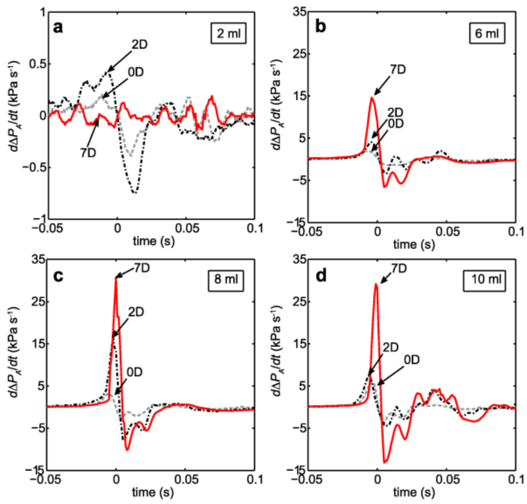

Fig. 5. Time derivative of pressure variation $d(\Delta P_A)/dt$ as a function of time for initial air volumes (V_0) of: a) 2 ml ($\boldsymbol{V'_a} = 0.09$), b) 6 ml ($\boldsymbol{V'_a} = 0.28$), c) 8 ml ($\boldsymbol{V'_a} = 0.37$), and d) 10 ml ($\boldsymbol{V'_a} = 0.45$) ascending through different plug thicknesses. Such quantities would be equivalent to gas volumes of 7, 22, 29 and 37m^3 at the volcanic scale, respectively. Note that ~80 Hz oscillations emerge on calculation of $d(\Delta P_A)/dt$ and that these plausibly represent high frequency but low amplitude half-wave resonance of gas above the flow in the experimental tube.

fluid flow as the gas slug expands through the water core. The resulting instabilities cause transient blocking of the slug's narrow path, adding significant complexity to the burst process. As a result, the slug pinches into shorter gas pockets, causing pulsatory bursting that modulates the associated ΔP_A signal after the main pulse. Finally, the fluid-dynamic instabilities cause the two liquids to inter-mingle; this effect is strongest when a large slug ascends through a thick viscous plug.

5. Volcano-scale simulation

A three-dimensional numerical simulation of the final ascent stage of a slug of gas at volcano scale (as in James et al., 2008; Chouet et al., 2010) was carried out using the FLOW-3D fluid dynamics simulation package (Video V05). The simulation was performed with a conduit diameter of 3 m, a plug thickness $h = 2D$ ($\sim$6 m), an underlying magma thickness of 194 m (simulating a total 200 m thick magma column), viscosities of 20 000 and 20 Pa, respectively, and a non-dimensional slug volume $V'_a = 0.28$ (equivalent to $\sim$22 m^3 of gas). This gave N_f values of $\sim$0.8 and $\sim$800 for the viscous plug and the underlying magma respectively. Although slightly lower than the 'canonical' volcanic system, these N_f values represent the minimum acceptable values for basaltic melts (e.g., Vergniolle and Jaupart, 1986); these were the highest values we could use without encountering numerical instabilities.

The CFD simulation shows a phenomenology similar to that observed experimentally (Fig. 6). Low viscosity liquid intrudes into and above the high viscosity plug, causing it to form an annulus as the gas bubble expands on ascent (Fig. 6a, b); gas follows the low viscosity intrusion through the high viscosity annulus, with the slug narrowing in the annulus and 'ponding' below the annulus (Fig. 6c). Ripples of instability form within the falling film below the annulus, and collapse of the low viscosity liquid above the annulus segments the ascending slug (Fig. 6d). This detailed level of similarity between our scaled experiment and the modelled volcanic scenario supports the applicability of the observed analogue phenomena to the natural volcanic case.

6. Implications for strombolian volcanic eruptions

Our laboratory experiments allow us to develop a general conceptual model for slug ascent and burst through a viscous plug (Fig. 7) that could give insight into key phenomena observed in natural strombolian eruptions. Firstly, several authors have described the simultaneous eruption, during a single strombolian explosion, of pyroclasts from magmas with contrasting textural and rheological properties, sometimes mingled within a single pyroclast (e.g., Taddeucci et al., 2004; Lautze and Houghton, 2005, 2007; Gurioli et al., 2014). Our experiments open a new possible scenario, in which mingling results from the fluid dynamic instabilities that develop when a slug expands through the self-organising geometry of a core of low-viscosity magma within an annular plug of high-viscosity magma. The instabilities cause the two magmas to mingle in the slug burst region, scavenging both into pyroclasts.

Secondly, high-speed videography has revealed the presence of ejection pulses – highly variable in duration and pyroclast velocity – within individual strombolian explosions (Taddeucci et al., 2012). Experimentally, these pulses are caused by transient blocking of the conduit by the same instabilities, supporting the hypothesis, proposed by Taddeucci et al. (2012), that "transient gas pockets formed by the repeated collapse of the liquid film lining conduit walls during the bursting of long slugs". We observe a semi-quantitative similarity between pyroclast ejection velocity at Stromboli and air pressure in the scaled experiments. The experimental timescale of the individual pressure pulses ($\sim$0.05 s) is about a factor of ten shorter than the duration of the whole bursting process ($\sim$0.5 s), matching well the scaling factor for the timescale of ejection pulses ($\sim$0.1–1 s) to that of strombolian explosions (a few seconds to tens of seconds).

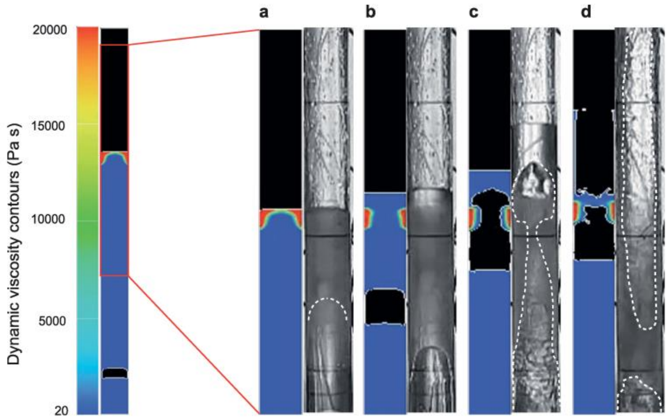

Fig. 6. Results from CFD simulation at the volcanic scale. The parameters of the simulation are $V_0 = 22$ m^3 ($\boldsymbol{V'_a} = 0.28$), $P_a = 10^5$ Pa, $\mu_1 = 20$ Pa s, $\mu_2 = 20\,000$ Pa s; $h = 6$ m (2D), D = 3 m, magma column height 200 m. Still frames (a, b, c, d) extracted from the simulation (see Video V05), show good comparison with experiments at the same scaled conditions $V_0 = 6$ ml ($\boldsymbol{V'_a} = 0.28$) and $h = 2.5$ cm (2D), in terms of burst dynamics and liquid film perturbations, supporting the experimental procedures.

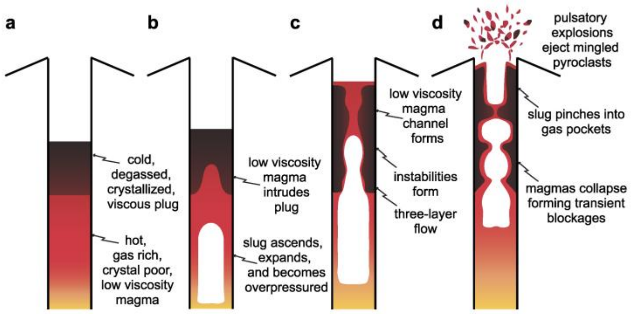

Fig. 7. A model illustrating the effect of viscous plugging on a strombolian eruption. a) Before slug ascent, degassing and cooling of a magma stagnating atop the conduit forms a high viscosity plug. b) Expansion of the slug, impeded by viscous resistance of the plug, causes low viscosity magma to intrude the plug. c) A three-layer flow forms as the slug enters the low viscosity channel, developing dynamic instabilities. d) Instabilities grow causing mingling of the two magmas, channel collapse, and slug disruption into smaller pockets. Accelerated slug expansion culminates in pulsatory bursting and ejection of mingled pyroclasts. The system then resets to a during the quiescence period before the next slug burst.

Our experimental findings provide a new reference for understanding, interpreting, and modelling strombolian volcanic eruptions. The instabilities that cause pulsations in the eruption are only observed in experiments that include a viscous plug (compare control experiments and previous studies, e.g., James et al., 2009; Lane et al., 2013), suggesting that the presence of a plug could be a plausible pre-requisite for the generation of complex multi-pulse behaviour, as may be observed from infrasound and videography. Furthermore, the formation of an annulus of higher-viscosity magma in our experiments advocates the existence of a 'dynamic' conduit geometry, which changes cyclically in response to the passage of slugs. The balance of timescales of plug-forming and plug-consuming processes (i.e., magma degassing, cooling, crystallisation, and entrainment of fall-back material, vs. the return time and volume of passing slugs) will create a complex feedback controlling the generation and recovery of the dynamic and effective conduit geometry (James et al., 2006), explosion dynamics, and the linked frequency and intensity of explosions.

Finally, our results indicate that the increase in explosivity and complexity of strombolian eruptions related to the presence of a viscous plug are mirrored by differences in the first time derivative of pressure variation $d(\Delta P_A)/dt$, i.e., atmospheric infrasound. In our experiments, a 'thick' plug increases peak pressure of the main 'burst' by a factor of 3 to 5 compared with no plug, and is associated with the development of more prominent secondary peaks. Extrapolating the observed trends in natural volcanic eruptions requires care and is beyond the intention of this work. However, a quick by-eye comparison with infrasonic signals generated by eruptions from the 'Hornito' 2012 vent at Stromboli (Fig. 6E in McGreger and Lees, 2004, shows remarkable similarity to the $d(\Delta P_A)/dt$ synthetic waveform from the 10-ml, 7D experiment (Fig. 8). Qualitatively the first pulse is well matched, in similarity to single viscosity systems (Lane et al., 2013); however, in contrast to the single viscosity system, the subsequent secondary oscillations are also well matched, suggesting that slug interaction with a thick viscous plug could provide a plausible first-order mechanism

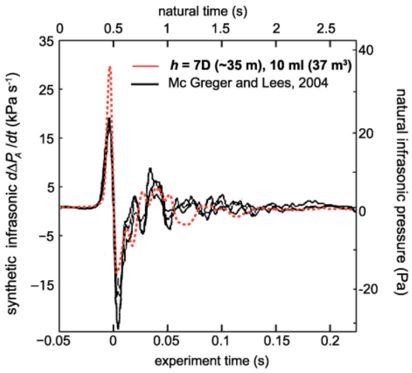

Fig. 8. The first time derivative of experimental excess pressure $d(\Delta P_A)/dt$, as a function of time, for the 10 ml, 2D experiment (dashed line) was compared to measured infrasonic signals at Stromboli reprinted from McGreger and Lees (2004 with permission from Elsevier, solid lines). Both time axis and pressure axis are adapted to best fit the experimental to the measured data.

for such infrasonic signals. Thus, we expect that, during volcanic eruptions, the presence and thickness of a viscous plug introduces another degree of freedom to the system, which may act to increase variability and reduce the certainty of interpretation of air and ground motion signals. This ultimately bears on the importance of multiple monitoring, during eruptions, of parameters such as erupted gas masses, and magma rheology, for a more accurate interpretation of infrasonic signals.

7. Conclusions

The presence of a viscous plug at the top of a volcanic conduit can play a major role in modifying the nature of strombolian explosions. A viscous plug increases the explosivity of strombolian eruptions by enhancing slug overpressure. The plug introduces complexities by modulating the slug expansion and burst process, explaining observed eruption pulses and secondary acoustic signals. The presence of a plug also explains the commonly observed eruption of mingled-texture pyroclasts. The key fluid-dynamic mechanism is the expansion of the ascending gas slug driving intrusion of low viscosity magma into the overlying plug. The resulting annulus of plug material surrounds an intrusion of low-viscosity magma through which the slug then rises to the free surface. The 'rapid' expansion of the gas slug through the low-viscosity intrusion destabilises the liquid annulus, which acts as a dynamic constriction of the conduit, modulating gas escape and strongly affecting the geophysical signals, such as infrasound, associated with the expansion and burst of the slug. For the same gas volume, a viscous plug leads to the generation of different types of pressure signals. Thus, our experimental results reveal some important aspects of the explosivity of basaltic systems. In particular, they evidence that besides gas volume, the presence and extent of viscous plugging must be considered for the interpretation of infrasonic measurements of strombolian eruptions. In this study, viscous plugs are modelled as discrete bodies, whereas in real volcanic systems, plugs are likely to be gradational features. Despite continuous monitoring of Stromboli volcano these features are still not predictable or fully understood. Further work is required to determine the impact that this has on our first order findings.

8. Video description

Videos V01, V02, V03, and V04 contain video sequences and synchronised pressure variations acquired during the following experiments: V01) control experiment (no viscous cap, $h = 0D$), 4 ml slug; V02) thin viscous cap ($h = 2D$), 4 ml slug; V03) thick viscous cap ($h = 7D$), 2 ml slug; V04) thick viscous cap ($h = 7D$), 10 ml slug. Unfiltered and filtered pressure variations are reported for both ΔP_A (pink and red lines, respectively) and ΔP_L (grey and black lines). Predicted atmospheric acoustic pressure (yellow line, $d\Delta P_A/dt$) is also reported for the three experiments in the movies that show P_A signals. Video V05 contain the result of the CFD simulation at the volcanic scale ($V_0 = 22$ m^3, $P_a = 10^5$ Pa, $\mu_1 = 20$ Pa s, $\mu_2 = 20000$ Pa s; $h = 6$ m, D = 3 m, magma column height 200 m) described in Section 5.

Acknowledgements

This work was partly supported by E.D. PhD project grant (University of Bologna) funded by INGV. A.C. received funding from the People Programme (Marie Curie Actions) of the European Union's Seventh Framework Programme (FP7/2007–2013) under the project NEMOH, REA grant agreement No. 289976. We thank Sylvie Vergniolle and an anonymous reviewer for their constructive comments, which helped improve the manuscript. We also thank Tamsin Mather for her editorial handling of the manuscript.

Appendix A. Supplementary material

Supplementary material related to this article can be found online at http://dx.doi.org/10.1016/j.epsl.2015.04.034.

References

Andronico, D., Corsaro, R.A., Cristaldi, A., Polacci, M., 2008. Characterizing high energy explosive eruptions at Stromboli volcano using multidisciplinary data: an example from the 9 January 2005 explosion. J. Volcanol. Geotherm. Res. 176, 541–550.

Bagdassarov, N.S., 1994. Pressure and volume changes in magmatic systems due to the vertical displacement of compressible materials. J. Volcanol. Geotherm. Res. 63, 95–100.

Blackburn, E.A., Wilson, L., Sparks, R.S.J., 1976. Mechanisms and dynamics of strombolian activity. J. Geol. Soc. 132, 429–440.

Burton, M., Allard, P., Muré, F., La Spina, A., 2007. Magmatic gas composition reveals the source depth of slug-driven strombolian explosive activity. Science 317, 227–230.

Chouet, B., 1974. Photoballistics of volcanic jet activity at Stromboli, Italy. J. Geophys. Res. 79, 4961–4976.

Chouet, B., Dawson, P.B., James, M.R., Lane, S.J., 2010. Seismic source mechanism of degassing bursts at Kilauea Volcano, Hawaii: results from waveform inversion in the 10–50 s band. J. Geophys. Res. 115, B09311.

Cimarelli, C., Di Traglia, F., Taddeucci, J., 2010. Basaltic scoria textures from a zoned conduit as precursors to violent Strombolian activity. Geology 38, 439–442.

Colò, L., Ripepe, M., Baker, D.R., Polacci, M., 2010. Magma vesiculation and infrasonic activity at Stromboli open conduit volcano. Earth Planet. Sci. Lett. 292, 274–280.

D'Auria, L., Martini, M., 2011. Slug flow: modeling in a conduit and associated elastic radiation. In: Meyers, R.A. (Ed.), Encyclopedia of Complexity and Systems Science. Springer, New York, NY, pp. 858–873.

D'Oriano, C., Bertagnini, A., Pompilio, M., 2010. Ash erupted during normal activity at Stromboli (Aeolian Islands, Italy) raises questions on how the feeding system works. Bull. Volcanol. 73, 471–477.

Del Bello, E., Llewellin, E.W., Taddeucci, J., Scarlato, P., Lane, S.J., 2012. An analytical model for gas overpressure in slug-driven explosions: insights into Strombolian volcanic eruptions. J. Geophys. Res. 117, B02206.

Gaudin, D., Taddeucci, J., Scarlato, P., Moroni, M., Freda, C., Gaeta, M., Palladino, D.M., 2014. Pyroclast tracking velocimetry illuminates bomb ejection and explosion dynamics at Stromboli (Italy) and Yasur (Vanuatu) volcanoes. J. Geophys. Res., Solid Earth 119, 5384–5397.

Gerst, A., Hort, M., Aster, R.C., Johnson, J.B., Kyle, P.R., 2013. The first second of volcanic eruptions from the Erebus volcano lava lake, Antarctica-energies, pressures, seismology, and infrasound. J. Geophys. Res., Solid Earth 118, 3318–3340.

Gurioli, L., Colo', L., Bollasina, A.J., Harris, A.J.L., Whittington, A., Ripepe, M., 2014. Dynamics of Strombolian explosions: inferences from field and laboratory studies of erupted bombs from Stromboli volcano. J. Geophys. Res., Solid Earth 119, 319–345.
James, M., Lane, S., Chouet, B., Gilbert, J., 2004. Pressure changes associated with the ascent and bursting of gas slugs in liquid-filled vertical and inclined conduits. J. Volcanol. Geotherm. Res. 129, 61–82.
James, M.R., Lane, S.J., Chouet, B.A., 2006. Gas slug ascent through changes in conduit diameter: laboratory insights into a volcano-seismic source process in low-viscosity magmas. J. Geophys. Res. 111, B05201.
James, M.R., Lane, S.J., Corder, S.B., 2008. Modelling the rapid near-surface expansion of gas slugs in low-viscosity magmas. Geol. Soc. (Lond.) Spec. Publ. 307, 147–167.
James, M.R., Lane, S.J., Wilson, L., Corder, S.B., 2009. Degassing at low magma-viscosity volcanoes: quantifying the transition between passive bubble-burst and Strombolian eruption. J. Volcanol. Geotherm. Res. 180, 81–88.
Johnson, J., Lees, J., 2000. Plugs and chugs—seismic and acoustic observations of degassing explosions at Karymsky, Russia and Sangay, Ecuador. J. Volcanol. Geotherm. Res. 101, 67–82.
Kobayashi, T., Namiki, A., Sumita, I., 2010. Excitation of airwaves caused by bubble bursting in a cylindrical conduit: experiments and a model. J. Geophys. Res. 115, B10201.
Kremers, S., Lavallée, Y., Hanson, J., Hess, K.-U., Chevrel, M.O., Wassermann, J., Dingwell, D.B., 2012. Shallow magma-mingling-driven Strombolian eruptions at Mt. Yasur volcano, Vanuatu. Geophys. Res. Lett. 39, L21304.
Kremers, S., Wassermann, J., Meier, K., Pelties, C., van Driel, M., Vasseur, J., Hort, M., 2013. Inverting the source mechanism of Strombolian explosions at Mt. Yasur, Vanuatu, using a multi-parameter dataset. J. Volcanol. Geotherm. Res. 262, 104–122.
Lane, S.J., James, M.R., Corder, S.B., 2013. Volcano infrasonic signals and magma degassing: first-order experimental insights and application to Stromboli. Earth Planet. Sci. Lett. 377–378, 169–179.
Lautze, N.C., Houghton, B.F., 2005. Physical mingling of magma and complex eruption dynamics in the shallow conduit at Stromboli volcano, Italy. Geology 33, 425.
Lautze, N.C., Houghton, B.F., 2007. Linking variable explosion style and magma textures during 2002 at Stromboli volcano, Italy. Bull. Volcanol. 69, 445–460.
Lighthill, M.J., 1978. Waves in Fluids. Cambridge University Press, Cambridge.
Llewellin, E.W., Del Bello, E., Taddeucci, J., Scarlato, P., Lane, S.J., 2012. The thickness of the falling film of liquid around a Taylor bubble. Proc. R. Soc., Math. Phys. Eng. Sci. 468, 1041–1064.
Lyons, J.J., Waite, G.P., Ichihara, M., Lees, J.M., 2012. Tilt prior to explosions and the effect of topography on ultra-long-period seismic records at Fuego volcano, Guatemala. Geophys. Res. Lett. 39.
McGreger, A.D., Lees, J.M., 2004. Vent discrimination at Stromboli Volcano, Italy. J. Volcanol. Geotherm. Res. 137, 169–185.
Métrich, N., Bertagnini, A., Landi, P., Rosi, M., Belhadj, O., 2005. Triggering mechanism at the origin of paroxysms at Stromboli (Aeolian Archipelago, Italy): the 5 April 2003 eruption. Geophys. Res. Lett. 32, L10305.
Murase, T., McBirney, A., 1973. Properties of some common igneous rocks and their melts at high temperatures. Geol. Soc. Am. Bull. 84, 3563–3592.
Nguyen, C.T., Gonnermann, H.M., Chen, Y., Huber, C., Maiorano, A.A., 2013. Film drainage and the lifetime of bubbles. Geochem. Geophys. Geosyst. 14, 3616–3631.
O'Brien, G.S., Bean, C.J., 2008. Seismicity on volcanoes generated by gas slug ascent. Geophys. Res. Lett. 35, L16308.
Parfitt, E.a, 2004. A discussion of the mechanisms of explosive basaltic eruptions. J. Volcanol. Geotherm. Res. 134, 77–107.
Polacci, M., Baker, D.R., Mancini, L., Favretto, S., Hill, R.J., 2009. Vesiculation in magmas from Stromboli and implications for normal Strombolian activity and paroxysmal explosions in basaltic systems. J. Geophys. Res. 114, B01206.
Polacci, M., Corsaro, R.A., Andronico, D., 2006. Coupled textural and compositional characterization of basaltic scoria: insights into the transition from Strombolian to fire fountain activity at Mount Etna, Italy. Geology 34, 201.
Ruth, D.C.S., Calder, E.S., 2013. Plate tephra: preserved bubble walls from large slug bursts during violent Strombolian eruptions. Geology 42, 11–14.
Sánchez, C., Álvarez, B., Melo, F., Vidal, V., 2014. Experimental modeling of infrasound emission from slug bursting on volcanoes. Geophys. Res. Lett., 6705–6711.
Seyfried, R., Freundt, A., 2000. Experiments on conduit flow and eruption behavior of basaltic volcanic eruptions. J. Geophys. Res. 105, 23727.
Taddeucci, J., Pompilio, M., Scarlato, P., 2004. Conduit processes during the July–August 2001 explosive activity of Mt. Etna (Italy): inferences from glass chemistry and crystal size distribution of ash particles. J. Volcanol. Geotherm. Res. 137, 33–54.
Taddeucci, J., Scarlato, P., Capponi, A., Del Bello, E., Cimarelli, C., Palladino, D.M., Kueppers, U., 2012. High-speed imaging of Strombolian explosions: the ejection velocity of pyroclasts. Geophys. Res. Lett. 39, L02301.
Vergniolle, S., Brandeis, G., 1996. Strombolian explosions 1. A large bubble breaking at the surface of a lava are only slightly damped explosions. J. Geophys. Res. 101, 433–447.
Vergniolle, S., Brandeis, G., Mareschal, J.-C., 1996. Strombolian explosions 2. Eruption dynamics determined from acoustic measurements. J. Geophys. Res. 101, 449–466.
Vergniolle, S., Jaupart, C., 1986. Separated two-phase flow and basaltic eruptions. J. Geophys. Res. 91, 12842–12860.
Viana, F., Pardo, R., Yánez, R., Trallero, J.L., Joseph, D.D., 2003. Universal correlation for the rise velocity of long gas bubbles in round pipes. J. Fluid Mech. 494, 379–398.
White, E.T., Beardmore, R.H., 1962. The velocity of rise of single cylindrical air bubbles through liquids contained in vertical tubes. Chem. Eng. Sci. 17, 351–361.

Appendix 2 – Capponi et al. 2016a

Earth and Planetary Science Letters 435 (2016) 159–170

Contents lists available at ScienceDirect

Earth and Planetary Science Letters

www.elsevier.com/locate/epsl

Gas slug ascent in a stratified magma: Implications of flow organisation and instability for Strombolian eruption dynamics

A. Capponi *, M.R. James, S.J. Lane

Lancaster Environment Centre, Lancaster University, Lancaster, LA1 4YQ, UK

ARTICLE INFO

Article history:
Received 12 August 2015
Received in revised form 9 December 2015
Accepted 20 December 2015
Available online xxxx
Editor: B. Marty

Keywords:
plugged conduit
magma mingling
slug dynamics
conduit geometry
flow configurations
analogue experiments

ABSTRACT

The canonical Strombolian paradigm of a gas slug ascending and bursting in a homogeneous low-viscosity magma cannot explain the complex details in eruptive dynamics recently revealed by field measurements and textural and geochemical analyses. Evidence points to the existence of high-viscosity magma at the top of the conduit of Strombolian-type volcanoes, acting as a plug. Here, new experiments detail the range of flow configurations that develop during the ascent and burst of a slug through rheologically stratified magma within a conduit. End-member scenarios of a tube fully filled with either high- or low-viscosity liquid bracket three main flow configurations: (1) a plug sufficiently large to fully accommodate an ascending gas slug; (2) A plug that can accommodate the intrusion of low-viscosity liquid driven by the gas expansion, but not all the slug volume, so the slug bursts with the nose in the plug whilst the base is still in the low-viscosity liquid; (3) Gas expansion is sufficient to drive the intrusion of low-viscosity liquid through the plug, with the slug bursting in the low-viscosity layer emplaced dynamically above the plug. We show that the same flow configurations are viable at volcanic-scale through a new experimentally-validated 1D model and 3D computational fluid dynamic simulations. Applied to Stromboli, our results demonstrate that the key parameters controlling the transition between each configuration are gas volume, plug thickness and plug viscosity. The flow processes identified include effective dynamic narrowing and widening of the conduit, instabilities within the falling magma film, transient partial and complete blockage of the conduit, and slug disruption. These complexities influence eruption dynamics and vigour, promoting magma mingling and resulting in pulsatory release of gas.

1. Introduction

Strombolian eruptions are characterised by short impulsive events. These typically occur in basaltic or andesitic magmas where viscosity is sufficiently low to allow gas segregation over short time scales (Blackburn et al., 1976; Parfitt, 2004; Houghton and Gonnermann, 2008). Explosions are interpreted as representing the arrival and burst of over-pressured large gas pockets (slugs) at the surface (Chouet et al., 1974; Blackburn et al., 1976). The slugs can form either by coalescence of smaller bubbles at geometrical discontinuities in the conduit (Vergniolle and Jaupart, 1986; Jaupart and Vergniolle, 1988) or by differential ascent rate of the bubbles with respect to the magma column (Parfitt and Wilson, 1995; Parfitt, 2004). Either way, the ascent, expansion and burst of slugs have almost always been considered in rheologically uniform media (e.g., Vergniolle and Brandeis, 1996; Vergniolle et al., 1996; Seyfried and Freundt, 2000; James et al., 2006, 2008; Kobayashi et al., 2010; Del Bello et al., 2012; Lane et al., 2013).

However, an increasing body of evidence (e.g., Lautze and Houghton, 2005, 2006; Polacci et al., 2009; D'Oriano et al., 2011; Colò et al., 2010; Gurioli et al., 2014) suggests that the cooling, degassing and crystallisation of the uppermost part of the magma column, along with mixing with recycled material from collapses of the conduit wall, re-entrained pyroclasts and lithics, could generate an evolved magma region at the top of the conduit. Gas slugs must ascend and burst through this stratified rheological heterogeneity. The rheological properties and thickness of this region may influence explosion intensity and style (Lautze and Houghton, 2005, 2006), while textural and geochemical variations in the ejecta may reflect mingling of magmas with different physical properties in the shallow conduit (Polacci et al., 2009; D'Oriano et al., 2011; Colò et al., 2010; Gurioli et al., 2014). Textural features observed in samples collected at Stromboli seem to correlate with explosion frequency and magnitude, with a high degree of mingling promoted by increased magma and gas flux (i.e., greater explosion frequency and vigour). In contrast, a lower flux

* Corresponding author.
E-mail address: a.capponi@lancaster.ac.uk (A. Capponi).

http://dx.doi.org/10.1016/j.epsl.2015.12.028
0012-821X/© 2015 Elsevier B.V. All rights reserved.

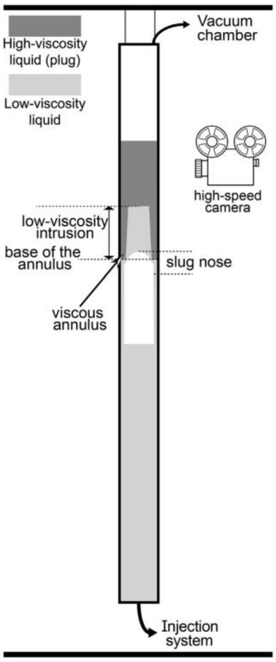

Fig. 1. The experimental apparatus comprised a 3-m-high vertical tube, with a diameter D of 0.025 m, connected to a vacuum chamber and a gas injection system. Scaling considerations dictated that experimental ambient pressure was varied between 3 kPa, 1 kPa and 300 Pa. Slug ascent, expansion and burst through the experimental liquids were imaged with a high-speed camera at 300 fps. As a slug ascended and expanded in the tube, it drove an intrusion of the underlying low-viscosity liquid into the plug, forming a low-viscosity channel (**low-viscosity intrusion**). The intrusion displaced and spread the high-viscosity liquid along the tube wall, creating a high-viscosity annulus (**viscous annulus**) that, in turn, enclosed the intrusion.

(i.e., low level of activity) leads to more restricted mingling (Lautze and Houghton, 2006). Complexities in eruptive dynamics, such as pulses within a single Strombolian eruption (Taddeucci et al., 2012; Gaudin et al., 2014), are also difficult to explain with simplified models of slug burst in a rheologically uniform fluid, although conduit discontinuities could play a role (James et al., 2006).

Such evidence motivated initial experimental work on the effects of a viscous upper layer (or 'plug') on eruptive dynamics (Del Bello et al., 2015). In this scenario, a gas slug ascending and expanding in a column of low-viscosity liquid overlaid by a plug drives an intrusion of low-viscosity liquid into the plug. The plug liquid thus creates a viscous annulus that, in turn, encloses the intrusion (Fig. 1). As the slug arrives at the plug base, it uses the low-viscosity intrusion to rise through the plug. The slug can burst in two different flow configurations: 1) whilst fully accommodated into the plug volume, or 2) whilst in a low-viscosity layer emplaced by the intrusion above the plug. Each configuration encompasses apparent dynamic narrowing and widening of the conduit for the slug, instabilities within the falling film surrounding the slug, transient partial blockages of the conduit, and slug disruption (Del Bello et al., 2015). These complexities gave insight into the generation of eruptive pulses and mingled pyroclasts, together with enhancement of slug overpressure with respect to a single-viscosity system (Del Bello et al., 2015); however, accurate scaling for slug expansion and viscosity contrast was not achieved.

Here, we build on the experimental foundation of Del Bello et al. (2015) to fully define the rich range of fundamental fluid configurations that can develop in association with slug flow through a viscous plug at the top of a volcanic conduit. We used comprehensively scaled laboratory experiments to identify flow organisation and instability within different fluid configurations expressed by varying relative plug and slug sizes. We developed a model to determine these configurations for a given set of parameters, and validated it against the laboratory data and, at volcano-scale, against the results of 3D computational fluid dynamics simulations. Finally, we explored the implications of flow richness in the shallow conduit for interpretation of Strombolian eruptive processes.

2. Methods

The complex volcanic system was simplified to explore the effect of a vertical rheology contrast on the behaviour of the slug during its ascent, expansion and burst in a constant-geometry tube filled with Newtonian liquids. The experimental apparatus (Fig. 1) comprised a vertical 3-m-high glass tube with internal diameter D of 0.025 m. The base of the tube was sealed, with the exception of the gas injection system. The top was connected to a vacuum chamber in order to reduce the ambient pressure, P_a, and enable slug expansion processes to be scaled (James et al., 2008). We used $AS100$ silicone oil (viscosity $\mu = 0.1$ Pa s, density $\rho = 990$ kg/m^3, Wacker Chemie AG) as analogue for low-viscosity magma (Table 1), improving on the experiments of Del Bello et al. (2015) by (a) providing more accurate scaling of viscosity contrast, and (b) enabling access to the explosive region of slug expansion (James et al., 2009; Del Bello et al., 2012). Immiscible castor oil ($\mu = \sim 1$ Pa s, $\rho = 961$ kg/m^3) represented the high-viscosity plug with a density less than that of the silicone oil and a suitably high viscosity. At both laboratory and volcanic scales, surface tension plays a negligible role (e.g., Seyfried and Freundt, 2000), and the inverse viscosity N_f controls the ascent of a slug:

$$N_f = (\rho/\mu)\sqrt{gD^3}, \tag{1}$$

where g is the gravitational acceleration. For the tube geometry, we obtain N_f values of $\sim$12 and $\sim$122 for the castor oil and silicone oil respectively (Table 1). These values lie in regions of the flow regime where the slug behaviour is controlled by viscosity in the plug, and by inertia with viscous contributions in the silicone oil (e.g., White and Beardmore, 1962).

The apparatus was filled to a height of $\sim$1.43 m with either silicone oil only, or with silicone oil overlain by a layer of castor oil. Layer thickness of the plug was non-dimensionalised as a function of the tube diameter, D: $\sim$2.5 ($1D$), $\sim$5 ($2D$), $\sim$12.5 ($5D$), $\sim$25 ($10D$) and $\sim$50 ($20D$) cm plugs, widening the range of Del Bello et al. (2015), which only considered $\sim$5 ($2D$) and $\sim$17.5 ($7D$) cm layers. In addition to the gas volumes (2, 4, 6, 8 and 10 ± 0.1 ml) and P_a ($P_a = 3$ kPa, limited by water boiling point) used in Del Bello et al. (2015), we injected volumes of air (V_0) of 17, 24, 32 and 49 ± 0.1 ml, with P_a reduced to 1 ± 0.1 kPa and 300 ± 0.1 Pa, greatly extending the range of gas expansion ratios.

The injected gas volumes non-dimensionalise through the parameter V'_a (Del Bello et al., 2012; Supplementary Content), giving $V'_a = 0.08$–2, 0.6–14 and 6–152 for experimental P_a of 3 kPa, 1 kPa and 300 Pa respectively. Scaled to the volcanic case, these values represent erupted gas volumes at atmospheric pressure of 4–90 m^3, 28–690 m^3 and 300–7300 m^3, and cover the range of gas volumes estimated for normal strombolian activity

Table 1
Comparison of experimental parameters from this study and from Del Bello et al. (2015) and scaling to the volcanic case.

Materials	Water[a]	Silicone oil[b]	Castor oil[a,b]	Underlying magma[e]	Plug[e]
Conduit radius, r_c (m)		0.0125		2.5	
Density (kg/m^3)	1000	990	961	900	1300
Viscosity (Pa s)	0.001	0.1	1	50–300	10 000–50 000
Inverse viscosity, N_f	12 380	122	12	630–105	4.5–0.91
Film cross section, A'[c]	0.16	0.41	0.52	0.26–0.36	0.53–0.54
Dimensionless film, λ'[d]	0.08	0.23	0.31	0.14–0.24	0.32–0.32
Film thickness, λ (m)	0.001	0.0029	0.0039	0.35–0.60	0.80–0.81
Slug radius, r_s (m)	0.011	0.0095	0.0085	1.89–2.14	1.67–1.68
Viscosity contrast	1000	10		33–1000	

[a] Used in Del Bello et al. (2015).
[b] Used in this study.
[c] Calculated from equation (28) in Del Bello et al. (2012).
[d] Calculated from equation (4.2) in Llewellin et al. (2012).
[e] Viscosity and density data reported in Gurioli et al. (2014).

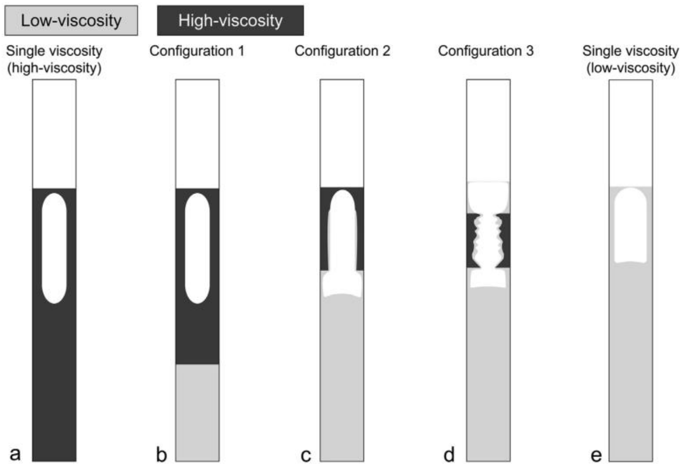

Fig. 2. Experimentally informed conceptual sketches of tubes filled with (**a**) high-viscosity and (**e**) low-viscosity liquid represent the configuration end-members that sandwiched three main flow configurations for the two-layer system. (**b**) Configuration 1: the viscous plug volume fully accommodates the gas slug. (**c**) Configuration 2: the plug volume cannot accommodate both the low-viscosity intrusion and the slug. At burst, the slug nose and main body are in the plug, whilst the base is still in the low-viscosity liquid. (**d**) Configuration 3: slug expansion drives the intrusion of low-viscosity liquid through the plug, extruding a low-viscosity layer above the plug in which the slug burst. Instabilities develop as the slug passes through the annulus into the extruded low-viscosity layer.

(Vergniolle and Brandeis, 1996; Vergniolle et al., 1996; Ripepe and Marchetti, 2002; Chouet et al., 2003; Harris and Ripepe, 2007; Mori and Burton, 2009) i.e., $2 - 2 \times 10^4$ m^3 (0.5–3000 kg), and for gas puffers, 50–190 m^3 (10–30 kg). Each experiment was imaged at 300 ± 0.1 frames per second with a Basler acA2000-340 km high-speed camera.

To extend our 1D numerical model to volcanic-scale, we considered an idealised system with a 200-m-high magma column within a conduit of radius 1.5, 2 or 2.5 m, covering the range of values appropriate to Stromboli (Taddeucci et al., 2012; Gaudin et al., 2014). Magma viscosities range between 10–50 kPa s and 50–500 Pa s, with densities of 1300 kg/m^3 and 900 kg/m^3, for the plug and the underlying magma respectively (Gurioli et al., 2014). These parameters give N_f values ~4.55 to ~0.42 for the plug and ~630 to ~29 for the underlying magma. Slug ascent is under dominant viscous control in the plug, but with a significant degree of inertial contribution within the underlying magma, a condition mimicked experimentally.

3. Results

The experiments revealed a rich set of flow configurations, reflecting variation in the ratio of the lengths of the high-viscosity plug and gas slug. The flow configurations can be conceptually considered within a spectrum of relative plug lengths, ranging from infinite (i.e. a conduit fully filled with the high-viscosity liquid) to zero (i.e. a conduit filled with the low-viscosity liquid). These single-viscosity end-members bracketed three distinct intermediate and more complex flow configurations. The transitions between these configurations were not sharp, and included intermediate behaviours. However, they encompassed the same processes observed in the main configurations and, thus, are not detailed here (see Supplementary Content for more information).

3.1. Single viscosity

We define infinitely thick and infinitely thin plugs as end-member configurations (Fig. 2a, e) in which slug ascent is effectively within a single-viscosity system. In the experiments, the

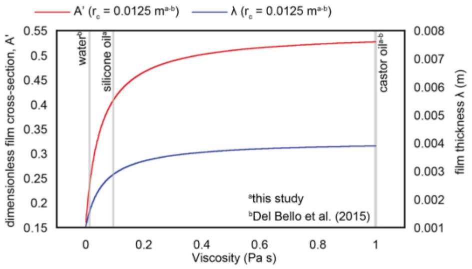

Fig. 3. Variations of the dimensionless film cross section A' (calculated from equation (28) in Del Bello et al., 2012) and thickness of the falling liquid film (m), λ, as a function of viscosity for a tube radius of 0.0125 m; shaded areas highlight the values for water ($\mu = 0.001$ Pa s, $\rho = 1000$ kg/m^3; used in Del Bello et al., 2015), silicone oil ($\mu = 0.1$ Pa s, $\rho = 990$ kg/m^3; this study) and castor oil ($\mu = 1$ Pa s, $\rho = 961$ kg/m^3; both this study and Del Bello et al., 2015).

injection of air at the base of the apparatus formed a slug (James et al., 2008; Lane et al., 2013; Del Bello et al., 2015) that rose, expanded and elongated surrounded by a falling liquid film. The slug burst when all the liquid head above it has flowed into the falling film, except for a thin layer forming a meniscus. When ascending in a low-viscosity liquid (Fig. 2e), the slug occupied almost all the cross sectional area of the tube, surrounded by a thin falling film of liquid (Fig. 3); for gas volumes larger than 17 ml, film instabilities developed with time. At burst, the meniscus ruptured, and its remnants were dragged upward by the released gas before falling or draining back on the liquid surface (Video V01). Small volumes of gas (2–8 ml) produced pre-burst oscillation of the slug nose at surface.

For slug ascent in high-viscosity liquids (Fig. 2a), the slug ascended with a lower velocity, surrounded by a thicker falling film, thus the fraction of the tube cross-section occupied by the film, A' (Del Bello et al., 2012; Supplementary Content), increased from $\sim$0.41 to $\sim$0.52 (Table 1, Fig. 3). Consequently the area of the tube occupied by the slug decreased, while its length increased. The rate of gas expansion was slower, driving a slower acceleration of the liquid surface. When at the liquid surface, the slug burst with a slow rupture of a thick viscous meniscus, which completely drained to the tube wall just above the burst point and without the ejection of any droplets or observable pre-burst oscillation.

3.2. Configuration 1

In a layered system in which the plug volume was significantly greater than the slug volume, a steady slug flow was established in both the low- and high-viscosity liquids (Fig. 2b), with a transitional period as the slug moved between the fluids (Video V02, 8–13 s). At the onset of an experiment the slug rose in the low-viscosity liquid. As it ascended, gas expansion drove an intrusion of low-viscosity oil into the plug, the extent of which depended on the relative volumes of the slug expansion and the plug. Around the intrusion, the high-viscosity liquid represented a viscous annulus, with an average radial thickness $\sim$4 mm, thinnest at the plug base (Fig. 3).

When the nose of the ascending slug reached the base of the annulus, the annulus acted as a dynamic change in the confining geometry. This forced the slug to ascend through a diameter reduction and into the intrusion (Fig. 4a, sketch II; Video V02, 8 s). For all configurations the intrusion volume must equal the slug volume expansion; therefore the intrusion was always smaller than the slug itself. Thus, at some point, the slug transited from ascending within the intrusion to within the main body of the plug itself, defining Configuration 1. Once this was complete, the high-viscosity plug liquid fully accommodated the bubble within it (Fig. 4a, sketch III). Ascent rate and slug morphology became more viscously dominated and burst processes reflected those in high-viscosity fluids (Video V02).

3.3. Configuration 2

For experiments in which the plug volume was insufficient to fully accommodate the slug, slug burst occurred with the slug nose within the plug liquid, and the slug base still in the low-viscosity liquid (Fig. 2c). As for Configuration 1, when the slug arrived at the base of the annulus, it used the intrusion as a pathway through the plug (Fig. 4b, sketch II; Video V03, 13–16 s) with, at some point, the slug nose entering the high-viscosity plug liquid (Fig. 4b, sketch III; Video V03, 16 s). At burst, the high-viscosity meniscus disrupted into small droplets (Video V03, 17 s). If the nose of the intrusion had almost reached the plug surface when the slug burst (mainly for $5D$ and $10D$ plugs and 10, 17 and 24 ml slugs), then the burst involved droplets of a mixture of low/high viscosity oil, ejected up the tube.

3.4. Configuration 3

Configuration 3 represents the scenario in which slug expansion is sufficiently large that the low-viscosity intrusion breaches the plug top and emplaces a layer of low-viscosity liquid above the annulus (Fig. 2d; Video V04, from 5 s onwards). Experimentally, the viscous annulus effectively generated two regions of geometry change for ascending slugs; at the base of the plug, the annulus created a dynamic restriction, whilst at the top, slugs passed back into the low-viscosity liquid only – effectively a dynamic widening (Fig. 4c, sketch II). The widening enabled the slug nose to accelerate and the abrupt change led to rapid draining of the liquid head around the slug (James et al., 2006). As the increased downward flux of liquid past the slug nose converged at the top of the annulus, the falling film thickened within the annulus, creating a narrowing neck around the slug. If this closed, the gas flow may be temporarily halted as the gas slug was broken into two (Fig. 3c, sketch III; Video V04, 16–18 s) or, if the processes were repeated, more offspring bubbles. The break-up process, always taking place in $<$1 s after the main bubble burst, generated up to 4 offspring bubbles in the experiments, bursting sequentially. We observed also partial restrictions of the gas escape pathway, at a mean frequency of 2 per second.

When the slug nose within the intrusion ascended above the top of the annulus, instabilities formed in the falling film around the slug body due to the dynamic geometry change; these instabilities propagated down the low-viscosity film within the annulus and continuously disrupted the boundary between the two liquids, initiating mingling (Fig. 4c, sketch II–III). Sometimes, for large gas volumes and thin plugs ($1D$ and $2D$), gas expansion caused rapid intrusion of low-viscosity liquid breaking through the plug: some of the high-viscosity annulus was detached, dragged upward within the low-viscosity liquid above and surrounding the slug body, and mixed into the low-viscosity liquid. As burst progressed, pockets of this mingled mixture were ejected (Fig. 4c, sketch IV). The burst process was highly variable: it involved bubble oscillations and detachment of the entire meniscus, or bubbles burst without any oscillation, with a complete disruption of the meniscus and droplets ejected high in the tube and followed by several collapses of the film lining the tube wall (Video V04).

4. Determination of flow configurations at volcano-scale

To determine the flow configuration (e.g., 1 to 3) for a specific set of parameters, we developed a first-order 1D model to de-

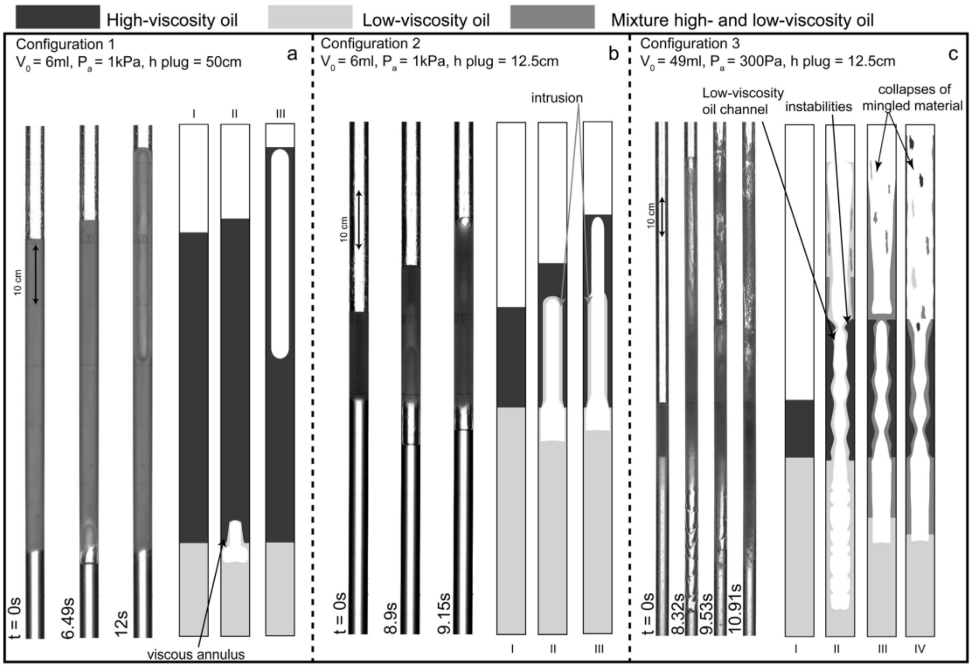

Fig. 4. Still frames and interpretative sketches from selected experiments representative of the identified flow configurations are shown. (**a**) Configuration 1: as the slug rose, gas expansion drove the intrusion of low-viscosity liquid into the plug (6.49 s); once the transition between the liquids was complete, the slug was fully accommodated within the plug (12 s). (**b**) Configuration 2: the slug exploited the low-viscosity intrusion, enclosed within the viscous annulus, to ascend through the plug (8.9 s). This tri-axial flow comprises ascending gas, descending low-viscosity liquid and, at flow timescale, relatively stationary high-viscosity liquid. At burst: (i) the slug nose was within the viscous plug, (ii) the low-viscosity film and the viscous annulus surrounded the slug main body (tri-axial flow), and (iii) the slug base remained in the low-viscosity liquid below the plug (annulus) base (9.15 s). (**c**) Configuration 3: the low-viscosity intrusion breached the plug top, and the slug burst into the extruded low-viscosity layer (8.32 s); instabilities formed and propagated along the falling film, leading to bubble break-up, partial blockage of the conduit and mixing between liquids (9.53 s). At burst, globules of this mixture fell back on the liquid surface (10.91 s).

scribe slug ascent, expansion and intrusion of liquid into the plug. The model is based on previously used geometrical representations of slug morphology (Vergniolle, 1998; Seyfried and Freundt, 2000; James et al., 2008, 2009; Del Bello et al., 2012) and, for simplicity, we neglected inertial forces on the liquid above the slug. Such inertial effects can be important when large rates of gas expansion are involved (James et al., 2008, 2009), but expansion rates will be generally reduced by the presence of the plug. Thus although the model will slightly overestimate gas expansion, this simplification is suitable for a model aimed only at estimating the active flow configurations. Furthermore, to retain the first-order approach and avoid the complexities involved with transitional behaviour and slug ascent within the intrusion, the model determines the active configuration no later than the point at which the slug nose reached the original plug base, without considering the full ascent up to slug burst.

The slug is represented as a cylinder of length L and constant radius r_s, ascending in a vertical tube of radius r_c (Fig. 5, Table 2 for notation). Above the slug, we consider three different sections; the lowest filled by the low-viscosity liquid only, viscosity μ_1 and density ρ_1, of height h_1. The uppermost section represents the viscous plug, with viscosity μ_2, density ρ_2, radius r_c and height h_3. The middle section represents the intrusion of low-viscosity liquid into the high-viscosity plug to form the annulus, with viscosity μ_1 and density ρ_1, length h_2 and radius r_ϕ. The radius r_ϕ is the result of $r_\phi = r_c - r_p$, where r_p is the thickness of the high-viscosity layer against the tube wall which forms the high-viscosity annulus. Due to the evolving nature of the annulus, r_p will vary in space and time. Consequently, in order to provide a characteristic first-order estimate in our straightforward model we assume a thickness as for a falling film surrounding a slug, which can be given as a function of the inverse viscosity, N_f (Llewellin et al., 2012; Supplementary Content):

$$r_p = \big(0.204 + 0.123\tanh(2.66 - 1.15\log_{10} N_f)\big)r_c. \quad (2)$$

Initial conditions are the height of the low-viscosity liquid above the slug nose, h'_1, the height of the plug, h'_3, the initial (magmastatic) bubble pressure, $P_0 = \rho g(h'_1 + h'_3) + P_a$, the slug length, L_0, and radius, $r_s = r_c - \lambda$, where λ is the thickness of the low-viscosity falling liquid film, determined by using equation (2) for the low-viscosity liquid (Fig. 3).

We assume constant velocity v_s for the slug base, thus, at any time, t, the height of the low-viscosity liquid column h_1 above the slug nose is given by:

$$h_1 = (L_0 - L) - v_s t + h'_1. \quad (3)$$

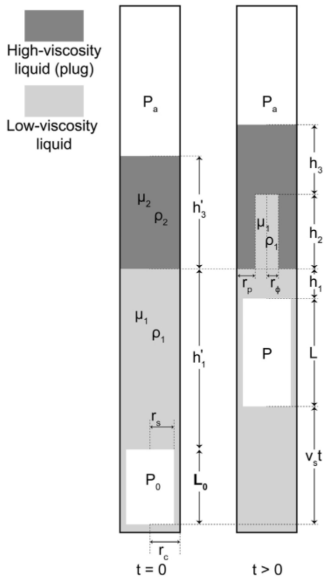

Fig. 5. The 1D model geometry for a gas slug ascending in a low-viscosity liquid overlaid by a high-viscosity liquid is shown. White regions represent the gas bubble, while grey-scale regions the liquids. See Table 2 for a complete geometrical notation.

Equating the intrusion volume to the gas expansion, the height of the low-viscosity liquid intrusion h_2 can be expressed as:

$$h_2 = -A(L_0 - L), \tag{4}$$

where $A = r_s^2/r_\phi^2$. Conservation of volume for the plug liquid yields:

$$\pi r_c^2(h_3 + h_2) - \pi r_\phi^2 h_2 = \pi r_c^2 h'_3, \tag{5}$$

where h_3 is the distance between the plug top and the intrusion (h_2) top. Simplifying and substituting for h_2, h_3 can be expressed as:

$$h_3 = h'_3 + (L_0 - L)(A - B), \tag{6}$$

where $B = r_s^2/r_c^2$.

The force on the liquid column above the slug due to the pressure difference between the slug and the surface is given by $F_p = \pi r_s^2(P - P_a)$. If the slug behaves like a perfect gas and adiabatic expansion, then $PV^\gamma = \text{constant}$ (where γ is the ratio of specific heat), and the slug pressure, with constant radius and pressure P_0 at $t = 0$, F_p can be expressed as:

$$F_p = \pi r_s^2\left(P_0 L_0^\gamma L^{-\gamma} - P_a\right). \tag{7}$$

The gravitational force is given by $F_g = -\pi r_s^2 \rho h g$, where ρ and h are respectively the density and the height of the involved liquid, and g is the acceleration due to gravity. Finally, assuming no-slip conditions at the wall, the Poiseuille law gives the viscous force for a laminar flow in a cylindrical pipe:

$$F_v = -8\pi \mu h V_f, \tag{8}$$

Table 2
Model notation.

Geometrical parameters	
P_a	ambient pressure
P_0	initial bubble pressure
P	bubble pressure
L_0	initial bubble length
L	bubble length
h'_1	initial height of low-viscosity liquid above the slug
h'_3	initial height of the plug
h_1	height of low-viscosity liquid above the bubble
h_2	height of low-viscosity intrusion
h_3	depth from the plug top to the intrusion
$v_s t$	depth from the bubble base to the tube base
r_c	tube radius
r_s	bubble radius
r_p	viscous annulus radius
r_Φ	intrusion radius
μ_1	viscosity of the liquid beneath the plug
μ_2	plug viscosity
ρ_1	low-viscosity liquid density
ρ_2	plug density

where μ is the viscosity of the liquid and V_f the flow velocity. If we assume that the liquid flow is equal to the volume flux controlled by the gas expansion, we obtain:

$$F_v = -8\pi \mu h \dot{L} B. \tag{9}$$

Equating the pressure force with the sum of the gravitational and viscous forces for the low-viscosity liquid column above the slug, the low-viscosity liquid intrusion, and the plug, we obtain:

$$\begin{aligned} &\pi r_s^2\left(P_0 L_0^\gamma L^{-\gamma} - P_a\right) \\ &\quad = -\pi r_s^2 \rho_1 g(h_1 + h_2) - \pi r_s^2 \rho_2 g h_3 - 8\pi \dot{L}\frac{r_s^2}{r_c^2}(\mu_1 h_1 + \mu_2 h_3) \\ &\qquad - 8\pi \dot{L}\frac{r_\phi^2}{r_c^2}\mu_1 h_2. \end{aligned} \tag{10}$$

Simplifying and substituting for both h_2 and h_3 yields:

$$\begin{aligned} &\left(P_0 L_0^\gamma L^{-\gamma} - P_a\right) \\ &\quad = -g\left[\rho_1\left(h_1 - A(L_0 - L)\right)\right] - g\left[\rho_2\left(h'_3 + (L_0 - L)(A - B)\right)\right] \\ &\qquad - 8\dot{L} r_c^{-2}\left[\mu_1 h_1 + \mu_2\left[h'_3 + (L_0 - L)(A - B)\right]\right] \\ &\qquad - 8\dot{L} r_\phi^2 \frac{r_c^{-2}}{r_s^2}\mu_1\left[-A(L_0 - L)\right], \end{aligned} \tag{11}$$

and finally:

$$\begin{aligned} \dot{L} = &\left\{-g\left[\rho_1\left(h_1 - A(L_0 - L)\right)\right] - g\left[\rho_2\left(h'_3 + (L_0 - L)(A - B)\right)\right] \right. \\ &\left. + \left(P_0 L_0^\gamma L^{-\gamma} - P_a\right)\right\} \Big/ \left\{8 r_c^{-2}\left[\mu_1 h_1 + \mu_2\left[h'_3 \right.\right.\right. \\ &\left.\left.\left. + (L_0 - L)(A - B)\right]\right] + 8 r_\phi^2 \frac{r_c^{-2}}{r_s^2}\mu_1\left[-A(L_0 - L)\right]\right\}. \end{aligned} \tag{12}$$

The first order differential is solved numerically in *Matlab*, using a Runge–Kutta formula. With the focus of the model being to determine flow configurations within the parameter space of a system, it is sufficient to consider the values determined when either the intrusion breaches the plug surface, $h_3 = 0$ (indicating Configuration 3) or when the slug reaches the plug base, $h_1 = 0$. In this latter case, Configuration 1 is identified if there is sufficient plug material to fully encompass the volume of the gas slug, otherwise Configuration 2 is determined.

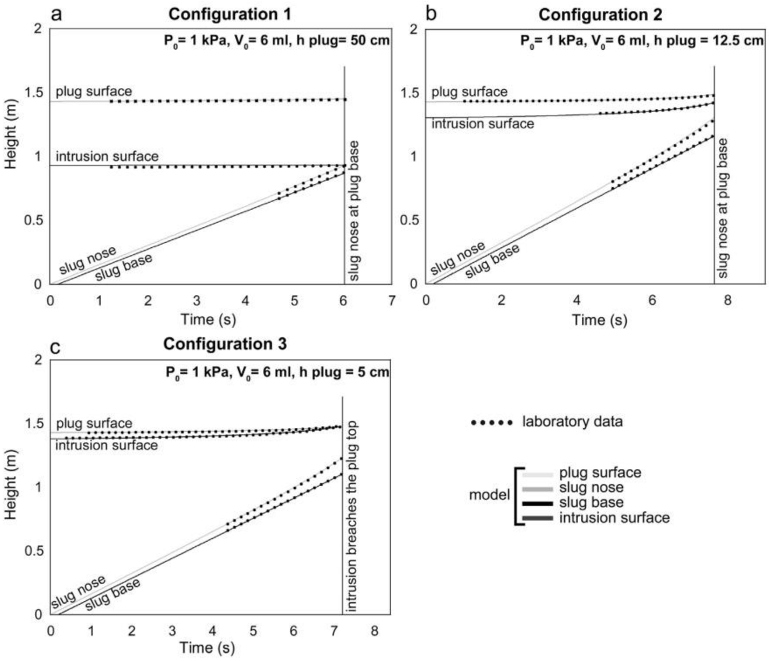

Fig. 6. Comparison of slug ascent profiles measured from laboratory video (symbols) and the 1D model (lines) for each flow configuration. A 6 ml slug ascends in a liquid column overlain by a plug of 50 cm (Configuration 1; **a**), 12.5 cm (Configuration 2; **b**) and 5 cm (Configuration 3; **c**) with a $P_a = 1$ kPa. In all cases the variations in position of the plug surface, intrusion surface, slug nose and slug base are well reproduced. For Configuration 3 (**c**), the intersection between the plug and intrusion curves indicates that the low-viscosity liquid breached the plug surface. The comparison with the experimental data is limited up to the moment the simulation stopped. Note that video data for the slug ascent are not available for heights $<\sim 0.5$ above the apparatus base, because of the camera field of view.

4.1. Model validation

To verify the suitability of equation (12), we compared modelled slug ascent to experimental data representative of each configuration (Fig. 6). For model inputs, we measured the ascent velocity of the base from the laboratory video, derived the initial slug length directly from the experimental gas volumes, and, to calculate the intrusion radius, assumed the value of the annulus radius equal to a falling film surrounding a slug. For Configuration 1 (Fig. 6a) and 2 (Fig. 6b), the model accurately reproduced the variations in position of the slug nose, base and the liquid surface, with the intrusion level always below the plug surface. For Configuration 3 (Fig. 6c), the model accurately predicted both the timing and position of the plug breach.

We neglected the inertial forces in the formulation of equation (12), so gas expansion is slightly overestimated by the model, as well as the intrusion volume, leading to small discrepancies between the laboratory experiments and model results (Fig. 7a). Larger slugs and rapid gas expansion, resulting in greater intrusion of low-viscosity liquid, cause the model prediction of Configuration 3 or 2 instead of Configuration 2 or 1 respectively. However, when compared to the experimental data and considering the simplifying assumptions, the model successfully identifies the dominant areas of parameter space for Configuration 1 and 3, separated by Configuration 2.

Applying the model to an idealised volcanic-scale scenario (Fig. 7b) indicated that a similar pattern of flow configurations could be relevant at Stromboli. To corroborate this, we carried out 3D computational fluid dynamics (CFD) simulations using the commercial software Flow3D (James et al., 2008; Chouet et al., 2010; Del Bello et al., 2015).

First, we modelled selected laboratory experiments to validate the CFD model against experimental data, recreating the same experimental conditions (apparatus geometry, injected slug volumes, experimental ambient pressures and plug thickness). The CFD simulations produced results similar to those observed in the laboratory in terms of both flow processes and slug and intrusion shapes (Fig. 8a, b; Video V05). The generation of the viscous annulus and the complex interaction between the two liquids were also accurately reproduced, together with the disruption of the slug and the generation of offspring bubbles and partial blockages of the conduit (Fig. 8c, d; Video V05).

For the volcanic scenario, a 300-m-high vertical cylinder with a radius of 1.5 m (for CFD simulations, only this conduit radius was used), closed at the lower boundary, represented the conduit. Although a closed condition was not realistic and more representative of the experimental condition, once a stable slug flow was established in the conduit, this boundary condition did not affect the flow (e.g., James et al., 2008; Chouet et al., 2010). The 200-m-high magma column was modelled as an incompressible Newtonian liquid with a temperature-dependent viscosity and di-

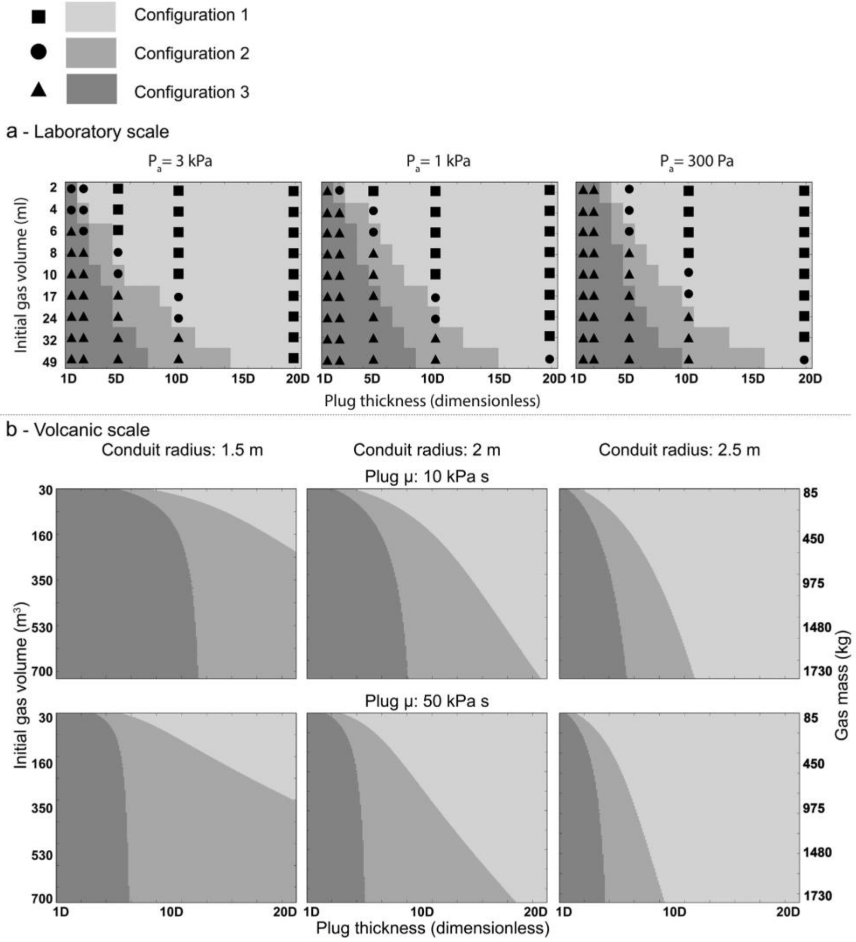

Fig. 7. (**a**) Comparison between experimental fluid configurations (symbols) and configurations determined by the 1D model (shaded regions) is shown as a function of initial gas volume (ml) and plug thickness (dimensionless), for ambient gas pressures of 3 kPa (left), 1 kPa (middle) and 300 Pa (right). (**b**) Flow configurations determination by the 1D model for an idealised volcanic scenario are shown, for a plug viscosity of 10 kPa s (upper row) and 50 kPa s (lower row), and as a function of initial gas volume (m^3), or gas mass (kg; right axis), plug thickness (dimensionless) and volcanic conduit radii of 1.5 (left), 2 (middle) and 2.5 (right) m; the configuration distribution is insensitive to the viscosity of magma beneath the plug within the limit 50–500 Pa s.

vided into two temperature regions. The first region covered the low-viscosity magma, while the second region defined the plug. Viscosity values ranged between 10–1000 Pa s for the magma beneath the plug and between 1–20 kPa s for the plug, lower than the typical value of Stromboli (1–50 kPa s, Gurioli et al., 2014): exceeding that range resulted in simulation initialisation problems. The gas slug was modelled as a continuous void region (contains no mass) governed by the equation $PV^{\gamma} = \text{constant}$.

The volcano-scale simulations, for plug thickness and gas volumes of 3–60 m and 30–250 m^3 respectively, showed changes in slug shape as it enters the annulus (Fig. 8e, f), and reproduced the generation of instabilities and slug disruption (Fig. 8g–l). As predicted, the slug transition from a low-viscosity magma to a viscous plug caused a sudden decrease in the slug ascent velocity. As for the burst process, different dynamics can be associated with the different configurations. Based purely on visual observation of the burst dynamics, Configuration 1 involved a slow fragmentation of the viscous meniscus above the slug, with almost no pyroclast ejection. In Configuration 2 the fragmentation of the magma meniscus was fast and its particles were ejected up to tens of meters above the burst point (note this is a minimum inertial height since no drag from expanding gas is applied). Configuration 3 explosions ranged in style depending on slug volumes, plug thickness, generation of secondary bubbles and blockages of the

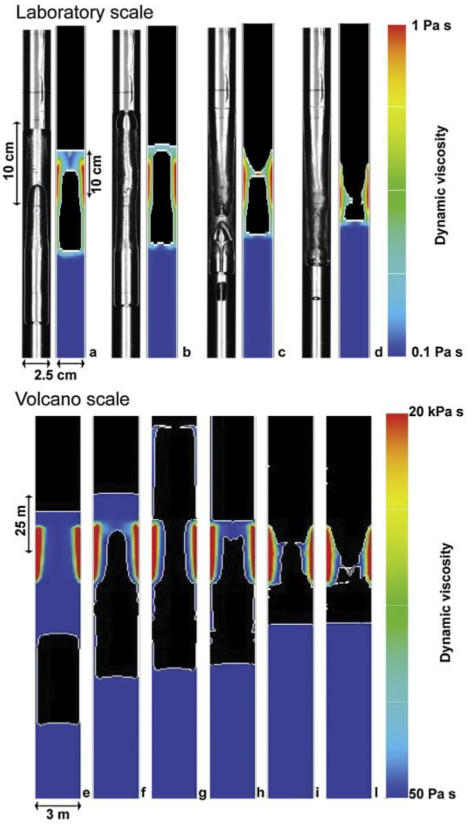

Fig. 8. (**Upper panel**) Still frames from a laboratory experiment and 3D CFD simulation for a 10 ml slug, expanding in a $P_a = 3$ kPa and a plug $h = 12.5$ cm (Configuration 3). The CFD simulation reproduced experimental observation well, including the variations in slug shape, intrusion dynamics, burst dynamics and bubble breakup process (see also Video V05). Note the asymmetry in panels **c** and **d** that demonstrate the requirement for full 3D simulation. (**Lower panel**) Still frames from a 3D CFD simulation at volcanic-scale. Input parameters are $V_0 = 140$ m^3, $P_a = 10^5$ Pa, $\mu_{magma} = 50$ Pa s, $\mu_{plug} = 20$ kPa s, $r_c = 1.5$ m, column $h = 200$ m, conduit radius $r_c = 1.5$ m, conduit $h = 300$ m, and plug $h = 15$ m. Note the visible asymmetry that develops once instabilities arise from panel **g** onward, underscoring the requirement for a 3D approach once dynamic instability develops.

conduit. In general the burst process seemed characterised by dynamics common to both Configuration 1 and 2, with ejection of material above the burst point but at heights inferior to Configuration 2. Furthermore, most of the ejecta appeared to be mingled and collapsed back in the conduit, creating partial blockages that forced the slug into smaller pockets of gas.

The simulations, showing flow processes similar to those observed in the scaled laboratory experiments, support the applicability of the 1D model and endorse the main roles played by slug volume and plug properties in determining the prevailing flow configuration. The computational fluid dynamics simulations also enabled investigation of the role of the underlying magma viscosity on the complex syn- and post-burst dynamics involved in Configuration 3. A lower viscosity magma drained faster along the conduit/annulus walls, accumulating at the top of the annulus. This promoted the fast and cyclic creation of narrowing necks around the slug. Every time a neck closed, the slug was disrupted, generating offspring bubbles and secondary bursts (pulses). Magma clots were also ejected at greater heights and their collapse produced partial blockages of the conduit, trapping the slug gas into smaller pockets and leading to sub-pulses. For each pulse and sub-pulse, burst depth gradually increased (Video V06, 21–34 s). With increasing magma viscosity, drainage along the conduit walls slowed, with the generation of fewer, or no, pulses but only partial blockages due to collapse of material back into the conduit (Video V06).

5. Implications for Strombolian eruptions

Our experiments characterised the spectrum of flow configurations for a set of liquid parameters, tube geometry and for single slug ascent in a rheologically stratified conduit. In our idealised volcanic scenario, both configuration model and CFD simulations indicate the sensitivity of configurations to initial gas volumes and plug properties (Fig. 7b). For a particular conduit radius, the distribution of configurations in parameter space was insensitive to the viscosity of the magma beneath the plug, which can be considered mainly as a means of delivering the slug into the plug (Fig. 7b, Video V06). In contrast, conduit radius had a strong influence on configuration transitions. The Configuration 1 domain increased with increasing radius (Fig. 7b) implying that, for identical magmatic conditions, vents of different radius could erupt with different style.

Under plugged conditions, it appeared both experimentally and numerically that the burst vigour was always greater when compared to an unplugged scenario. As previous models in single-viscosity systems demonstrated, slug overpressure varies with the thickness of the falling film, controlled by magma viscosity (James et al., 2009; Del Bello et al., 2012). Hence, the same initial gas volume burst with a lower overpressure in a low-viscosity liquid (thin film, Fig. 2e) compared to in a higher viscosity liquid (thick film, Fig. 2a). This effect occurred in Configuration 1; however, because the slug was initially ascending in a low-viscosity magma, its overpressure also increased due to pressurisation of the conduit below the plug. The greater the plug thickness and viscosity, the more pressure can be retained to be released during a more vigorous burst.

Within Configuration 2, gas expansion intruded a substantial volume of low-viscosity liquid into the plug; the further the intrusion penetrated, the higher the slug can ascend within the low-viscosity channel enclosed within the viscous annulus. The greater thickness of the complex "double" falling film resulted in increased slug lengthening to accommodate gas expansion, opposed by the presence of the un-intruded plug above, and enhancing the generation of overpressure. In Configuration 3, the full development of an open low-viscosity channel through the plug removed the 'capping' effect, allowing the slug to expand more freely and, compared to the other two configurations, reducing slug overpressure. Furthermore, the partial constriction of the tube and the gas slug break-up into smaller pockets produced multiple bursts and modulation of the gas release within Configuration 3.

In support of the role of different flow configurations on slug overpressure, Del Bello et al. (2015) quantified similar effects for their experiments, that can be now categorised as Configurations 1 and 3 (Configuration 2 was not identified). All of their plugged experiments, regardless plug thickness, showed a greater acoustic amplitude and an increase in slug overpressure with respect to the single-viscosity experiments (Figs. 3 and 4 in Del Bello et al., 2015). In Configuration 1, Del Bello et al.'s slugs showed a greater increase in both conduit pressurisation during slug ascent and acoustic amplitude at burst compared to slugs bursting in Configuration 3. In Configuration 3, slugs were characterised by a lower overpressure but also by highly variable gas release rates, both in terms of magnitude and time, and generated a range of pressure pulses (burst of offspring bubbles) and sub-pulses (conduit constriction) (Del Bello et al., 2015).

Therefore, for volcanoes where multiple vents are constantly active (e.g., Stromboli and Yasur, Vanuatu), each active vent may be characterised by plugs with different properties, controlling both burst dynamics and explosion magnitude, thus affecting acoustic amplitudes. However, a unique explanation of a particular acoustic amplitude is further complicated because the same gas mass can lead to different flow configurations sensitive to conduit width (Fig. 7b). Slug parameterisation and the linking of field results and fluid dynamic models, so far based on single-viscosity scenarios suggesting a positive correlation for the burst pressure with both initial slug volume and magma viscosity (e.g., Vergniolle and Brandeis, 1996; James et al., 2009; Del Bello et al., 2012; Lane et al., 2013), becomes more poorly constrained with the added degrees of freedom provided by rheological complexity.

5.1. Magma mingling

As a result of interactions between the different viscosity magmas, the textural and geochemical properties of the ejected pyroclasts will also depend on the flow processes occurring within the plug. Our experiments reveal that mingling of material may occur in two ways. If the low-viscosity magma intrudes the plug deep enough but without breaching it, the slug approaches the surface surrounded by a low-viscosity magma film, enclosed in turn by the high-viscosity annulus forming a tri-axial flow (Del Bello et al., 2015), i.e., at the boundary of Configuration 2 with 3. At burst, the fragmenting meniscus will comprise layers of both low- and high-viscosity magma, promoting mingling and ejection of mingled pyroclasts. However, with only the meniscus region involved, mingling is expected to be a relatively localised process. A more extended mingling occurs within Configuration 3 (Figs. 2d and 4c), where: (a) globules of the annulus are mixed into the low-viscosity liquid during rapid intrusion and (b) flow instabilities (also observed by Del Bello et al., 2015) produce cyclic collapses of the low-viscosity film which, in turn, initiate a broader mingling with the high-viscosity liquid of the annulus within the tri-axial flow. The same instabilities are responsible for slug break-up and for creating partial blockages in the conduit that force the slug into smaller pockets. The effect is a pulsatory bursting with these processes coexisting. Both laboratory observations (Video V04, V07) and, particularly, CFD simulations for Stromboli (Video V06) showed that the secondary burst depths changed with time. Initially, the slug burst in the low-viscosity magma above the plug. Slug break-up then occurred at the top of the viscous annulus and secondary bubbles and transient gas pockets burst inside a region of mingled material or within the plug, with the burst depth gradually increasing. Ejected material was, therefore, scavenged at increasing depth with time, sampling different regions of the complex collapsing liquid structure. Physical changes in magma should then occur at two different scales, and the level of mingling could help in determining the flow configurations. If mixing occurs mainly during slug ascent (Configuration 3), mingling is a predominant process, likely showing, e.g., the coexistence of different vesicle populations. In contrast, the lower the mingling in the ejecta, the more restricted is the process, reflecting a possible mingling only at burst, during magma fragmentation (Configuration 2). Analysis of the mingling textures within ejecta from a strombolian eruption could, therefore, provide evidence of the near-surface flow dynamics within the conduit.

5.2. Pulsatory behaviour

At Stromboli, Gaudin et al. (2014) related individual pyroclast ejection pulses to successive pressure release pulses and sub-pulses of duration between 0.05–2 s and an average pulse rate of 7 per second, with a minimum of 3 up to 120 pulses per eruption. As a general trend, with some exceptions, the greater the number of pulses and sub-pulses, the longer the explosions, with greater gas masses involved (Gaudin et al., 2014). In our experiments, secondary bursts (pulses), followed by several partial blockages (sub-pulses) of the gas path, were achieved only in Configuration 3, with their larger number resulting from the disruption of larger gas volumes (24–49 ml). Smaller volumes (8–17 ml) generated offspring bubbles, without any sub-pulses, and shorter burst times. With these volumes scaled to the volcanic-case, CFD simulations showed the same positive correlation between volumes and number of pulses and sub-pluses as measured in the experiments. Although no formal scaling exists for these processes at laboratory-scale, the trend observed in both laboratory and CFD simulations is similar to the one derived from field observations, also suggesting the presence of a plug as a pre-requisite for pulsatory behaviour. Furthermore, CFD simulations showed that greater initial gas volume and lower viscosity of the underlying magma favour secondary bursts from offspring bubbles and sub-pulses generated by partial blockages of the conduit, while a higher viscosity led mainly to sub-pulses (restriction of gas escape pathway), with the generation of fewer, or no, secondary bubbles (blockage of gas escape pathway; Video V06). Hence, while not measurably affecting the pre-burst processes, the viscosity of the underlying magma can noticeably influence syn- and post-burst dynamics and therefore any measured geophysical signals.

6. Conclusions

Based on scaled laboratory experiments we define a framework to describe the characteristic styles of the flow organisation involved with the ascent and burst of slugs in a rheologically stratified conduit, where a high-viscosity plug overlies a low-viscosity magma. Conduits that are fully filled with either high- or low-viscosity magma represent end-member scenarios that can be considered as infinitely thick or thin high-viscosity plugs respectively. In between, our experiments demonstrated three fundamental flow configurations, determined by the ratio of plug size and slug gas volume. In Configuration 1, the plug was sufficiently large to fully accommodate the ascending slug. In Configuration 2, a smaller plug was sufficient to accommodate the volume change due to expansion of the slug on ascent, but not the full volume of the slug. Consequently, when the slug burst at the surface of the plug, its base was still in the low-viscosity liquid. Finally, in Configuration 3, slug expansion drove an intrusion of low-viscosity liquid right through the plug, enabling slug burst to occur within the low-viscosity liquid, with the plug acting only as a region of effectively reduced conduit diameter.

We developed a model, validated with the laboratory experiments and by 3D CFD simulations at volcano-scale, to explore configuration parameter space. Our results showed how gas volume, plug thickness and plug viscosity were the key parameters controlling the transitions between different configurations; transitions were much less sensitive to properties of the underlying magma. Each configuration encompassed a variety of processes: dynamic narrowing and widening of the effective conduit, generation of instabilities along the falling liquid film, transient blockages of the slug path and slug break-up. These complexities influenced the slug ascent dynamics and gas overpressure at burst, and thus also the resulting eruptive style and, by implication, geophysical signals.

The complex flow processes can also promote magma mingling, not only by fragmentation of a rheologically layered meniscus but also through instabilities in the falling film and surrounding fluid annulus, leading to more localised or distributed regions of mingling respectively. In Configuration 3, flow instabilities cause a narrowing of the gas escape pathway causing sub-pulses within the eruption process. The flow instabilities can be sufficient to seal the gas escape pathway and cause slug break-up through the creation of transient blockages, resulting in a pulsatory, multi-bubble burst process. A widening of the conduit was needed for the slug break-up and falling film collapses, and both the viscosity of the underlying magma and the gas volume seemed to determine the frequency of pulses and sub pluses.

Our results showed how these flow configurations can influence eruption vigour, style and pyroclast properties. The configuration framework should be considered when interpreting slug-burst related geophysical signals, and points the way to more detailed links between fluid dynamic models and acoustic signals.

7. Video description

Videos **V01**, **V02**, **V03** and **V04** show the flow processes occurring during slug ascent, expansion and burst in the following experiments: (**V01**) Single and low-viscosity system, plug $h = 0$ cm ($0D$), $P_a = 1$ kPa, $V_0 = 6$ ml; (**V02**) Configuration 1, plug $h = 50$ cm ($20D$), $P_a = 1$ kPa, $V_0 = 6$ ml; (**V03**) Configuration 2, plug $h = 12.5$ cm ($5D$), $P_a = 1$ kPa, $V_0 = 6$ ml. (**V04**) Configuration 3, plug $h = 12.5$ cm ($5D$), $P_a = 300$ Pa, $V_0 = 49$ ml. Video **V05** shows the comparison between a laboratory experiment and a CFD simulation for a 10 ml slug, $P_a = 3$ kPa and plug $h = 5$ cm ($2D$); frame rate of the laboratory video has been accelerated to allow an easier video comparison. Video **V06** shows the comparison between three different CFD simulations at volcanic-scale, for the same gas volume, $V_0 = 140$ m^3, ascending in a 300-m-high volcanic conduit of radius 1.5 m, filled with magma beneath the plug (plug $h = 15$ m [5D]) of viscosities 50 (left), 150 (middle) and 300 (right) Pa s. Video **V07** contains a sequence of the bubble break-up process from an experiment of a 24 ml slug, $P_a = 3$ kPa and plug $h = 12.5$ cm (5D).

Acknowledgements

This research is part of A.C. PhD at Lancaster University, funded by the People Programme (Marie Curie Actions) of the European Union's Seventh Framework Programme (FP7/2007-2013) under the project NEMOH, REA grant agreement No. 289976. We thank Kathy Cashman and Sylvie Vergniolle for thorough and constructive comments that greatly improved the manuscript, and the editor Bernard Marty.

Appendix A. Supplementary material

Supplementary material related to this article can be found online at http://dx.doi.org/10.1016/j.epsl.2015.12.028.

References

Blackburn, E.A., Wilson, L., Sparks, R.S.J., 1976. Mechanisms and dynamics of strombolian activity. J. Geol. Soc. 132 (4), 429–440. http://dx.doi.org/10.1144/gsjgs.132.4.0429.

Chouet, B., Hamisevicz, N., Mcgetchin, T.R., 1974. Photoballistics of volcanic jet activity at Stromboli, Italy. J. Geophys. Res. 79 (32), 4961–4976.

Chouet, B., Dawson, P., Ohminato, T., Martini, M., Saccorotti, G., Giudicepietro, F., De Luca, G., Milana, G., Scarpa, R., 2003. Source mechanisms of explosions at Stromboli Volcano, Italy, determined from moment-tensor inversions of very-long-period data. J. Geophys. Res. 108 (B1), 2019. http://dx.doi.org/10.1029/2002JB001919.

Chouet, B.A., Dawson, P.B., James, M.R., Lane, S.J., 2010. Seismic source mechanism of degassing bursts at Kilauea Volcano, Hawaii: results from waveform inversion in the 10–50 s band. J. Geophys. Res. 115, B09311. http://dx.doi.org/10.1029/2009JB006661.

Colò, L., Ripepe, M., Baker, D.R., Polacci, M., 2010. Magma vesiculation and infrasonic activity at Stromboli open conduit volcano. Earth Planet. Sci. Lett. 292 (3–4), 274–280. http://dx.doi.org/10.1016/j.epsl.2010.01.018.

D'Oriano, C., Bertagnini, A., Pompilio, M., 2011. Ash erupted during normal activity at Stromboli (Aeolian Islands, Italy) raises questions on how the feeding system works. Bull. Volcanol. 73 (5), 471–477. http://dx.doi.org/10.1007/s00445-010-0425-0.

Del Bello, E., Llewellin, E.W., Taddeucci, J., Scarlato, P., Lane, S.J., 2012. An analytical model for gas overpressure in slug-driven explosions: insights into Strombolian volcanic eruptions. J. Geophys. Res. 117 (B2), B02206. http://dx.doi.org/10.1029/2011JB008747.

Del Bello, E., Lane, S.J., James, M.R., Llewellin, E.W., Taddeucci, J., Scarlato, P., Capponi, A., 2015. Viscous plugging can enhance and modulate explosivity of Strombolian eruptions. Earth Planet. Sci. Lett. (ISSN 0012-821X) 423 (1), 210–218. http://dx.doi.org/10.1016/j.epsl.2015.04.034.

Gaudin, D., Taddeucci, J., Scarlato, P., Moroni, M., Freda, C., Gaeta, M., Palladino, D.M., 2014. Pyroclast tracking velocimetry illuminates bomb ejection and explosion dynamics at Stromboli (Italy) and Yasur (Vanuatu) volcanoes. J. Geophys. Res. 119 (7), 5384–5397. http://dx.doi.org/10.1002/2014JB011096.

Gurioli, L., Colò, L., Bollasina, A.J., Harris, A.J.L., Whittington, A., Ripepe, M., 2014. Dynamics of strombolian explosions: inferences from field and laboratory studies of erupted bombs from Stromboli volcano. J. Geophys. Res. 119, 319–345. http://dx.doi.org/10.1002/2013JB010355.

Harris, A., Ripepe, M., 2007. Temperature and dynamics of degassing at Stromboli. J. Geophys. Res. 112, B03205. http://dx.doi.org/10.1029/2006JB004393.

Houghton, B.F., Gonnermann, H.M., 2008. Basaltic explosive volcanism: constraints from deposits and models. Chem. Erde (ISSN 0009-2819) 68 (2), 117–140. http://dx.doi.org/10.1016/j.chemer.2008.04.002.

James, M.R., Lane, S.J., Chouet, B.A., 2006. Gas slug ascent through changes in conduit diameter: laboratory insights into a volcano-seismic source process in low-viscosity magmas. J. Geophys. Res. 111 (B5), B05201. http://dx.doi.org/10.1029/2005JB003718.

James, M.R., Lane, S.J., Corder, S.B., 2008. Modelling the rapid near-surface expansion of gas slugs in low viscosity magmas. Geol. Soc. (Lond.) Spec. Publ. 307 (1), 147–167. http://dx.doi.org/10.1144/SP307.9.

James, M.R., Lane, S.J., Wilson, L., Corder, S.B., 2009. Degassing at low magma-viscosity volcanoes: quantifying the transition between passive bubble-burst and Strombolian eruption. J. Volcanol. Geotherm. Res. 180 (2–4), 81–88. http://dx.doi.org/10.1016/j.jvolgeores.2008.09.002.

Jaupart, C., Vergniolle, S., 1988. Laboratory models of Hawaiian and Strombolian eruptions. Nature 331 (6151), 58–60.

Kobayashi, T., Namiki, A., Sumita, I., 2010. Excitation of airwaves caused by bubble bursting in a cylindrical conduit: experiments and a model. J. Geophys. Res. 115 (B10). http://dx.doi.org/10.1029/2009JB006828.

Lane, S.J., James, M.R., Corder, S.B., 2013. Volcano infrasonic signals and magma degassing: first-order experimental insights and application to Stromboli. Earth Planet. Sci. Lett. 377–378, 169–179. http://dx.doi.org/10.1016/j.epsl.2013.06.048.

Lautze, N.C., Houghton, B.F., 2005. Physical mingling of magma and complex eruption dynamics in the shallow conduit at Stromboli volcano, Italy. Geology 33 (5), 425. http://dx.doi.org/10.1130/G21325.1.

Lautze, N.C., Houghton, B.F., 2006. Linking variable explosion style and magma textures during 2002 at Stromboli volcano, Italy. Bull. Volcanol. 69 (4), 445–460. http://dx.doi.org/10.1007/s00445-006-0086-1.

Llewellin, E.W., Del Bello, E., Taddeucci, J., Scarlato, P., Lane, S.J., 2012. The thickness of the falling film of liquid around a Taylor bubble. Proc. R. Soc., Math. Phys. Eng. Sci. 468 (2140), 1041–1064. http://dx.doi.org/10.1098/rspa.2011.0476.

Mori, T., Burton, M., 2009. Quantification of the gas mass emitted during single explosions on Stromboli with the SO_2 imaging camera. J. Volcanol. Geotherm. Res. 188 (4), 395–400. http://dx.doi.org/10.1016/j.jvolgeores.2009.10.005.

Parfitt, E.A., Wilson, L., 1995. Explosive volcanic eruptions: IX the transition between Hawaiian-style lava fountaining and Strombolian explosive activity. Geophys. J. Int. 121, 226–232.

Parfitt, E.A., 2004. A discussion of the mechanisms of explosive basaltic eruptions. J. Volcanol. Geotherm. Res. 134 (1–2), 77–107. http://dx.doi.org/10.1016/j.jvolgeores.2004.01.002.

Polacci, M., Baker, D.R., Mancini, L., Favretto, S., Hill, R.J., 2009. Vesiculation in magmas from Stromboli and implications for normal Strombolian activity and paroxysmal explosions in basaltic systems. J. Geophys. Res. 114, B01206. http://dx.doi.org/10.1029/2008JB005672.

Ripepe, M., Marchetti, E., 2002. Array tracking of infrasonic sources at Stromboli volcano. Geophys. Res. Lett. 29 (22), 33-1. http://dx.doi.org/10.1029/2002GL015452.

Seyfried, R., Freundt, A., 2000. Experiments on conduit flow and eruption behaviour of basaltic volcanic eruptions. J. Geophys. Res. 105 (B10), 727–740. http://dx.doi.org/10.1029/2000JB900096.

Taddeucci, J., Scarlato, P., Capponi, A., Del Bello, E., Cimarelli, C., Palladino, D.M.,

Kueppers, U., 2012. High-speed imaging of Strombolian explosions: the ejection velocity of pyroclasts. Geophys. Res. Lett. 39 (2), L02301. http://dx.doi.org/10.1029/2011GL050404.
Vergniolle, S., Jaupart, C., 1986. Separated two-phase flow and basaltic eruptions. J. Geophys. Res. 91 (B12), 12842–12860.
Vergniolle, S., Brandeis, G., 1996. Strombolian explosions 1. A large bubble breaking at the surface of a lava column as a source of sound. J. Geophys. Res. 101 (B9), 433–447.
Vergniolle, S., Brandeis, G., Mareschal, J.C., 1996. Strombolian explosions 2. Eruption dynamics determined from acoustic measurements. J. Geophys. Res. 101 (B9), 449–466.
Vergniolle, S., 1998. Modelling two-phase flow in a volcano. In: Proc. 13th Australasian Fluid Mech. Conf. Aristoc. Offset. Monash University, Melbourne, pp. 647–650.
White, E.T., Beardmore, R.H., 1962. The velocity of rise of single cylindrical air bubbles through liquids contained in vertical tubes. Chem. Eng. Sci. 17, 351–361.

Appendix 3 – Capponi et al. 2016b

Bull Volcanol (2016) 78:13
DOI 10.1007/s00445-016-1001-z

RESEARCH ARTICLE

Recycled ejecta modulating Strombolian explosions

Antonio Capponi[1,2] · Jacopo Taddeucci[2] · Piergiorgio Scarlato[2] ·
Danilo M. Palladino[3]

Received: 23 September 2015 / Accepted: 27 January 2016

Abstract Two main end-members of eruptive regimes are identified from analyses of high-speed videos collected at Stromboli volcano (Italy), based on vent conditions: one where the vent is completely clogged by debris, and a second where the vent is open, without any cover. By detailing the vent processes for each regime, we provide the first account of how the presence of a cover affects eruptive dynamics compared to open-vent explosions. For clogged vents, explosion dynamics are controlled by the amount and grain size of the debris. Fine-grained covers are entirely removed by explosions, favouring the generation of fine ash plumes, while coarse-grained covers are only partially removed by the explosions, involving minor amounts of ash. In both fine- and coarse-grained cases, in-vent ground deformation of the debris reflect variations in the volumetric expansion of gas in the conduit, with rates of change of the deformation comparable to ground inflation related to pre-burst conduit pressurization. Eruptions involve the ejection of relatively slow and cold bombs and lapilli, and debris is observed to both fall back into the vent after each explosion and to gravitationally accumulate between explosions by rolling down the inner crater flanks to produce the cover itself. Part of this material may also contribute to the formation of a more degassed, crystallized and viscous magma layer at the top of the conduit. Conversely, open-vent explosions erupt with hotter pyroclasts, with higher exit velocity and with minor or no ash phase involved.

Keywords Strombolian eruptions · Vent processes · Eruption dynamics · Plume dynamics · Ejection velocity · High-speed video

Introduction

Strombolian eruptions are characterized by relatively mild, impulsive releases of gas and pyroclasts that typically last a few to tens of seconds and eject a gas-particle mixture to several tens to hundreds of metres in height (e.g. Houghton and Gonnermann 2008; Cashman and Sparks 2013; Taddeucci et al. 2015). Eruptions result from the arrival and burst of overpressured gas pockets (slugs) at the free-surface (Chouet et al. 1974; Blackburn et al. 1976; Parfitt 2004; Houghton and Gonnermann 2008). This widely accepted scenario is supported by a large body of literature focused on understanding the mechanism behind explosions at Stromboli volcano (Aeolian Islands, Italy) via, for example, interpretation of seismic and infrasonic data (e.g. Vergniolle et al. 1996; Chouet et al. 2003, 2008; Marchetti and Ripepe 2005), experimental studies (e.g. James et al. 2004, 2006, 2008; Lane et al. 2013), and field observations (e.g. Chouet et al. 1974; Blackburn et al. 1976; Ripepe et al. 1993, 2005; Patrick et al. 2007; Harris et al. 2012; Taddeucci et al. 2012a, b; Gaudin et al. 2014; Bombrun et al. 2015).

Editorial responsibility: P-S Ross

Electronic supplementary material The online version of this article (doi:10.1007/s00445-016-1001-z) contains supplementary material, which is available to authorized users.

✉ Antonio Capponi
a.capponi@lancaster.ac.uk

1 Lancaster Environment Centre, Lancaster University, Lancaster LA1 4YQ, UK

2 Istituto Nazionale di Geofisica e Vulcanologia, Via di Vigna Murata 605, 00143 Rome, Italy

3 Dipartimento di Scienze della Terra, Sapienza-Università di Roma, Rome, Italy

Published online: 15 February 2016

However, none of these studies have focused on detailing how the gas is physically released into the atmosphere, i.e. the vent processes.

Increasing textural, experimental and field evidence suggests that the Strombolian paradigm of slugs ascending and bursting in a rheologically uniform melt is too simplistic, pointing instead to the coexistence of melts with different rheological properties in the shallower conduit (Gurioli et al. 2014; Leduc et al. 2015). Cooling and degassing of the uppermost part of the magma column may lead to the generation of a more viscous and evolved magma layer in which a gas pocket bursts (Gurioli et al. 2014). The properties and thickness of this layer may have an impact on the eruptive dynamics, to cause variations in explosion intensity and style (Lautze and Houghton 2005, 2006). Textural and geochemical analyses of ejected pyroclasts at Stromboli support the coexistence of melts with contrasting rheologies (Lautze and Houghton 2005; D'Oriano et al. 2011; Colò et al. 2010), leading to magma mingling during the ascent and burst of a slug (Gurioli et al. 2014; Leduc et al. 2015).

Recent experimental investigation endorses the presence of a plug (Fig. 1), demonstrating how the interaction of an ascending slug with a high-viscosity plug heavily affects fluid dynamic processes in the conduit and explaining some of the key phenomena observed at Stromboli, such as the eruptive pulses and sub-pulses and the occurrence of mingled pyroclasts (Del Bello et al. 2015). The presence of a plug also affects the degree of slug overpressurization, leading to an increase in the explosivity of Strombolian eruptions (Del Bello et al. 2015).

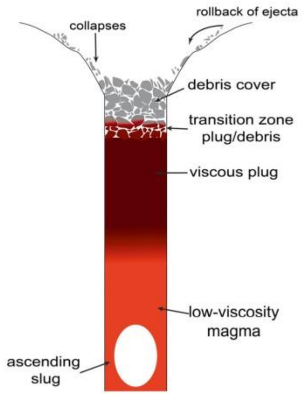

Fig. 1 Conceptual sketch of the volcanic conduit, in which a gas slug ascends through a rheologically stratified magma column, and the vent clogged by debris. The debris cover is generated by fallback of pyroclasts into the vent and collapses of the conduit wall; a transition zone exists between the degassed layer at the top of the magma column (plug) and the debris cover filling the vent

A second surficial layer may be also present due to temporary blockage of the vent due to backfilling of the conduit (Fig. 1). This has been proposed to result from collapses and slumping of the conduit wall, by rollback of erupted pyroclasts and lithic clasts into the vent (McGetchin et al. 1974), or magma draining back into the conduit, favouring the generation of ash plumes due to grinding of the back-fill clasts during the explosive event (Patrick et al. 2007). In light of these new findings, understanding the dynamics and evolution of vent processes during explosions at Stromboli has gained more importance if we are to unravel the complete mechanism responsible for the persistent but extremely variable explosive activity, such as that classically observed at Stromboli. In this paper, we investigate how the presence of a debris cover affects the style of Strombolian eruptions through analysis of high-speed videos acquired at Stromboli. We identify two main eruptive regimes depending on the vent conditions (i.e. open vent vs. clogged vent) and show how the nature and amount of a debris cover strongly modify the vent processes and, eventually, explosion dynamics, magnitude and pyroclasts ejection velocity.

Terminology

Explosions at Stromboli, although relatively mild and of short duration, can be very complex in terms of both dynamics and evolution. An individual "explosion" is characterized by multiple, second-long "pulses" and sub-second-long "sub-pulses", each pulse being characterized by the ejection of particles at similar velocities which then decrease in time (Taddeucci et al. 2012a; Gaudin et al. 2014; Bombrun et al. 2015). In addition we can observe multiple emission points during a single event. Thus we use the term "vent" to indicate an area of emission points active during a single event.

Eruptions at Stromboli

Stromboli is the northernmost island of the Aeolian arc. It covers an area of ~12.2 km^2, with its summit at 924 m above sea level (a.s.l.). The current volcanic activity has persisted for at least 1400 years (Rosi et al. 2000) in the constantly evolving crater terrace located at ~800 m a.s.l. (Washington 1917; Rosi et al. 2000; Harris and Ripepe 2007), comprising three vent areas within the North-East (NEC), Central (CC) and South-West (SWC) craters (Fig. 2). This typical state of explosive activity at Stromboli is usually classified as "normal activity" and consists of recurrent mild explosions and continuous degassing (Barberi et al. 1993; Harris and Ripepe 2007; Burton et al. 2007), with inter-explosion time intervals of 10–10^3 s, and ejecting a gas/pyroclast mixture at a few tens to hundreds of metres of height (e.g. Houghton and

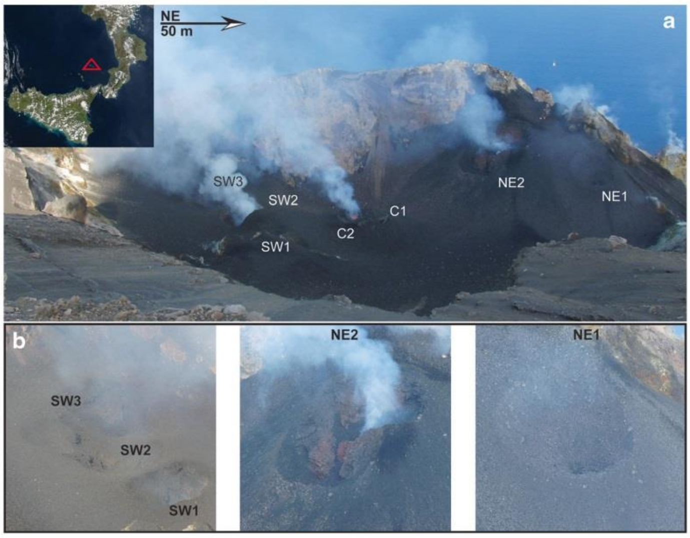

Fig. 2 (**a**) View of the crater terrace at Stromboli from Pizzo Sopra la Fossa on September 2, 2008. *SW*, *C*, and *NE* mark the South-West, Central and North-East vent areas, respectively, while *numbers* mark individual vents in each vent area. (**b**) Close-up of the active vents imaged during the data acquisition at the North-East (*NE*) and South-West (*SW*) vent areas (satellite image courtesy of Jeff Schmaltz, MODIS Rapid Response Team, NASA GSFC, NASA Earth Observatory)

Gonnermann 2008; Cashman and Sparks 2013; Taddeucci et al. 2013a). The "normal activity" is characterized by three main types of explosions: *Type 1* are ballistic-dominated events, with minor occurrence or absence of an ash plume; *Type 2* events involve a noticeable ash plume and can be either ballistic-rich (*Type 2a*) or ballistic-poor (*Type 2b*) (Patrick et al. 2007). Recently, this classification has been expanded by the introduction of a new eruption type, *Type 0*, which involves gas-dominated jets, characterized by the ejection of few and small juvenile pyroclasts, together with recycled material at high velocities (Leduc et al. 2015).

Methods

Equipment and data collection

Data presented here were obtained using a high-speed camera NAC HotShot 512SC. This self-contained high-speed video system records videos using a C-MOS monochromatic sensor sensitive into the near-infrared spectral region (down to about 0.1 μm), so that hot particles can be distinguished visually from cold particles by their lighter tone. At Stromboli the camera was operated at variable frame rates from 250 to 500 frames per second (fps), a resolution of 512×512 pixels with an 8-bit greyscale, bit density of 10 bits, and variable exposure times. The 4 GB on-board memory allowed 32.6 s of recording time at 500 fps, and 65.2 s at 250 fps.

The camera was tripod-mounted at Pizzo Sopra la Fossa, from where a complete view of the crater terrace is available (Fig. 2). This location was 288 m away and 165 m above the NE crater, 293 m away and 182 m above the SW crater, and the camera was tilted downward towards the vent of interest at an angle of 32°. The distance from the vents at the time of filming was determined by a laser telemeter (with a resolution of ± 0.5 m) and used to scale image size. A 300 mm professional lens was used, with a resulting field of view of 1.5°. Depending on the vent involved, each pixel had a width between 1.52 and 1.60 cm. All videos were acquired during daylight.

The high-speed camera data used in this study were collected during three field missions for a total of 6 days of shooting at the NE and SW craters zone: 4 and 5 September 2008, 17–19 June 2009 and 27 October 2009. A total of 49 explosions were recorded: 21 were from the NE crater and 28 from the SW crater. These covered a wide range of eruption styles, i.e.: ballistic-poor, ash-free and gas-dominated explosions (*Type 0*), ballistic-rich and ash-free explosions (*Type 1*), ash- and ballistic-rich explosions (*Type 2a*), ash-rich ballistic-free explosions (*Type 2b*). Each video covers a single vent, but occasionally—depending on the camera position—multiple active vents were involved simultaneously. In both of the crater zones several vents were active, which we refer to as NE1, NE2 and SW1, SW2, SW3 (Fig. 2, Table 1).

In addition, we use one example from the SW crater obtained on May 20, 2013, using a FLIR SC640 thermal camera

Table 1 Parameters (vent location, duration, maximum ejection velocity, vent condition and number of measured pyroclasts) for each explosion imaged by the high-speed camera

Explosion	Date	GMT	Vent	Duration (s)	FPS	V max (m/s)	Vent condition	*N*
1	04/09/2008	12:20	NE1	>30 s	500	62.94 ± 3.3	coarse-grained cover	284
2	04/09/2008	12:33	NE1	4 s	500	50.07 ± 3.7	coarse-grained cover	286
3	04/09/2008	13:30	NE1	>30 s	500	69.15 ± 12.6	coarse-grained cover	606
4	04/09/2008	11:00	NE2	15 s	500	188.74 ± 10.3	open	398
5	04/09/2008	11:20	NE2	6 s	500	323.14 ± 74	open	336
6	04/09/2008	11:36	NE2	>30 s	500	256.45 ± 10.1	open	949
7	04/09/2008	14:37	SW3	13 s	500	37.87 ± 10.4	coarse-grained cover	232
8	04/09/2008	16:55	SW1	>30 s	500	–	coarse-grained cover	–
9	05/09/2008	10:20	SW1 + 2	10 s	500	19.28 ± 1.7	fine-grained cover	131
10	05/09/2008	10:39	SW1 + 2	8 s	500	19.12 ± 0.9	fine-grained cover	37
11	05/09/2008	10:45	SW1 + 2	20 s	500	16.58 ± 0.8	fine-grained cover	237
12	05/09/2008	11:13	SW1 + 2	12 s	500	21.1 ± 2.6	fine-grained cover	117
13	05/09/2008	11:51	SW1 + 2 + 3	25 s	250	19.07 ± 3.3	fine-grained + open	167
14	05/09/2008	12:03	SW1 + 2 + 3	>56 s	250	28.6 ± 1.1	fine-grained + open	656
15	05/09/2008	12:20	SW1 + 2 + 3	25 s	250	17.18 ± 2.05	fine-grained + open	466
16	17/06/2009	09:xx	SW1	~60 s	250	388.02 ± 70.7	open	1887
17	17/06/2009	09:57:23	NE1	>30 s	500	–	–	–
18	17/06/2009	11:16:30	SW1	>30 s	500	152.21 ± 11.3	open	478
19	17/06/2009	11:35:42	SW1	>30 s	500	205.81 ± 4	partially covered	821
20	17/06/2009	12:02:20	SW1	>30 s	500	259 ± 6.6	partially covered	3370
21	17/06/2009	12:25:13	SW1	>30 s	500	230 ± 2.2	open	4001
22	17/06/2009	13:05:17	SW1	~32 s	500	172 ± 13.7	open	2425
23	17/06/2009	13:17:39	SW1 + 2	22 s	500	26.08 ± 1	open + coarse-grained	116
24	17/06/2009	13:36:55	SW1 + 2	7 s	500	–	coarse-grained cover	–
25	17/06/2009	14:14:58	SW1	>30 s	500	224.84 ± 12.8	partially covered	667
26	17/06/2009	14:30:28	SW1	~32 s	500	181.96 ± 12.9	open	1089
27	17/06/2009	14:41:44	SW1	20 s	500	138.76 ± 17.4	open	538
28	17/06/2009	15:26:50	SW1	26 s	250	409.82 ± 6.9	open	1802
29	18/06/2009	11:xx	NE2	20 s	500	74.7 ± 9	coarse-grained cover	283
30	18/06/2009	10:34:50	NE2	7 s	500	120.85 ± 2.6	coarse-grained cover	129
31	18/06/2009	10:59:20	NE2	10 s	500	53.9 ± 2.5	coarse-grained cover	174
32	18/06/2009	12:06:xx	NE2	7 s	500	–	–	–
33	19/06/2009	09:30:xx	NE1	17 s	500	367.90 ± 1.2	open	351
34	19/06/2009	10:48:29	NE1	10 s	500	226.22 ± 17	open	599
35	19/06/2009	11:04:46	NE1	25 s	500	365.49 ± 12.1	open	599
36	19/06/2009	11:26:08	NE1	20 s	500	316.93 ± 29.6	open	477
37	19/06/2009	12:04:41	NE1	18 s	500	168.89 ± 6.5	open	2706
38	19/06/2009	12:15:30	NE1	12 s	500	197.09 ± 1.6	open	708
39	19/06/2009	12:39:57	NE1	12 s	500	166.46 ± 13.5	open	644
40	19/06/2009	13:01:34	NE1	15 s	500	268.71 ± 7.8	open	624
41	19/06/2009	13:18:38	NE1	11 s	500	127.44 ± 2.2	open	1616
42	19/06/2009	13:32:34	NE1	20 s	500	324.24 ± 10.2	open	769
43	27/10/2009	11:38:37	SW1	?	500	–	–	–
44	27/10/2009	11:53:21	SW1	11 s	500	370 ± 3	open	1250
45	27/10/2009	12:03:35	SW1	8 s	500	199.12 ± 2.5	open	873
46	27/10/2009	12:23:15	SW1	9 s	500	337 ±	open	494
47	27/10/2009	12:40:02	SW1	5 s	500	190.47 ± 17.7	open	411
48	27/10/2009	13:32:51	SW1	6 s	500	367 ± 18.2	open	1405
49	27/10/2009	13:58:55	SW1	13 s	500	405 ± 28.2	open	1479

FPS frames per second, *N* number of measured pyroclasts (total *N* covering all events = 37,687 particles manually tracked)

(7.5—13 μm) recording at 50 fps with a 640 × 480 pixel resolution. We also include four examples from NE crater activity filmed on 4 September 2008, at 300 fps with a 512 × 384 pixel resolution using a Casio Exilim camcorder. A few visual observations from other field campaigns are also referred to in the text.

Analysis

The first analysis step was a qualitative description of the videos. This initial analysis allowed us first to evaluate the overall quality of the videos in terms of visibility, sharpness, focus, and disturbances from vents active outside of the camera field of view. Among all of the videos, two were discarded because the files were corrupt, and two because the erupting vent was outside of the field of view. We next described each explosion in terms of: (1) overall particle size and velocity trends, (2) variations in jet orientation, (3) multiple ejection pulses within a single explosion, (4) the presence or absence of plumes, (5) the abundance of juvenile vs. accidental pyroclasts, and (6) any additional processes observed.

Explosion duration

Explosion duration was measured using the onset of the explosion as defined by the time at which the first particle is observed in the ballistic-rich explosions, or the first ash emission in the ash-rich events. The on-board memory and the fps settings of the camera limit the maximum recording time. Thus, only for 10 cases it was impossible to define the end of the explosion, due to the memory limit or the view of the vent being obscured by the presence of ash.

Ejection velocities

Quantitative measurements were performed using ImageJ, a public domain Java-based image processing programme (Abramoff et al. 2004), and the MTrackJ plug-in (Meijering et al. 2012). The MTrackJ plug-in allows manual tracking of moving objects within an image stack, and was used for parameterizing the ejection velocity of pyroclasts. Velocities were manually measured for centimetre-sized clasts, where selected particles exiting the vent were tracked for 4–10 frames. One or more new trajectories were initiated every 2–4 frames, covering the fastest visible pyroclasts. For each trace we measured the mean velocity (m/s) over all traced points forming the trajectory (and standard deviation, σ). All the measurements were made as close as possible to the vent. The ejection velocity was measured for all explosions ejecting clearly traceable particles. Out of 45 videos, 15 were selected as the most representative of the overall variability and were processed for their entire duration so as to be used as reference models, and covered each vent in each of the measurement day. For the remaining videos, velocity measurements focused on the onset of the explosion and key moments, selected based on qualitative observations (e.g. peak of activity, onset of multiple pulses). For each explosion, we measured a minimum of 37 up to a maximum of 4001 pyroclasts (Table 1).

Activity description

Based on specific vent conditions at the time of the video acquisition, we identified two end-members of eruptive regimes, depending on the state of the vent before an explosion: one where the vent was completely obstructed by debris (ranging from blocks to ash in size), and a second where the vent was open, without any cover. In between, explosions featuring processes common to both groups occurred.

Activity at clogged vents

In the first regime, all explosions were preceded by the uplift of the debris cover, but the type of debris comprising the vent infill resulted in remarkably different processes. With coarse debris, once the cover reached a critical degree of inflation (Fig. 3a, b), several breaches between the blocks were formed, from which jets of relatively cold, fine particles started to propagate. Ash emission from the breaches produced an ash plume (Fig. 3c, d), whose height often exceeded the camera field of view (9 m, Fig. 3e), followed closely by the ejection of juvenile pyroclasts (Fig. 3f). In some cases, this initial pulse managed to remove only part of the debris from the vent. The following jets managed to make their way through the remaining blocks and to propagate from a small localized point of emission. These were collimated jets that reached a height exceeding the limit of the camera field of view, alternating with poorly collimated ones (Video 1).

Slumping of the inner crater walls and rollback of ejecta down the inner crater slopes towards the vent was evident. In a few cases we observed the formation of a new, very small and localized emission point near the main one, characterized by continuous gas and pyroclast emission reaching heights well within the camera field of view ($\leq$9 m). Initial ejection velocities reached up to 63 ± 3 m/s, with few velocity fluctuations, followed by rapid velocity pulses with occasional fluctuations and increasing velocities. Emissions from secondary points reached velocities up to ~70 m/s, while the shortest and weakest pulses had an average velocity of <30 m/s, featuring several velocity peaks up to 50 ± 4 m/s. In contrast, when the initial pulse was energetic enough to entrain and clear-out all the debris in the vent, the explosions involved the ejection of a

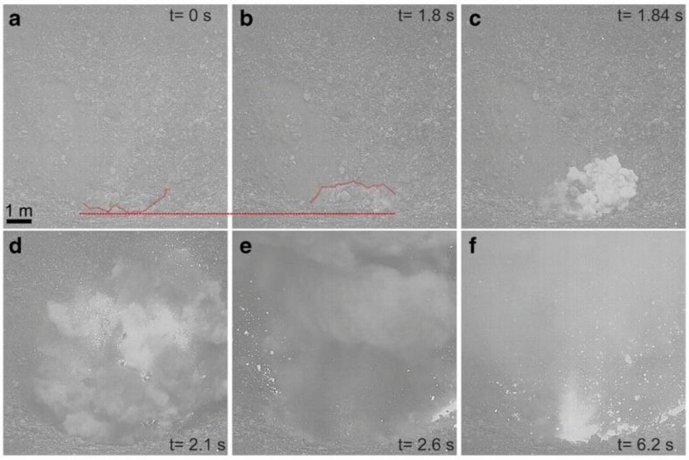

Fig. 3 Vents with a coarse-grained debris cover: representative still-frames of an explosion at the NE1 vent. *Red polylines* highlight the debris profile before (**a**) and after (**b**) the ground inflation preceding the explosion (**c**), with the dashed line representing the initial lowest position. An ash plume, accompanied by ejection of juvenile (*brighter tones*) and few accidental (*darker tones*) pyroclasts (**d**–**e**), is followed by collimated jets of pyroclasts (**f**)

mixture of juvenile and recycled, ash- to block-sized, pyroclasts (Video 2).

The inflation process that preceded these explosions lasted for up to tens of minutes, and was followed by subsequent deflation (Video 3). These vent cover motions reach vertical displacements up to 1.9 m, with velocities up to 0.91 m/s where debris doming accelerated nonlinearly in the few seconds preceding an explosion (Figs. 3a, b and 4).

For vents covered by fine particles, explosions were preceded by a slow and uniform expansion of the cover, until a sudden increase in the expansion velocity led to a breach in its central section from which jets began to propagate (Fig. 5a, b). These jets involved gas, ash and lapilli-sized pyroclasts emission, with few block-sized pyroclasts, and the development of a conspicuous ash plume, which often visually obscured many of the lapilli-sized pyroclasts. Occasionally, the fine-grained debris was displaced en-masse and its collapse triggered a pyroclastic density current that travelled for some tens of metres away from the vent (Fig. 6, Video 4). The explosions continued with an initial gas thrust phase and the ejection of juvenile pyroclasts and lithics, but the high-concentration of ash made it difficult to impossible to discern pulses, except for powerful ones when hot material overtook the front of the plume. Sometimes, falling of veils of ash seemed to mark the end of the explosion (Fig. 5c), only for ejection of juvenile and lithic clasts to resume from the same emission point, often along with the emission of a conspicuous ash plume from a new emission point within the vent or from a nearby vent (Fig. 5d, Video 5). Despite a vigorous gas thrust phase, these explosions were characterized by low ejection velocities, with a maximum of 21 ± 3 m/s, and lasted from a minimum of ~8 up to ~20 s. All explosions were preceded, and followed, by rolling of blocks and sliding of finer material down the inner crater slopes and towards the vent.

Activity at open vents

Vents that were clear of debris displayed a faint glow and the emission of fume. In these cases, ballistic-dominated (*Type 1*) explosions occurred, with minor or no associated ash phase. All explosions began with a diffuse spray of a few hot pyroclasts, exiting the vent and followed by more heavily loaded pulses of coarser pyroclasts (a similar behaviour for *Type 1* explosions was also observed by Harris et al. 2012), occasionally interspersed by sub-pulses (Fig. 7). Often, the ejection of metre-sized spatter also occurred. These molten clots were flattened on landing on the inner crater walls. Often, ejecta fell back around and into the vent, and then seemed to be reworked and ejected again in the following sub-pulses. The explosions lasted between 5 s and >33 s. When it was possible to observe the whole explosions, a gradual decrease in the amount of ejected material over time was evident, mirrored by a well-defined coda of decreasing pyroclast velocity (Video 6). The average velocities ranged between 20 and 50 m/s, featuring tens of high velocity peaks: usually <250 m/s (Fig. 8a, b), but in some cases exceeding 300 m/s, with an observed maximum of 410 ± 7 m/s (Explosion 28). These pulses and sub-pulses occurred so frequently that their individual velocity decay trends merged together. This explosive behaviour was characteristic of the SW vents during two working days in June 2009. As an extreme example of this type of behaviour, a *Type 0* explosion

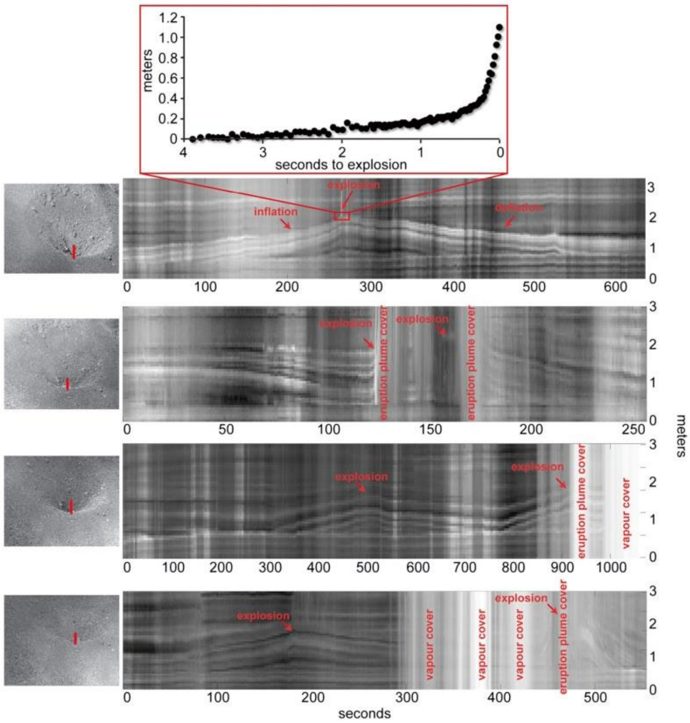

Fig. 4 Ground deformation of the NE1 vent shows that, cycles of inflation-deflation may last several minutes. Each plot displays the temporal evolution of *grey levels* in the videos along a *vertical line crossing the vent* (*red line*, about 3 m long, on the left-hand still-frames). Inflation accelerates nonlinearly a few seconds before an explosion (*top inset*)

occurred on May 24, 2013, from a metre-sized, glowing, round hole in the SW vent area, with the ejection of relatively few lapilli-sized ejecta, and attained pyroclast velocities of 498 ± 19 m/s.

Intermediate and transitional cases

In several cases, the incandescent surface of the top of the magma column was visible in the vent partially covered by blocks and lapilli from previous explosions. In the very first seconds of an explosion, this surface was disrupted by the bursting of variable sized gas bubbles, which reworked the debris without cleaning-out the vent, until—but not always—a more energetic pulse cleared the vent (Video 7). Individual reworked blocks, when finally ejected, often showed coexisting hot and cold surfaces. In the study cases, bubbling of the surface lasted from ~ 4 to ~ 7 s. The first pulse was followed by an increase in the bubble-burst number and occurrence rate, until pyroclast ejection became almost continuous with multiple pulses and sub-pulses. As in previous cases, spatter was ejected and fell back into the vent, or become plastered onto the inner crater walls, to be recycled by the following pulses. The angles of the jet axes in the main pulses varied widely, between ~90 and ~45°.

In several cases, two adjacent vents in the SW crater (SW1 and SW2) were observed to erupt simultaneously (Figs. 6 and 9): one was clearly covered by fine particles and was characterized first by degassing (Fig. 9b), then by ash emission (Fig. 9c); the second was partially obscured and involved ballistic-dominated and ash-free emission (Fig. 9b–c). Explosions lasted from ~15 up to 56 s and were characterized by low peak velocities, with a maximum just of 29 ± 1 m/s. In all cases, velocity time series showed several distinct decay trends lasting 0.2–1 s.

Discussion

Based on visual features, we identified two end-member conditions of the volcanic vents producing Strombolian

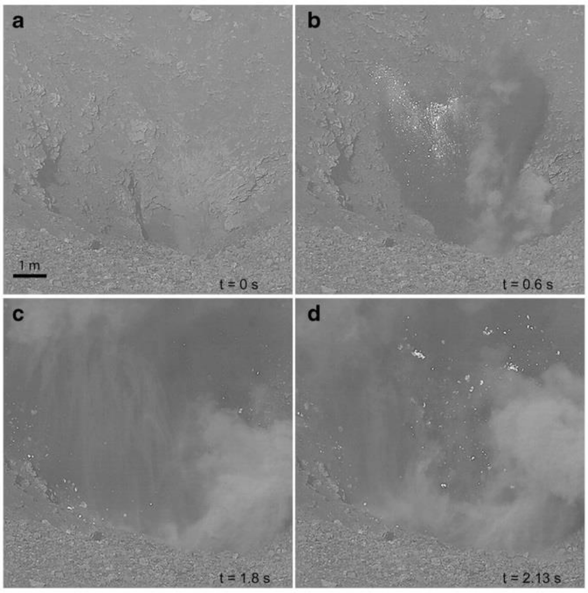

Fig. 5 Vents with a fine-grained debris cover: explosion at the SW1 vent (**a**). When a fine-grained debris cover is breached, a mixture of ash and coarse pyroclasts is released (**b**). A substantial amount of fine material falls back into the vent (**c**), followed by a new, weaker emission of ash and coarse pyroclasts (**d**)

explosions, i.e. clogged vs. open vents, which seem to have affected both the style and vigour of the eruptions.

Effect of the cover

The presence and nature of vent cover has been hypothesized to influence explosion style at Stromboli by Patrick et al. (2007), and more recently by Leduc et al. (2015). Our observations provide the first direct confirmation to this hypothesis. Within our limited number of observations, *Type 0* explosions invariably occurred through open vents, *Type 1* through open or sparsely covered vents and *Type 2* through heavily covered vents. The dynamics of vent cover incorporation in the erupted gas/pyroclast mixture controlled the explosion style (and type). A weak explosion through a coarse-grained debris cover (Fig. 3) would be classified as a bomb-free *Type 2b* explosion according to Patrick et al. (2007). In this case, weakly overpressured gas may have effectively elutriated only the finer particles from the overall coarse-grained cover. A stronger explosion at the same vent would also mobilize coarser pyroclasts in a bomb-rich *Type 2a* explosion. Fine-grained covers were usually entrained entirely into the plume. A thick, fine-grained cover in a narrow vent can be ejected en-masse, resulting in a small-scale pyroclastic density current (Fig. 6, Video 4) preceding the main explosion.

Several lines of evidence suggest that covered vent explosions are less energetic than open-vent explosions. Covered vent explosions have lower pyroclast ejection velocity and are never associated with visible shock or pressure waves (Taddeucci et al. 2014). Likewise, ash-rich (*Type 2*) explosions at Mt. Yasur (Vanuatu) are associated with lower acoustic amplitudes than ash-free (*Type 1*) events (Spina et al. 2015). The presence of a debris cover in the vent may affect the gas behaviour both before its release from the magma (i.e. at fragmentation), when the gas has to lift and dislodge the cover, as well as after fragmentation, when the gas has to either accelerate the debris or percolate through it. Recent experimental investigation shows how the presence of a viscous plug at the top of the magma column acts to increase the pressure at burst of slugs (Del Bello et al. 2015). We found no evidence for such an increase in the presence of cover, which apparently did not affect the growth and pressurization of the gas slugs. This is probably because the debris cover is too weak - as it is unconsolidated - to hinder gas expansion and, thus, increase slug overpressure at burst. Conversely, the presence of cover acted to dampen the energy of the event, because part of the energy stored in the gas overpressure dissipated through percolation and was used in debris acceleration. The final outcome of an explosion thus results from the competition between the amount, coherence and size of the clogging material, and the volume and

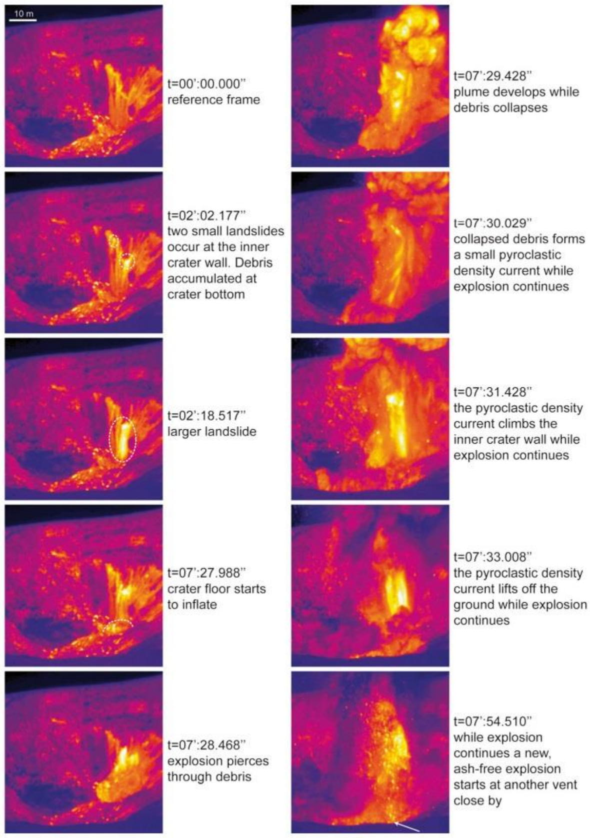

Fig. 6 Selected frames of a thermal video from the SW vent, covering 7′:55″: landslides (*dashed circles*, 02′:02.177″ and 02′:18.517″) and ground deformation (*dashed line*, 07′:27.988″) precede an initial ash emission breaking through the debris cover. Debris collapse triggers a small-scale pyroclastic density current (07′:30.029″). While the explosion continues, a new ash-free explosion starts from a nearby vent (*white arrow*, 07′:54.510″)

pressure of the gas slug arriving at the base of the plug. In analogy to other explosive processes, we propose that this competition can be expressed by the scaled depth concept (the thickness of the debris cover divided by the cube root of the stored energy), which has been shown experimentally to control ejecta velocity and pressure wave amplitude (Taddeucci et al. 2013b).

The vertical motion of the debris cover (Fig. 4) could be linked to volumetric changes in the conduit before and after an explosion. These changes occurred in the timescale of hundreds of seconds, which is comparable to the timescale of pre-explosion conduit pressurization recorded by ground motion (Genco and Ripepe 2010), and is also compatible with time scales of bubble rise and growth in a basaltic magma (Nishimura 2009). The accelerating trend of inflation of the debris that we observed in the seconds before an explosion also matched the surface motion of a liquid column hosting a rising, pressurized gas slug (James et al. 2008, 2009). We conclude that, before an explosion, the vent-filling debris is pushed upward by the magma head which, in turn, is rising under the effect of the ascending and expanding gas slug. After the explosion, the remaining debris cover subsides back into the vent. The rate of subsidence could be controlled by the gravitational collapse of the debris into an empty conduit or the gradual sinking of the magma head. Our observations do not allow a conclusive discrimination between the two cases. However, the similar rates of debris inflation and deflation seem more readily explained by gradual magma sinking rather than debris collapse.

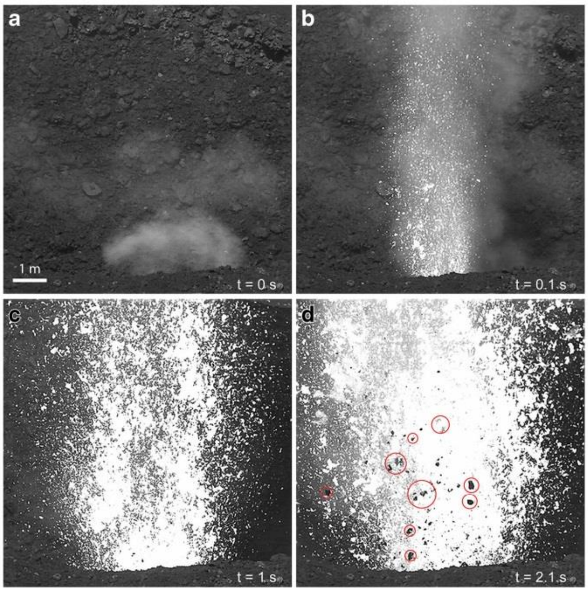

Fig. 7 Open vent: at the NE1 vent (**a**), a dominant, well-collimated jet of fast pyroclasts (**b**) decays rapidly, followed by tens of pulses and sub-pulses that evolve quickly with a wider exit angle (**c**). Concomitant to the peaks of activity, decimetre-sized, colder recycled clasts (*red circles*) are ejected (**d**) and, at the same time, both the eruption rate and exit angle increase

Origin of the cover

Fallback of pyroclasts into the vent is the prime process for the formation of the debris cover. Pyroclasts were observed to fall back directly from the plume, during or after an explosion, and from the inner flanks of craters, by rolling and sliding (also, ejecta from the NEC have been observed to fall into open vents in SWC: thus, one vent may produce clog material for another one; Andy Harris, personal communication, 2015). Central to the formation of the cover is the relationship between energy and dynamics of the explosions on the one hand, which controls the size, range and trajectory of the pyroclasts, and the morphology of the vent area on the other, which controls pyroclast accumulation and distribution. At the timescale of weeks–months, the two factors are not independent at Stromboli, where periods of more frequent activity are also marked by stronger activity (Taddeucci et al. 2013a). A stronger and more frequent activity implies a wider dispersal of products and higher emission rates, promoting the growth of positive landforms around vent areas and limiting fallback (up to the formation of hornito structures). On the contrary, weaker and less frequent activity implies smaller dispersal of pyroclasts and negligible variations in the vent settings, both favouring debris accumulation, as also speculated by Patrick et al. (2007). At the timescale of hours-days a positive feedback may arise between debris accumulation resulting in weaker explosions, causing reduced ejecta range and, consequently, increasing clast fallback towards the vent. The feedback may be broken by an occasional explosion strong enough to clean the vent. The extreme sensitivity of this feedback to local conditions is well illustrated by cases of two neighbour vents erupting simultaneously but with different styles (Figs. 6 and 9), where minor variations result in different degrees of vent cover and explosion types even at two interconnected vents.

The mechanical and thermal state of the vent cover is open to speculations. For instance, the source of ash in *Type 2* explosions could be milling from repeated collisions among coarser clasts over multiple explosions or brittle fragmentation of cooled and crystallized magma, as argued by Patrick et al. (2007). We directly observed milling and fallback of ash into the vents (Figs. 3 and 6). However, we also note that, with respect to coarser pyroclasts, ash was easily wind-advected outside the vent areas, suggesting that an internal source of ash (i.e. magma fragmentation) may be required for prolonged *Type 2* activity periods. The presence of degassed and crystallized magma at the top of the Stromboli conduits is well established (e.g. Lautze and Houghton 2006; Gurioli et al. 2014), along with the potential role of clast recycling on its formation (D'Oriano et al. 2014). Indeed, there must be an

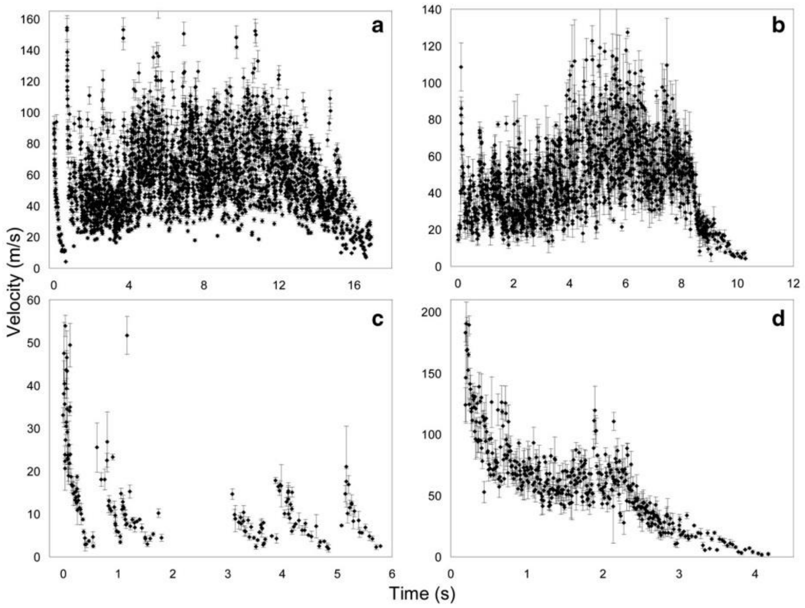

Fig. 8 Examples of ejection velocity of pyroclasts over time for explosions at open vent NE1 (**a**, **b**), coarse-cover vent NE2 (**c**) and fine-cover vent SW1 (**d**) vent. Each point represents the velocity of a single centimetre-sized pyroclast, averaged over 4–10 frames. *Time* = *0* corresponds to the time at which the first pyroclast is observed

interface, or transition zone, between the degassed layer at the top of the magma column and the debris cover filling the vent (Fig. 1). Direct evidence for this zone is provided by the observed partially molten clasts, and by the high temperature of the ash filling the vent (Fig. 6). The mixing with fallen back debris, due to pre- and post-explosion disruption of the debris cover, would increase the viscosity of the magma residing in the topmost part of the conduit, by enhanced cooling and addition of solids (crystals and cold scoria fragments), thus promoting its brittle behaviour and fine fragmentation.

Conclusions

High-speed observations of vent activity at Stromboli show how open vent vs. debris-clogged vent conditions affect the style of explosive activity. The debris cover forms by

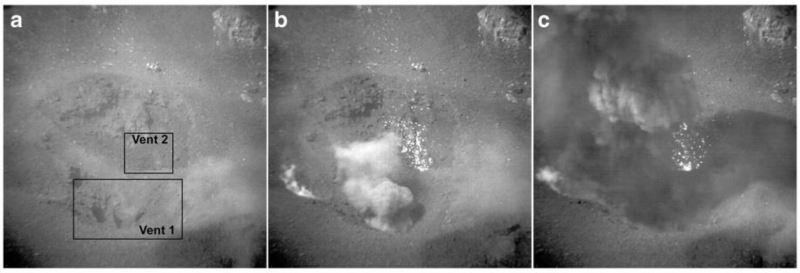

Fig. 9 SW1 and SW2 vents (**a**), showing different eruptive styles during simultaneous activities: SW1 is characterized by degassing (**b**) and ash emission (**c**), while SW2 shows ballistic-rich and ash-free explosions (**b**–**c**)

accumulation of pyroclasts into the vent by fallback and rolling/sliding along the inner crater walls, controlled by the interplay of frequency and intensity of the explosions. The effects of the vent cover can be summarized as follows:

1. with respect to explosions at open vents, clogged vents feature the ejection of slower (and colder) pyroclasts, the presence of a debris cover effectively dampening and slowing down the gas expansion process;
2. for debris-covered vents, explosion dynamics are sensitive to the amount and grain size distribution of the debris: while *Type 2a* explosions are observed mainly from vents with fine-grained cover, weaker *Type 2b* explosions occur through vents with a coarse-grained cover. This observation confirms previous hypothesis on the origin of different explosion types (e.g. Patrick et al. 2007; Leduc et al. 2015);
3. metre-scale vertical motions of the debris cover precede (inflation) and follow (deflation) explosions on a time-scale of tens of minutes, paralleling motions of the magma head. The rise rate of the debris cover is compatible with that expected for the rise and expansion of a pressurized gas slug towards the top of the magma column;
4. the debris cover is observed to thermally and mechanically interact with the magma at the top of the conduit, possibly resulting in cooling and increased viscosity, in turn promoting brittle, finer fragmentation of the top magma layer.

The observed phenomena show how the presence and nature of debris cover may lead to complex eruptive dynamics, by affecting gas expansion, eruption intensity, grain size distribution and ejection velocity of erupted material. These findings need to be considered and integrated in future models to better understand how the interaction among arriving gas slugs, a possible viscous plug and a near-surface debris cover controls explosion style and vigour.

Acknowledgments A.C. was funded by MIUR (Ministry of Education, University and Scientific Research of Italy) grant "Parameterizing the Dynamics of Strombolian Eruptions through High-Speed Video Analysis" and, as part of his PhD at Lancaster University, from the People Programme (Marie Curie Actions) of the European Union's Seventh Framework Programme (FP7/2007-2013) under the project NEMOH, REA grant agreement n° 289976. We are indebted with U. Kueppers, E. Del Bello, Zazà, and all other colleagues, friends, and scecchi who helped us in the many field campaigns at Stromboli. We thank journal reviewers Matt Patrick and Andy Harris, and associate Editor Pierre-Simon Ross for thorough and constructive comments that greatly improved the manuscript.

References

Abramoff MD, Magelhaes PJ, Ram SJ (2004) Image processing with ImageJ. Biophotonics Int 11:36–42

Barberi P, Rosi M, Sodi A (1993) Volcanic hazard assessment at Stromboli based on review of historical data. Acta Vulcanol 3: 173–187

Blackburn EA, Wilson L, Sparks RSJ (1976) Mechanisms and dynamics of strombolian activity. J Geol Soc. doi:10.1144/gsjgs.132.4.0429

Bombrun MA, Harris A, Gurioli L, Battaglia J, Barra V (2015) Anatomy of a Strombolian eruption: inferences from particle data recorded with thermal video. J Geophys Res. doi:10.1002/2014JB011556

Burton MR, Mader HM, Polacci M (2007) The role of gas percolation in quiescent degassing of persistently active basaltic volcanoes. Earth Planet Sci Lett. doi:10.1016/j.epsl.2007.08.028

Cashman KV, Sparks RSJ (2013) How volcanoes work: a 25 year perspective. Geol Soc Am Bull 125:664–690

Chouet B, Hamisevicz N, McGetchin TR (1974) Photoballistics of volcanic jet activity at Stromboli, Italy. J Geophys Res 79:4961–4976

Chouet B, Dawson P, Ohminato T, Martini M, Saccorotti G, Giudicepietro F, De Luca G, Milana G, Scarpa R (2003) Source mechanisms of explosions at Stromboli Volcano, Italy, determined from moment-tensor inversions of very-long-period data. J Geophys Res. doi:10.1029/2002JB001919

Chouet B, Dawson P, Martini M (2008) Shallow-conduit dynamics at Stromboli Volcano, Italy, imaged from waveform inversions. In: Lane SJ, Gilbert JS (Eds.), Fluid Motions in Volcanic Conduits: A Source of Seismic and Acoustic Signals. Geol Soc, London, Special Publications, 307:57–84

Colò L, Ripepe M, Baker DR, Polacci M (2010) Magma vesiculation and infrasonic activity at Stromboli open conduit volcano. Earth Planet Sci Lett. doi:10.1016/j.epsl.2010.01.018

D'Oriano C, Bertagnini A, Pompilio M (2011) Ash erupted during normal activity at Stromboli (Aeolian Islands, Italy) raises questions on how the feeding system works. Bull Volcanol. doi:10.1007/s00445-010-0425-0

D'Oriano C, Bertagnini A, Cioni R, Pompilio M (2014) Identifying recycled ash in basaltic eruptions. Sci Rep. doi:10.1038/srep05851

Del Bello E, Lane SJ, James MR, Llewellin EW, Taddeucci J, Scarlato P, Capponi A (2015) Viscous plugging can enhance and modulate explosivity of strombolian eruptions. Earth Planet Sci Lett. doi:10.1016/j.epsl.2015.04.034

Gaudin D, Taddeucci J, Scarlato P, Moroni M, Freda C, Gaeta M, Palladino DM (2014) Pyroclast Tracking Velocimetry illuminates bomb ejection and explosion dynamics at Stromboli (Italy) and Yasur (Vanuatu) volcanoes. J Geophys Res Sol-Ea. doi:10.1002/2014JB011096

Genco R, Ripepe M (2010) Inflation-deflation cycles revealed by tilt and seismic records at Stromboli volcano. Geophys Res Lett. doi:10.1029/2010GL042925

Gurioli L, Colò L, Bollasina AJ, Harris AJL, Whittington A, Ripepe M (2014) Dynamics of strombolian explosions: inferences from field and laboratory studies of erupted bombs from Stromboli volcano. J Geophys Res Sol-Ea. doi:10.1002/2013JB010355

Harris AJL, Ripepe M (2007) Synergy of multiple geophysical approaches to unravel explosive eruption conduit and source dynamics—a case study from Stromboli. Chemie der Erde – Geochemistry 67:1–35

Harris AJL, Ripepe M, Hughes EA (2012) Detailed analysis of particle launch velocities, size distributions and gas densities during normal explosions at Stromboli. J Volcanol Geoth Res. doi:10.1016/j.jvolgeores.2012.02.012

Houghton BF, Gonnermann HM (2008) Basaltic explosive volcanism: constraints from deposits and models. Chemie der Erde – Geochemistry. doi:10.1016/j.chemer.2008.04.002

James MR, Lane SJ, Chouet B, Gilbert JS (2004) Pressure changes associated with the ascent and bursting of gas slugs in liquid-filled vertical and inclined conduits. J Volcanol Geoth Res 129:61–82

James MR, Lane SJ, Chouet BA (2006) Gas slug ascent through changes in conduit diameter: Laboratory insights into a volcano-seismic source process in low-viscosity magmas. J Geophys Res. doi:10.1029/2005JB003718

James MR, Lane SJ, Corder SB (2008) Modelling the rapid near-surface expansion of gas slugs in low viscosity magmas. Geol Soc London Spec Pub. doi:10.1144/SP307.9

James MR, Lane SJ, Wilson L, Corder SB (2009) Degassing at low magma-viscosity volcanoes: quantifying the transition between passive bubble-burst and Strombolian eruption. J Volcanol Geotherm Res. doi:10.1016/j.jvolgeores.2008.09.002

Lane SJ, James MR, Corder SB (2013) Volcano infrasonic signals and magma degassing: first-order experimental insights and application to Stromboli. Earth Planet Sci Lett. doi:10.1016/j.epsl.2013.06.048

Lautze NC, Houghton BF (2005) Physical mingling of magma and complex eruption dynamics in the shallow conduit at Stromboli volcano. Italy Geology. doi:10.1130/G21325.1

Lautze NC, Houghton BF (2006) Linking variable explosion style and magma textures during 2002 at Stromboli volcano. Italy Bull Volcanol. doi:10.1007/s00445-006-0086-1

Leduc L, Gurioli L, Harris A, Colò L, Rose-Koga EF (2015) Types and mechanisms of strombolian explosions: characterization of a gas-dominated explosion at Stromboli. Bull Volcanol. doi:10.1007/s00445-014-0555-5

Marchetti E, Ripepe M (2005) Stability of the seismic source during effusive and explosive activity at Stromboli Volcano. Geophys Res Lett. doi:10.1029/2004GL021406

McGetchin TR, Settle M, Chouet BA (1974) Cinder cone growth modeled after Northeast Crater, Mount Etna, Sicily. J Geophys Res 79:3257–3272

Meijering E, Dzyubachyk O, Smal I (2012) Methods for cell and particle tracking. Methods Enzymol 504:183–200

Nishimura T (2009) Ground deformation caused by magma ascent in an open conduit. J Volcanol Geotherm Res. doi:10.1016/j.jvolgeores.2009.09.001

Parfitt EA (2004) A discussion of the mechanisms of explosive basaltic eruptions. J Volcanol Geother Res. doi:10.1016/j.jvolgeores.2004.01.002

Patrick MR, Harris AJL, Ripepe M, Dehn J, Rothery DA, Calvari S (2007) Strombolian explosive styles and source conditions: insights from thermal (FLIR) video. Bull Volcanol. doi:10.1007/s00445-006-0107-0

Ripepe M, Rossi M, Saccorotti G (1993) Image processing of explosive activity at Stromboli. J Volcanol Geotherm Res 54:335–351

Ripepe M, Harris AJL, Marchetti E (2005) Coupled thermal oscillations in explosive activity at different craters of Stromboli volcano. Geophys Res Lett. doi:10.1029/2005GL022711

Rosi M, Bertagnini A, Landi P (2000) Onset of the persistent activity at Stromboli Volcano (Italy). Bull Volcanol. doi:10.1007/s004450000098

Spina L, Taddeucci J, Cannata A, Gresta S, Lodato L, Privitera E, Scarlato P, Gaeta M, Gaudin D, Palladino DM (2015) Explosive volcanic activity at Mt. Yasur: a characterization of the acoustic events (9–12th July 2011). J Volcanol Geother Res. doi:10.1016/j.jvolgeores.2015.07.027

Taddeucci J, Scarlato P, Capponi A, Del Bello E, Cimarelli C, Palladino DM, Kueppers U (2012a) High-speed imaging of Strombolian explosions: the ejection velocity of pyroclasts. Geophys Res Lett. doi:10.1029/2011GL050404

Taddeucci J, Alatorre-Ibargüengoitia MA, Moroni M, Tornetta L, Capponi A, Scarlato P, Dingwell DB, De Rita D (2012b) Physical parameterization of Strombolian eruptions via experimentally-validated modelling of high-speed observations. Geophys Res Lett. doi:10.1029/2012GL052772

Taddeucci J, Palladino DM, Sottili G, Bernini D, Andronico D, Cristaldi A (2013a) Linked frequency and intensity of persistent volcanic activity at Stromboli (Italy). Geophys Res Lett. doi:10.1002/GRL.50652

Taddeucci J, Valentine GA, Sonder I, White JDL, Ross P-S, Scarlato P (2013b) The effect of pre-existing craters on the initial development of explosive volcanic eruptions: an experimental investigation. Geophys Res Lett. doi:10.1002/grl.50176

Taddeucci J, Sesterhenn J, Scarlato P, Stampka K, Del Bello E, Pena Fernandez JJ, Gaudin D (2014) High-speed imaging, acoustic features, and aeroacoustic computations of jet noise from Strombolian (and Vulcanian) explosions. Geophys Res Lett. doi:10.1002/2014GL059925

Taddeucci J, Edmonds M, Houghton B, James MR, Vergniolle S (2015) Hawaiian and Strombolian eruptions. In: Sigurdsson H, Houghton B, Rymer H, Stix J, McNutt S (eds) The encyclopedia of volcanoes, 2nd edn. Academic Press, Amsterdam, pp 485–503

Vergniolle S, Brandeis G, Mareschal JC (1996) Strombolian explosions 2. Eruption dynamics determined from acoustic measurements. J Geophys Res 101:449–466

Washington HS (1917) Persistence of vents at Stromboli and its bearing on volcanic mechanism. G Soc Am B 28:249–278

Appendix 4 – Technical datasheets

BOC Edwards CG16K capsule dial gauges

CG16K capsule dial gauges

Barometrically compensated dial gauges with NW flange fittings.

Edwards CG 16K capsule dial gauges cover the range from atmosphere down to 1 mbar absolute.

These robust gauges provide accurate, repeatable performance even at low pressures making them equally suited for non-corrosive process plant or for laboratory applications.

Fitting is simple: the gauges can be mounted direct or panel mounted using the kit supplied.

Features and benefits

- Accurate to ±2% F.S.D.
- Barometrically compensated unaffected by changes in atmospheric pressure
- Reading independent of gas type
- Rugged aluminium casing with removeable bezel for cleaning

Applications

- Backfilling
- Portable equipment
- Degassing
- Refrigeration
- Flammable vapours
- Upgrade from Bourdons
- Packaging

product datasheet

EDWARDS
Vacuum science... product solution.

Technical data

Accuracy	± 2% of F.S.D.
Materials in vacuum	Inconel, aluminium, nickel, glass, nitrile, copper, alloy
Internal volume	160 cm^3
Maximum applied pressure	2 bar absolute (1 bar gauge)
Weight	0.8 kg
Vacuum connection	NW16
Accessories supplied	Clamp and studs for panel mounting

Dimensions - mm (inch)

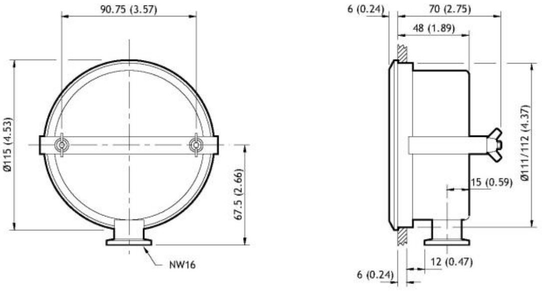

Ordering information

Product description	Ordering information
CG16K capsule dial gauge 01040 mbar	D35610000
CG16K capsule dial gauge 0125 mbar	D35611000
CG16K capsule dial gauge 050 mbar	D35612000
CG16K capsule dial gauge 025 mbar	D35613000
CG16K capsule dial gauge 0760 Torr	D35630000
CG16K capsule dial gauge 0100 Torr	D35631000
CG16K capsule dial gauge 040 Torr	D35632000
CG16K capsule dial gauge 020 Torr	D35633000
6 mm pipe union for CG16K	D35610201

Edwards offers a calibration service traceable to national standards for new or returned gauges and controllers. Please contact Edwards for details.

Global contacts

EUROPE
UK Crawley +44 1293 528844
UK (local rate) 08459 212223
Belgium Brussels +32 2 300 0730
France Paris +33 1 4121 1256
Germany Munich 0800 000 1456
Italy Milan +39 02 48 4471

USA
Niagara (toll free) +1 800 848 9800
BRAZIL
Sao Paulo +55 11 3952 5000
ISRAEL
Qiryat-Gat +972 8 681 0633

ASIA PACIFIC
China (toll free) +86 400 111 9618
India, Pune +91 20 4075 2222
Japan, Yachiyo +81 47 458 8831
Korea, Bundang +82 31 716 7070
Singapore +65 6546 8408
Taiwan R.O.C. Jhunan Town +886 3758 1000

WWW.EDWARDSVACUUM.COM

info@edwardsvacuum.com

Publication Number: D05900895, Issue C

Active Strain Gauge BOC Edwards A.S.G.2000/1000

The BOC Edwards Active Strain Gauge (ASG) is a rugged, corrosion resistant diaphragm gauge which provides accurate, gas independent measurement from 2000 mbar to 1 mbar. It can be used as a stand-alone transducer allowing OEMs and system builders to develop low cost, flexible solutions to their vacuum instrumentation needs. Alternatively, it can be connected to the Active Gauge Controller where it can be combined with many other sensor types to provide a complete vacuum instrument solution.

Features & Benefits

- Drive electronics combined in the gauge head
  - Simplifies system design
  - Saves valuable rack space
- Wide range, regulated internal power supply
  - Runs from standard dc power supplies +13.5 to +36V
  - Tolerant to voltage fluctuations
- Standard analogue output 0 to 10V dc
  - Easy to interface with a computer or PLC
- High accuracy and stability
  - Accuracy ±0.2% full scale
  - Stability 0.2% full scale
- Corrosion resistant, rugged design
  - Only material exposed to vacuum is stainless steel 316
  - Enclosure rating IP65
- Gas independent measurement
  - Pressure measurement is completely independent of gas type making this gauge ideal for applications where gases other than nitrogen are used
- Excellent high pressure resolution
  - Ability to resolve 1 mbar changes in system pressure even at pressures near atmospheric makes the gauge ideal for monitoring large, slow-pumping systems
- Part of the Active gauge range
  - Standard supply requirements and output voltage allow simple integration into systems using active Pirani, thermocouple, inverted magnetron, strain, wide range and ionization gauges. All of these are compatible with the Active Gauge Controller, a multi-channel digital display and controller

BOC EDWARDS

TECHNICAL DATA

SPECIFICATIONS

• Full scale pressure ranges	2000, 1000 mbar
• Accuracy	±0.2% full scale
• Stability	0.2% full scale
• Temperature coefficient	0.05% full scale per °C
• Power Supply	+ 13.5 +36V dc
• Power Consumption	0.4W
• Output Signal	
Operating	0 to 10V dc linear
Output impedance	>200Ω
Minimum load	50kΩ
Response Speed	5 msec
Adjustments	Set full scale and set zero
• Temperature Range	
Compensated	+10 to +50°C
Operating	-20 to +90°C
• Materials exposed to vacuum	Stainless steel 316
• Internal Volume	1.25cm^3
• Weight	120g
• Electrical connector	Miniature 4 pin Din
• Vacuum fitting	$^1/_8$" NPT male or NW16
• Standards	
Electronic design	EN 61010-1
Electromagnetic compatibility	EN 61326 (Class B Emissions)
Enclosure rating	IP 65

PIN ALLOCATION

Miniature Din (Gauge Head only)

1. Power supply positive
2. Power supply common
3. Gauge output
4. Signal common

FCC-68 (with adaptor cable)

1. Power supply positive
2. Power supply common
3. Gauge output
4. Gauge identification
5. Signal common
6. No connection
7. No connection
8. No connection

OUTPUT CHARACTERISTICS / DIMENSIONS (mm)

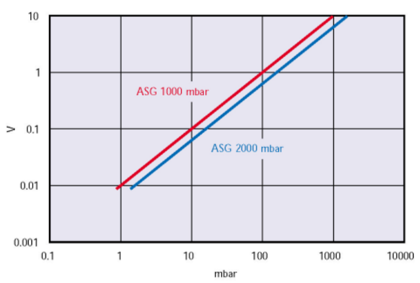

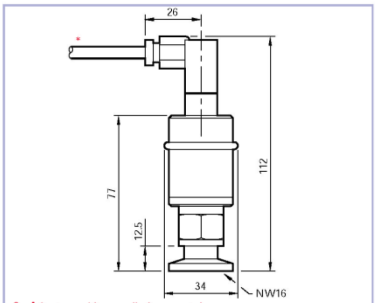

* *Adaptor cable supplied separately*

ORDERING INFORMATION

PRODUCT DESCRIPTION	ORDERING INFORMATION
ASG NW16 1000 mbar	D357-26-000
ASG NW16 2000 mbar	D357-28-000
ASG $^1/_8$" NPT 1000 mbar	D357-25-000
ASG $^1/_8$" NPT 2000 mbar	D357-27-000
ASG adaptor cable (0.5m) miniature DIN to female FCC68	D400-03-060

PRODUCT DESCRIPTION	ORDERING INFORMATION
Cable assemblies (include FCC68 compatible connectors at both ends)	
0.5m	D400-01-005
1m	D400-01-010
3m	D400-01-030
5m	D400-01-050
10m	D400-01-100
15m	D400-01-150
25m	D400-01-250
50m	D400-01-500
100m	D400-01-999
Non standard lengths and screened cables available on request	

GLOBAL CONTACTS

EUROPE
Crawley, UK +(44) 1293 528844
Guildford, UK +(44) 1483 579857
Cumbernauld, UK +(44) 1236 730575
Brussels, BELGIUM +(32) 2 363 0030
Paris, FRANCE +(33) 1 47 98 24 01
Munich, GERMANY +(49) 89 99 19 18 0
Milan, ITALY +(39) 2 48 4471

ISRAEL
Qiryat Gat +(972) 7 681 0633

USA
Wilmington, MA +(1) 978 658 5410
Toll free (USA only) 1800 848 9800
Santa Clara, CA +(1) 408 496 1177
Tempe, AZ +(1) 480 777 7007
Austin, TX +(1) 512 491 6622

ASIA PACIFIC
Hong Kong +(852) 2796 9111
Shanghai, CHINA +(86) 21 5866 7558
Tianjin, CHINA +(86) 22 2834 1981
Toufen Town, TAIWAN R.O.C. +(886) 37 611 422
Singapore +(65) 546 8408

KOREA
Bundang +(82) 31 716 7070

JAPAN
Tokyo (Vacuum/Abatement) +(81) 3 5470 6530
Tokyo (Electronic Gases) +(81) 3 3434 6789
Osaka +(81) 6 384 7052
Kyushu +(81) 96 326 7300
Sendai +(81) 22 373 8525

http://www.bocedwards.com
Publication No: D357-10-895

Differential pressure transducers (Honeywell 163PC01D75)

Pressure Sensors

160PC Series

Low Pressure Differential, Gage, Vacuum Gage/Amplified

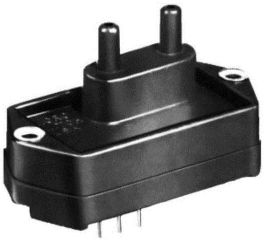

FEATURES
- Low pressure measurement
- PCB terminals on opposite side from the ports
- Fully signal conditioned

Amplified

160PC SERIES PERFORMANCE CHARACTERISTICS at 8.0 ±0.01 VDC Excitation, 25°C (Exception 163PC at 10 ±0.01 VDC Excitation, 25°C)

	Min.	Typ.	Max.	Units
Excitation	6.00	8.00	16	VDC
Supply Current	---	8.00	20	mA
Current Sourcing Output	---	---	10	mA
Null Offset (161/162/164PC)*	0.95	1.00	1.05	V
Null Offset (163PC)**	3.45	3.50	3.55	V
Output at Full Pressure (161/162/164PC)	5.90	6.00	6.10	V
Output at Full Vacuum (163PC)	0.80	1.00	1.20	V
Span (161/162/164PC)	4.85	5.00	5.15	V
Span (163PC)**	---	5.00	---	V
Ratiometricity Error 7 to 8 V or 8 to 9 V 9 to 12 V	 --- ---	 ±0.50 ±2.00	 --- ---	%Span
Stability over One Year	---	±0.50	---	%Span
Response Time	---	---	1.00	msec
Weight	---	28	---	grams
Short Circuit Protection	Output may be shorted indefinitely to ground			
Output Ripple	None, DC device			
Ground Reference	Supply and output are common			

*Positive (or negative) pressure measurement.
**Positive AND negative pressure measurement.

ENVIRONMENTAL SPECIFICATIONS

Operating Temperature	−40° to +85°C (−40° to +185°F)
Storage Temperature	−55° to +125°C (−67° to +257°F)
Compensated Temperature	−18° to +63°C (0° to +145°F)
Shock	MIL-STD-202, Method 213 (50 g, half sine, 6 msec)
Vibration	MIL-STD-202, Method 204 (10 to 2000 Hz at 10 g)
Media	P2 port Wetted materials; polyester housing, epoxy adhesive, silicon, borosilicate glass,and silicon-to-glass bond*
	P1 port Dry gases only

*Liquid media containing some highly ionic solutions could potentially neutralize the chip-to-glass tube bond.

160PC SERIES ORDER GUIDE, VACUUM GAGE AND GAGE TYPE

Catalog Listing	Pressure Range "H_2O	Shift Null, Sensitivity, Combined** 25 to 5° 25 to 45°C Max.	25 to −18° 25 to +63°C Max.	25 to −40° 25 to 85°C Max.	Sensitivity V/"H_2O	Overpressure psi Max.	Linearity, B.F.S.L. P2 > P1 %Span Max.	P2 < P1 %Span Max.	Repeatability & Hysteresis %Span Typ.
161PC01D	0-27.68	---	±1.00	±2.00	0.18	5	---	±1.00	±0.15 Vacuum Gage
162PC01G	0-27.68	---	±1.00	±2.00	0.18	5	---	±1.00	±0.15 Gage

160PC SERIES ORDER GUIDE, DIFFERENTIAL TYPE

Catalog Listing	Pressure Range "H_2O	Shift Null, Sensitivity, Combined** 25 to 5° 25 to 45°C Max.	25 to −18° 25 to +63°C Max.	25 to −40° 25 to 85°C Max.	Sensitivity V/"H_2O	Overpressure psi Max.	Linearity, B.F.S.L. P2 > P1 %Span Max.	P2 < P1 %Span Max.	Repeatability & Hysteresis %Span Typ.
162PC01D	0-27.68	---	±1.00	±2.00	0.18	5	±2.00	---	±0.15
163PC01D36	±5	±1.00	---	---	0.50	5	±2.00	±1.00	±0.25
164PC01D37	0-10	±1.00	---	---	0.50	5	±2.00	---	±0.25
163PC01D75	±2.5	±1.25	---	---	1.00	5	±2.00	±1.00	±0.25
164PC01D76	0-5	±1.25	---	---	1.00	5	±2.00	---	±0.25

160PC SERIES ORDER GUIDE, DIFFERENTIAL TYPE @ 10 VDC ±0.01 EXCITATION, 25°C

Catalog Listing	Pressure Range cmH_2O	Shift Null, Sensitivity, Combined** 25 to 5° 25 to 45°C Max.	25 to −18° 25 to +63°C Max.	25 to −40° 25 to 85°C Max.	Sensitivity V/cmH_2O	Overpressure cmH_2O Max.	Linearity, B.F.S.L. P2 > P1 %Span Max.	P2 < P1 %Span Max.	Repeatability & Hysteresis %Span Typ.
163PC01D48	−20 to +120	±0.75*	---	---	0.36	350	±1.5	---	±0.15

*Null shift. Span shift is ±1.00/Span
**% Span specification applies to each shift independently (Null, Sensitivity, or Combined)

INTERNAL CIRCUITRY

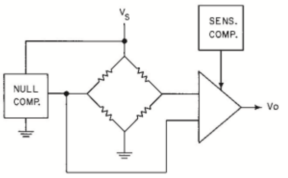

NOTES

1. Terminals are labeled on the sensor.
2. Input and output share a common ground.
3. R_L must be greater than or equal to 3000 ohms.

RATIOMETRICITY

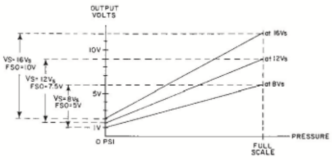

Ratiometricity refers to the output voltage being directly proportional to supply voltage. 160PC sensors in this catalog are calibrated at 8 VDC supply voltage (except 163PC) to provide a 1-6 volt (5 V Span) output swing. For example, if supply increases by 50% to 12 VDC, the output voltage increased by 50% to 1.5-9 volts (7.5 V Span).

NOTE

The output is not perfectly ratiometric. See Accuracy specifications for the degree of error.

NULL AND SENSITIVITY TEMPERATURE SHIFT

Amplified pressure sensor are 100% tested to insure that the maximum null and sensitivity temperature shift does not exceed the specification. The diagram below illustrates how null and sensitivity shift relates to temperature. Note that the maximum shift occurs at temperature extremes. Therefore, if a sensor is not exposed to the entire temperature range, the maximum null and sensitivity shift will actually be less than the value specified.

This diagram indicates the temperature shift pertaining to a few listings. Maximum null and sensitivity shift varies from listing to listing.

NULL AND SENSITIVITY SHIFT (% F.S.O.)

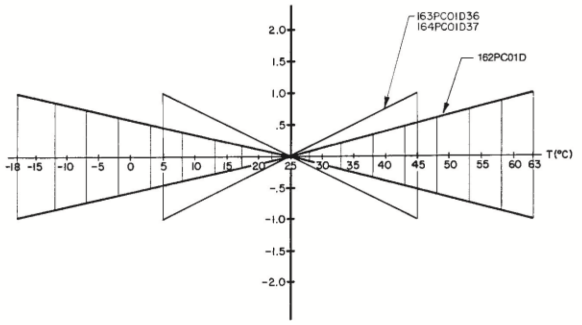

SCALING OF 160PC SERIES SENSORS WITH 8V EXCITATIONS

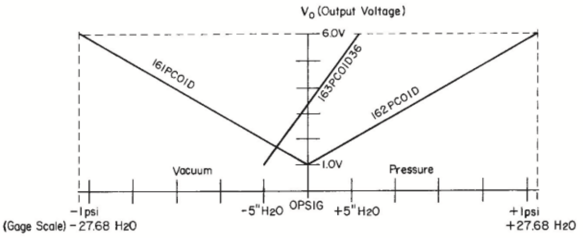

161PC01D	Vacuum Gage	V_O = 1 V at 0 psig & 6 V at –1 psig
162PC01D	Differential	V_O = 1 V at 0 psig & 6 V at 1 psig
163PC01D36	Differential	V_O = 1 V at –5" H_2O & 6 V at –5" H_2O

NOTE: 161PC sensors are scaled for greater pressure on the P1 side of the chip. 162PC sensors are scaled for greater pressure on the P2 side of the chip. Other scalings available upon request.

MOUNTING DIMENSIONS (For reference only)

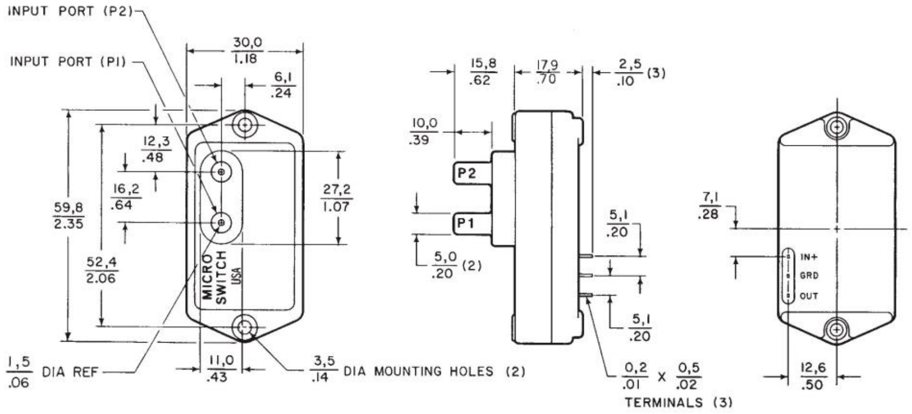

160PC CONSTRUCTION

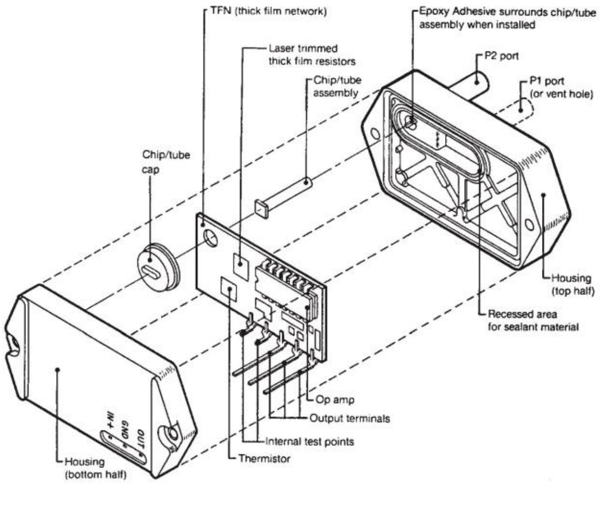

High-speed camera Basler acA2000-340km

All You Need is ace

The Basler ace camera line covers the entire spectrum including cost sensitivity, ultra-fast speeds and high tech in a very small housing. The camera's price-driven design underpins our quality commitment by applying the technical knowledge we've acquired from former camera designs. High quality and performance levels combined with a low starting list price of only €199 make Basler ace cameras one of the world's best selling cameras with thousands of satisfied customers.

With the ace series, you can choose from the most popular data interfaces in the vision market: the popular Gigabit Ethernet interface with 100-meter cable length, the new USB 3.0 interface with plug and play capability, and the field-proven Camera Link interface with wide bandwidth. All Basler ace cameras come with an option to provide camera power and data via a single cable. They also offer separate input/output ports for triggering or flash control. And like all Basler cameras, the ace family comes with a long list of firmware features.

Analog cameras are very easy to replace because the Basler ace offers the same 29 mm × 29 mm footprint and the same bottom mounting options that have been standard on analog cameras for many years. Some existing Camera Link, FireWire, and USB 2.0 cameras with the same 29 mm × 29 mm footprint can also be replaced. The Basler ace matches most of these cameras in terms of mechanics, and often beats them on price and ease of use.

Want to do things better? Then get yourself one of these innovative digital cameras that are specifically targeted at industrial, medical, and traffic applications – and profit from a convincing price/performance ratio to boot. This ace of cameras is available with several resolutions and speeds, and with sensors from all leading manufacturers so you can easily find the right ace camera model for your application. Basler ace is all you need.

Your benefits include:

- Support for standard vision interfaces GigE Vision, USB3 Vision, and Camera Link
- Broadest sensor portfolio ever: CMOS and CCD including NIR-enhanced versions, I/O flexibility with minimum delay and jitter time
- One cable solutions: Gigabit Ethernet with PoE, Camera Link with PoCL, USB 3.0
- Field-proven Basler pylon Camera Software Suite with advanced drivers
- Outstanding price/performance ratio

Specifications

Basler ace	acA2000-340km/kc	acA2000-340kmNIR	acA2040-180km/kc	acA2040-180kmNIR
Camera				
Resolution (H × V pixels)	2048 × 1088	2048 × 1088	2048 × 2048	2048 × 2048
Sensor	CMOSIS CMV2000	CMOSIS CMV2000 NIR-enhanced	CMOSIS CMV4000	CMOSIS CMV4000 NIR-enhanced
Sensor Size (optical)	2/3"	2/3"	1"	1"
Sensor Technology	CMOS, global shutter	CMOS, global shutter	CMOS, global shutter	CMOS, global shutter
Pixel Size [µm²]	5.5 × 5.5	5.5 × 5.5	5.5 × 5.5	5.5 × 5.5
Frame Rate [fps]	340	340	180	180
Mono/Color	Mono/Color	Mono NIR-enhanced	Mono/Color	Mono NIR-enhanced
Interface	Camera Link (base, medium, or full)			
Synchronization	Via external trigger or free run			
Exposure Control	Trigger width or timed			
Mechanical/Electrical				
Housing Size (L × W × H)	43.5 mm × 29 mm × 29 mm			
Housing Temperature	Up to 50 °C			
Lens Mount	C	C	C	C
Digital I/O	1 opto-isolated input or output (GPIO)			
Power Requirements	12VDC (±10%), Power over Camera Link (PoCL) or via IO connector			
Power Consumption (typical)	3.0 W			
Weight (typical)	96 g			
Conformity	CE, FCC, RoHS, GenICam, Camera Link, UL (in preparation)			
Software/Driver				
Driver	Basler pylon Camera Software Suite or 3rd party Camera Link Software			
Operating System	Windows, Linux - 32 bit and 64 bit			
Conformity	Camera Link, GenICam			

Specifications are subject to change without prior notice. Latest specifications can be found on our website. Please visit www.baslerweb.com/manuals for the detailed camera User's Manual and www.baslerweb.com/thirdparty for information on third party software.

For availbility please refer to our website www.baslerweb.com/ace

Dimensions (in mm)

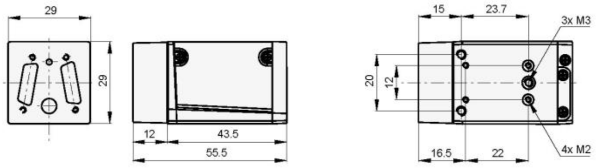

Frame grabber NI PCIe-1433

A
Specifications

This lists specifications for the NI PCIe-1433. These specifications are typical at 25 °C, unless otherwise stated.

Features

Supported camera standard .... Camera Link 1.2

Supported configurations .... Base, Medium, Full, Extended Full

Camera connectors .... Two 26-pin MDR

PCI Express Interface

PCI Express compliance 1.1

Native link width.................................... x4

Up-plugging availability x8, x16

Note Some system devices limit data transfer rates for plug-in devices in an up-plugging configuration. Refer to the documentation provided by the computer manufacturer to determine if your computer will support a x4 plug-in device at a x4 data rate in a larger slot.

Trigger Characteristics

Number of external trigger I/O lines...... 1

Trigger input
- Voltage range.................................. 0 to 5 V (TTL)
  - Input high voltage.................... 2.0 V
  - Input low voltage..................... 0.8 V
- Polarity... Programmable, active high or active low

Trigger output	
Voltage range	0 to 5 V (TTL)
Output high voltage	3.06 V at 3 mA source
Output low voltage	0.55 V at 3 mA sink
Polarity	Programmable, active high or active low
Maximum pulse rate	2 MHz

Clocks

Pixel clock frequency range	20 MHz to 85 MHz[1]

Note The Camera Link specification requires cameras to transmit at a minimum of 20 MHz.

Serial Interface

Baud rates supported	9.6, 19.2, 38.4, 57.6, 115.2, 230.4, 460.8, or 921.6 kbps

Power Requirements

Voltage	+3.3 V (1.5 A) +12 V (1.25 A)

Power Over Camera Link (PoCL)

Voltage	12 V nominal
Average power output	4 W maximum
SafePower	Supported

Physical Characteristics

Dimensions	10.7 cm × 17.5 cm (4.2 in. × 6.9 in.)
Weight	205 g (7.23 oz)

[1] This value corresponds to the serialized Camera Link cable transmission rate of 140 to 595 MHz.

Environment

The NI 1433 is intended for indoor use only.

Operating Environment

Operating temperature	0 °C to 50 °C Tested in accordance with IEC-60068-2-1 and IEC-60068-2-2.
Relative humidity range	10% to 90%, noncondensing Tested in accordance with IEC-60068-2-56.
Altitude	2,000 m at 25 °C ambient temperature
Pollution Degree	2

Storage Environment

Ambient temperature range	–20 °C to 70 °C Tested in accordance with IEC-60068-2-1 and IEC-60068-2-2.
Relative humidity range	5% to 95%, noncondensing Tested in accordance with IEC-60068-2-56.

Note Clean the device with a soft, non-metallic brush. Make sure the device is completely dry and free from contaminants before returning it to service.

Shock and Vibration

Operational shock	30 g peak, half-sine, 11 ms pulse Tested in accordance with IEC-60068-2-27. Test profile developed in accordance with MIL-PRF-28800F.

Random vibration

Operating ....5 to 500 Hz, 0.3 grms

Nonoperating ....5 to 500 Hz, 2.4 grms
Tested in accordance with IEC-60068-2-64. Nonoperating test profile exceeds the requirements of MIL-PRF-28800F, Class 3.

Safety

This product meets the requirements of the following standards of safety for electrical equipment for measurement, control, and laboratory use:

- IEC 61010-1, EN 61010-1
- UL 61010-1, CSA 61010-1

Note For UL and other safety certifications, refer to the product label or the *Online Product Certification* section.

Electromagnetic Compatibility

This product meets the requirements of the following EMC standards for electrical equipment for measurement, control, and laboratory use:

- EN 61326 (IEC 61326): Class A emissions; Basic immunity
- EN 55011 (CISPR 11): Group 1, Class A emissions
- AS/NZS CISPR 11: Group 1, Class A emissions
- FCC 47 CFR Part 15B: Class A emissions
- ICES-001: Class A emissions

Note For the standards applied to assess the EMC of this product, refer to the *Online Product Certification* section.

Note For EMC compliance, operate this device with shielded cables and according to the documentation.

CE Compliance CE

This product meets the essential requirements of applicable European Directives as follows:

- 2006/95/EC; Low-Voltage Directive (safety)
- 2004/108/EC; Electromagnetic Compatibility Directive (EMC)

Data logger PCI National Instrument 6034E

Low-Cost E Series Multifunction DAQ – 12 or 16-Bit, 200 kS/s, 16 Analog Inputs

NI E Series – Low-Cost

- 16 analog inputs at up to 200 kS/s, 12 or 16-bit resolution
- Up to 2 analog outputs at 10 kS/s, 12 or 16-bit resolution
- 8 digital I/O lines (TTL/CMOS); two 24-bit counter/timers
- Digital triggering
- 4 analog input signal ranges
- NI-DAQ driver that simplifies configuration and measurements

Families

- NI 6036E
- NI 6034E
- NI 6025E
- NI 6024E
- NI 6023E

Operating Systems

- Windows 2000/NT/XP
- Real-time performance with LabVIEW
- Others such as Linux® and Mac OS X

Recommended Software

- LabVIEW
- LabWindows/CVI
- Measurement Studio
- VI Logger

Other Compatible Software

- Visual Basic, C/C++, and C#

Driver Software (included)

- NI-DAQ 7

Family	Bus	Analog Inputs	Input Resolution	Max Sampling Rate	Input Range	Analog Outputs	Output Resolution	Output Rate	Output Range	Digital I/O	Counter/Timers	Triggers
NI 6036E	PCI, PCMCIA	16 SE/8 DI	16 bits	200 kS/s	±0.05 to ±10 V	2	16 bits	10 kS/s[1]	±10 V	8	2, 24-bit	Digital
NI 6034E	PCI	16 SE/8 DI	16 bits	200 kS/s	±0.05 to ±10 V	0	–	–	–	8	2, 24-bit	Digital
NI 6025E	PCI, PXI	16 SE/8 DI	12 bits	200 kS/s	±0.05 to ±10 V	2	12 bits	10 kS/s[1]	±10 V	8	2, 24-bit	Digital
NI 6024E	PCI, PCMCIA	16 SE/8 DI	12 bits	200 kS/s	±0.05 to ±10 V	2	12 bits	10 kS/s[1]	±10 V	8	2, 24-bit	Digital
NI 6023E	PCI	16 SE/8 DI	12 bits	200 kS/s	±0.05 to ±10 V	0	–	–	–	8	2, 24-bit	Digital

[1] 10 kS/s typical when using the single DMA channel for analog output. 1 kS/s maximum when using the single DMA channel for either analog input or counter/timer operations. 1 kS/s maximum for PCMCIA DAQCard devices in all cases.

Table 1. Low-Cost E Series Model Guide

Overview and Applications

National Instruments low-cost E Series multifunction data acquisition devices provide full functionality at a price to meet the needs of the budget-conscious user. They are ideal for applications ranging from continuous high-speed data logging to control applications to high-voltage signal or sensor measurements when used with NI signal conditioning. Synchronize the operations of multiple devices using the RTSI bus or PXI trigger bus to easily integrate other hardware such as motion control and machine vision to create an entire measurement and control system.

Highly Accurate Hardware Design

NI low-cost E Series DAQ devices include the following features and technologies:

Temperature Drift Protection Circuitry – Designed with components that minimize the effect of temperature changes on measurements to less than 0.0010% of reading/°C.

Resolution-Improvement Technologies – Carefully designed noise floor maximizes the resolution.

Onboard Self-Calibration – Precise voltage reference included for calibration and measurement accuracy. Self-calibration is completely software controlled, with no potentiometers to adjust.

NI DAQ-STC – Timing and control ASIC designed to provide more flexibility, lower power consumption, and a higher immunity to noise and jitter than off-the-shelf counter/timer chips.

NI MITE – ASIC designed to optimize data transfer for multiple simultaneous operations using bus mastering with one DMA channel, interrupts, or programmed I/O.

NI PGIA – Measurement and instrument class amplifier that guarantees settling times at all gains. Typical commercial off-the-shelf amplifier components do not meet the settling time requirements for high-gain measurement applications.

PFI Lines – Eight programmable function input (PFI) lines that you can use for software-controlled routing of interboard and intraboard digital and timing signals.

RTSI or PXI Trigger Bus – Bus used to share timing and control signals between two or more PCI or PXI devices to synchronize operations.

RSE Mode – In addition to differential and nonreferenced single-ended modes, NI low-cost E Series devices offer the referenced single-ended (RSE) mode for use with floating-signal sources in applications with channel counts higher than eight.

Onboard Temperature Sensor – Included for monitoring the operating temperature of the device to ensure that it is operating within the specified range.

NATIONAL INSTRUMENTS

		Full-Featured E Series				Low-Cost E Series		Basic
Models		NI 6030E, NI 6031E, NI 6032E, NI 6033E	NI 6052E	NI 6070E, NI 6071E	NI 6040E	NI 6034E, NI 6036E	NI 6023E, NI 6024E, NI 6025E	PCI-6013, PCI-6014
Measurement Sensitivity[1] (mV)		0.0023	0.0025	0.009	0.008	0.0036	0.008	0.004
Nominal Range (V)		Absolute Accuracy (mV)						
Positive FS	**Negative FS**							
10	-10	1.147	4.747	14.369	15.373	7.560	16.504	8.984
5	-5	2.077	0.876	5.193	5.697	1.790	5.263	2.003
2.5	-2.5	–	1.190	3.605	3.859	–	–	–
2	-2	0.836	–	–	–	–	–	–
1	-1	0.422	0.479	1.452	1.556	–	–	–
0.5	-0.5	0.215	0.243	0.735	0.789	0.399	0.846	0.471
0.25	-0.25	–	0.137	0.379	0.405	–	–	–
0.2	-0.2	0.102	–	–	–	–	–	–
0.1	-0.1	0.061	0.064	0.163	0.176	–	–	–
0.05	-0.05	–	0.035	0.091	0.100	0.0611	0.106	0.069
10	0	0.976	1.232	6.765	7.269	–	–	–
5	0	1.992	2.119	5.391	5.645	–	–	–
2	0	0.802	0.850	2.167	2.271	–	–	–
1	0	0.405	0.428	1.092	1.146	–	–	–
0.5	0	0.207	0.242	0.558	0.583	–	–	–
0.2	0	0.098	0.111	0.235	0.247	–	–	–
0.1	0	0.059	0.059	0.127	0.135	–	–	–

Note: Accuracies are valid for measurements following an internal calibration. Measurement accuracies are listed for operational temperatures within ±1 °C of internal calibration temperature and ±10 °C of external or factory-calibration temperature. One-year calibration interval recommended. The Absolute Accuracy at Full Scale calculations were performed for a maximum range input voltage (for example, 10 V for the ±10 V range) after one year, assuming 100 pt averaging of data.

[1]Smallest detectable voltage change in the input signal at the smallest input range.

Table 2. E Series Analog Input Absolute Accuracy Specifications

		Full-Featured E Series				Low-Cost E Series		Basic
Models		NI 6030E, NI 6031E, NI 6032E, NI 6033E	NI 6052E	NI 6070E, NI 6071E	NI 6040E	NI 6034E, NI 6036E	NI 6023E, NI 6024E, NI 6025E	PCI-6013, PCI-6014
Nominal Range (V)		Absolute Accuracy (mV)						
Positive FS	**Negative FS**							
10	-10	1.430	1.405	8.127	8.127	2.417	8.127	3.835
10	0	1.201	1.176	5.685	5.685	–	–	–

Table 3. E Series Analog Output Absolute Accuracy Specifications

High-Performance, Easy-to-Use Driver Software

NI-DAQ is the robust driver software that makes it easy to access the functionality of your data acquisition hardware, whether you are a beginning or advanced user. Helpful features include:

Automatic Code Generation – DAQ Assistant is an interactive guide that steps you through configuring, testing, and programming measurement tasks and generates the necessary code automatically for NI LabVIEW, LabWindows/CVI, or Measurement Studio.

Cleaner Code Development – Basic and advanced software functions have been combined into one easy-to-use yet powerful set to help you build cleaner code and move from basic to advanced applications without replacing functions.

High-Performance Driver Engine – Software-timed single-point input (typically used in control loops) with NI-DAQ achieves rates of up to 50 kHz. NI-DAQ also delivers maximum I/O system throughput with a multithreaded driver.

Test Panels – With NI-DAQ, you can test all of your device functionality before you begin development.

Scaled Channels – Easily scale your voltage data into the proper engineering units using the NI-DAQ Measurement Ready virtual channels by choosing from a list of common sensors and signals or creating your own custom scale.

LabVIEW Integration – All NI-DAQ functions create the waveform data type, which carries acquired data and timing information directly into more than 400 LabVIEW built-in analysis routines for display of results in engineering units on a graph.

***For information on applicable hardware for NI-DAQ 7, visit* ni.com/dataacquisition.**

Visit* ni.com/oem *for quantity discount information.

Buffalo 12TB DriveStation Quad

BUFFALO
PERFORMANCE MATTERS

DriveStation™ Quad

HD-QLU3R5

HIGH CAPACITY

USB 3.0 STORAGE AND BACKUP

Buffalo's DriveStation Quad USB 3.0 Hard Drive Array is a 4-drive, RAID enabled USB 3.0 storage solution for small servers, creative professionals, offices and consumers who need large, redundant and high performance external storage. Support for hardware RAID 0, RAID 5 and RAID 10 provides flexible redundancy, capacity and performance operations. With USB 3.0 support and backward compatibility with USB 2.0, DriveStation Quad USB 3.0 works with almost any PC or Mac® computer and provides interface speeds up to 5 Gbps*.

FEATURES

EASY TO USE STORAGE

With terabytes of storage, DriveStation Quad USB 3.0 provides a reliable, easy to use storage for your PC and Mac® computer. Quickly expand the capacity of your computer for your favorite music, photos, videos and more. The simple USB 2.0 interface offers plug and play setup and universal connectivity.

EASY SCHEDULED BACKUP

DriveStation Quad USB 3.0 is perfect for backing up your important files. Disaster and hard drive failures can occur unexpectedly; don't leave your important files and treasured memories in the hands of chance. Schedule regular backups for your PC with Buffalo Backup Utility or use Time Machine for your Mac. Protect all of your data, down to the last byte.

BUFFALO TOOLS

Buffalo Tools is a feature-rich suite of optional software included on many Buffalo DriveStation and MiniStation storage products. Any or all of the following components of Buffalo Tools may be installed on Windows PCs.

- Buffalo's Backup Utility for Windows PCs and can be used to back up one or multiple computers with a single Buffalo external hard drive.
- eco Manager is an energy efficiency tool used to conserve energy and reduce battery consumption.
- RAMDISK is a simple utility that allows you to create a RAM disk on your Windows PC.
- SecureLock for Windows® provides complete control of the data encryption on your Buffalo external hard drive, providing password protection and software data encryption.

NOVABACKUP® BUSINESS ESSENTIALS

DriveStation Quad USB 3.0 comes with one license of NovaBACKUP® Business Essentials, an easy to use, complete backup solution for Windows® PCs, Windows® Servers, and SQL/Exchange databases.

MEDIA STORAGE CAPACITY

HDD Size	Photos*	Movies†	Songs‡
4 TB	1,800,000	4,000	1,000,000
6 TB	2,700,000	6,000	1,500,000
8 TB	3,600,000	8,000	2,000,000
12 TB	5,400,000	12,000	3,000,000
16 TB	7,200,000	16,000	4,000,000

Results will vary based on individual factors.
** Figures represent the average number of photos taken with a 10 megapixel camera with an average file size of 2.2 MB per photo.*
† Figures represent the number of movies based on an average file size of 1 GB per movie.
‡ Figures represent the number of MP3 files at an average length of 00:03:25/160 Kbps with an average file size of 4 MB per song.
1 MB = 1,000,000 bytes, 1 GB = 1,000,000,000 bytes, 1 TB = 1,000,000,000,000 bytes. Total accessible capacity varies depending on operating environment.

www.BuffaloAmericas.com

BUFFALO
PERFORMANCE MATTERS

DriveStation™ Quad

HD-QLU3R5

FLEXIBLE STORAGE AND REDUNDANCY

RAID 0 offers optimal performance and capacity by evenly storing data across both hard drives with zero redundancy

RAID 5 stripes the data across all four drives, interspersing parity data to provide an efficient blend of fault tolerance and storage capacity

RAID 10 mirrors two sets of hard drives and combines them into a single array, striping data across all mirrored sets for fault tolerance and increased performance

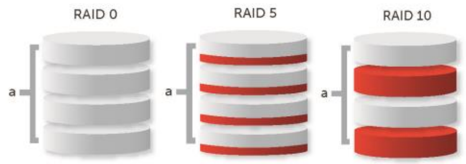

MODELS

HD-QL8TU3R5, HD-QL12TU3R5, HD-QL16TU3R5

BOX CONTENTS

DriveStation Quad USB 3.0, Quick-Setup Guide, AC Adapter, Warranty Statement

SPECIFICATIONS

24/7 TECH SUPPORT | 1 YEAR WARRANTY
(866) 752-6210 | USA & Canada Only

INTERNAL HARD DRIVES	
Number of Drives	4
Hard Drive Sizes:	2 TB, 3 TB, 4 TB
Total Hard Drives:	8 TB, 12 TB, 16 TB
Drive Interface	SATA 3 Gbps
Supported RAID Levels	0, 5, 10
Max. Disk Transfer Rate	235 MB/s (RAID 0, sequential read)
USB INTERFACE	
Standard Compliance	USB 3.0 / 2.0
Number of Ports	1
Data Transfer Rate	Max: 5 Gbps (USB 3.0) Max. 480 Mbps (USB 2.0)
OTHER	
Dimensions (W x H x D in)	5.9 x 6.1 x 9.2
Weight (lbs)	12.5 Average
Operating Enviroment	41-95°
Power Supply	AC 100-240V 50/60 Hz
Client OS Support	Windows® 8 (32-bit/64-bit), Windows® 7 (32-bit/64-bit), Windows Vista® (32-bit/64-bit), Windows® XP, Windows®2000, Windows Server® 2003 (32-bit)*, Windows Server® 2003 R2 (32-bit)*, Windows Server® 2008 (32-bit/64-bit)*, Windows Server® 2008 R2 (64-bit)*, Mac OS® X 10.5 or later**

** The HDD default format is NTFS; to work with Mac, reformat the HDD using Mac Disk Utility. Only basic external hard drive functionality is supported with this operating system; some included utilities may not work.

*1 TB = 1,000,000,000,000 bytes; total accessible capacity varies depending on operating environment. Data rate, features and performance may vary based on the configuration of your system and other factors. Buffalo Technology (Buffalo Inc.) shall not be responsible for data loss and shall have no liability arising out of damages from lost data.

www.BuffaloAmericas.com

Appendix 5 – LabVIEW code

The code for the data logging VI was written by Antonio Capponi in LabVIEW 2014. The following code allows the simultaneous acquisition of high-speed video and the transducers signals (Chapter 4, §4.3). LabVIEW uses a graphical programming language, so in order to insert the entire code it has been saved as four sequential images, attached below

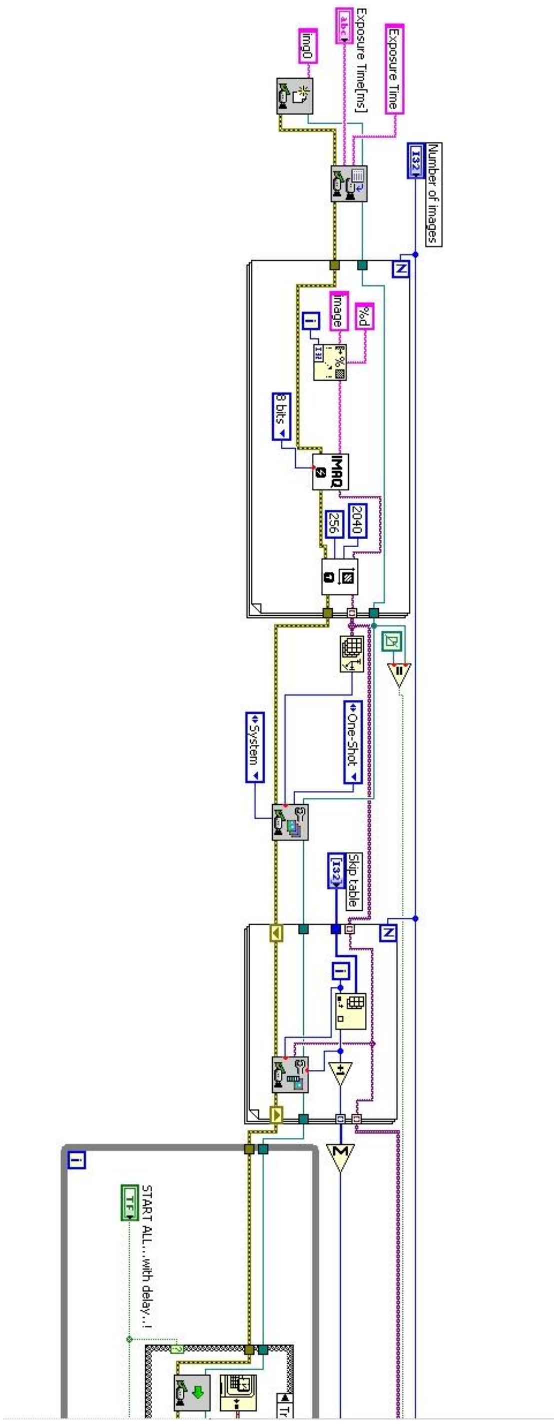

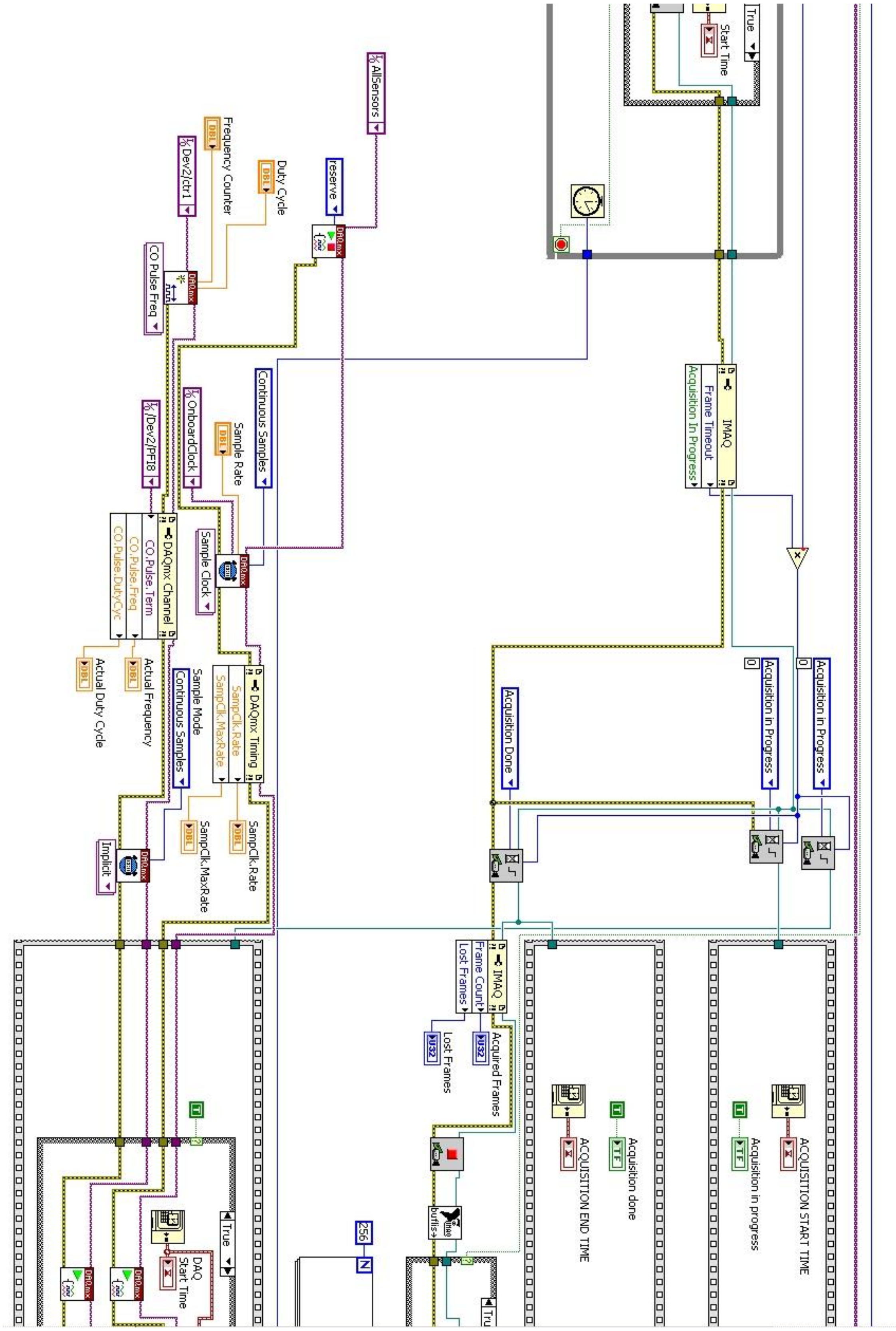

AllSensors
reserve
Duty Cycle
Frequency Counter
Dev2/ctr1
CO Pulse Freq
Continuous Samples
Sample Rate
OnboardClock
/Dev2/PFI8
DAQmx Channel
CO.Pulse.Term
CO.Pulse.Freq
CO.Pulse.DutyCyc
Actual Frequency
Actual Duty Cycle
Sample Clock
DAQmx Timing
SampClk.Rate
SampClk.MaxRate
Sample Mode
Continuous Samples
SampClk.MaxRate
SampClk.Rate
Implicit
True
DAQ Start Time
Start Time
IMAQ
Frame Timeout
Acquisition In Progress
Acquisition Done
Acquisition in Progress
Acquisition in Progress
IMAQ
Frame Count
Lost Frames
Acquired Frames
Lost Frames
256
ACQUISITION END TIME
Acquisition done
ACQUISITION START TIME
Acquisition in progress

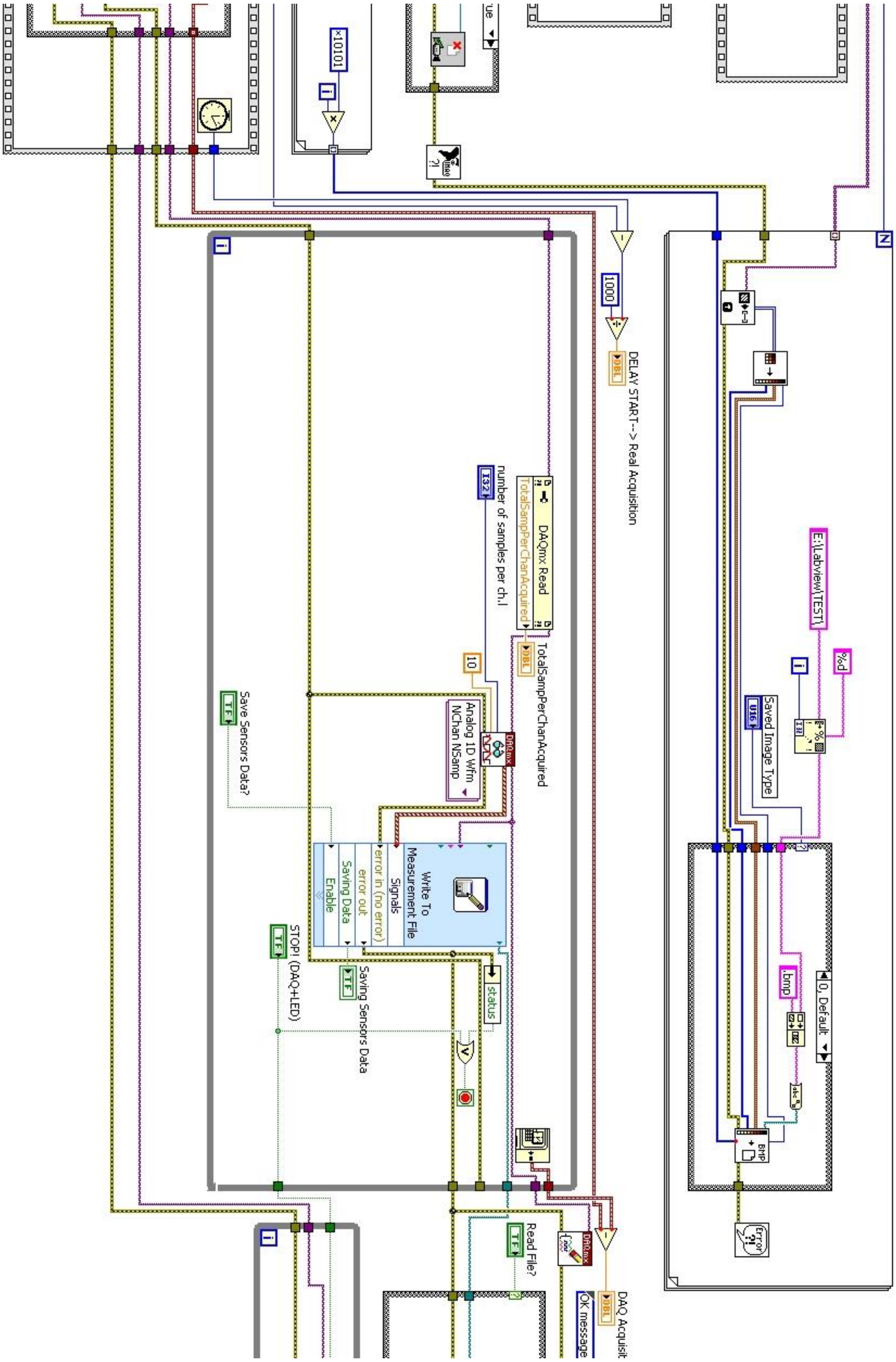
DAQmx Read
TotalSampPerChanAcquired
TotalSampPerChanAcquired
number of samples per ch.
10
Analog 1D Wfm
NChan NSamp
Write To
Measurement File
Signals
error in (no error)
error out
Saving Data
Enable
Save Sensors Data?
Saving Sensors Data
status
STOP! (DAQ+LED)
1000
DELAY START--> Real Acquisition
Read File?
DAQ Acquisit
OK message
E:\Labview\TEST\
%d
Saved Image Type
.bmp
0, Default

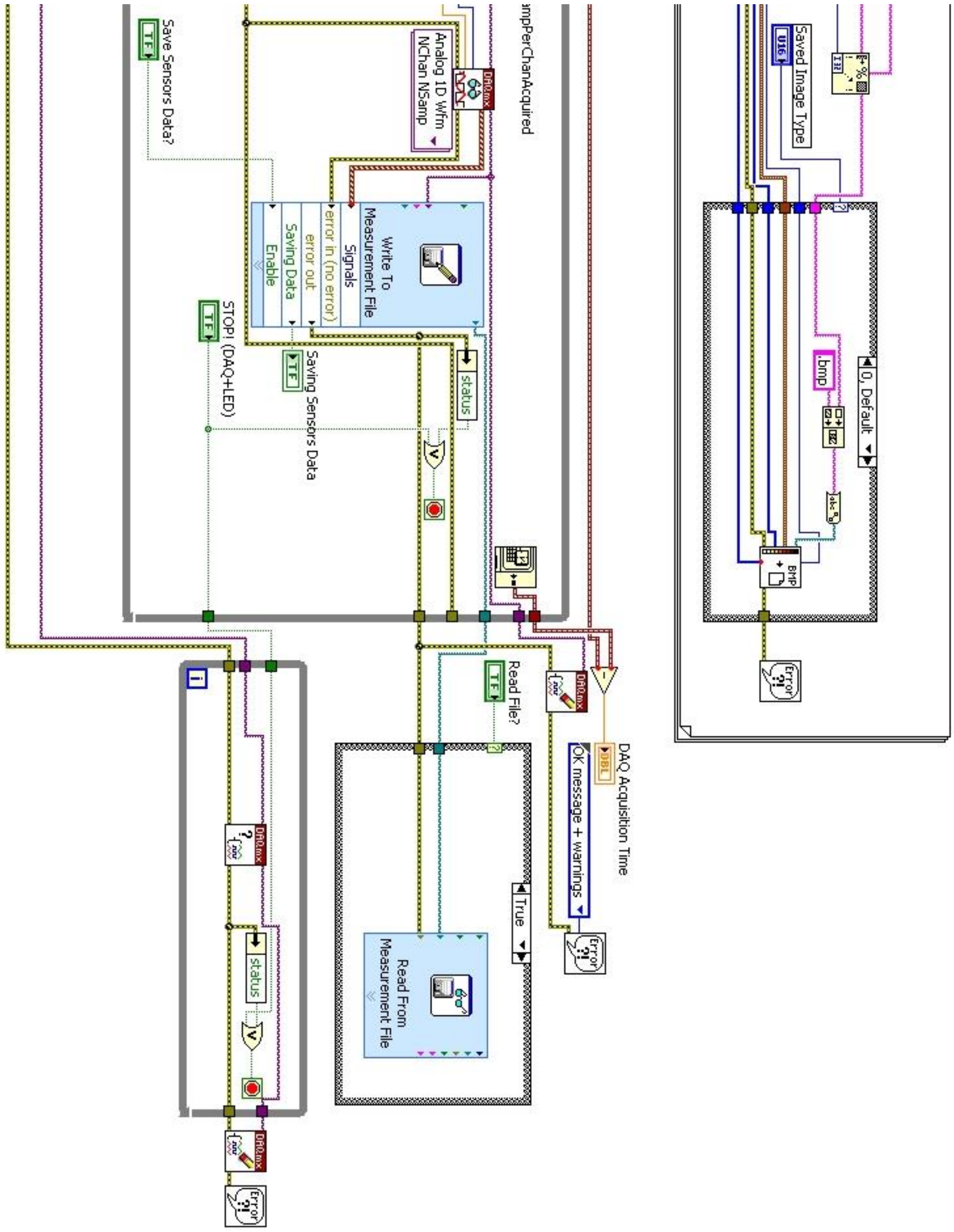
Save Sensors Data?
Analog 1D Wfm
NChan NSamp
DAQmx
Write To
Measurement File
Signals
error in (no error)
error out
Saving Data
Enable
status
STOP! (DAQ+LED)
Saving Sensors Data
Read File?
True
Read From
Measurement File
DAQ Acquisition Time
DBL
OK message + warnings
Saved Image Type
U16
0, Default
.bmp
BMP
status

Appendix 6 – Flow3D script for the 3D model

The following code is a template of the script needed to run 3D fluid dynamic simulations in Flow3D. From here it is possible to define, for example, conduit geometry, slug properties, liquid properties, simulation time, mesh properties, boundary conditions and computational parameters.

```
Gas slug ascent in a circular, magma-filled tube

3D model (1e5 Pa upper boundary pressure)
magma-appropriate surface tension
units are SI
400 m conduit, 300 m magma level, 100 m viscous cap
Viscosity: 50 - 20000 Pa
SLUG V:142 m3 (--> 10 ml @ 1 kPa Experimental volume)
********** GENERAL PARAMETERS ***************
 $xput
   remark='!! Remarks beginning with "!! " are automatically added and removed by FLOW-
   3D.',
   remark='!! Do not begin any user added remarks with with "!! ". They will be removed',
   twfin=350,     remark='stop time: 350 s',
   itb=1,
   ifenrg=2,
   ifvisc=1,          remark='new for 9.1: Newtonian viscosity model flag',
   ifvis=1,
   ifsft=1,           remark='surface tension model',
   impvis=1,
   impsft=1,          remark='implicit surface tension',
   impbub=0,
   ifvof=6,           remark='new for 9.1: split Lagrangian VOF advection model',
   cfpk=0.1,
   ifdynconv=1,
   ifrest=0,
   trest=0,
   itrst=1,
   ihtrst=1,
   irstoe=1,
   iphchg=3,          remark='new for 9.1: adiabatic bubble, no phase change',
   ifrho=0,
   gy=0,              remark='tube inclined at 0degr. to vertical',
   gz=-9.81,
   ipdis=1,
```

```
   idpth=1,
   ithead=1,
   istnr=1,
   ifmu=1,
   delt=0.1,
   tpltd(1)=0.1,
   thpltd(1)=0.1,
   tapltd(1)=1,
  iovoid=1,         remark='void history',
 $end

******** COMPUTATIONAL PARAMETERS ************

 $limits
   itmax=2000,
   itflmx=500,
   irpr= 1, jbkpr= 1, ktpr= 1,
 $end

************ FLUID PROPERTIES ****************

$props
   units='si',
   tunits='u',
   gamma=1.1,
   mu1=20,                    remark='Default fluid viscosity',
   cangle=85.0,               remark='Contact angle for fluid/solid',
   fluid1='magma',
   rhof=1000.,                remark='Fluid density',
   sigma=0.4,                 remark='Surface tension coefficient for magma',
   thc1=0.00000001,           remark='Set negligible thermal conductivity',
   irhof=1,
   imu1=1,                    remark='Fluid viscosity defined by table (see end)',
$end

 $scalar
   itracer=1,
 $end

 &PCAP
 /

********** BOUNDARY CONDITIONS **************

 $bcdata
```

```
  remark='!! Boundary condition X Min',
  ibct(1)=2, remark='symmetry',

  remark='!! Boundary condition X Max',
  ibct(2)=2,

  remark='!! Boundary condition Y Min',
  ibct(3)=2, remark='symmetry',

  remark='!! Boundary condition Y Max',
  ibct(4)=2,

  remark='!! Boundary condition Z Min',
  ibct(5)=2, remark='wall',

  remark='!! Boundary condition Z Max',
  ibct(6)=5,
  ipbctp(6)=1,
  pbct(1, 6)=100000.0,          remark='upper boundary and void space at 10^5 Pa',
  fbct(1, 6)=0.0,

  remark='!! Boundary condition common parameters',
  timbct(1)=0.0,
$end

************ MESH PROPERTIES ****************

$mesh
  nxcelt=32,
  px(1)=-1.6,
  px(2)=1.6,

  nycelt=32,
  py(1)=-1.6,
  py(2)=1.6,

  nzcelt=952,
  pz(1)=0,
  pz(2)=400,
 $end


************** OBSTACLES *****************

$obs
```

```
  nobs=2,

  remark='!! Component 1',
  ifCompEnabled(1)=0,

  remark='!! Subcomponent 1',
  iob(1)=1,                        remark='Component 1 = tube',
  ioh(1)=1,        remark='sub-component 1 = tube block',
  xl(1)=-12.0,
  xh(1)=12.0,
  yl(1)=-12.0,
  yh(1)=12.0,
  zl(1)=0.0,
  zh(1)=400.0,

  remark='!! Subcomponent 2',
  iob(2)=1,                        remark='sub-component 2 = tube hole',
  ioh(2)=0,
  rah(2)=1.5,                      remark='INTERNAL RADIUS',
  zl(2)=0,
  zh(2)=400.0,

  remark='!! Component 1 properties',
  itpobs(1)=0,
  iaqsrb(1)=0,

  remark='!! Subcomponent 3',
  iob(3)=2,                remark='Component 2 = tube base',
  ioh(3)=1,                remark='sub-component 3 = tube base',
  xl(3)=-2.0,
  xh(3)=2.0,
  yl(3)=-2.0,
  yh(3)=2.0,
  zl(3)=-1.0,
  zh(3)=0,

  remark='!! Component 2 properties',
  ifrco(2)=1,      remark='Calculate forces on Component 2',
  itpobs(2)=0,
  iaqsrb(2)=0,

  remark='!! Component common parameters',
  avrck=-3.1,
$end
```

********* FLUID INITIALISATION *************

```
$fl
  nfls=1,

  remark='!! Fluid Region 1',
  fioh(1)=0,                    remark='SLUG REGION DEFINITION',
  preg(1)=6020000,
  fzl(1)=0,
  fzh(1)=38,                    remark='initial volume',
  frah(1)=1.09,

  remark='!! Region Pointer 1',
  xvr(1)=0.2,
  yvr(1)=0.0,
  zvr(1)=0,                     remark='slug void pointer',
  pvrd(1)=3043000.,             remark='10^5 Pa + 300.0 m of magma',
  pvoid=100000.0,
  flht=300,          remark='300.0 m of magma',
  iflinittyp=1,
$end

$bf
$end

$temp
  ntmp=1,

  remark='!! Temperature Region 1',
  treg(1)=300.,
  ttrnz(1)=200.0,
  tzl(1)=0,
  tzh(1)=100,
  trah(1)=2,
  tempi=1200.,
$end

&MOTN
/
```

************ OUTPUTS ****************

```
  $grafic
  nwinf=202,            remark='Force windows to record viscous stresses',
```

```
remark='!! Sampling Volume 1',
fortl(1)='F1: tube sec. 0-2 m',
xf1(1)=-2.2,
xf2(1)=2.2,
yf1(1)=-2.2,
yf2(1)=2.2,
zf1(1)=0.0,
zf2(1)=2.0,

remark='!! Sampling Volume 2',
fortl(2)='F2: tube sec. 2-4 m',
xf1(2)=-2.2,
xf2(2)=2.2,
yf1(2)=-2.2,
yf2(2)=2.2,
zf1(2)=2.0,
zf2(2)=4.0,
......
remark='!! Sampling Volume 199',
fortl(199)='F199: tube sec. 396-398 m',
xf1(199)=-2.2,
xf2(199)=2.2,
yf1(199)=-2.2,
yf2(199)=2.2,
zf1(199)=396.0,
zf2(199)=398.0,

remark='!! Sampling Volume 200',
fortl(200)='F200: tube sec. 398-400 m',
xf1(200)=-2.2,
xf2(200)=2.2,
yf1(200)=-2.2,
yf2(200)=2.2,
zf1(200)=398.0,
zf2(200)=400.0,

remark='!! Sampling Volume 201',
fortl(201)='F1: full viscous component',

remark='!! Sampling Volume 202',
fortl(202)='F2: total force',
anmtyp(1)='mu',
anmtyp(2)='p',
anmtyp(3)='rhoe',
anmtyp(4)='stnr',
```

```
  anmtyp(5)='thead',
  anmtyp(6)='vel',
  $end


&HEADER
  project='Configuration1',
  version='single',
  nprocs=0,
  runser=1,
/

$parts
$end

#start tables:

#fluid1:
#mu1t
0 20000
500 20000
1000 150
1500 150
#end mu1t
#end fluid1
#end start tables
#start tables:
#component(1):
#end component(1)
#component(2):
#end component(2)
#fluid1:
#end fluid1
```

Appendix 7 – Matlab code for the 1D model

The code for the model (Chapter 6, §6.4) was written by Antonio Capponi. Three files are required to run the model:

- Run_slugforces (for input parameters, it calls the main function, creates plots, calls the script for determining the flow configuration)
- Slug_forces (main function)
- Config2 (it determines the flow configuration for the set of parameters specified in run_slug_forces)

Script 1 – run_slugforces.m

Contents


```
clear all
close all
clc

%%%% General Parameters
g = 9.81;                          % Gravity (m s-2)
gamma = 1;                         % Gamma
radcond = 2.5;                     % Conduit radius (m)
```

Plug density and viscosity

```
rhol_2 = 1300;                     % Plug density
viscl_2 = 10000;                   % Plug viscosity
```

Fresh magma density and viscosity

```
rhol = 900;                        % Liquid density (kg m-3)
viscl = 150;                        % Liquid viscosity (Pa s)
```

Inverse viscosity plug, intrusion radius (from film thickness of the plug)

```
Nf_plug = ( rhol_2/viscl_2 ) * sqrt ( 8 * 9.81 * radcond^3 );
% Inverse viscosity plug
lambda_plug = ( 0.204 + 0.123 * tanh ( 2.66 - 1.15 * log10(Nf_plug) ) ) *
radcond; % film thickness plug
```

```
radphi = radcond - lambda_plug;
% Radius of intrusion
```

Inverse Viscosity, Fr and slug ascent velocity

```
Nf_lv = ( rhol/viscl ) * sqrt ( 8 * 9.81 * radcond^3 ); % Inverse viscosity
fresh magma
Fr = 0.34 * ( ( 1 + ( 31.08 / Nf_lv )^1.45 )^-0.71);    % Froude number
slvel = Fr * sqrt ( 9.81 * ( radcond * 2 ) );           % Slug ascent
velocity
```

Slug Radius

```
lambda_lv = ( 0.204 + 0.123 * tanh ( 2.66 - 1.15 * log10(Nf_lv) ) ) *
radcond; % dimensionless film thickness fresh magma
radsl = radcond - lambda_lv;                 % slug radius

A = (radcond/radphi)^2; % Parameters used to simplify functions in the
%script
 B = (radsl/radphi)^2;    % Parameters used to simplify functions in the
%script
 D = (radsl/radcond)^2;

 k1 = 0;
 Rr = [];

psuptot = 100000; % P atm

for  k = 1:length(psuptot);           % Pressure above top liquid surface
           psup = psuptot(k);

          Dimtot = 1:0.5:20;
      for t = 1:length(Dimtot);  %     % "Dimensionless" thickness of the
slug
                    Dim = Dimtot(t);
               lzerotot = 2:1:30;
          for   q = 1:length(lzerotot) % Initial slug length
                    lzero = lzerotot(q);
              k1 = k1 + 1;

hplugzero = Dim * ( radcond * 2 );  % Thickness of the plug (m), function of
%the tube diameter

hzero = 200 - hplugzero;           % Initial height of low viscosity liquid
%above slug nose (m)
```

Define initial pressure of the slug (magmastatic)

```
pzero = rhol*g*( hzero + hplugzero) + psup;
```

Messages for the command window

```
disp(['P0V0 = ' num2str(pzero*pi*radsl^2*lzero)] )
disp(['H0 = ' num2str(hzero) ])
disp(['D = ' num2str(Dim)] )
disp(['lzero = ' num2str(lzero) ])
disp(['psup =' num2str(psup) ])

%%%%% Do your magic..
% T = Time
% H = Height of liquid above slug nose
% L = Slug length
% Ldot = rate of change of slug length
[ T, H, L, lv_liq_suf_ht, sl_nose_ht, sl_base_ht, intr_suf_ht, plug_suf_ht,
H_plug, H_intr, event_indx ]=...
    slug_forces(hzero, lzero, pzero, slvel, radsl,...
        radcond, rhol, rhol_2, viscl, viscl_2, g, psup, gamma, hplugzero,
radphi, A, B);
%%%%%
```

Plot ascent profile (Slug base & nose, fresh magma and plug surfaces, plug base)

```
 figure(1)
 plot(T, [plug_suf_ht intr_suf_ht lv_liq_suf_ht sl_nose_ht sl_base_ht]);
 legend( {'plug surface' 'intrusion top' 'plug base' 'sl nose' 'sl base'},
'Location', 'SouthEast')

% %%% Call script for Configurations Forecast
 run('config2')

MAP(k1,:) = [psup, Dim, lzero,  R];
           end
      end
end
```

Save flow configurations in a matrix

```
for p = 1:length(Dimtot)
    q = Dimtot(p);
    REGIME{p} = MAP(MAP(:,2)== q,4);
end



FlowConfig = cell2mat(REGIME);
%%%% Plot Configurations Diagram
figure(32)
F = FlowConfig;
```

```
imagesc(F);
colormap([]);

print('Flow Configuration vis. 150-10000 r.c.5m', '-dpng', '-r500');
```

Script 2 – Main function (slugforces.m)

```
function [ T, H, L, lv_liq_suf_ht, sl_nose_ht, sl_base_ht, intr_suf_ht,
plug_suf_ht, H_plug, H_intr, event_indx ] = ...
    slug_forces_mod(  hzero, lzero, pzero, slvel, radsl, ...
        radcond, rhol, rhol_2, viscl, viscl_2, g, psup, gamma, hplugzero,
radphi, A, B)

%    The function is called by running the script "run_slugforces"
%
%    Step 1: I define 1) the time interval for the integration and 2) the
%            event function to stop the solver, specified at the very end of
%            the script
%            All the input parameters, plots and initial P are defined in
%            the script "run_slugforces".
%    Step 2: The solver starts, desired outputs are the Time vector, the
%            Length of the slug at each time step and the event triggered
%    Step 3: For each time step, we calculate the value of "l", to be used
%            for calculating Ldot
%    Step 4: With all the parameters available, it is now possible to
%            measure h1, h2 and h3 (functions defined after the ODE
%            equation)
%    Step 5: With all the h values, we create history vectors for the slug
%            base, nose, LV liquid surface, intrusion and HV liquid surface.
%
%   ARGUMENTS:
%   hzero     = Initial depth of slug nose (m).
%   lzero     = Initial length of slug (m).
%   pzero     = Initial slug pressure (Pa).
%   slvel     = Ascent velocity of the slug base (m/s).
%   radsl     = Slug radius (m).
%   radcond   = Conduit radius (m).
%   radphi    = Intrusion radius (m).
%   rhol      = Low viscosity liquid density (kg m-3).
%   rhol_2    = High viscosity liquid density (kg m-3).
%   viscl     = Low viscosity liquid viscosity (Pa s).
%   viscl_2   = High viscosity liquid viscosity (Pa s).
%   g         = Acceleration due to gravity.
%   psup      = Surface pressure above liquid (Pa).
%   gamma     = Ratio of specific heats of the gas phase.
%   A         = (slug radius/intrusion radius)^2
%   B         = (slug radius/conduit radius)^2
```

```
%
% RETURNS:
%   T           =    Time vector.
%   L           =    The length of the gas slug.
%   Ldot        =    The rate of change of the length of the gas slug.
%   H           =    The height of liquid above the slug nose.
%   liq_suf_ht =    The fluid surface height (0 at T=0)
%   sl_nose_ht =    The position of the slug nose (-hzero at T=0)
%   sl_base_ht =    The position of the slug base (-(hzero+lzero) at T=0)
%   intr_suf_ht=    The position of the low viscosity liquid intrusion into
%                   the plug
%   plug_suf_ht=    The position of the plug surface

%%%%%%%%%%%%%%%%%%%%%%%%%%%%%%STEP 1%%%%%%%%%%%%%%%%%%%%%%%%%%%%%%%%%%%%%%
% Estimate time span for simulation to solve over.
% The TMax corresponds to the time at which the slug nose reaches the plug
% base
tspan = [ 0  ( hzero ) / slvel ];
disp(['tspan = ' num2str(tspan)] )

% Define events for the solver. (see end of the script)
options = odeset( 'Events', @events );

%%%%%%%%%%%%%%%%%%%%%%%%%%%%%%STEP 2%%%%%%%%%%%%%%%%%%%%%%%%%%%%%%%%%%%%%%
% ODE solver
% - "tspan" : time interval for the integration
% - "options" : tells the solver to stop when it meets an "event" (slug
% below the plug, intrusion breaches the plug)
% - Initial condition: Length of the slug and plug at t= 0 (lzero)
% %
% Function for ODE solver defined at the end of this function.
% Desired OUTPUT:
% T = time vector
% Ltmp = slug length value
% event_indx = triggered "event"

[T, Ltmp, ~, ~, event_indx] = ...
   ode45(@slugforces, tspan, lzero, options, ...
         hzero, lzero, pzero, slvel, radsl, ...
            radcond, rhol, rhol_2, viscl, viscl_2, g, psup, gamma,
hplugzero,  radphi, A, B);

% [L] Slug length
% Saving the vector L with all the values of L calculated by the solver. L
% will be used to calculate the parameter H.
L = Ltmp;

%%%%%%%%%%%%%%%%%%%%%%%%%%%%%%STEP 3%%%%%%%%%%%%%%%%%%%%%%%%%%%%%%%%%%%%%%
```

```
% [Ldot] Slug expansion
% disp(L)
for iter=1:length(T)
    t = T(iter);
    l = L(iter);
    dl = slugforces( t, l,  hzero, lzero, pzero, slvel, radsl, ...
        radcond, rhol, rhol_2, viscl, viscl_2, g, psup, gamma,
        hplugzero,  radphi, A, B);
 end


%%%%%%%%%%%%%%%%%%%%%%%%%%%%%%%STEP 4%%%%%%%%%%%%%%%%%%%%%%%%%%%%%%%%%%%%%
% Calculate H, H intrusion and H plug, calling the functions at the bottom
of the script

  H = Hliqf (T, L, hzero, lzero, slvel);
  H_intr = H_intrf (T, L, A, B, H, hzero, lzero, slvel, radcond, radsl,
  radphi);
  H_plug = H_plugf( H, hplugzero, A, lzero, hzero, slvel, T, L, B, radcond,
  radsl, radphi );

%%%%%%%%%%%%%%%%%%%%%%%%%%%%%%%STEP 5%%%%%%%%%%%%%%%%%%%%%%%%%%%%%%%%%%%%%
% Generate history vectors for the slug base, slug nose, low viscosity
% liquid surface, low viscosity intrusion and plug surface
sl_base_ht     =  -lzero + slvel*T;
sl_nose_ht     = sl_base_ht + L;
lv_liq_suf_ht  = sl_nose_ht + H ;
intr_suf_ht    = lv_liq_suf_ht + H_intr;
plug_suf_ht    = intr_suf_ht + H_plug;



disp('Engage')

%%%%%%%%%%%%%%%%%%%%%%%%%%%%%%%%%%%%%%%%%%%%%%%%%%%%%%%%%%%%%%%%%%%%%%%%%%%%
%%%%%%%%%%%%%%%%%%%
% Defined function for ODE solver
function dl = slugforces( t, l, hzero, lzero, pzero, slvel, radsl,...
        radcond, rhol, rhol_2, viscl, viscl_2, g, psup, gamma, hplugzero,
         radphi, A, B)


    Hliq   = Hliqf(t, l, hzero, lzero, slvel);
    H_intr = H_intrf(t, l, A, B, Hliq, hzero, lzero, slvel, radcond, radsl,
             radphi);
    H_plug = H_plugf( Hliq, hplugzero, A, lzero, hzero, slvel, t, l, B,
             radcond, radsl, radphi );
```

```
    dl = ( ( - g * ( rhol * ( Hliq + H_intr ) + ( rhol_2 * H_plug ) ) ) ...
        + pzero * lzero^gamma * l^(-gamma) - psup ) / ...
            ( 8 * ( (radcond^-2 * viscl * Hliq ) + (radcond^-2 * viscl_2 *
               H_plug ) + ( radphi^2*(radcond^-2/...
                  radsl^2) * viscl *  H_intr) ) ) ;


  % Artificially remove possibility for oscillation by forcing dl to be +ve
    if dl < 0, dl = 0 ; end
%   disp(dl)


%%%%%%%%%%%% Functions for the height of LV liquid, LV intrusion and plug.
%%%%%%%h1
function Hliq = Hliqf(t, l, hzero, lzero, slvel)

 Hliq = lzero - l - ( slvel * t )+ hzero;

%%%%%%%h2
function H_intr = H_intrf (t, l, A, B, Hliq, hzero, lzero, slvel, radcond,
radsl, radphi)

 H_intr = - A * ( lzero - l );

%%%%%%%h3
function H_plug = H_plugf ( Hliq, hplugzero, A, lzero, hzero, slvel, t, l,
B, radcond, radsl, radphi )


  H_plug = hplugzero + ( lzero - l ) * ( A - B );

%%%%%%%%%%%%%%%%%%%%%%%%%%%%%%%%%%%%%%%%%%%%%%%%%%%%%%%%%%%%%%%%%%%%%%%%%%%%%
% Event function for ODE solver

function [value,isterminal,direction] = events ( t, l, hzero, lzero, pzero,
     slvel, radsl,...
        radcond, rhol, rhol_2, viscl, viscl_2, g, psup, gamma, hplugzero,
         radphi, A, B)

     Hliq    = Hliqf(t, l, hzero, lzero, slvel);
     H_intr  = H_intrf(t, l, A, B, Hliq, hzero, lzero, slvel, radcond,
               radsl, radphi);
     H_plug  = H_plugf( Hliq, hplugzero, A, lzero, hzero, slvel, t, l, B,
               radcond, radsl, radphi );

   % Event 1 STOP event at liq ht above slug nose = 0.01 m (slug at the plug
   % base) or
   % at h plug above slug nose = 0.01 m (plug completely intruded)
```

```
    value = [ H_plug - 0.01  ; Hliq - 0.01];
    isterminal = [1; 1];
    direction = [0; 0];
```

Script 3 - Script for Configurations determination (conf2.m)

```
% Calculate lengths
  L_slug = L(end);
  L_intr = H_intr(end);
  L_plug = H_plug(end);

% Regime forecasting

if isempty(event_indx) == 1

        disp ('ERROR')
        R = 5;

elseif event_indx == 1

        disp ('REGIME 3')
        R = 3;

elseif event_indx == 2 && ( radcond^2 * L_plug )/( radcond^2 - radphi^2 ) >
B * L_slug

        disp ('REGIME 1')
        R = 1;

else disp ('REGIME 2')
        R = 2;
end
```

Bibliography

Abramoff MD, Magelhaes PJ, Ram SJ (2004) *Image processing with ImageJ*. Biophotonics Int 11:36–42

Allard P, Carbonnelle J, Metrich N, Loyer H, Zettwoog P (1994) *Sulphur output and magma degassing budget of Stromboli volcano.* Nature 368:326–330

Allard P (2010) *A CO_2-rich gas trigger of explosive paroxysms at Stromboli basaltic volcano, Italy*. J Volcanol Geotherm Res 189:363-374

Andronico D, Corsaro RA, Cristaldi A, Polacci M (2008) *Characterizing high energy explosive eruptions at Stromboli volcano using multidisciplinary data: an example from the 9 January 2005 explosion*. J Volcanol Geotherm Res 176:541–550. doi:10.1016/j.jvolgeores.2008.05.011

Aster R, Mah S, Kyle P, McIntosh W, Dunbar N, Johnson J, Ruiz M, McNamara S (2003) *Very long period oscillations of Mount Erebus Volcano*. J Geophys Res 108:2522, doi:10.1029/2002JB002101

Barberi P, Rosi M, Sodi A (1993) *Volcanic hazard assessment at Stromboli based on review of historical data*. Acta Vulcanol 3:173–187

Batchelor GK (1967) *An Introduction to Fluid Dynamics*. Cambridge University Press

Bagdassarov NS (1994) *Pressure and volume changes in magmatic systems due to the vertical displacement of compressible materials*. J Volcanol Geotherm Res 63:95–100.

Beckett FM, Mader HM, Phillips JC, Rust AC, Witham F (2011) *An experimental study of low-Reynolds-number exchange flow of two Newtonian fluids in a vertical pipe*. J Fluid Mech 682:652–670, doi:10.1017/jfm.2011.264

Blackburn EA, Wilson L, Sparks RSJ (1976) *Mechanisms and dynamics of strombolian activity*. J Geol Soc 132:429–440, doi: 10.1144/gsjgs.132.4.0429.

Bombrun MA, Harris A, Gurioli L, Battaglia J, Barra V (2015) *Anatomy of a Strombolian eruption: Inferences from particle data recorded with thermal video*. J Geophys Res. doi:10.100 2/2014JB 011556

Bonaccorso A, Calvari S, Garfı G, Lodato L, Patanè D (2003) *Dynamics of the December 2002 flank failure and tsunami at Stromboli volcano inferred by volcanological and geophysical observations.* Geophys Res Lett, 30(18):1941, doi:10.1029/2003GL017702, 2003

Bretherton FP (1961), *The motion of long bubbles in tubes*. J Fluid Mech 10:166–188, DOI: 10.1017/S0022112061000160

Brown RAS (1965), *The Mechanics of Large Gas Bubbles in Tubes 1. Bubble Velocities in Stagnant Liquids*. Can J Chem Eng, 43:217-223

Bugg JD, Saad GA (2002) *The velocity field around a Taylor bubble rising in a stagnant viscous fluid: numerical and experimental results*. Int J Multiphas Flow, 28(5):791-803

Burton M, Allard P, Mure F, La Spina A (2007a) *Magmatic Gas Composition Reveals the Source Depth of Slug-Driven Strombolian Eruptive Activity*, Science, 37:227-230

Burton MR, Mader HM, Polacci M (2007b) *The role of gas percolation in quiescent degassing of persistently active basaltic volcanoes*. Earth Planet Sci Lett. doi:10.1016/j.epsl.2007.08.028

Calvari S, Büttner R, Cristaldi A, Dellino P, Giudicepietro F, Orazi M, Peluso R, Spampinato L, Zimanowski B, Boschi E (2012) *The 7 September 2008 Vulcanian explosion at Stromboli volcano: Multiparametric characterization of the event and quantification of the ejecta*. J Geophys Res, doi:10.1029/2011JB009048

Campos JBLM, Guedes de Carvalho JRF (1988a) *An experimental study of the wake of gas slugs rising in liquids*. J. Fluid Mech. 196:27–37

Campos JBLM, Guedes de Carvalho JRF (1988b) *Mixing induced by air slugs rising in narrow columns of water*. Chem Eng Sci, 43(7):1569-1582

Capponi A (2010) *Applicazione della videoripresa ad alta velocita allo studio delle eruzioni Stromboliane*, Sapienza University of Rome, unpublished thesis.

Capponi A, James MR, Lane SJ (2016a) *Gas slug ascent in a stratified magma: Implications of flow organisation and instability for Strombolian eruption dynamics*. Earth Planet. Sci. Lett., http://dx.doi.org/10.1016/j.epsl.2015.12.028.

Capponi A, Taddeucci J, Scarlato P, Palladino DM (2016b) *Recycled ejecta modulating Strombolian explosions*. Accepted for publication, Bull Volcanol

Cashman KV, Sparks RSJ (2013) *How volcanoes work: A 25 year perspective*. Geol Soc Am Bull 125:664–690

Chouet B, Hamisevicz N, Mcgetchin TR (1974) *Photoballistics of Volcanic Jet Activity at Stromboli, Italy*. J Geophys Res, 79(32):4961–4976

Chouet B, Saccarotti G, Dawson P, Martini M, Scarpa R, De Luca G, Milana G, Cattaneo M (1999) *Broadband measurements of the sources of explosions at Stromboli volcano, Italy*. Geophys Res Lett, 26(13):1937-1940

Chouet B, Dawson P, Ohminato T, Martini M, Saccorotti G, Giudicepietro F, De Luca G, Milana G, Scarpa R (2003) *Source mechanisms of explosions at Stromboli Volcano, Italy, determined from moment-tensor inversions of very-long-period data*. J Geophys Res, 108(B1):2019, doi:10.1029/2002JB001919

Chouet B, Dawson P, Martini M (2008) *Shallow-conduit dynamics at Stromboli Volcano, Italy, imaged from waveform inversions*. In: Lane SJ, Gilbert JS (Eds.), *Fluid Motions in Volcanic Conduits: A Source of Seismic and Acoustic Signals*. Geol Soc London Special Publications, 307:57–84

Chouet BA, Dawson PB, James MR, Lane SJ (2010) *Seismic source mechanism of degassing bursts at Kilauea Volcano, Hawaii: Results from waveform inversion in the 10–50 s band*. J Geophys Res, 115:B09311, doi:10.1029/2009JB006661

Chouet BA, Matoza RS (2013) *A multi-decadal view of seismic methods for detecting precursors of magma movement and eruption*. J Volcanol Geoth Res, 252:108-175

Cimarelli C, Di Traglia F, Taddeucci J (2010) *Basaltic scoria textures from a zoned conduit as precursors to violent Strombolian activity*. Geology 38:439–442

Colò L, Ripepe M, Baker DR, Polacci M (2010) *Magma vesiculation and infrasonic activity at Stromboli open conduit volcano*. Earth Planet Sci Lett, 292(3-4):274–280, doi: 10.1016/j.epsl.2010.01.018

D'Auria L, Martini M (2011) *Slug flow: modeling in a conduit and associated elastic radiation*. In: Meyers RA (Ed.) *Encyclopedia of Complexity and Systems Science*. Springer, New York, NY, 858–873

D'Oriano C, Bertagnini A, Pompilio M (2011) *Ash erupted during normal activity at Stromboli (Aeolian Islands, Italy) raises questions on how the feeding system works*. Bull Volcanol, 73(5):471–477, doi: 10.1007/s00445-010-0425-0

D'Oriano C, Bertagnini A, Cioni R, Pompilio M (2014) *Identifying recycled ash in basaltic eruptions*. Sci Rep. http://dx.doi.org/10.1038/srep05851

Davies RM, Taylor G (1950) *The mechanics of large bubbles rising through extended liquids and through liquids in tubes*, P Roy Soc Lond A Mat, 200:375-390

Del Bello E, Llewellin EW, Taddeucci J, Scarlato P, Lane SJ (2012) *An analytical model for gas overpressure in slug-driven explosions: Insights into Strombolian* *volcanic eruptions*. J Geophys Res, 117(B2):B02206, doi: 10.1029/2011JB008747

Del Bello E, Lane SJ, James MR, Llewellin EW, Taddeucci J, Scarlato P, Capponi A (2015) *Viscous plugging can enhance and modulate explosivity of strombolian eruptions*. Earth Planet Sci Lett, 423:210-218, ISSN 0012-821X, http://dx.doi.org/10.1016/j.epsl.2015.04.034

Delle Donne D, Ripepe M (2012) *High-frame rate thermal imagery of Strombolian explosions: Implications for explosive and infrasonic source dynamics*. J Geophys Res, 117:B09206, doi:10.1029/2011JB008987

Dumitrescu DT (1943) *Strömung an einer Luftblase im senkrechten Rohr*. Z Angew Math Mech, 23(3):139-149

Francalanci L, Davies GR, Lustenhouwer W, Tommasini S, Mason PR, Conticelli S (2005). *Intra-grain Sr isotope evidence for crystal recycling and multiple magma reservoirs in the recent activity of Stromboli volcano, Southern Italy*. J Petrol, 46:1997–2021

Gaudin D, Taddeucci J, Scarlato P, Moroni M, Freda C, Gaeta M, Palladino DM (2014) *Pyroclast Tracking Velocimetry illuminates bomb ejection and explosion dynamics at Stromboli (Italy) and Yasur (Vanuatu) volcanoes*. J Geophys Res, 119(7):5384–5397, doi: 10.1002/2014JB011096

Genco R, Ripepe M (2010) *Inflation-deflation cycles revealed by tilt and seismic records at Stromboli volcano*. Geophys Res Lett. doi:10.1029/2010GL042925

Gerst A, Hort M, Kyle PR, Vöge M (2008) *4D velocity of Strombolian eruptions and man-made explosions derived from multiple Doppler radar instruments*. J Volcanol Geotherm Res. doi:10.1016/j.jvolgeores.2008.05.022

Gerst A, Hort M, Aster RC, Johnson JB, Kyle PR (2013) *The first second of volcanic eruptions from the Erebus volcano lava lake, Antarctica-energies, pressures, seismology, and infrasound*. J Geophys Res, Solid Earth, 118:3318–3340

Gibson AH (1913), *Motion of long air bubbles in a vertical tube*. Phil Mag (6)26:952–965

Giudicepietro F, D'Auria L, Martini M, Caputo T, Peluso R, De Cesare W, Orazi M, Scarpato G (2009) *Changes in the VLP seismic source during the 2007 Stromboli eruption*. J Volcanol Geoth Res, 182(3):162-171

Goldsmith HL, Mason SG (1962) *The movement of single large bubbles in closed vertical tubes*. J Fluid Mech. 10:42–58

Gurioli L, Colò L, Bollasina AJ, Harris AJL, Whittington A, Ripepe M (2014) *Dynamics of strombolian explosions: inferences from field and laboratory studies of erupted bombs from Stromboli volcano*. J Geophys Res, 119:319–345, doi:10.1002/2013JB010355.

Harris AJL, Ripepe M (2007a) *Synergy of multiple geophysical approaches to unravel explosive eruption conduit and source dynamics – A case study from Stromboli*. Chem Erde Geochem, 67:1–35

Harris A, Ripepe M (2007b) *Temperature and dynamics of degassing at Stromboli*. J Geophys Res, 112:B03205, doi:10.1029/2006JB004393

Harris AJL, Ripepe M, Hughes EA (2012) *Detailed analysis of particle launch velocities, size distributions and gas densities during normal explosions at Stromboli*. J Volcanol Geoth Res. doi:10.1016/j.jvolgeores.2012.02.012

Hattori S (1935), Rep Aeronaut Res Inst, Tokyo Imp Univ, 115

Houghton BF, Gonnermann HM (2008) *Basaltic explosive volcanism: Constraints from deposits and models*. Chemr Erde Geochem, 68(2):117-140, ISSN 0009-2819, http://dx.doi.org/10.1016/j.chemer.2008.04.002

James MR, Lane SJ, Chouet BA, Gilbert JS (2004) *Pressure changes associated with the ascent and bursting of gas slugs in liquid-filled vertical and inclined conduits*. J Volcanol Geotherm Res, 129:61-82

James MR, Lane SJ, Chouet BA (2006) *Gas slug ascent through changes in conduit diameter: Laboratory insights into a volcano-seismic source process in low-viscosity magmas*. J Geophys Res, 111(B5):B05201, doi: 10.1029/2005JB003718

James MR, Lane SJ, Corder SB (2008) *Modelling the rapid near-surface expansion of gas slugs in low viscosity magmas*. Geol Soc, London, Special Publications, 307(1):147–167, doi: 10.1144/SP307.9

James MR, Lane SJ, Wilson L, Corder SB (2009) *Degassing at low magma-viscosity volcanoes: Quantifying the transition between passive bubble-burst and Strombolian eruption*. J Volcanol Geotherm Res, 180(2-4):81–88, doi: 10.1016/j.jvolgeores.2008.09.002

James MR, Robson S (2014) *Sequential digital elevation models of active lava flows from ground-based stereo time-lapse imagery*, J Photogram Rem Sens, 97:160-170, doi:10.1016/j.isprsjprs.2014.08.011

Jaupart C, Vergniolle S (1988) *Laboratory models of Hawaiian and Strombolian eruptions*. Nature, 331:6151, 58-60

Jaupart C, Vergniolle S (1989) *The generation and collapse of a foam layer at the roof of a basaltic magma chamber*. J Fluid Mech, 203:347-380

Johnson J, Lees J (2000) *Plugs and chugs—seismic and acoustic observations of degassing explosions at Karymsky, Russia and Sangay, Ecuador*. J Volcanol Geotherm Res, 101:67–82

Johnson JB (2003) *Generation and propagation of infrasonic airwaves from volcanic explosions*. J Volcanol Geother Res, 121(1–2):1–14

Johnson JB, Aster RC, Kyle PR (2004) *Volcanic eruptions observed with infrasound*. Geophys Res Lett, 31(14)

Johnson JB, Ripepe M (2011) *Volcano infrasound: A review*. J Volcanol Geother Res, 206(3):61-69

Kang CW, Quan S, Lou J (2010) *Numerical study of a Taylor bubble rising in stagnant liquids*. Phys Rev E, 81(6):066308

Kawaguchi R,. Nishimura T (2015) *Numerical investigation of temporal changes in volcanic deformation caused by a gas slug ascent in the conduit*. J Volcanol Geother Res, 302:1-10

Kobayashi T, Namiki A, Sumita I (2010) *Excitation of airwaves caused by bubble bursting in a cylindrical conduit: Experiments and a model*. J Geophys Res, doi: 10.1029/2009JB006828

Kremers S, Lavallée Y, Hanson J, Hess KU, Chevrel MO, Wassermann J, Dingwell DB (2012) *Shallow magma mingling driven Strombolian eruptions at Mt. Yasur volcano, Vanuatu*. Geophys Res Lett, 39:L21304

Kremers S, Wassermann J, Meier K, Pelties C, Van Driel M, Vasseur J, Hort M (2013) *Inverting the source mechanism of Strombolian explosions at Mt. Yasur, Vanuatu, using a multi-parameter dataset*. J Volcanol Geotherm Res, 262:104–122

Landi P, Métrich N, Bertagnini A, Rosi M (2004) *Dynamics of magma mixing and degassing recorded in plagioclase at Stromboli (Aeolian Archipelago, Italy).* Contrib Mineral Petrol, 147: 213-227, doi: 10.1007/s00410-004-0555-5

Lane SJ, Chouet BA, Phillips JC, Dawson P, Ryan GA, Hurst E (2001) *Experimental observations of pressure oscillations and flow regimes in an analogue volcanic system*. J Geophys Res-Sol Ea, 106(B4):6461-6476

Lane SJ, James MR, Corder SB (2013) *Volcano infrasonic signals and magma degassing: First-order experimental insights and application to Stromboli*. Earth Planet Sci Lett, 377-378:169–179, doi: 10.1016/j.epsl.2013.06.048

Lautze NC, Houghton BF (2005) *Physical mingling of magma and complex eruption dynamics in the shallow conduit at Stromboli volcano, Italy*. Geology, 33(5):425, doi: 10.1130/G21325.1

Lautze NC, Houghton BF (2006) *Linking variable explosion style and magma textures during 2002 at Stromboli volcano, Italy*. Bull Volcanol, 69(4):445–460, doi: 10.1007/s00445-006-0086-1

Leduc L, Gurioli L, Harris A, Colò L, Rose-Koga EF (2015) *Types and mechanisms of strombolian explosions: characterization of a gas-dominated explosion at Stromboli*. Bull Volcanol. doi:10.1007/s00445-014-0555-5

Lighthill MJ (1978) *Waves in Fluids*. Cambridge University Press, Cambridge

Llewellin EW, Mader HM, Wilson SDR (2002), *The rheology of a bubbly liquid*. Proc R Soc Lond, A458:987–1016.

Llewellin EW, Del Bello E, Taddeucci J, Scarlato P, Lane SJ (2012) *The thickness of the falling film of liquid around a Taylor bubble*. Proc R Soc Math Phys Eng Sci, 468(2140):1041–1064, doi: 10.1098/rspa.2011.0476

Lyons JJ, Waite GP, Ichihara M, Lees JM (2012) *Tilt prior to explosions and the effect of topography on ultra-long-period seismic records at Fuego volcano, Guatemala*. Geophys Res Lett, 39, doi:10.1029/2012GL051184

Mangan M, Mastin L, Sisson T (2004) *Gas evolution in eruptive conduits: combining insights from high temperature and pressure decompression experiments with steady-state flow modeling*. J Volcanol Geotherm Res, 129:23-36

Marchetti E, Ripepe M (2005) *Stability of the seismic source during effusive and explosive activity at Stromboli Volcano*. Geophys Res Lett, 32:L03307, doi: 10.1029/2004GL21406

McGetchin TR, Settle M, Chouet BA (1974) *Cinder cone growth modeled after Northeast Crater, Mount Etna, Sicily*. J Geophys Res 79:3257–3272

McGreger AD, Lees JM (2004) *Vent discrimination at Stromboli volcano, Italy*. J Volcanol Geotherm Res, 137:169–185, doi: http://dx.doi.org/10.1016/j.jvolgeores.2004.05.007.

McNutt SR, Roman DC (2015) *Volcanic Seismicity*, in Sigurdsson H, Houghton B, McNutt, SR, Rymer H, Stix J (Eds.) *The Encyclopedia of Volcanoes*, 2nd edn, Academic Press, Amsterdam, 485–503

Meijering E, Dzyubachyk O, Smal I (2012) *Methods for cell and particle tracking*. Methods Enzymol 504:183-200

Métrich N, Bertagnini A, Landi P, Rosi M (2001) *Crystallization driven by decompression and water loss at Stromboli Volcano (Aeolian Islands, Italy)*. J Petrol, 43(8):1471-1490

Métrich N, Bertagnini A, Landi P, Rosi M, Belhadj O (2005) *Triggering mecha-nism at the origin of paroxysms at Stromboli (Aeolian Archipelago, Italy): the 5 April 2003 eruption*. Geophys Res Lett, 32:L10305

Misiti V, Vetere F, Mangiacapra A, Behrens H, Cavallo A, Scarlato P, Dingwell DB (2009), *Viscosity of high-K basalt from the 5th April 2003 Stromboli paroxysmal explosion*. Chem Geol, 260(3-4):278-285, doi: 10.1016/j.chemgeo.2008.12.023

Mori T, Burton M (2009) *Quantification of the gas mass emitted during single explosions on Stromboli with the SO2 imaging camera*. J Volcanol Geotherm Res, 188(4):395-400, doi:10.1016/j.jvolgeores.2009.10.005

Murase T, McBirney AR (1973) *Properties of some common igneous rocks and their melts at high temperatures*. Geol Soc Am Bull, 84:3563-3592

Neuberg J, Luckett R, Ripepe M, Braun T (1994) *Highlights from a seismic broadband array on Stromboli volcano*. Geophys Res Lett, 21(9):749-752

Nguyen CT, Gonnermann HM, Chen Y, Huber C, Maiorano AA (2013) *Film drainage and the lifetime of bubbles*. Geochem Geophys Geosyst, 14:3616–3631

Nishi K, Hendrasto M, Mulyana I, Rosadi U, Purbawinata MA (2007) *Micro-tilt changes preceding summit explosions at Semeru volcano, Indonesia*. Earth Planets Space 59:151–156

Nishimura T (2009) *Ground deformation caused by magma ascent in an open conduit*. J Volcanol Geotherm Res. doi:10.1016/j.jvolgeores.2009.09.001

Nishimura T, Iguchi M, Yakiwara H, Oikawa J, Kawaguchi R, Aoyama H, Nakamichi H, Ohta Y, Tameguri T (2013) *Mechanism of small Vulcanian eruptions at Suwanosejima Volcano, Japan, as inferred from precursor inflations and tremor signals*. Bull Volcanol. 75:1–12

Nogueira S, Rietmuler ML, Campos JBLM, Pinto AMFR (2006a) *Flow in the nose region and annular film around a Taylor bubble rising through vertical columns of stagnant and flowing Newtonian liquids*. Chem Engine Sci, 61(2):845 – 857, doi: 10.1016/j.ces.2005.07.038

Nogueira S, Riethmuller ML, Campos JBLM. Pinto AMFR (2006b) *Flow patterns in the wake of a Taylor bubble rising through vertical columns of stagnant and* *flowing Newtonian liquids: An experimental study*. Chem Engine Sci, 61(22):7199-7212

O’Brien GS, Bean CJ (2008) *Seismicity on volcanoes generated by gas slug ascent*. Geophys Res Lett. 35:L16308

Parfitt EA, Wilson L (1995) *Explosive volcanic eruptions: IX The transition between Hawaiian-style lava fountaining and Strombolian explosive activity*. Geophys J Int, 121:226-232

Parfitt EA (2004) *A discussion of the mechanisms of explosive basaltic eruptions*. J Volcanol Geotherm Res, 134(1–2):77–107, doi:10.1016/j.jvolgeores.2004.01.002

Patrick MR (2007) *Dynamics of Strombolian ash plumes from thermal video: Motion, morphology, and air entrainment*. J Geophys Res, 112:B06202, doi:10.1029/2006JB004387

Patrick MR, Harris AJL, Ripepe M, Dehn J, Rothery DA, Calvari S (2007) *Strombolian explosive styles and source conditions: insights from thermal (FLIR) video*. Bull Volcanol. doi: 10.1007/s00445-006-0107-0

Pino NA, Moretti R, Allard P, Boschi E (2011) *Seismic precursors of a basaltic paroxysmal explosion track deep gas accumulation and slug upraise*. J Geophys Res, 116:B02312, doi:10.1029/2009JB000826

Pioli L, Bonadonna C, Azzopardi BJ, Phillips JC, Ripepe M (2012) *Experimental constraints on the outgassing dynamics of basaltic magmas*. J Geophys Res, 117:B03204, doi:10.1029/2011JB008392

Pistolesi M, Delle Donne D, Pioli L, Rosi M, Ripepe M (2011) *The 15 March 2007 explosive crisis at Stromboli volcano, Italy: Assessing physical parameters through a multidisciplinary approach*. J Geophys Res, 116:B12206, doi:10.1029/2011JB008527

Polacci M, Corsaro RA, Andronico D (2006) *Coupled textural and compositional characterization of basaltic scoria: insights into the transition from Strombolian to fire fountain activity at Mount Etna, Italy*. Geology 34:201

Polacci M, Baker DR, Mancini L, Favretto S, Hill RJ (2009) *Vesiculation in magmas from Stromboli and implications for normal Strombolian activity and paroxysmal explosions in basaltic systems*. J Geophys Res, 114:B01206, doi: 10.1029/2008JB005672

Proussevitch AA, Sahagian DL, Anderson AT (1993) *Dynamics of diffusive bubble growth in magmas: Isothermal case*. J Geophys Res, 98:22283-22308.

Proussevitch AA, Sahagian DL (1996), *Dynamics of coupled diffusive and decompressive bubble growth in magmatic systems.* J Geophys Res, 101:17447-17445

Ripepe M, Rossi M, Saccorotti G (1993) *Image processing of explosive activity at Stromboli*. J Volcanol Geotherm Res, 54:335-351

Ripepe M, Poggi P, Braun T, Gordeev E (1996) *Infrasonic waves and volcanic tremor at Stromboli*. Geophys Res Lett, 23(2):181-184

Ripepe M, Gordeev E (1999) *Gas bubble dynamics model for shallow volcanic tremor at Stromboli*. J Geophys Res, 104(B5):10639-10654

Ripepe M, Ciliberto S, Della Schiava M (2001) *Time constraints for modeling source dynamics of volcanic explosions at Stromboli*. J Geophys Res-Sol Ea, 106(B5):8713-8727

Ripepe M, Marchetti E (2002) *Array tracking of infrasonic sources at Stromboli volcano*. Geophys Res Lett, 29(22):33-1. doi: 10.1029/2002GL015452

Ripepe M, Harris AJL, Carniel R (2002) *Thermal, seismic and infrasonic evidences of variable degassing rates at Stromboli volcano*. J Volcanol Geotherm Res, 118:285-297

Ripepe M, Marchetti E, Ulivieri G (2007) *Infrasonic monitoring at Stromboli Volcano during the 2003 effusive eruption: insights on the explosive and degassing process of an open conduit system*. J Geophys Res-Sol Ea 112

Ripepe M, Delle Donne D, Harris A, Marchetti E, Ulivieri G (2008) *Dynamics of Strombolian activity. The Stromboli Volcano: An Integrated Study of the 2002-2003 Eruption*, 39-48

Ripepe M, Delle Donne D, Lacanna G, Marchetti E, Ulivieri G (2009) *The onset of the 2007 Stromboli effusive eruption recorded by an integrated geophysical network*. J Volcanol Geotherm Res, 182:131-136

Rosi M, Bertagnini A, Landi P (2000) *Onset of the persistent activity at Stromboli Volcano (Italy)*. Bull Volcanol. doi: 10.1007/s004450000098

Ruth DCS, Calder ES (2013) *Plate tephra: preserved bubble walls from large slug bursts during violent Strombolian eruptions*. Geology 42:11–14

Sánchez C, Álvarez B, Melo F, Vidal V (2014) *Experimental modeling of infra-sound emission from slug bursting on volcanoes*. Geophys Res Lett, 41(19):6705–6711

Seyfried R, Freundt A (2000) *Experiments on conduit flow and eruption behaviour of basaltic volcanic eruptions*. J Geophys Res, 105(B10):727-740, doi: 10.1029/2000JB900096

Shaw HR (1969) *Rheology of Basalt in the Melting Range*. J Petrol, 10:510-535

Sousa RG, Pinto AMFR, Campos JBLM (2006) *Effect of gas expansion on the velocity of a Taylor bubble: PIV measurements*. Int J Multiphas Flow, 32:1182-1190

Spina L, Taddeucci J, Cannata A, Gresta S, Lodato L, Privitera E, Scarlato P, Gaeta M, Gaudin D, Palladino DM (2015) *Explosive volcanic activity at Mt. Yasur: A characterization of the acoustic events (9–12th July 2011)*. J Volcanol Geotherm Res.

Sparks RSJ (1978) *The dynamics of bubble formation and growth in magmas: A review and analysis*. J Volcanol Geotherm Res, 3:1-37

Sparks RSJ (2003) *Dynamics of magma degassing* in Oppenheimer C, Pyle DM, Barclay J (Eds) *Volcanic Degassing*, 5-22, Geol Soc, London

Taddeucci J, Pompilio M, Scarlato P (2002) *Monitoring the explosive activity of the July–August 2001 eruption of Mt Etna (Italy) by ash characterization*. Geophys Res Lett 29:1029–1032, DOI:10.1029/2001GL014372

Taddeucci J, Pompilio M, Scarlato P (2004) *Conduit processes during the July–August 2001 explosive activity of Mt Etna (Italy): inferences from glass chemistry and crystal size distribution of ash particles*. J Volcanol Geotherm Res 137:33–54, DOI:10.1016/j.jvolgeores.2004.05.011

Taddeucci J, Scarlato P, Capponi A, Del Bello E, Cimarelli C, Palladino DM, Kueppers U (2012a) *High-speed imaging of Strombolian explosions: The ejection velocity of pyroclasts*. Geophys Res Lett, 39(2):L02301, doi: 10.1029/2011GL050404

Taddeucci J, Alatorre-Ibargüengoitia MA, Moroni M, Tornetta L, Capponi A, Scarlato P, Dingwell DB, De Rita D (2012b) *Physical parameterization of Strombolian eruptions via experimentally-validated modelling of high-speed observations*. Geophys Res Lett. doi:10.1029/2012GL052772

Taddeucci J, Palladino DM, Sottili G, Bernini D, Andronico D, Cristaldi A (2013a) *Linked frequency and intensity of persistent volcanic activity at Stromboli (Italy)*. Geophys Res Lett. doi: 10.1002/GRL.50652

Taddeucci J, Valentine GA, Sonder I, White JDL, Ross P-S, Scarlato P (2013b) *The effect of pre-existing craters on the initial development of explosive volcanic* *eruptions: an experimental investigation*. Geophys Res Lett. doi: 10.1002/grl.50176

Taddeucci J, Sesterhenn J, Scarlato P, Stampka K, Del Bello E, Pena Fernandez JJ, Gaudin D (2014) *High-speed imaging, acoustic features, and aeroacoustic computations of jet noise from Strombolian (and Vulcanian) explosions*. Geophys Res Lett. doi:10.1002/2 014GL05992 5

Taddeucci J, Edmonds M, Houghton B, James MR, Vergniolle S (2015) *Hawaiian and Strombolian Eruptions*. In: Sigurdsson H, Houghton B, Rymer H, Stix J, McNutt S (eds.) *The Encyclopedia of Volcanoes*, 2nd edn, Academic Press, Amsterdam, 485–503

Taha T, Cui ZF (2006) *CFD modelling of slug flow in vertical tubes*. Chem Eng Sci, 61(2):676-687

Tamburello G, Aiuppa A, Kantzas EP, McGonigle AJS, Ripepe M (2012) *Passive vs. active degassing modes at an open-vent volcano (Stromboli, Italy)*. Earth Planet Sci Lett, 359:106-116

Toramaru A (1995) *Numerical study of nucleation and growth of bubbles in viscous magmas*. J Geophys Res-Sol Ea, 100(B2):1913-1931

Valentine GA, Krier D, Perry FV, Heiken G (2005) *Scoria cone construction mechanisms, Lathrop Wells volcano, southern Nevada, USA*. Geology 33:629–632, DOI 10.1130/G21459.1

Valentine GA, Gregg TKP (2008) *Continental basaltic volcanoes – Processes and problems*. J Volcanol Geother Res, 177:857–873, doi:10.1016/j.jvolgeores.2008.01.050

Vergniolle S, Jaupart C (1986) *Separated two-phase flow and basaltic eruptions*. J Geophys Res, 91(B12):12842-12860

Vergniolle S, Brandeis G (1994) *Origin of the sound generated by Strombolian explosions*. Geophys Res Lett, 21(18):1959-1962

Vergniolle S (1996) *Bubble size distribution in magma chambers and dynamics of basaltic eruptions*. Earth Planet Sci Lett, 140(1):269-279

Vergniolle S, Brandeis G (1996) *Strombolian explosions 1. A large bubble breaking at the surface of a lava column as a source of sound*. J Geophys Res, 101(B9):433–447

Vergniolle S, Brandeis G, Mareschal JC (1996) *Strombolian explosions 2. Eruption dynamics determined from acoustic measurements*. J Geophys Res, 101(B9):449-466

Vergniolle S (1998) *Modelling two-phase flow in a volcano*. In: Proc 13th Australian Fluid Mech Conf Aristoc Offset, Monash University, Melbourne, 647-650

Vergniolle S, Boichu M, Caplan-Auerbach J (2004) *Acoustic measurements of the 1999 basaltic eruption of Shishaldin volcano, Alaska 1. Origin of Strombolian activity*. J Volcanol Geother Res, 137:109-134, doi:10.1016/j.volgeores.2005.05.003

Verne J (1864) *Voyage au centre de la terre*. Hetzel.

Viana F, Pardo R, Yanez R, Trallero J, Joseph D (2003) *Universal correlation for the rise velocity of long gas bubbles in round pipes*. J Fluid Mech, 494:379-398

Vona A, Romano C, Dingwell DB, Giordano D (2011) *The rheology of crystal-bearing basaltic magmas from Stromboli and Etna*. Geochim Cosmochim Acta, 75:3214–3236, doi:10.1016/j.gca.2011.03.031

Wallace P, Anderson AT (2000) *Volatiles in Magmas*, In Sigurdsson H, Houghton B, McNutt SR, Rymer H, Stix J (Eds) *Encyclopedia of Volcanoes*, 149-170, Academic Press, San Diego, California

Wallace P (2005) *Volatiles in subduction zone magmas: concentrations and fluxes based on melt inclusion and volcanic gas data*. J Volcanol Geother Res 140:217-240

Wallis GB (1969) *One-dimensional Two-phase Flow*. McGraw Hill, New York

Washington HS (1917) *Persistence of vents at Stromboli and its bearing on volcanic mechanism*. G Soc Am B 28:249-278

Weill A, Brandeis G, Vergniolle S, Baudin F, Bilbille J, Fèvre JF, Piron B, Hill X (1992) *Acoustic sounder measurements of the vertical velocity of volcanic jets at Stromboli volcano*. Geophys Res Lett, 19(23):2357-2360

White ET, Beardmore RH (1962) *The velocity of rise of single cylindrical air bubbles through liquids contained in vertical tubes*. Chem Eng Sci,17:351–361

Wilson L, Head III JW (1981) *Ascent and Eruption of Basaltic Magma on the Earth and Moon*. J Geophys Res, 86(B4):2971-3001

Woulff G, McGetchin TR (1976) *Acoustic noise from volcanoes — theory and experiment*. Geophys J Roy Astron Soc, 45 (3):601–616

Zukoski EE (1966) *Influence of viscosity, surface tension, and inclination angle on motion of long bubbles in closed tubes*. J Fluid Mech, 25:821–837